Emergence and Control of Crystal Chirality via Achiral Precursor in Sodium Chlorate Chiral Crystallization from Aqueous Solution

Hiromasa Niinomi

TABLE OF CONTENTS

CHAPTER 1
INTRODUCTION

1.1 Chirality

1.1.1 Fundamental of Chirality

Chirality is the concept that a certain three-dimensional structure is non-superimposable with its mirror image, that is, a lack of mirror symmetry. Shapes of our hands are intuitively understandable examples of chiral structure (Fig. 1.1). Left hand is the mirror image of right hand and their structures are non-superimposable with each other. In connection with this, the term chirality comes from "cheir", which means "hands" in Greek. Another understandable example is helix structure such as a screw. Helix of right-screw (right-handed helix) is non-superimposable with that of left-screw (left-handed helix). The strict definition of chirality is the lack of "improper rotation axis", which is denoted as S_n in accordance with the Schönflies notation, in symmetry elements of a structure. The improper rotation is the combination of rotation operation, C_n, in arbitrary axis with reflection operation, σ, in the plane perpendicular to the axis (Fig. 1.2). Indeed, the shape of hands and helix structure similarly lack S_n. Conversely, a structure which contains S_n in its symmetry elements is called as "achiral". The concept of chirality is not just symmetry operation but has great significance in our lives because the concept is fundamental and ubiquitous property in nature. Instances which exhibits chirality include the molecular structure of amino acids, the double helix structure of DNA, the crystal structure of quartz, the shapes of snails, the helix of winding plants and forth other than the structure of our hands, showing that the concept of chirality widely spreads at various scale and location (Fig.1.1). Therefore, it can be said that chirality is a significant concept to describe our lives and nature.
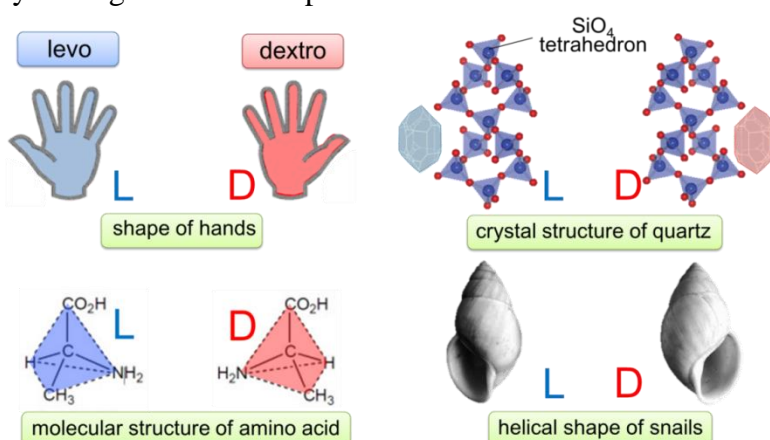
Fig. 1.1 Typical examples of chiral structure. Chirality widely exists in various hierarchies from molecular structure to macroscopic morphologies of living organisms.
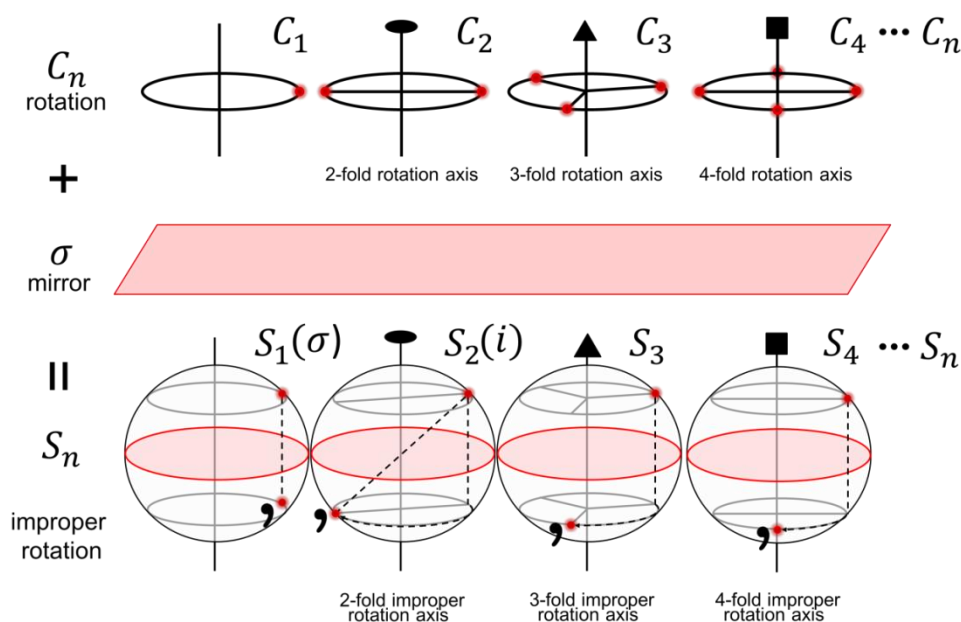
Fig. 1.2 Schematic illustration showing improper rotation. Improper rotation is the combination of rotation and mirror. Chirality is the lack of improper rotation.

One of a pair of chiral mirror isomers is often dubbed as "enantiomer" and either of the enantiomers is designated as "*l*"-type and "*d*"-type for the other. The prefix letters "*l*" and "*d*" come from "*levo*" and "*dextro*", which respectively mean "left" and "right" in Greek, in correspondence with the expression likened to "handedness". Accordingly, when one specifies each "handedness" of a pair of chiral molecules the enantiomers are discriminated as "*l- molecular name*" and "*d- molecular name*" respectively. Although there are other notations to specify "handedness" of chiral objects in practice, e.g. "L" and "D", "S" and "R" or "(-)" and "(+)", the notation "*l*" and "*d*" or "(-)" and "(+)" are adopted when chiroptical property of a chiral material is focused. On the other hand, the notation "L" and "D" or "S" and "R" are adopted when structure of a chiral compound is focused. The former notation comes from the direction of optical rotation originating from optical activity, which chiral materials intrinsically exhibit. The optical activity is the property that rotates a plane of polarized light. Since chiral materials have optical activity, the plane of a polarized light which passed through a chiral material rotates to clockwise direction or counter-clockwise direction depending on the handedness of the objects. If either of enantiomers rotates the plane of polarized light clockwise the other certainly rotates the plane counter-clockwise, meaning that the direction of optical rotation is opposite between a pair of enantiomers. This property which rotate plane of the light counter-clockwise and clockwise is reworded as "*levorotatory*" and

"*dextrorotatory*", respectively, and the notation "*l*" and "*d*" come from the initial letters of these two words. Namely, the enantiomer which exhibits levorotatory is defined to be "*l*"-type and the one which exhibits dextrorotatory is defined to be "*d*"-type (Fig. 1.3). In addition, the notations "(-)" and "(+)" corresponds to "*l*" and "*d*", respectively. The latter notations, "L" and "D" or "S" and "R," are labeled from a viewpoint of structure of chiral objects. The rule of thumb for determining the "D" or "L" isomeric form of **amino acid** is the "CORN" rule. The rule is as follows. If one draws a circle with following the order 1.**CO**OH (carboxyl group), 2.**R** (side-chain)**,** 3.**NH**$_2$ (amino group), 4.H, which are arranged around the chiral carbon center, and the orbital of the circle is clockwise, the enantiomer is labeled as "D" and *vice versa*. On the other hand, determination of the "D" or "L" isometric structure of **crystal structure** follows the handedness of helical chain of constituent atoms. In the case of the crystal structure of quartz (SiO$_2$), the tetrahedral of silicate connect with each other like chain and the chain forms helical structure, The handedness of the helix determines "D" or "L" and if the helix is right-handed the crystal is labeled as "D" and *vice versa*. This thesis uses the notation of "*l*" and "*d*" or "L" and "D" depending on context. One should note that "*l*" does not necessarily correspond to "L" and *vice versa*, meaning that L-crystal does not necessarily show levorotatory and sometimes exhibits dextrorotatory.
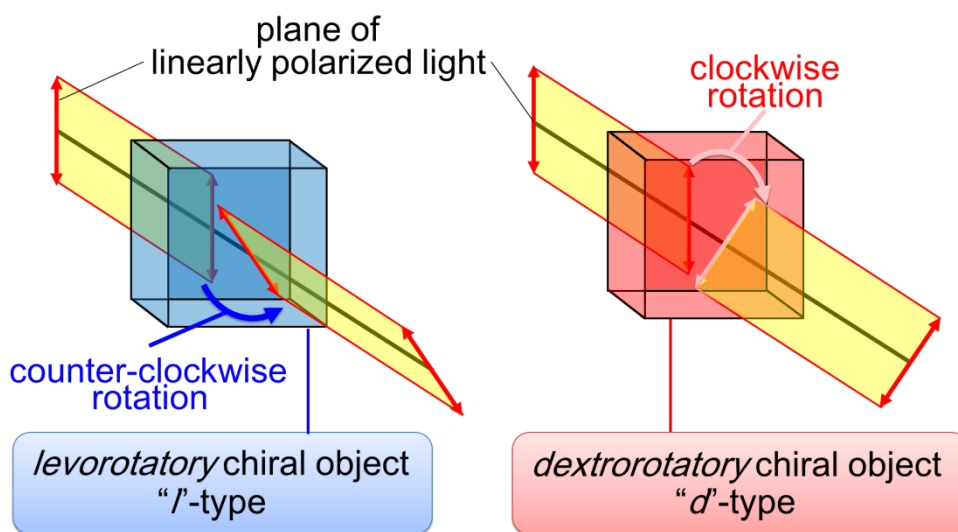
Fig. 1.3 Optical rotation by chiral object. The plane of linearly polarized light that passed through a chiral medium rotates to clockwise or counter-clockwise depending on the handedness of the chiral medium. The handedness that rotates the plane clockwise is designated as "*d*"(dextrorotatory) and *vice versa*.

In principle, a pair of enantiomers shows the same physical and chemical properties, such as melting point, solubility, mass and forth, except for chirally asymmetric interaction with electromagnetic field due to optical activity mentioned above. Therefore, a pairs of enantiomers have the same thermodynamic stability. In practice, it is known that artificial chemical synthesis of chiral compounds yields an equal amount of two enantiomers. Namely, the both of enantiomers should arise in equal amount and probability.

1.1.2 Chiral Symmetry Breaking and Our life

Despite of the thermodynamic equality in enantiomers, nature on the earth crucially prefers chirally asymmetric state [1]. For instance, when one looks for snails having helical shell at seaside almost only either of the two enantiomeric form can be found and also when one looks for winding plant in forest only either of helicity can be found. Furthermore, in microscopic view, living organisms on the earth preferentially selects one type of two enantiomeric molecules as constituent of their body. Amino acids which construct proteins in our body are only "l"-type, and only "d"-sugars are adopted as the constituent (Fig. 1.4). "Chiral Symmetry Breaking" is the term used to describe such the occurrence of an imbalance between enantiomers. Namely, chiral symmetry in living organisms on the earth is completely broken from molecular level. The contradiction between the thermodynamic equality of enantiomers and the asymmetric nature has fascinated many scientists. However, the origin of chiral imbalance and its amplification process still remain controversial. This problem is known as "homochirality problem".

Since human body is constructed by only either of two enantiomers, the body sensitively recognizes the handedness of enantiomers. As a consequence, the body shows entirely different reactions depending on the handedness of a chiral compound when a chiral compound is dosed to their body. For instance, limonene molecule is chiral and the each enantiomer shows different bioactivity. Whereas D-form of limonene has a flavor of lemon, L-form has a flavor of orange. In addition, difference of bioactivity in enantiomers of chiral pharmaceutical agent sometimes brings about serious situations. Although D-Thalidomide is harmlessly utilized as a medicine for travel-sickness, L-thalidomide has strong teratogenicity. The famous thalidomide disaster was the tragedy caused by the contamination of the harmful L-form in a commercial medicine. Therefore, methodologies for enantioselective fabrication and separation of chiral compounds are strongly desired to be established.

As written above, chirality plays crucial role for our life. The important point is to understand how to achieve chiral separation and its mechanism.
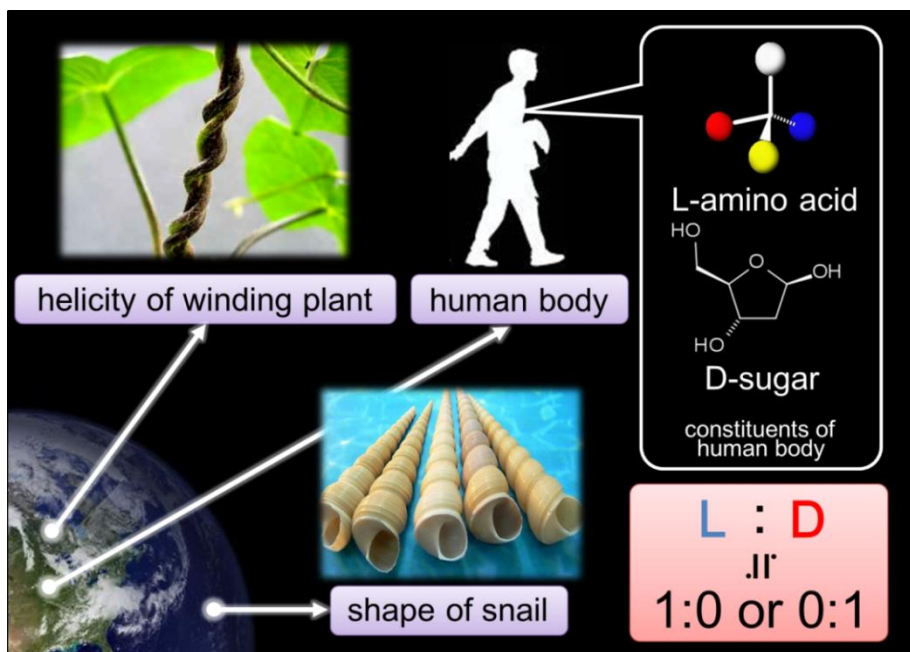
Fig. 1.4 Biohomochirality on the earth. Chiral symmetry is broken in living organism on the earth. This schematic indicates the instances, winding plants, snails, amino acids and sugars that construct human body.

1.1.3 Crystal Chirality and its Significance in Our Lives

1.1.3.1 Origin of Biohomochirality and Crystal Chirality

The origin of the biohomochirality on the earth is rationalized by various hypotheses. They are mainly classified into three scenarios: (1) Intrinsic scenario, (2) extraterrestrial scenario (3) Terrestrial scenario. The Intrinsic scenario is based on parity violating energy difference (PVED) [2]. Electro weak quantum calculations show that two enantiomers exhibits a very small difference between them [3-5], which is about in the magnitude of 10^{-12} (Jmol^{-1}) [2], and the small difference is considered to be the origin of chiral asymmetry in the intrinsic scenario. However, the PVED is small and would require amplification by factors $\leq 10^{17}$ to account for homochirality [6]. Furthermore, a relationship between the biohomochirality and the parity violation is not yet supported by experimental findings. The extraterrestrial scenario ascribes the origin of asymmetry to selective excitation and decomposition of D-amino acid on incoming meteorite by right-handed circularly polarized light emitted from an object in space [7]. This scenario is based on the fact that the small enantiomeric excess was found in amino acid on Murchison meteorite[8], implying the possibility that the chiral asymmetry comes from somewhere in out space. Although circularly polarized light emission from

5

star-formation region was actually observed [7], it is not easy to prove the extraterrestrial scenario because direct evidence cannot be obtained. Finally, in terrestrial scenario, the origin of the chiral asymmetry is ascribed to asymmetric interaction between **chiral crystal surface** and chiral organic compounds. It is known that a chiral surface of a crystal asymmetrically interacts with a chiral molecule. Calcite crystal, whose space group is achiral, forms enantiomorphic crystal surface structures on $(3\bar{1}21)$ and $(21\bar{3}1)$ faces of the common $[21\bar{3}1]$ trigonal scalenohedral of the crystal. The chiral surfaces exhibit significant enantioselective adsorption of chiral aspartic acid when a rhombohedral calcite crystal with the enantiomorphic faces was immersed in an aqueous solution of racemic (i.e. mixture of equal amount of two enantiomers) aspartic acid (Fig. 1.5)[9]. Moreover, the shape of growth hillocks of the calcite crystal surface is asymmetrically modified by the addition of L- or D-aspartic acid during crystal growth. Calcite crystal has two steps acute to the {104} cleavage plane and two steps obtuse to the cleavage plane while forming rhombus. The two obtuse steps are related through a glide-plane symmetry element, as are the two acute steps. On the other hand, the acute and obtuse steps are in the relationship of mirror image. The shape of theses chiral surfaces are asymmetrically modified by addition of chiral aspartic acid and its shape depends on the handedness of the additive, whereas the addition of an achiral glycine does not break the symmetry of the glide plane (Fig. 1.6) [10]. Depending on the handedness of the aspartic acid, the growth rates of the enatiomorphic crystals steps and terraces changed asymmetrically and this resulted in an overall macroscopic chiral shape [11,12]. These demonstrations of asymmetric interaction between chiral crystal surface and prebiotic chiral amino acid provided the hypothesis that nurture of prebiotic organic compounds on the chiral surface is origin of biohomochirality. Furthermore, it has also reported that a chiral inorganic crystal acts as chiral initiator of asymmetric autocatalysis [13]. Asymmetric autocatalysis in which the chiral product of the chemical reaction serves as a catalyst to produce itself more and to suppress of the opposite enantiomer yields high enentiomeric excess, defined as $(N_R-N_S)/(N_R+N_S)$ where N_R and N_S are the numbers of R-enantiomer and S-enantiomer respectively, that is, significant chiral imbalance from almost racemic state, thus providing a mechanistic model for the evolution of homocirality [14]. (S)-5-Pyrimidyl alkanols with 98 % enantiomeric excess were obtained by asymmetric autocatalysis in the presence of *d*-sodium chlorate crystals and *vice versa* [13]. This enantioselective amplification of chirality directed by the presence of chiral crystal surface actually demonstrated that the direction of handedness of biohomochirality by the crystal surface may occur in practice. The hypothesis of

chiral crystal-surface-mediated biohomochirality has been supported by many experimental findings, thus it can be said that crystal chirality has a great possibility to play a crucial role on the origin and evolution of biohomochirality.
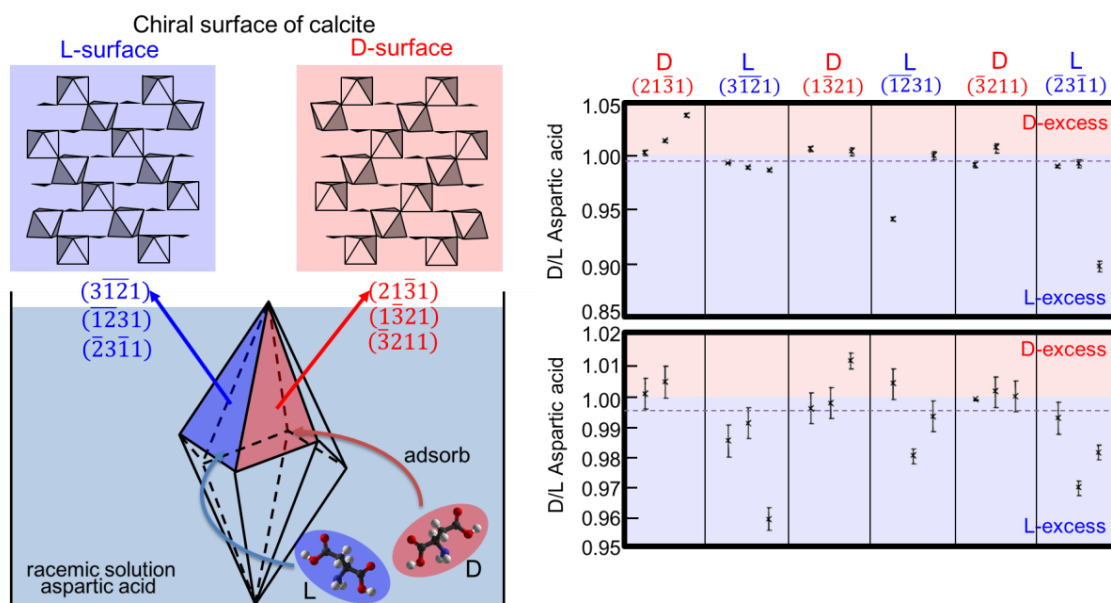
Fig. 1.5 Enantioselective adsorption of chiral aspartic acid on chiral surfaces of calcite crystal in Ref. [9]. Left schematic shows the overview of the experimental procedure in Ref. [9]. Right figure shows the ratio of both enantiomers that adsorbed on each chiral surface. The figure indicates D-aspartic acid preferentially adsorbs on D-chiral surface of calcite and *vice versa*.
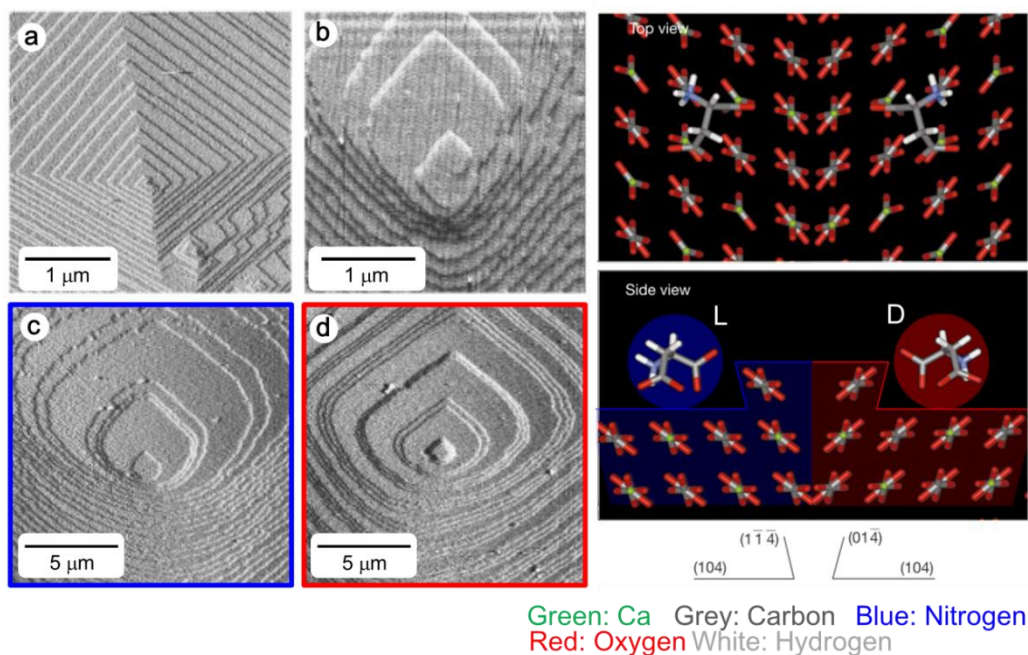
Fig. 1.6 Surface morphology modification of calcite crystal by addition of chiral aspartic acid, reported by Orme *et al*. [10]. Left micrographs shows surface morphologies modified by various conditions; (a) AFM image of growth hillock of calcite in pure aqueous solution. (b) in supersaturated solutions with 0.01 M achiral glycine molecule. (c) with 0.01 M L-aspartic acid. (d) with 0.01 M D-aspartic acid. Right schematic indicates the geometry of binding for aspartic acid adsorbed on the single (104) steps of calcite. Upper and lower schematics are top and side views of L-aspartic acid (blue) and D-aspartic acid (red) binding to the steps of calcite with $(1\bar{1}\bar{4})$ risers and $(0\bar{1}\bar{4})$ risers, respectively.

1.1.3.2 Pharmaceutical Industry and Crystal Chirality

As stated above, methodologies for optical resolution, separation of two enantiomers, are desired to be established in the field of pharmaceutical industry because of distinct bioactivity of the enantiomers. Here it should be noticed that the important process is not only the separation of enantiomers but also the crystallization of chiral pharmaceutical compounds because chiral drugs are generally dosed in the form of crystal. There are three distinct types of crystals constructed by a chiral molecule: (1) Racemic crystal, (2) Conglomerate crystal, (3) Pseudoracemate. The racemic crystal is a crystal in which equal numbers of two enantiomers is packed alternately (Fig. 1.7). Optical activity of racemic crystal is thus inactivated as a consequence of the alternative arrangement of enantiomers. The conglomerate crystal is a crystal composed by only either of two enantiomers. Namely, the conglomerate crystal is enentiomerically pure. Pseudoracemate means a solid solution composed by randomly packed two enantiomers. Crystallization from solution is considered to be one of the useful methods for optical resolution. As demonstrated by Louis Pasteur's classic experiment of tartaric acid crystallization from a racemic aqueous solution [15], spontaneous optical resolution from a racemic solution can be easily achieved by crystallization if the target compound belongs to the system which yields conglomerate crystal as the most thermodynamically stable crystal. However, most of chiral compounds, 90 % of systems, belong to the system in which racemic crystal is the most stable crystal, being challenge on the optical resolution by means of crystallization. Achievement to resolve enantiomer in such the system by crystallization leads to the reduction of cost and process involved in the purification of enantiomers by chemical reaction, motivating engineers in the field of industrial crystallization. The method for optical resolution by crystallization includes the preferential crystallization method, asymmetric crystallization method and forth (Here, the author introduce the methods that do not involve the chemical reaction.). In the preferential crystallization method, seeding of an enantiomerically pure conglomerate crystal in a supersaturated racemic solution leads to efficient optical resolution because the seed crystal grows with consumption of the same enantiomer as the seed crystal in the solution. In the asymmetric crystallization, optical resolution is led by establishing the difference in the nucleation rate of two enantiomers using a chiral tailor-made co-solute [16]. As described above, the crystal chirality and its crystallization technique are closely related to pharmaceutical industry. Therefore, chirality in crystal and crystallization has a crucial role on our life.
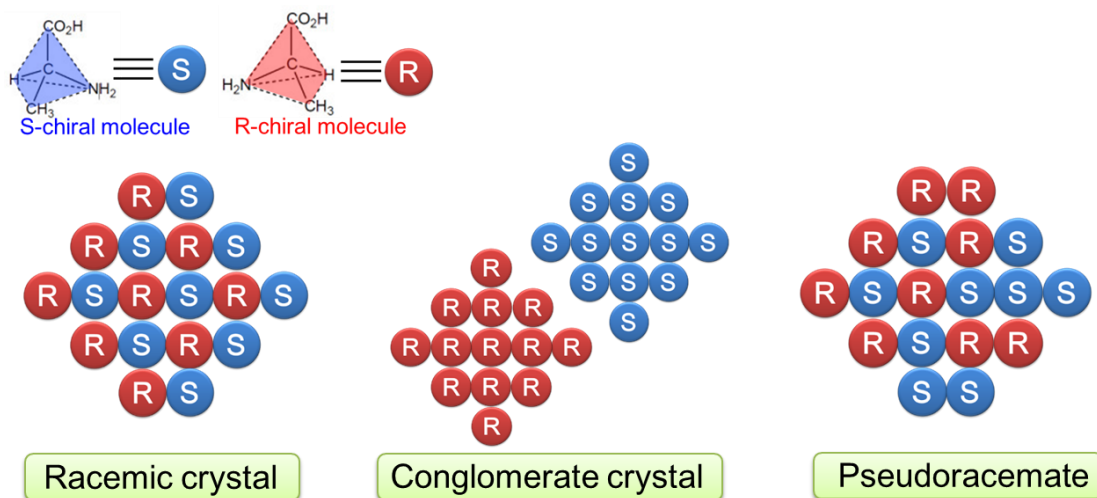
Fig. 1.7 Three types of crystals composed by chiral molecules. Left schematic indicates racemic crystal, in which the equal numbers of both enantiomers are alternately packed. Middle schematic indicates enantiomerically pure conglomerate crystal, which is constructed by only either of enantiomer. Right schematic indicates pseudoracemate, in which the equal numbers of enantiomers are randomly packed in the crystal structure.

1.1.3.3Materials for Spintronics Devices and Crystal Chirality

Recently, magnet materials with chiral crystal structure have been received increasing attention in the field of material science and spintronics because the properties of the electronic spin texture called as "skyrmion" uniquely underlying in the chiral crystal structure is considered to provide a great advantage for high-density and low-current driven magnetic storage devices [17]. The skyrmion is a topologically stable particle-like object, which appears as a vortex-like swirling spin texture, and shows chirality originating from the freedom in the direction of curl in the vortex. Because the skyrmion lattice is based on helical arrangement of magnetic moment resulted from the competition between ferromagnetic exchange interaction, which tries to align all the magnetic moments in the same direction, and the relativistic spin-orbit Dzyaloshinskii-Moriya (DM) interaction, which favors screw-like arrangement of magnetic moment. It should be noted that the DM interaction is canceled out in achiral crystal structure but the interaction becomes effective in a chiral crystal structure [18]. Therefore, the skyrmion lattice occurs uniquely in the magnets that have chiral crystal structure. Moreover, the handedness of the skyrmion is unambiguously correlated with the handedness of chiral crystal structure. Because control of size and handedness of the skyrmion is required for application, the method to control crystal chirality will be desired to be established not only in the pharmaceutical industry but also in the field of

material science especially for future spintronic devices.

Instance of materials for chiral magnets includes manganese silicide (MnSi) crystal belonging to chiral space group $P2_13$ (see next section) with cubic lattice (Fig. 1.8) [19]. In most cases, the compounds that construct chiral magnets are inorganic materials that are intrinsically achiral, thus acquiring chirality during crystallization process. Such a system should be distinguished from the system in which compounds are intrinsically chiral seen in crystallization of drugs. The details are described in the next section.

Fig. 1.8 Correspondence of the handedness of MnSi crystal, chiral magnet crystal, and the handedness of skyrmion observed in the crystal. Crystal structure of MnSi comprises of achiral atoms but has chirality because of chiral space group $P2_13$. Skyrmion, nanoscopic vortex like spin texture, can be observed in MnSi crystal under adequate condition. The handedness of skyrmion and the handedness of the crystal structure show one-to-one correspondence. [19]

1.2 Chiral Symmetry Breaking in Sodium Chlorate Crystallization from a Stirred Aqueous Solution

1.2.1 Chiral Crystallization -Crystallization and Chirality-

Some achiral compounds crystallize as chiral enantiopure crystal with chiral space groups summarized in Table 1.1 (chiral space group can be reworded as non-centrosymmetric space group). Namely, those compounds acquire chirality during crystallization. Crystallization of achiral compounds into a crystal with chiral space groups is called as "chiral crystallization". Whereas two mirror isomers of chiral molecule are dubbed as enantiomers, the two of chiral crystal are dubbed as "enantiomorphs". Instance of chiral crystallization includes crystallization of α-quartz. While tetrahedral structure of SiO_4, which is building unit of quartz crystal, is achiral, periodic chains of the building units are helically arranged in the crystal structure. Because of the helical arrangement, quartz crystal exhibits chiral space group of $P3_121$. Namely, chirality and optical activity emerge from optically inactive achiral state during crystallization process. Several researchers have considered that emergence of chirality by chiral crystallization has possibility to bear the origin of chiral asymmetric state on the earth [20]. In addition, most of the crystallization of the chiral magnetic materials belongs to the system of chiral crystallization, implying that research of chiral crystallization will increasingly become important in the future.

Table 1.1 Chiral space groups

Crystal system	Class	Chiral space group
Triclinic	1	$P1$
Monoclinic	2	$P2$, $P2_1$, $C2$
Orthorhombic	222	$P222$, $P222_1$, $P2_12_12$, $P2_12_12_1$, $C222_1$, $C222$, $F222$, $I222$, $I2_12_12_1$
Tetragonal	4	PA, $P4_1$, $P4_2$, $P4_3$, $I4$, $I4_1$
	422	$P422$, $P42_12$, $P4_122$, $P4_12_12$, $P4_222$, $P4_22_12$, $P4_322$, $P4_32_12$, $I422$, $I4_122$
Trigonal and Rhombohedral	3	$P3$, $P3_1$, $P3_2$, $R3$
	32	$P312$, $P321$, $P3_112$, $P3_121$, $P3_212$, $P3_121$, $R32$
Hexagonal	6	$P6$, $P6_1$, $P6_5$, $P6_2$
	622	$P622$, $P6_122$, $P6_522$, $P6_222$, $P6_422$, $P6_322$
Cubic	23	$P23$, $F23$, $I23$, $P2_13$, $I2_13$
	432	$P432$, $P4_232$, $F432$, $F4_132$, $I432$, $F4_332$, $P4_132$, $I4_132$

1.2.2 Chiral Crystallization and Sodium Chlorate

Crystallization of sodium chlorate ($NaClO_3$) from aqueous solution is a typical example of chiral crystallization. Solution of this salt is optically inactive, that is, achiral because the solution consists of only achiral components: spherical sodium cations, pyramidal chlorate anions having C_{3v} symmetry and water molecules [21] (Fig. 1.9). The achiral solution yields chiral enantiopure crystals having cubic chiral space group $P2_13$ with lattice constant $a = 6.583$ (Å) (Fig. 1.9)[22]. The crystal structure may be considered as a slightly distorted NaCl structure with replacement of chloride to chlorate. The planes outlined by O_3 groups of pyramidal chlorate anions are not parallel but arranged in helical configuration [23,24]. This configuration gives rise to optical activity. L-crystal exhibits levorotatory and *vice versa* (the notation of "L/D" orderly corresponds to "*l/d*"). The handedness of the enantiomorph is easily identified by use of a pair of polarizers owing to optical isotropy of cubic crystals whereas it is not easy to identify the handedness of chiral crystals with non-cubic symmetry. Fig. 1.10 shows the identification of handedness of $NaClO_3$ crystal. The $NaClO_3$ crystals set between a pair of polarizer exhibits slightly bright color when the polarizers are orthogonally oriented (crossed nicols orientation). Rotating the upper polarizer to clockwise from the crossed nicols orientation, a *d*-crystal becomes dark and *vice versa*. Thus, it is possible to identify the handedness of the crystal.

In 1898, Kipping and Pope have investigated the occurrence ratio of the enantiomorphs which crystalize from static saturated solution by simple evaporation. They have performed 46 separate crystallizations and analyzed the handedness of 3137 resulting crystals. According to their analysis, 1571 crystals out of the 3137 crystals were *d*-crystals, meaning that crystal enantiomeric excess (CEE), which is an indicator for the degree of chiral asymmetry and is defined as

$$\text{CEE} = \frac{n_d - n_l}{n_d + n_l} \qquad (1.1)$$

where n_d is the number of *d*-crystal and n_l is the number of *l*-crystal, was almost 0 %. This results show that crystallization from a static solution provides statistically equal numbers of the two enantiomorphs [25]. It is intuitive that the two enantiomorphs appeared in equal probability since two enantiomorphs are thermodynamically identical.
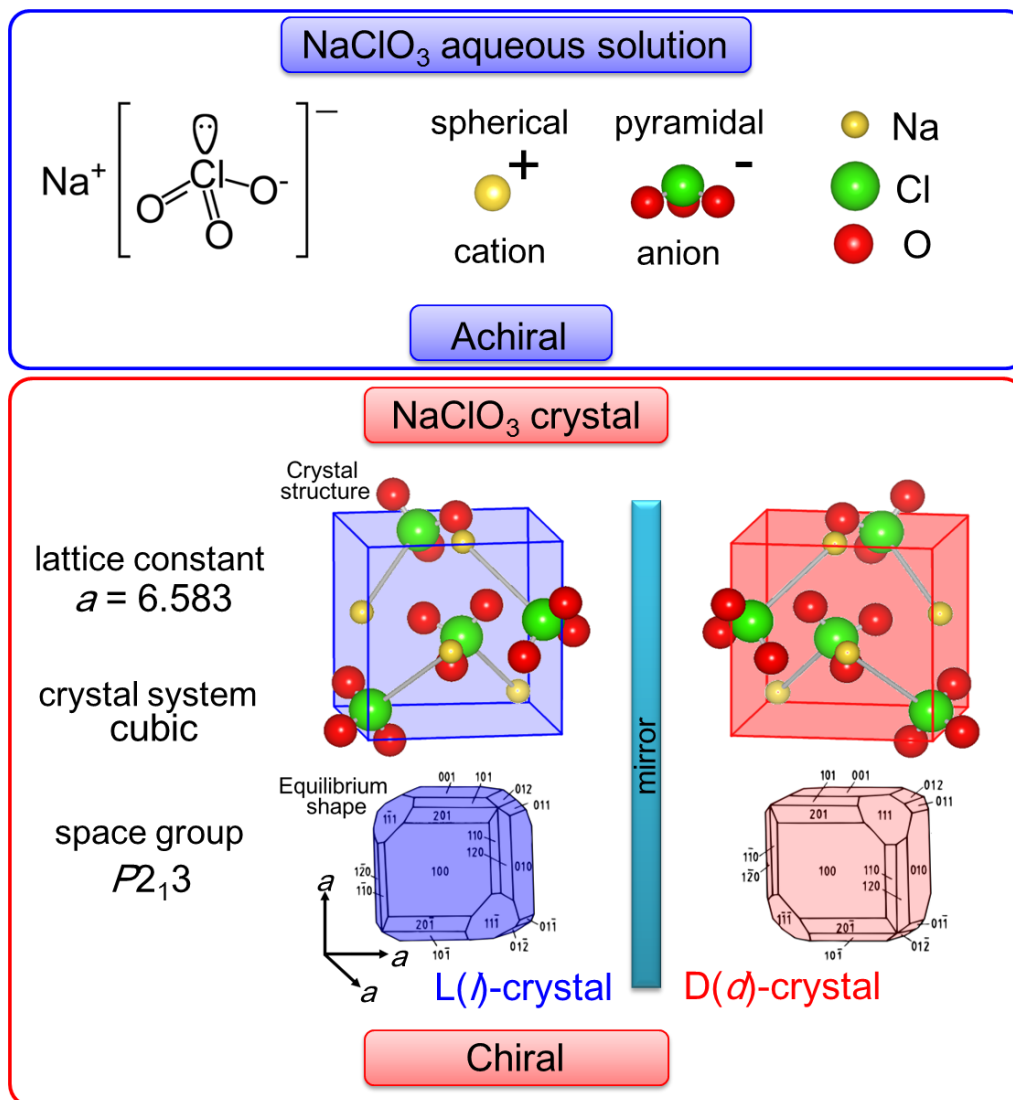
Fig. 1.9 Achiral ions of sodium chlorate (NaClO₃) and chiral crystal structure of NaClO₃. Upper schematic shows structure of ionized NaClO₃. Sodium cation is spherical shape and Chlorate anion is pyramidal shape having C_{3v} symmetry. Lower schematic shows crystal structure of NaClO₃. The space group of the structure belongs to chiral space group $P2_1 3$ [22].
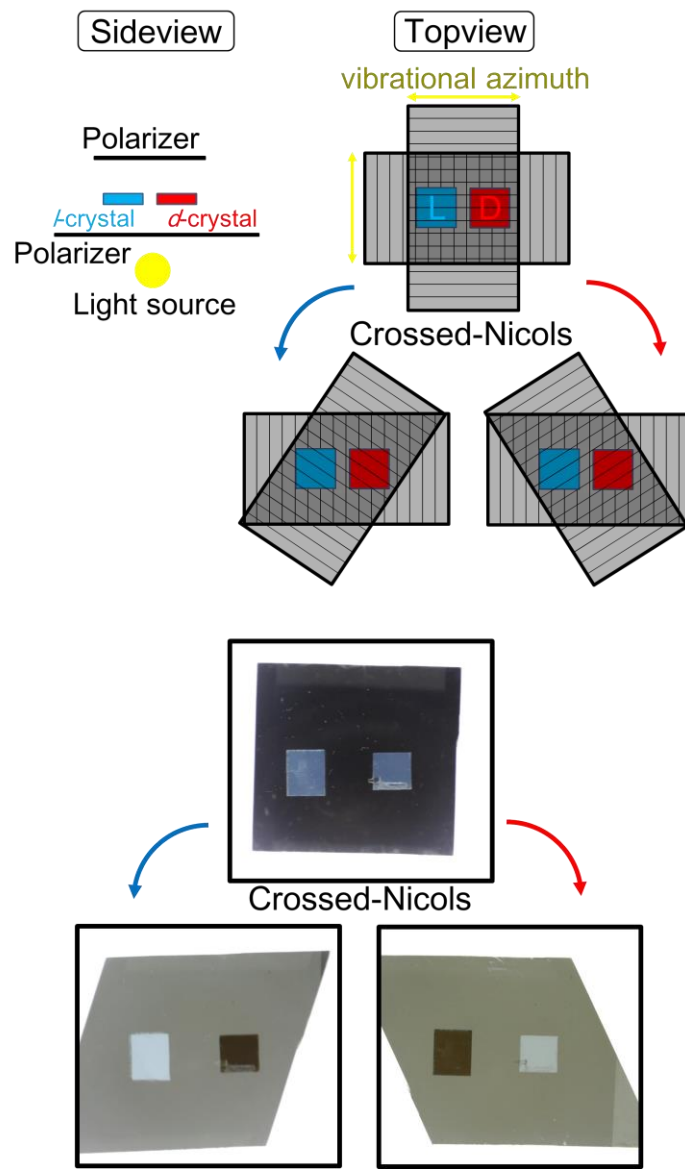
Fig. 1.10 Identification of the handedness of NaClO$_3$ chiral crystals using a pair of polarizers. Under crossed nicols orientation, both enantiomorphs exhibit the same contrast. D-crystal exhibits extinction when the upper polarizer is rotated to clockwise and *vice versa*.

1.2.3 Chiral Symmetry Breaking in NaClO₃ Crystallization from a Stirred Aqueous Solution

<u>*1.2.3.1Chiral Symmetry Breaking in NaClO₃ Crystallization under*</u>
<u>*Far-From-Equilibrium and Secondary Nucleation Scenario*</u>

As described above, evaporation of $NaClO_3$ aqueous solution yields statistically equal numbers of both enantiomorphs in accordance with the equal thermodynamic stability. However, in 1990, Kondepudi *et al.* have strikingly reported that continuous stirring of an aqueous solution during crystallization results in the occurrence of almost only either of the two enantiomorphs (Fig. 1. 11 and Fig. 1. 12) [26]. This phenomenon is called as "chiral symmetry breaking in crystallization" and has been of great interest because understanding of its mechanism has possibility to provide insights into the prebiotic process of biohomochirality and practical methodologies for chiral separation of chiral magnet and chiral pharmaceuticals [27-28]. In the experiment, $NaClO_3$ unsaturated aqueous solution poured in 100 mL beaker was allowed to be evaporated at 25 °C with the solution stirred using magnetic stirrer bar with rotation rate of 100 rpm. The crystallization experiment was repeated 32 times in total. The average CEE was 0, however, its frequency distribution showed two sharp peaks at homochiral state as shown Fig. 1. 11. This stirring experiment has been expanded to crystallization of 1, 1'-binaphthyl from its achiral melt [29]. Kondeoudi *al.* attributed the chiral symmetry breaking to kinetic predominance of secondary nucleation from a one-single "Eve" crystal, which firstly appeared in the solution, over primary nucleation. This is the so-called secondary nucleation scenario. The details of secondary nucleation scenario are as follows (Fig. 1.13). First, one-single chiral crystal, called "Eve" crystal, appears in the aqueous solution by primary nucleation because of the increment of supersaturation caused by the spontaneous evaporation of the solution. Second, the "Eve" crystal produces many secondary nuclei when it collides with the stir bar or is exposed to shear flow, amplifying the number of the same enantiomorph as the "Eve" crystal. Third, the nucleation of the enantiomorph with opposite handedness is suppressed by the generation of secondary nuclei followed by the reduction in the solution concentration. These three steps are widely considered to lead to significant chiral bias and indeed can satisfy three requirements for chiral symmetry breaking proposed by Frank a half century ago; (1) the emergence of chirality (chiral imbalance), (2) the amplification of chirality, (3) the suppression of the opposite handedness (mutual inhibition) [30].
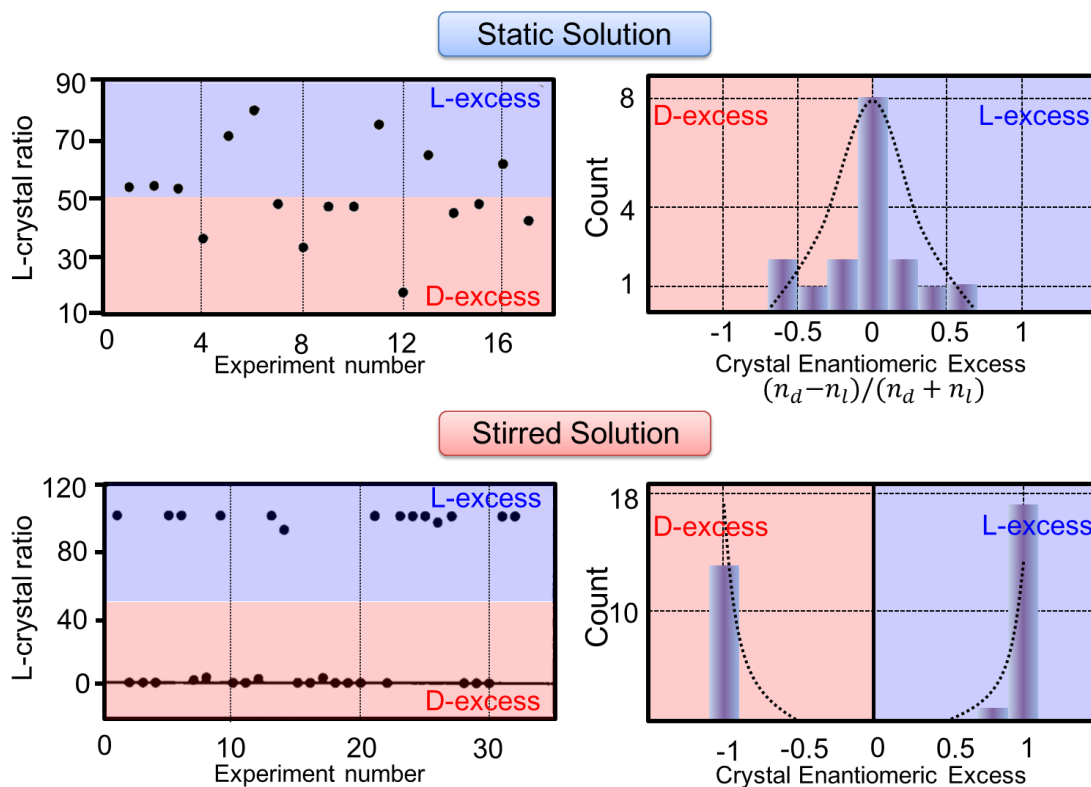
Fig. 1.11 Comparison of L-crystal ratio crystallized from static solutions and stirred solutions. Upper graphs are the case of static solution. Left shows L-crystal ratio in each batch crystallization. Kondepudi *et al.* performed 17 batch crystallization from static solutions and ploted L-crystal ratio in the graph. Right shows frequency distribution for Crystal Enantiomeric Excess. The frequency distribution shows monomodal feature whose median is 0, meaning that crystallization from static solution yields racemic mixture. On the other hand, lower graphs are the case of stirred solution. Left and right graphs shows L-crystal ratio in each crystallization and frequency distribution. The distribution shows bimodal feature whose peaks are -1 or 1, indicating that homochiral state is achieved in each batch crystallization.[26]
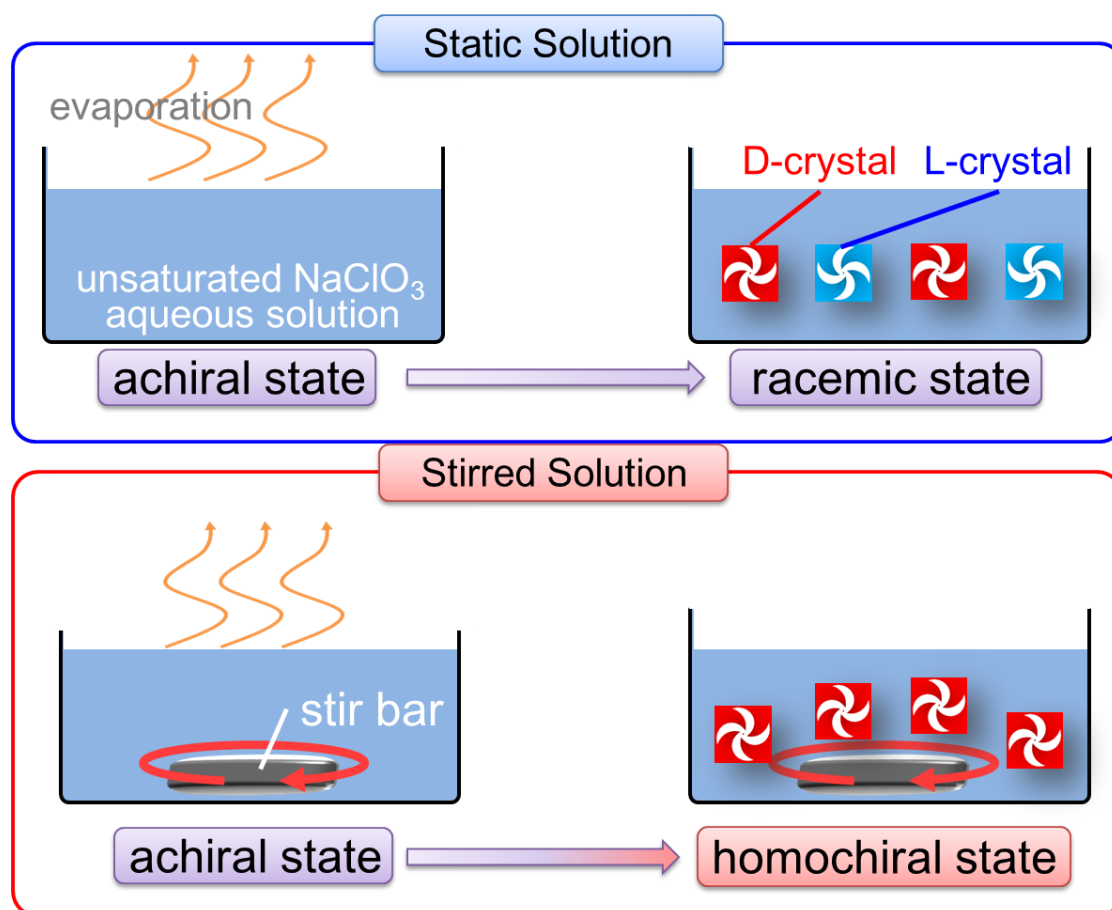
Fig. 1.12 Schematic overview of Kondepudi's experiment. Crystallization from static aqueous solution yields racemic mixture of two enantiomorphs. Crystallization from the stirred solution yields homochral state.
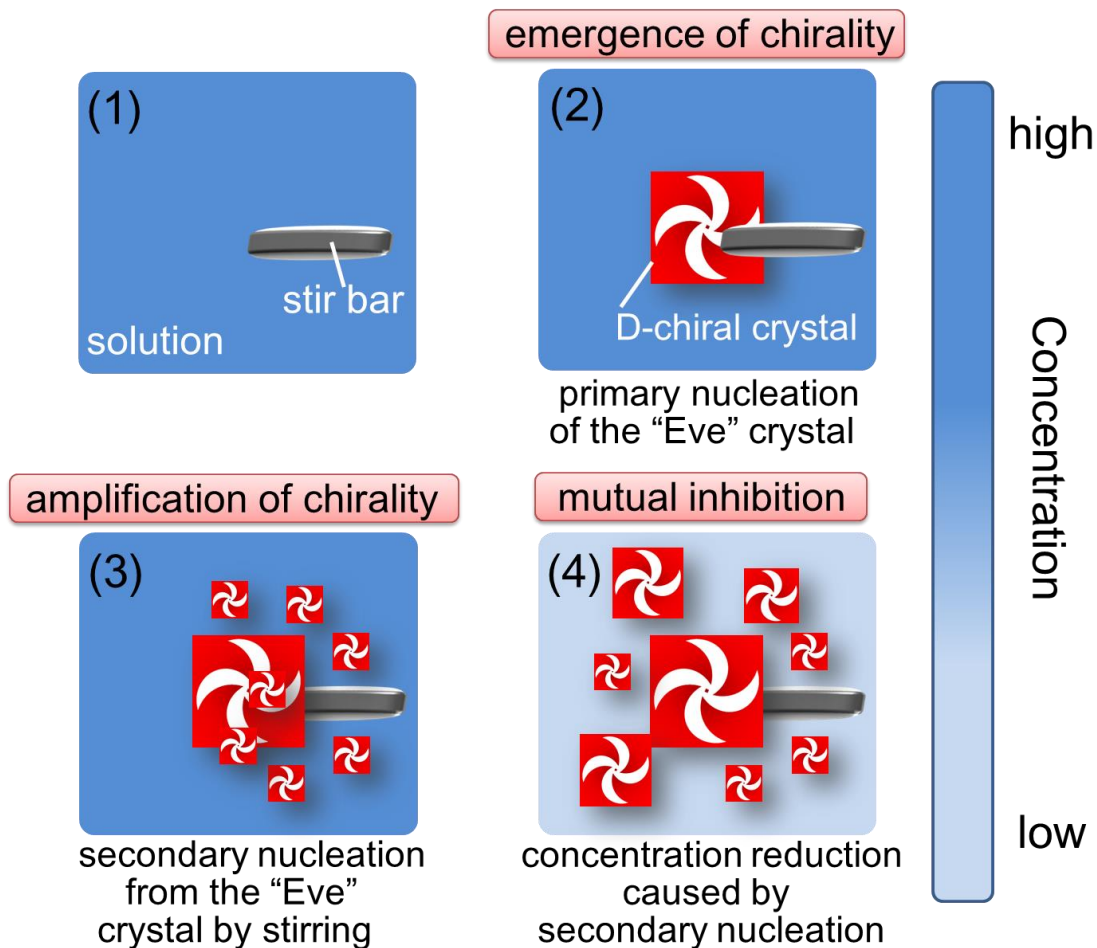
Fig. 1.13 Secondary nucleation scenario. (1)-(2) the process of emergence of chirality. Primary nucleation of one-single "Eve" crystal is responsible for the emergence process. (3) The process of amplification of chirality. Secondary nucleation from the "Eve" crystal corresponds to the amplification process. (4) The process of mutual inhibition. The reduction of concentration of solution caused by the generation of secondary nuclei is responsible for the inhibition process. Gradation of the blue color indicates the degree of concentration. Strong blue indicates the high concentration and *vice versa*.

Frank, who has firstly developed a mathematical model for an autocatalytic reaction mechanism explaining the evolution of homochirality, suggested that autocatalysis in which each enantiomer catalyzes its own production while suppressing the production of its opposite enantiomer, may have nonlinear dynamics leading to the amplification of small initial fluctuations in the concentration of the enantiomers. The basis of his theory is summarized below in accordance with a review paper written by Saito *et al.* [31]. Frank has proposed a chemical reaction model in which an achiral reactant A changes into chiral products, R or S enantiomers, when the achiral reactant contacts with R or S enantiomer with a rate constant k_1. In addition, an opened system is assumed so that the supply of the reactant A keeps the concentration of the reactant a.

$$k_1 : A + R \rightarrow 2R, \qquad A + S \rightarrow 2S \qquad (1.2)$$
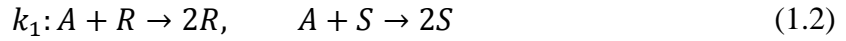
This linearly autocatalytic process corresponds to "amplification of chirality". Frank has additionally introduced the process in which the contact of the two opposite enantiomers results in the annihilation of the enantiomers from the system with a rate constant μ. This process is expressed as

$$\mu : R + S \rightarrow 0. \qquad (1.3)$$

He called this process "mutual antagonism", which may correspond to "mutual inhibition" process mentioned avobe. In order to quantify these chemical reactions, the time variation with linear autocatalysis and mutual antagonism is described by the following rate equations;

$$\frac{dr}{dt} = k_1 ra - \mu rs, \quad \frac{ds}{dt} = k_1 sa - \mu rs \qquad (1.4)$$

where r is the concentration of R-enantiomer and s is the concentration of S-enantiomer. With the time, the system relaxes to the fixed point determined by $dr/dt = ds/dt = 0$ (steady state). A racemic fixed point can be found from Eq. (1.4) as follows,

$$r^* = s^* = k_1 a / \mu \qquad (1.5)$$

It should be noted that the fixed point is unstable because the concentration difference

exponentially diverges as;

$$r - s = (r_0 - s_0)e^{k_1 at},\qquad(1.6)$$

where r_0 and s_0 denote the initial concentration of r and s, respectively. The state approaches to the fixed point only when the initial state is completely racemic. If there exists even slight imbalance of chirality at the initial state ($r_0 - s_0 \neq 0$), the concentration difference exponentially increases and the major enantiomer at the initial state dominates over the minor enantiomer. Numerical analysis of the rate equations provides the flow in the $r-s$ phase space (Fig. 1.14). The system asymptotically approaches to homochiral states $(r, s) = (0, \infty) or (\infty, 0)$. A qualitative description of this kinetic reaction model is shown in Fig. 1. 15.

Introducing chiral order parameter (or the enantiomeric excess, EE) makes chasing the evolution of homochiral state easier. The parameter is defined as:

$$\phi = \frac{r-s}{r+s}\qquad(1.7)$$

Eq. (1.6) and Eq. (1.7) leads to the following equation for the order parameter $\phi(t)$:

$$\frac{d\phi}{dt} = \frac{\mu(r+s)}{2}\phi(1-\phi^2)\qquad(1.8)$$

The effect of mutual antagonism explicitly appears in Eq. (1.8) since its coefficient is in the equation, indicating that the EE does not varies without the process of mutual antagonism ($\mu = 0$). Therefore, the process of mutual antagonism is indispensable for chiral symmetry breaking. In addition, as can be seen Eq. (1.6), the process of amplification of chirality and initial imbalance of chirality are also indispensable for the chiral symmetry breaking. This Frank model is the most classical and fundamental model that describes the evolution of homochirality. Although Frank model was established for chemical reaction, this model is often analogically compared with the crystallization experiment of chiral symmetry breaking.
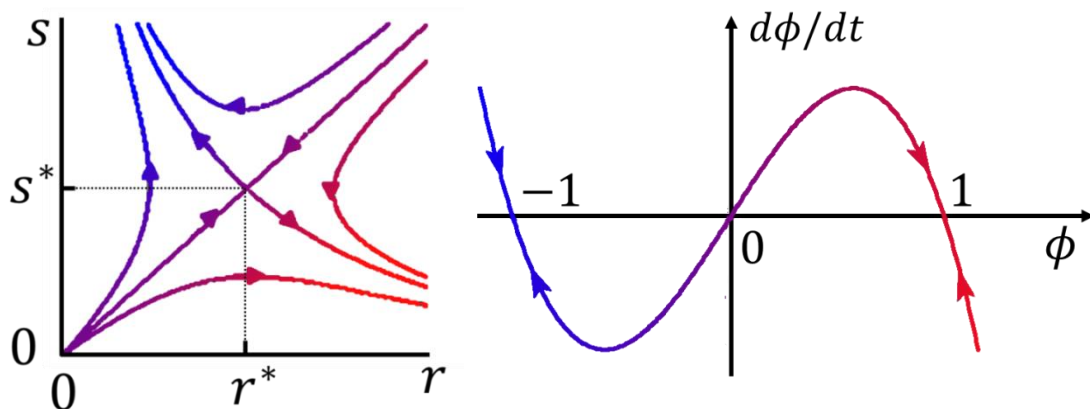
Fig. 1.14 Time-evolution of Frank model. Left shows a flow diagram of time-evolution of chiral state in r-s phase space. The flow diagram has one unstable fixed point at (r^*, s^*). The fixed point can be reached only when the initial state is completely racemic. Otherwise, the system approaches to homochiral state while amplifying the initial chiral imbalance. Right shows the relation between the chiral order parameter, ϕ, and its variation $d\phi/dt$. The relationship indicates the three fixed point at $\phi = -1, 0, 1$. [30,31]
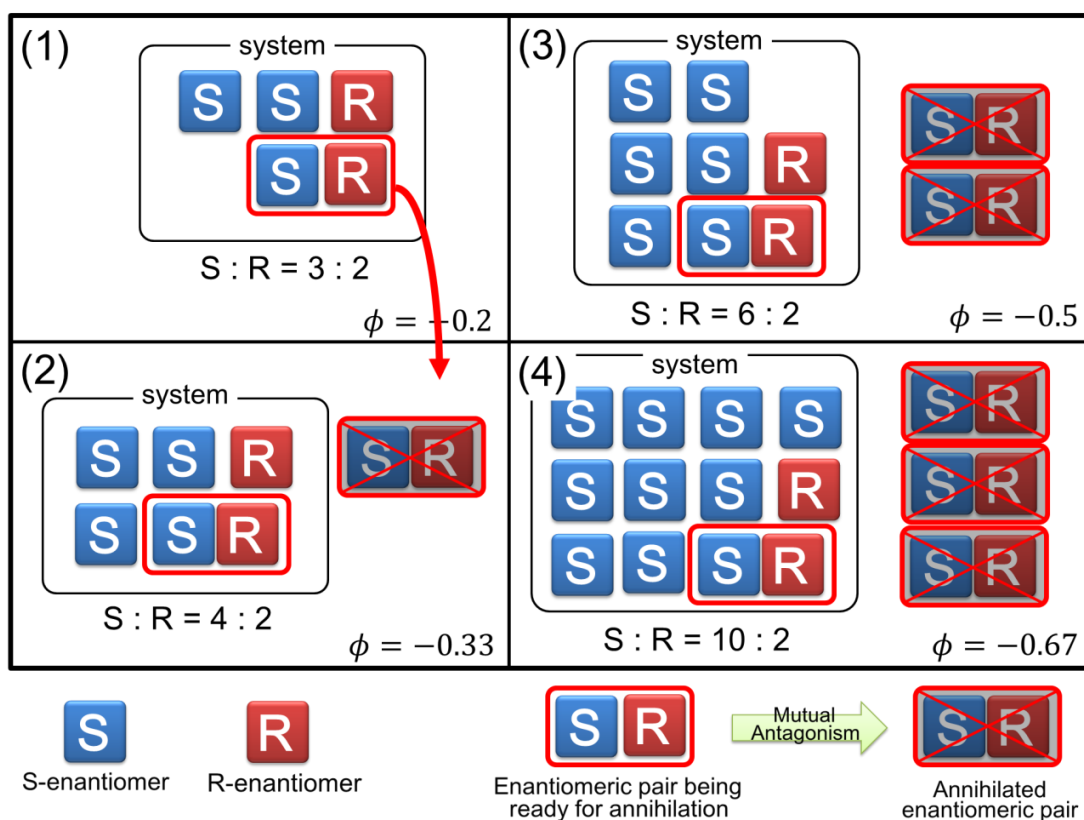
Fig. 1.15 Qualitative description of Frank model. Both enantiomers replicate themselves each steps in chemical reaction by autocatalytic reaction. Mutual antagonism follows the coupling a pair of two enantiomers in the system. Mutual antagonism eliminates the couple from the system. Repeating this process leads to homochiral state. [27]

The secondary nucleation scenario is supported by several experimental and theoretical findings. Numerical simulations by Cartwright *et al.*, where the physics of crystal nucleation (primary and secondary) and growth is added to a model that couples autocatalytic process and chaotic advection by simulating particles undergoing the autocatalytic reaction in journal-bearing advection in eccentric cylinder, successfully illustrated the process of chiral symmetry breaking. This simulation indicates the validity of the secondary nucleation process [32,33]. The simulation also indicates the kinetic effect of the secondary nucleation against the primary nucleation by showing the variation of CEE value as a function of primary nucleation rate and advection rate. The numerical simulations have provided comprehensive description of significance of secondary nucleation, on the other hand, the experimental findings serves more detailed mechanisms how the secondary nucleation replicates the same enantiomorph as the "Eve" crystal. Kondepudi *et al.* have monitored solution concentration during the stirred/non-stirred crystallization using a refractometer. The monitor experiment confirmed rapid drop of the concentration which may be accompanied with the secondary nucleation. [34]. Moreover, McBride *et al.* have observed the secondary nucleation process using *in-situ* video recording system. It has been found that a large amount of small crystals appears from the periphery of a large seed crystal as the "Eve" crystal when stir bar stroked the "Eve" crystal. The observation confirmed that the seed crystal acts as the center of secondary nucleation [35]. A cause of the generation of secondary nuclei still remains controversial. Kondepudi *et al.* have observed a $NaClO_3$ single crystal crystallized by evaporating aqueous solution using scanning electron microscope (SEM). They have found that tiny 10–100 μm-sized needle-like crystals are attached on the surface of the single crystal. They proposed that the tiny needle-like crystals are broken off by stroke of the stir bar or shear flow and the detached needle-like crystals become secondary crystals [36]. Not only a stroke by the stir bar or strong shear flow but also convection in solution has been also proposed as a cause of secondary nucleation by Bush *et al.* In their experiment, a saturated $NaClO_3$ aqueous solution was flowed over a surface of $NaBrO_3$ single seed crystal, which is an isomorphous of $NaClO_3$ crystal, followed by drift into a supersaturated $NaClO_3$ aqueous solution. It should be noted that this experiment involves no mechanical crushing. Nevertheless, the crystallization was founded to results in chiral asymmetric state. They have attributed the asymmetric state to transportation of secondary nuclei caused by "Embryo Coagulation Secondary Nucleation (ECSN)" mechanism on the surface of the $NaBrO_3$ crystal by the convection flow [37]. The ECSN is a model of secondary

nucleation proposed by Qian *et al.* The model combines three well-established notions in the field of crystallization and colloid science; the postulation of the classical nucleation theories about (1) the existence of embryos, solute clusters, in supersaturated solutions, (2) the long-range attractive forces between macroscopic bodies due to the van der Waals forces between molecules, and (3) the theory of rapid coagulation of colloid particles. The combination leads to a qualitative picture: when a seed crystal is introduced into the supersaturated solution the embryos existing in bulk solution are attracted by the van der Waals field of the crystal. Some of the embryos reach the surface of seed crystal, attach to it and are incorporated inside the growing seed. In a relatively high supersaturated solution, a high concentration of large embryos is created in the region near the crystal which leads to rapid coagulation of the large embryos and to the formation of clusters larger than the critical nuclei [38]. Qian *et al.* and Bush *et al.* have stated the surface of chiral seed crystal may catalyze the "embryos" that possesses the same handedness as the seed, and hydrodynamic shear due to the convection flow may induce the secondary nucleation by removing the "embryos" from the surface. Namely, they have ascribed the cause of secondary nucleation to removal of "embryos" coagulated on the "Eve" crystal rather than mechanical crush of the "Eve" crystal. As described above, the secondary nucleation scenario has been widely accepted as the theory that explains Kondepudi's experiment, and the mechanism of secondary nucleation has now become the center of the discussion.

  Whereas the secondary nucleation scenario is widely accepted, it is also true that the scenario does not necessarily rationalize all experiments of chiral symmetry breaking in $NaClO_3$ crystallization from an aqueous solution. Especially, the scenario is considered to be difficult to explain crystallization from higly-supersaturated solution. Viedma has performed stirred crystallization from a highly supersaturated $NaClO_3$ aqueous solution. In his experiment, supersaturation of the starting mother solution is approximately 58 %. The highly supersaturated metastable aqueous solution being ready for nucleation was vigorously stirred with rotation rate of 1000 rpm, inducing a catastrophic primary nucleation of $NaClO_3$ chiral crystals. Even though the generation of the large amount of crystals caused by primary nucleation should lead to chiral symmetric state in accordance with the secondary nucleation scenario since the chirally symmetric stochastic nature of primary nucleation should result in the absence of the specific one-single "Eve" crystal, the crystallization of Viedma resulted in strong chiral asymmetric state as begin similar to the Kondepudi's experiment. On the basis of this result, Viedma has suggested the possibility of chiral asymmetric state at primary

24

nucleation stage or even earlier stage of crystallization [39]. Moreover, El-Hachemi *et al.* has performed crystallization from a boiling aqueous solution by withdrawal of solvent from a reflux flow. A unsaturated $NaClO_3$ aqueous solution in a glass flask connected to a reflux condenser was boiling and then, solvent in the condenser was withdrawn from the reflux flow. They found that crystal powder generated by condensation of the boiling solution shows strong chiral bias. They have also mentioned high supersaturation state at the interface between air and solution, which leads to high primary nucleation rate, suppresses the possibility that handedness of the crystal powder was originated from one-single "Eve" crystal. Therefore, secondary nucleation may be not the predominant factor for the asymmetric state. They have advocated that crucial process for chiral symmetry breaking is continuous association/dissociation of chiral clusters, whose size is smaller than the critical size for nucleation, with chiral recognition. Namely, they have indicated that transition towards homochiral state proceeds during the earlier stage of crystallization before primary nucleation. In addition, they have considered that transition towards the homochiral state is due to the reduction of degree of freedom in Gibbs phase rule from one to zero by mutual chiral recognition of chiral clusters. In the early of 19 centuries, Van't Hoff has demonstrated that the enantiomorphic phases are thermodynamically "identical" on the ground of the fact that the experimental behavior of the system involving the enantiomorphic phase violates the Gibbs phase rule when the two enantiomorphs are recognized as distinguishable phase (Gibbs phase rule is described as $F = C+2-P$, where F is the degree of freedom, C is the number of chemical components and P is the number of phases that cannot be shared. Since there are two components, H_2O and $NaClO_3$, and four phases, vapor, solution, L and D solid, the degree of freedom is 0. Therefore, the four-phase coexistence region, i.e. racemic state, should be represented by a point in P-T-component diagram. However, the racemic state can be widely observed in various conditions. Therefore, both L and D solid phases should be recognized as thermodynamically identical phase.) [40]. On the other hand, Crusats *et al.* has proposed that the two enantiomorphic phases becomes distinguishable in stirred or vigorously perturbed solution because of the chiral recognition originating from interaction between chiral pre-nucleation crystalline clusters. They argued conceivable differences in behavior of chiral clusters detached from a crystal surface between in a stagnant solution and in a perturbed solution. Whereas the chiral clusters detached from crystal surface are immediately re-incorporated to the surface without interplay with other chiral clusters, clusters in a perturbed solution is dispersed and asymmetrically

interplay with other chiral clusters. Thus, the system may recognizes the presence of two distinct solid phases. Since the two enantiomorphs are distinguishable, the degree of freedom becomes 0, resulting that homochiral state is stable [41-43]. In contrast to the kinetic secondary nucleation scenario, the idea of the Gibbs's phase rule is based on thermodynamics. According to the idea, the most sable state of the system is homochiral state under a certain perturbation and might be capable of explaining experimental results comprehensively. However, there is no experimental support because it is difficult to investigate the dynamics of chiral clusters whose size is below crystal size of nucleation.

1.2.3.2 Chiral Symmetry Breaking in $NaClO_3$ Crystallization under Quasi-Equilibrium

  The crystallization experiments that cannot be explained by the secondary nucleation scenario are not only the experiments introduced above. In 2005, Viedma has demonstrated that a racemic 50:50 mixture of $NaClO_3$ enantiomorphs in contact with a saturated solution converts to a complete pure homochiral state by continuous abrasion-grinding the aqueous suspension in the presence of glass beads (Fig. 1.16)[44]. In addition, it was found that time-evolution of CEE exhibits nonlinear or exponential dynamics (Fig. 1.17). In his experiment, equal numbers of two enantiomorphs exist in the solution preliminarily, ruling out the existence of "Eve" crystal postulated in secondary nucleation scenario. Moreover, the solution is seemingly equilibrium state because the evaporation of solution was suppressed by hermetically closing the solution, ruling out the primary nucleation event. This experiment, which is seemingly irrelevant to primary nucleation, is sometimes called as "chiral symmetry breaking under *quasi-equilibrium* condition" in order to discriminate from the crystallization experiments involving primary nucleation, called as chiral symmetry breaking under *far-form equilibrium* condition. In contrast to the chiral symmetry breaking under far-from equilibrium, where an opened system was assumed so that achiral reactant was supplied into the system continuously owing to supersaturation originating from the evaporation of solution, the Viedma's experiment is closed system without supply of achiral reactant. Therefore, Frank model cannot be applied to explain this experiment.
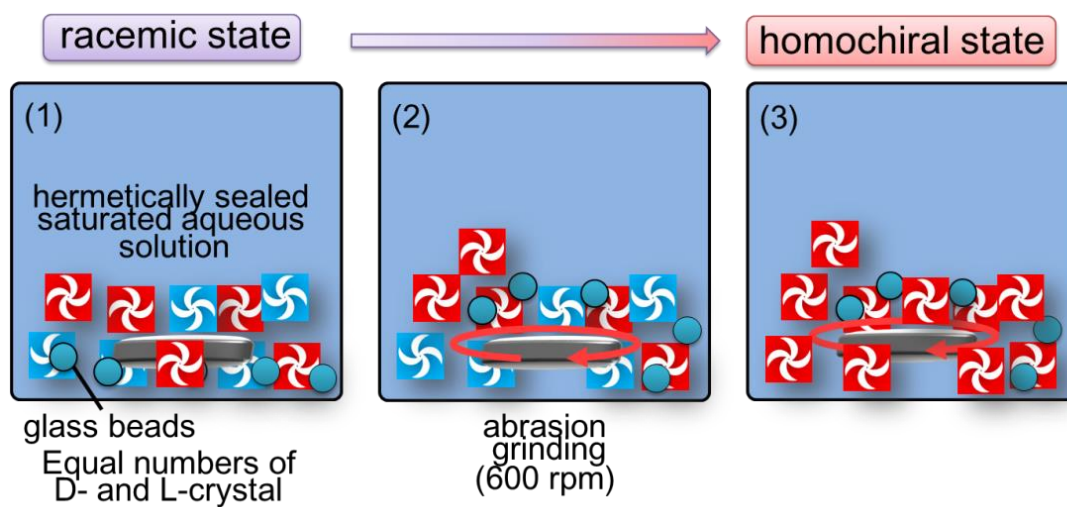
Fig. 1.16 Schematic overview of Viedma's experiment, called "Viedma deracemization".
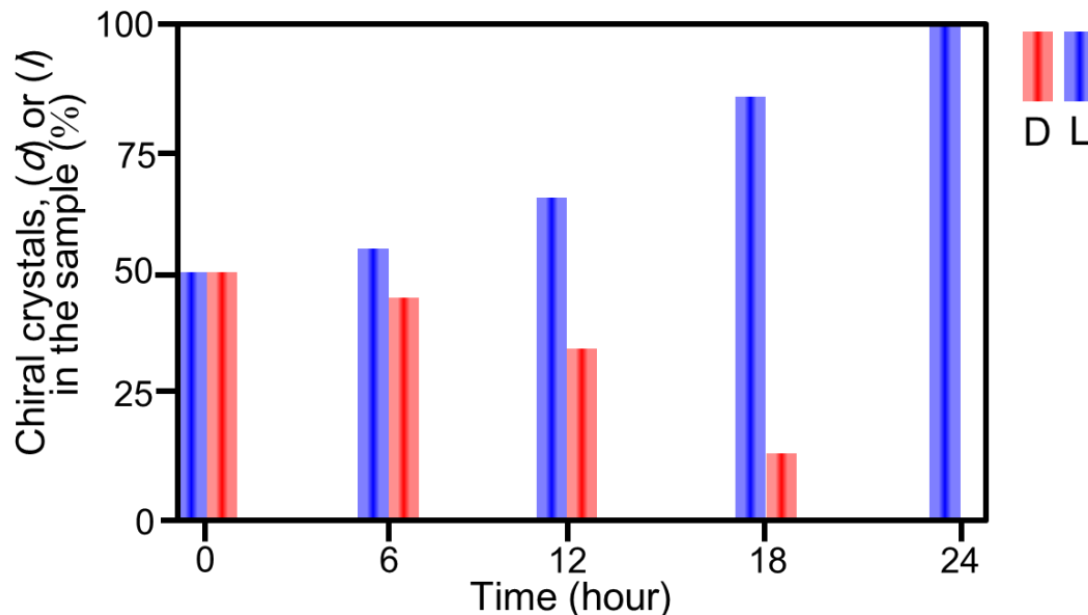
Fig. 1.17 Time-evolution of ratio of the two enantiomoerphs during the "Viedma deracmization". It should be noted that the ratio of the enantiomorphs nonlinearly increase (decrease) with time. Ultimately, the ratio reaches to 100 % or 0%, indicating that complete enantiopure state is achieved. [44]

Saito *et al.* has theoretically considered the possibility of evolution to homochiral state in a closed system based on a chemical reaction model as similar to Frank model before the Viedma's experiment was done. They have taken "back reaction" into account, where chiral products resulted from autocatalytic reaction is decomposed to achiral reactant, instead of mutual antagonism process. Their numerical analysis has shown that the "back reaction" is indispensable for achievement of complete pure homochiral state in a closed system [45]. Taking this result into account, Viedma has ascribed the homochiral state in his experiment to (1) "induced" secondary nucleation caused by continuous grinding as autocatalytic amplification process and (2) enhanced dissolution of microcrystalline resulted from the grinding as the "back reaction" process. The continuous grinding crushes the crystals into microcrystals, allowing autocatalytic amplification of chirality. Simultaneously, the fragmentation promotes the dissolution of the microcrystals because of the Gibbs-Thomson effect, whereby the solubility of a small particle is relatively higher than that of bulk state [46]. The chiral microcrystals back into achiral monomer by the dissolution. Thus, the dissolution corresponds to the "back reaction" process. Moreover, the enhanced dissolution of the microcrystal causes a concentration gradient leading to re-incorporation of achiral monomer to chiral crystals (recycle of the achiral monomer). Viedma has stated that repeating these processes; "autocatalysis", "back reaction" and "recycle", leads to complete chiral purity. This so-called "Viedma deracemization" has been expanded to the system of crystallization of organic molecules having chirality intrinsically [47] and has successfully achieved complete chiral purification in several systems in which the target compound quickly racemize in solution. Therefore, the Viedma deracemization is expected to be practical methodology for enantiomer separation in pharmaceutical industry. They have suggested that key mechanism of chirality conversion is the Ostwald ripening caused by the Gibbs-Thompson effect.

The mechanism of Viedma deracemization in $NaClO_3$ crystallization still being the matter of debate. Many theoretical analyses have been carried out to elucidate ascendant factors underlying the mechanism of Viedma deracemization. Especially, the center of discussion is what kind of mechanism can rationalize the nonlinear dynamics seen in the time-evolution of CEE. Uwaha *et al.* have firstly succeeded to reproduce the nonlinear dynamics in the time-evolution of CEE by modeling enantioselective coagulation of chiral pre-nucleation clusters and dissociation from the chiral cluster into achiral monomer on the basis of a reaction-type model [48]. His model described the time-evolution of the system with masses of the following five components: the D- and

28

L-crystals denoted by D and L, respectively; D- and L-chiral units (tetramer of achiral molecule) D_u and L_u, respectively; the achiral molecule A. He considered following cluster reactions and adopted following rate equations to chase the time-evolution in the masses of each component:

$$k_0: A + A \rightarrow D_u, A + A \rightarrow L_u: \qquad \text{formation of chiral cluster} \qquad (1.9)$$

$$k_c: D_u + D_u \rightarrow D, L_u + L_u \rightarrow L \qquad \text{nucleation by cluster coagulation} \qquad (1.10)$$

$$k_u: D_u + D \rightarrow D, L_u + L \rightarrow L \qquad \text{crystal growth by cluster addtion} \qquad (1.11)$$

$$k_1: A + D \rightarrow D, A + L \rightarrow L \qquad \text{growth by monomer addtion} \qquad (1.12)$$

$$\lambda_0: D_u \rightarrow A + A, L_u \rightarrow A + A \qquad \text{cluster decay into monomer} \qquad (1.13)$$

$$\lambda_1: D \rightarrow D + A, L \rightarrow L + A \qquad \text{crystal decay emitting monomer} \qquad (1.14)$$

$$\lambda_u: D \rightarrow D + D_u, L \rightarrow L + L_u \qquad \text{crystal decay emitting cluster} \qquad (1.15)$$
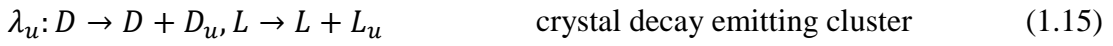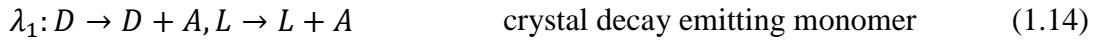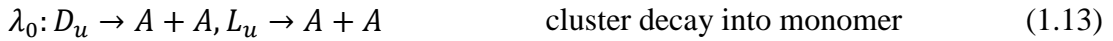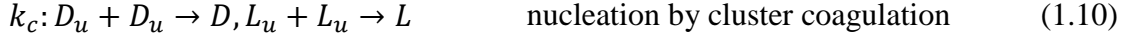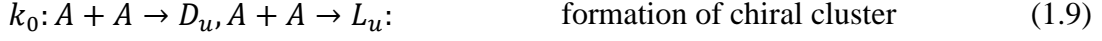
$$\frac{dD}{dt} = k_1 AD + k_u D_u D + k_c D_u^2 - \lambda_1 D - \lambda_u D \qquad (1.16)$$

$$\frac{dL}{dt} = k_1 AL + k_u L_u L + k_c L_u^2 - \lambda_1 L - \lambda_u L \qquad (1.17)$$

$$\frac{dD_u}{dt} = k_0 A^2 + k_u D_u D + k_c D_u^2 + \lambda_u D - \lambda_0 D_u \qquad (1.18)$$

$$\frac{dL_u}{dt} = k_0 A^2 + k_u L_u L + k_c L_u^2 + \lambda_u L - \lambda_0 L_u \qquad (1.19)$$

$$\frac{dA}{dt} = -2k_0 A^2 - k_1 AD - k_1 AL + \lambda_1 D + \lambda_1 L + \lambda_0 D_u + \lambda_0 L_u \qquad (1.20)$$

where k_0 is the rate of cluster formation, k_c is the rate constant of crystal nucleation, k_1 is the rate of growth by import of monomer, k_u is the rate of growth by import of chiral unit, and corresponding dissociation process $(\lambda_0, \lambda_1, \lambda_u)$. In the rate equations, it is assumed that a chiral unit is formed by two achiral monomers and two chiral units form a critical nucleus. The combination of monomer addition growth and cluster addition growth may be corresponds to the autocatalysis and the dissociation process corresponds to the "back reaction", respectively. The feature of the time-evolution described by this cluster reaction model showed the nonlinear dynamics, indicating that the model have succeeded to reproduce the feature of Viedma deracemization (Fig. 1.18).
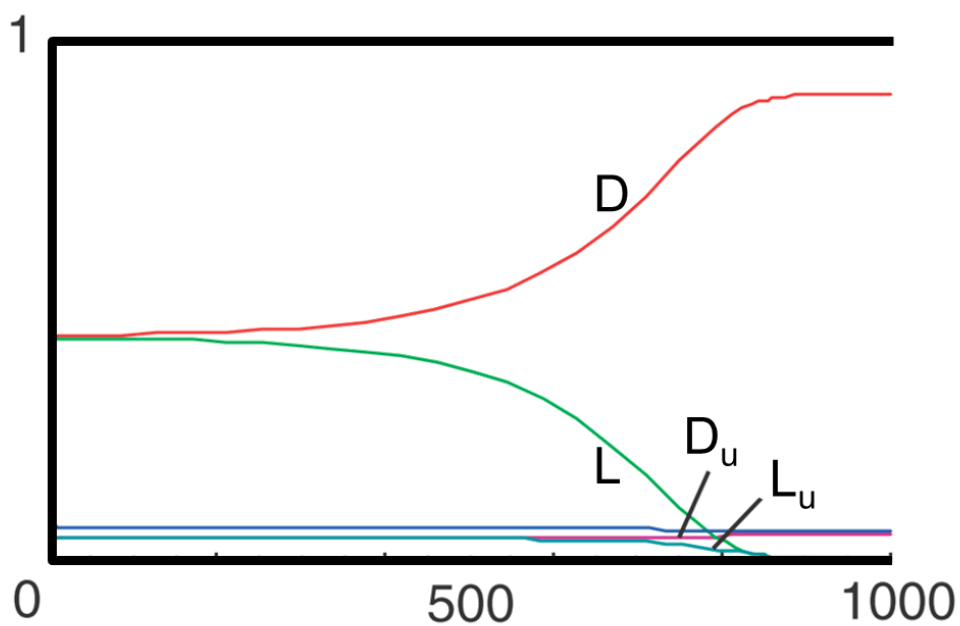
Fig. 1.18 Time-evolution of masses of both enantiomorphs and chiral clusters for $D(0) = 0.101$, $L(0) = 0.100$, and $D_u(0) = L_u(0) = 0$ with $k_0 = 0.1, k_1 = k_u = 1$, $k_c = 0.01, \lambda_0 = 0.1$ and $\lambda_1 = \lambda_u = 0.05$ in Uwaha's cluster reaction model. The red line indicates the mass of D, the purple for D_u, the green for that of L, the seagreen for L_u. [48]

On the other hand, several groups have advocated that Ostwald ripening can explain the nonlinear behavior in the time-evolution of CEE. Cartwright *et al.* have analyzed the effect of Ostwald ripening by introducing the process in which fragments of chiral crystals by attrition dissolve into achiral monomer the numerical simulation system for analysis of secondary nucleation, described above, as the process of Ostwald ripening [49]. The results of the numerical simulation successfully reproduced complete chiral purity and nonlinear time-evolution of CEE. However, it should be noted that the process which is introduced in this simulation may not correspond to Ostwald ripening because the crystal size distribution of larger enantiomorph and smaller one, which is driving force of Ostwald ripening, was not chased. Noorduin *et al.* have shown the effect of Ostwald ripening on the nonlinear dynamics based on a theoretical background. They have chased the change of crystal size distribution with time during the attrition-grinding by means of Monte Carlo simulation and revealed total crystal surface area, A, remains approximately constant during the attrition process. Therefore, they wrote the following equation

$$A_D(t) + A_L(t) \approx A \tag{1.21}$$

where $A_D(t)$ and $A_L(t)$ are the total crystal surface areas of the D- and L-crystal, respectively. Since Ostwald ripening leads to a transfer of crystal surface area from one enantiomorph to the other accompanying the detachment of molecules from the surface of the one and the attachment of the molecules to the surface of the other, the transfer may be the linear dynamics that depends on the difference in crystal surface area between the two enantiomorphs. Therefore, the rate equation of the chiral conversion can be written as

$$-\frac{dA_L}{dt} = \frac{dA_D}{dt} = k(A_D - A_L) = k(2A_D - A) \tag{1.22}$$

where k is the rate constant. After integration this results in

$$\ln\left[\frac{2A_D(t) - A}{2A_D(0) - A}\right] = kt \tag{1.23}$$

for D-enantiomorph. Eq. (1.23) can be expressed as a function of the enantiomeric

excess in the crystal phase assuming steady state normalized crystal size distributions for populations of two enentiomorphs:

$$\text{ee} = \frac{N_D - N_L}{N_D + N_L} \approx \frac{A_D - A_L}{A_D + A_L} = \frac{2A_D - A}{A} \qquad (1.24)$$

resulting in

$$\text{ee}(t) = ee(0)exp(kt) \qquad (1.25)$$

It can be seen from Eq. (1.25) that the initial enantiomeric excess is amplified exponentially. As described above, Noorduin *et al.* have explained the nonlinear time-evolution of CEE by Ostwald ripening. Against the explanation by Ostwald ripening, Uwaha has advocated that the Ostwald ripening may not be key mechanism on the ground of comparison in time-evolution of cluster size distribution between Ostwald ripening process without grinding and grinding process [50]. Moreover, Saito *et al.* have also inferred that Ostwald ripening is not necessary to reproduce the nonlinear dynamics of CEE by building a simple lattice-gas model studied by kinetic Monte Carlo simulations (Fig. 1.19). In their lattice-gas model, crystal growth process is assumed to be irreversible, meaning that the Ostwald ripening process never happens in the system. Achiral molecule, A, were randomly distributed at a concentration c on a square lattice of a size L^2. The molecules randomly jump into arbitrary empty lattice site with a constant rate. When two achiral molecules are happened to jump in a nearest neighbor sites, the molecules are bonded to irreversibly form a chiral dimer, D_2 or L_2 with a constant rate. Once a chiral dimer is formed, it is assumed to be immobile. In addition, when an achiral molecule jumps into a nearest neighbor site of a chiral dimer, the achiral molecule turns into chiral molecule whose handedness is identical to that of the chiral dimer and incorporates with the dimer. The effect of the attrition was expressed by dividing the square lattice into small lattices and shuffling the lattices, which allows chiral clusters to dissociate up to achiral molecule level. A long-range jumping distance of inter-lattice site of achiral molecule was also introduced to express the grinding effect. Their analysis has reproduced the nonlinear dynamics in time-evolution of CEE even in the absence of Ostwald ripening process (Fig. 1.20)[51]. They attributed the cause of the nonlinear dynamics to mutual disturbance in the change of achiral molecule into chiral unit resulting from occupation of nearest neighbor site by the opposite chiral unit. They

called this process as "mutual antagonism". As can be seen above, the main stream of the debate is now which effect, Ostwald ripening or enantioselective association of chiral clusters via recycling achiral monomers, is ascendant factor to reproduce the feature of "Viedma deracemization".
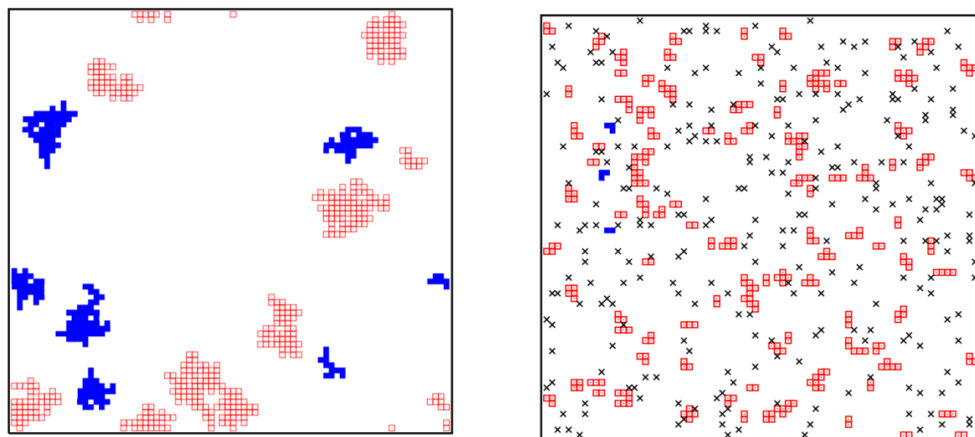
Fig. 1.19 Final configuration of two enantiomers in Saito's lattice gas model with kinetic Monte Carlo simulations. Blue square and red square indicates L-enantiomer and D-enantiomer, respectively, and black cross indicates achiral molecule *A*. Left figure indicates the case without grinding. Without grinding, the system reaches to racemic state. Right figure indicates the case with grinding. In this case, either of the enantiomers dominates over the other. [51]
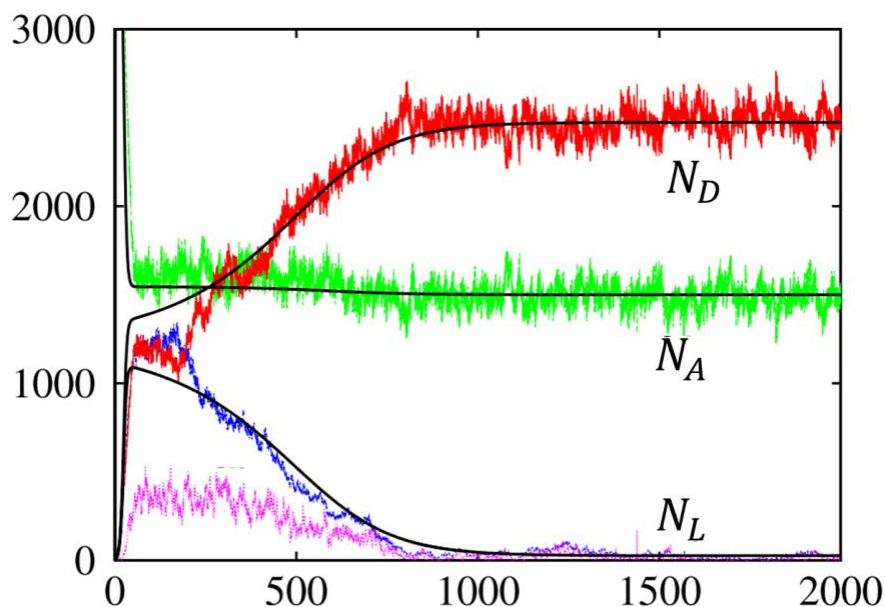
Fig. 1.20 Time-evolution of the population of enantiomers in the Saito's model. Red line indicates the population of D-enantiomer. Blue line indicates the population of L-enantiomer. Green for the population of achiral molecule. [51]

More recently, Blanco *et al.* have tried to theoretically provide a comprehensive explanation for Viedma deracemization by simplifying the experimental phenomena to the reaction cycle that can achieve the homochiral state, as indicated by Frank [30], rather than providing the detailed description of actual mechanism of crystal growth and dissolution (the term secondary nucleation, Ostwald ripening or cluster-cluster coagulation here.) [52]. Their theory is reaction type model taking the thermodynamic description of classical nucleation theory (CNT) into account in order to express rate constants of processes. The concepts of CNT are the existence of critical size for nucleation, that is, the free energy of crystals changes depending on their size. Whereas the increment in size of a nucleus whose size is below the critical size (precritical cluster) is endergonic process, that in a nucleus above the critical size (postcritical cluster) is exergonic process. Namely, the precritical cluster tends to shrink to a monomer and the postcritical cluster tends to become larger. They have combined this behavior of crystal cluster with the chemical reaction expressing the growth of clusters. The summary of their theory is shown in Fig. 1.21. Dissociation of precritical clusters contributes to mutual inhibition process because the quasi-equilibrium constant, $K_{quasi-equili}$, can be written as

$$K_{quasi-equil} \approx \frac{[A]^{2n}}{[D_n][L_n]} \tag{1.26}$$

owing to the continuous attrition. This relationship means that once the number of either of chiral clusters dominates that of the opposite cluster the number continues to increase while suppressing the opposite chiral cluster. On the other hand, the associations of postcritical clusters contribute to enantioselective aoutocatalysis process. Although the combination of these two processes would results in bimodal cluster size distribution, meaning the stop of the reactions, the redistribution of cluster size driven by the attrition lead to continuous reaction. As a consequence of this cycle, homochiral state was achieved. The essence of this theory is that the achievement of homochiral state requires a certain adequate cluster size distribution where the postcritical clusters and the precritical clusters simultaneously coexist for a certain period and moderate supersaturation.
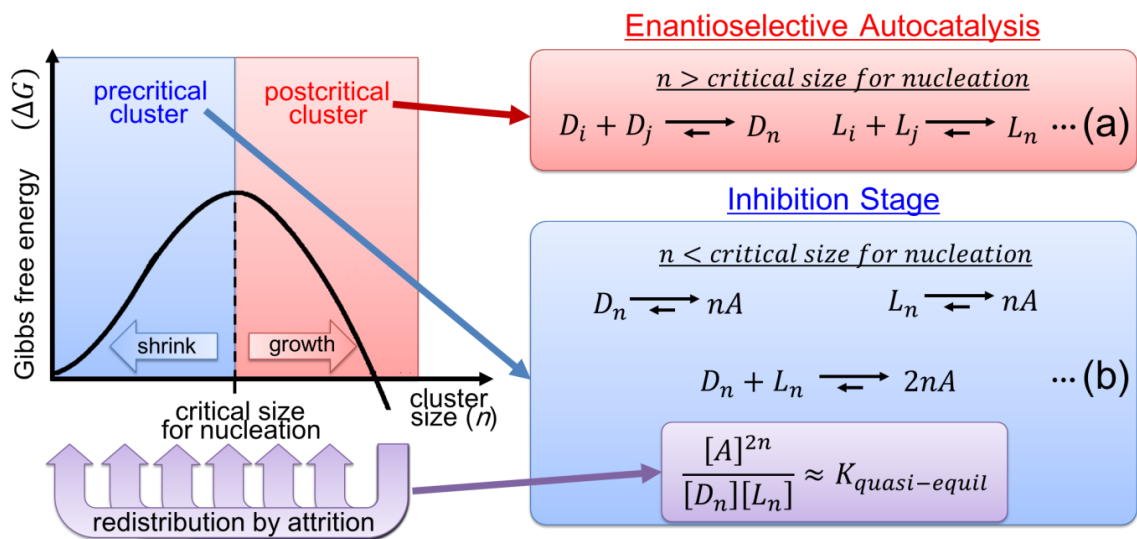
Fig. 1.21 Schematic overview of the Blanco's theory. Left graph shows thermodynamic description of Classical Nucleation Theory. Precritical clusters, whose size is below critical size for nucleation, contributes to the enantioselective autocatalytic process as shown in the reaction denoted by (a). Postcritical clusters, whose size is above the critical size, contributes to mutual inhibition process as shown in the reaction denoted by (b) and the rate constant $K_{quasi-equili}$.

1.3Summary of Chapter 1 and Approach in This Study

As can be seen above, crystallization of chiral materials closely relates to our life from the past to the future, current pharmaceutical industry, futural spintronic devices, past biohomochirality. To understand the emergence and amplification of chirality in crystallization has significance not only for elucidation of puzzle in biohomochirality but also for establishment of methodology to control handedness of chiral materials. This thesis especially focuses on the process of emergence of chirality during $NaClO_3$ chiral crystallization from an aqueous solution and the mechanism of chiral symmetry breaking in $NaClO_3$ crystallization. Experiments of chiral symmetry breaking in $NaClO_3$ chiral crystallization can be roughly classified into two types according to whether primary nucleation is involved or not: (1) *far-from equilibrium* involving primary nucleation process, as represented by Kondepudi's experiment and (2) *quasi-equilibrium* seemingly irrelevant to primary nucleation, as represented by Viedma's demonstration. Regarding symmetry breaking in *far-from equilibrium*, the kinetic secondary nucleation scenario is widely accepted as the mechanism explaining homochiral state. However, the rationalization by secondary nucleation scenario is suffering from the fact that homochiral state can be achieved even in the crystallization from highly supersaturated solution. It has been alternatively proposed that the mutual chiral recognition of chiral prenucleation clusters leads to the transition towards homochiral state before primary nucleation in accordance with thermodynamic constraint. Moreover, Viedma's demonstration of symmetry breaking in *quasi-equilibrium* demands the reconsideration on the secondary nucleation scenario. The cause of the homochiral state in *quasi-equilibrium* has been ascribed to recycle of achiral monomer fragmented by attrition, which is driven by Ostwald ripening, or the process couples the enatioselective chiral cluster coagulation with the fragmentation. However, the unified view has not been achieved yet, and there moreover exists the problem that the numerical analysis precedes the experimental analysis, namely, there exists the problem on deficiency of experimental findings.

The approach of the previous experimental studies solely remains indirect. The mechanism was estimated by analyzing the crystals resulted from the crystallization experiments, namely, non-growing "dead" crystals were analyzed. Therefore, it is unclear what actually happens in the initial stage of crystallization, which should be responsible for determination of chirality. In addition, the approach in the previous study is deductive because the microscopic mechanism is estimated from the experimental conditions and the resulting CEE. In contrast with the approach in the

previous study, the current study takes an inductive approach, in which the emergence process of chirality in crystal was directly investigated by *in-situ* microscopic observation one-by-one. The aim of this thesis is to elucidate the emergence process of chirality during $NaClO_3$ chiral crystallization from an aqueous solution by directly observing the process *in-situ*, and to provide a new insight on the mechanism of chiral symmetry breaking (Fig. 1. 22).
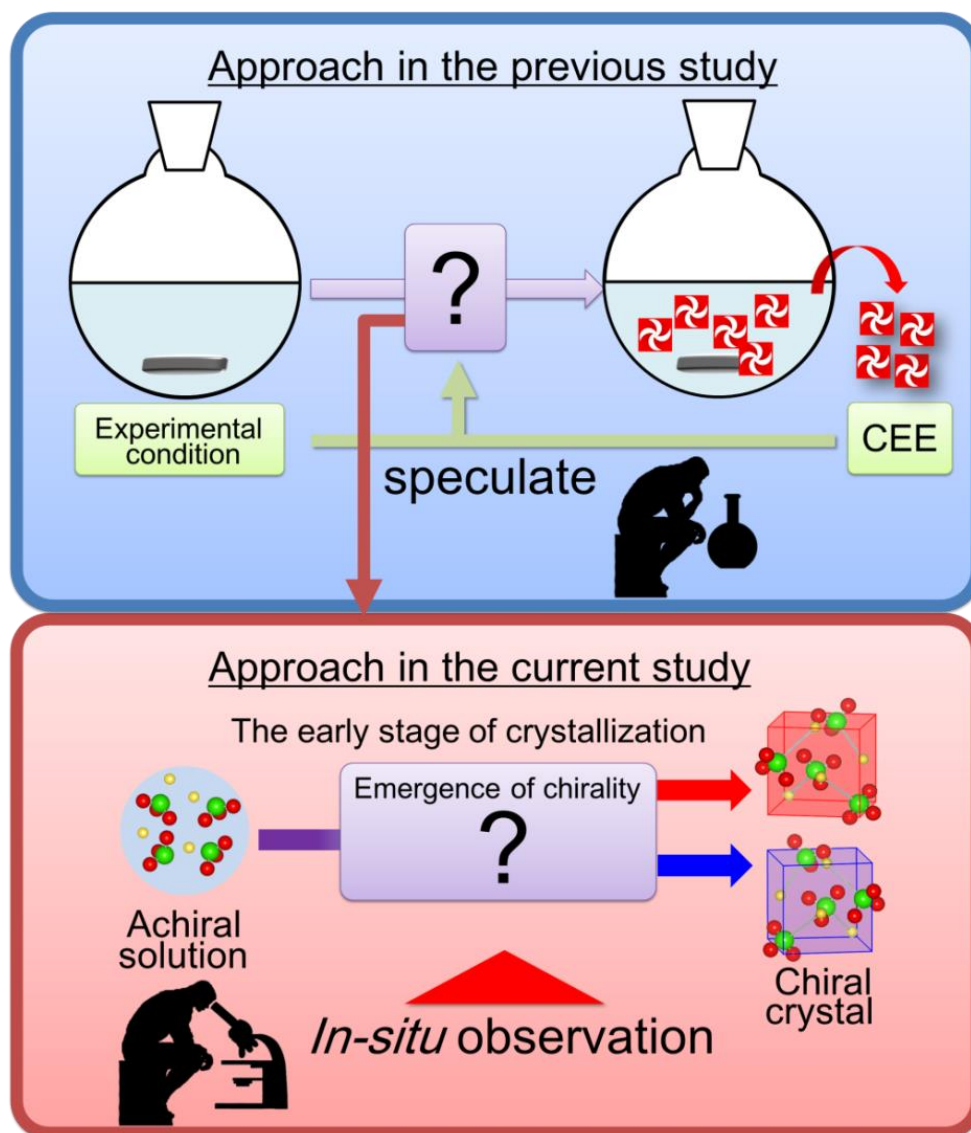
Fig. 1.22 Comparison of the approach in the previous study and the current study. In the previous study, the process of crystal growth was indirectly estimated from the experimental condition and resulting Crystal Enantiomeric Excess. In contrast to this, the current study directly investigates the process of emergence of chirality by observing the early stage of crystallization process one-by-one *in-situ*.

1.4 Aim and Construction of this thesis

As described in the previous sections, chirality in crystal structure broadly has significance in our life, especially for pharmaceutical industry, material science for future spintronic devices and the origin of biohomochirality. In any field, it is considered to be important to understand the mechanism of the emergence of chirality and the amplification of one-single handedness. Chiral crystallization, where chirality emerges in the course of the crystallization, is considered to be responsible for the origin of biohomochirality and is the crystallization manner undertaken by chiral magnetic materials. Therefore, to elucidate the mechanism of emergence of chirality in chiral crystallization has a possibility to provide a new insight not only for the mechanism of chiral symmetry breaking in crystallization but also for the methodology to control the handedness of crystal chirality. However, the previous studies solely have paid attention to the crystal resulting the crystallization, that is, non-growing crystal. Thus, there exists the problem that practical process of crystallization tends to be missed when one discusses phenomenon involving chiral crystallization, leading to the stereotypical common consciousness that the handedness of crystal is already determined at primary nucleation. Here, the aim of this thesis is to clarify the mechanism of emergence of chirality in chiral crystallization using sodium chlorate ($NaClO_3$) as model compound by investigating the early stage of crystallization one-by-one by means of direct *in-situ* microscopic observation. Based on the knowledge obtained from the observation, this thesis discusses the emergence process of chirality and amplification process of one-handedness in chiral symmetry breaking on $NaClO_3$ chiral crystallization. Moreover, to exploit the possibility to control chirality in chiral crystallization, the author performed laser-induced crystallization using circularly polarized light, which asymmetrically interacts with chiral compound.

Construction of this thesis is briefly described below. The chapter 1 describes the background and aim of this study. The chapter 2 shows the existence of unknown precursor of $NaClO_3$ chiral crystal. The chapter 3 describes the analysis on the unknown precursor. The analysis showed that the precursor is an achiral metastable crystalline phase. The chapter 4 describes the detail observation of t achiral-chiral polymorphic transformations that may play the role on the emergence of chirality and amplification of one-handedness. In the chapter 5, the author proposed the conceivable formation process of $NaClO_3$ chiral crystal intermediated by achiral precursor on the basis of the results shown in chapters 2-4. Additionally, the author proposed a conceivable scenario that explains the chiral symmetry breaking in $NaClO_3$ chiral crystallization on the basis

of the formation process the author proposed. In the chapter 6, the author attempted to control chirality of NaClO$_3$ chiral crystal by means of laser-induced crystallization using circularly polarized light and shows a possibility to control chirality. Finally, the author summarizes the knowledge obtained in this study in the chapter 7 as a conclusion of this study.

References

[1] M. Gardner, "The New Ambidextrous Universe: Symmetry and Asymmetry from Mirror Reflections to Superstrings" (Dover Publications, New York) 3rd Edition (2005).

[2] M. Quack, *Angew. Chem. Int. Ed.* **41**, (2002), 4618.

[3] D. Rein, *ATOMKI Közl.* **16**, (1974), 185.

[4] B. Y. Zel'dovich, D. B. Saakyan and I. I. Sobel'man, *JETP Lett.* **25**, (1977), 94.

[5] D. W. Rein, R. A. Hegstrom and P. G. H. Sandars, *Phys. Lett. A* **71**, (1979), 499.

[6] S. F. Mason, *Chem. Soc. Rev.* **17**, (1988), 347.

[7] W. A. Bonner, *orig. Life* **21**, (1991), 59.

[8] S. Pizzarello, *Acc. Chem. Res.* **39**, (2006), 231.

[9] R. M. Harzen, T. R. Filley and G. A. Goodfriend, *Proc. Natl. Acad. Sci. USA* **98(10)**, (2001), 5487.

[10] C. A. Orme, A. Noy, A. Wierzbicki, M. T. McBride, M. Gratham, H. H. Teng, P. M. Dove, P. M. Dove and J. J. DeYoreo, *Science* **411**, (2001), 775.

[11] P. Cintas, *Angew. Chem. Int. Ed.* **41(7)**, (2002), 1139.

[12] L. Addadi and S. Weiner, *Nature* **411**, (2001), 753.

[13] I. Sato, K. Kadowaki, Y. Ohgo and K. Soai, *J. Mol. Catal. A: Chem.* **216(2)**, (2004), 209.

[14] D. G. Blackmond, *Proc. Natl. Acad. Sci. USA* **101(16)**, (2004), 5732.

[15] L. Pasteur, *Ann. Chem. Phys.* **24**, (1848), 442.

[16] M. Yokota, N. Doki and K. Shimizu, *Cryst. Growth Des.* **6(7)**, (2006), 1588.

[17] A. Tonomura, X. Yu, K. Yanagisawa, T. Matsuda, Y. Onose, N. Kanazawa, H. S. Park and Y. Tokura, *Nano Lett.* **12**, (2012), 1673.

[18] C. Pappas, *Physics* **5**, (2012), 28.

[19] D. Morikawa, K. Shibata, N. Kanazawa, X. Z. Yu and Y. Tokura, *Phys. Rev. B.* **88**, (2013), 024408.

[20] T. Kawasaki, K. Suzuki, Y. Hakoda and K. Soai, *Angew. Chem. Int. Ed.* **47**, (2008), 496.

[21] H. D. Flack, *Helv. Chim. Acta.* **86(4)**, (2003), 905.

[22] W. H. Z. Zacharlasen, *Kristallogr.* **71**, (1929), 517.

[23] W. A. Wooster, *Rep. Progr. Phys.* **16**, (1953), 67.

[24] G. N. Ramachandran, *Acta Cryst.* **10**, (1957), 671.

[25] W. S. Kipping and W. J. Pope, *J. Chem. Soc. Trans.* **73**, (1898), 606.

[26] D. K. Kondepudi, R. J. Kaufman and N. Singh, *Science* **250**, (1990), 975.

[27] D. G. Blackmond, *Cold Spring Harb. Perspect. Biol.* **2**, (2010), 002147.

[28] Y. Kousaka, T. Koyama, M. Miyagawa, K. Tanaka, J. Akimitsu and K. Inoue, *J. Phys.: Conf. Ser.* **502**, (2014), 012019.

[29] D. K. Kondepudi, J. Laudadio and K. Asakura, *J. Am. Chem. Soc.* **121(7)**, (1999), 1448.

[30] F. C. Frank, *Biochim. Biophys. Acta* **11**, (1953), 459.

[31] Y. Saito and H. Hyuga, *Rev. Mod. Phys.* **85(2)**, (2013), 603.

[32] J. H. E. Cartwright, J M. García-Ruiz, O. Piro, C. I. Sainz-Díaz and I. Tuval, *Phys. Rev. Lett.* **93**, (2004), 035502.

[33] G. Metcalf and J. M. Ottino, *Phys. Rev. Lett.* **72(18)**, (1994), 2875.

[34] D. K. Kondepudi, K. L. Bullock, J. A. Digits, J. K. Hall and J. M. Miller, *J. Am. Chem. Soc.* **115**, (1993), 10211.

[35] J. M. McBride and R. L. Carter, *Angew. Chem.. Int. Ed.* **30(3)**, (1991), 293.

[36] D. K. Kondepudi and C. Sabanayagam, *Chem. Phys. Lett.* **217(4)**, (1994), 364.

[37] T. Buhse, D. Durand, D. K. Kondepudi, J. Laudadio and S. Spilker, *Phys. Rev. Lett.* **84**, (2000), 4405.

[38] R. Y. Qian and G. D. Botsaris, *Chem. Eng. Sci.* **53(9)**, (1998), 1745.

[39] C. Viedma, *J. Cryst. Growth.* **261(15)**, (2004), 118.

[40] J. H. van't Hoff, *Ber. Dtsch. Chem. Ges.* **35**, (1902), 4252.

[41] J. Crusats, S. Veintemillas-Verdaguer and J. M. Ribó, *Chem. Eur. J.* **12**, (2006), 7776.

[42] Z. El-Hachemi, J. Crusats, J. M. Ribó and S. Veintemillas-Verdaquer, *Cryst. Growth Des.* **9(11)**, (2009), 4802.

[43] Z. El-Hachemi, J. Crusats, J. M. Ribó, J. M. McBride and S. Veintemillas-Verdaquer, *Angew. Chem. Int. Ed.* **50**, (2011), 2359.

[44] C. Viedma, *Phys. Rev. Lett.* **94**, (2005), 065504.

[45] Y. Saito and H. Hyuga, *J. Phys. Soc. Jpn.* **73(1)**, (2004), 33.

[46] J. W. Gibbs, *"collected works* Vol. 1. *Thermodynamics"* (Longmans and Green, New York) (1928)

[47] W. L. Noorduin, T. Izumi, A. Millemaggi, M. Leeman, H. Meekes, W. J. P. Van Enckevort, R. M. Kellogg, B. Kaptein, E. Vlieg and D. G. Blackmond, *J. Ame. Chem. Soc.* **130**, (2008), 1158.

[48] M. Uwaha, *J. Phys. Soc. Jpn.* **73(10)**, (2004), 2601.

[49] J. H. E. Cartwright, O. Piro and I. Tuval, *Phys. Rev. Lett.* **98**, (2007), 165501.

[50] M. Uwaha, *J. Phys. Soc. Jpn.* **78(2)**, (2009), 023601.

[51] Y. Saito and H. Hyuga, *J. Phys. Soc. Jpn.* **79(8)**, (2010), 083002.

[52] C. Blanco, J. Crusats, Z. El-Hachemi, A. Moyano, S. Veintemillas-Verdaquer, D. Hochberg and J. M. Ribó, *ChemPhysChem* **14**, (2013), 3982.

CHAPTER 2
UNKNOWN UNSTABLE CRYSTAL FORMING PRIOR TO CHIRAL CRYSTALS

2.1 Brief Introduction

As written in the Chapter 1, the early stage of $NaClO_3$ chiral crystallization, which could be responsible for the emergence and amplification process of chirality, still remains ambiguous because of the lack of direct microscopic observation. In this chapter, in order to clarify what actually happens in the early stage, the author performed *in-situ* microscopic observations of the early stage of $NaClO_3$ crystallization using polarized light microscopy, which can identify handedness of cubic chiral crystal, and this chapter shows that the early stage is more complex process than previously considered.

2.2 Classical Nucleation Theory

Main interest is nucleation process of $NaClO_3$ crystallization from an aqueous solution. Before detailed explanation of the observational setup, in order to understand quantitative and qualitative description of nucleation phenomena thermodynamic description of the Classical Nucleation Theory (CNT) is briefly introduced in this section because CNT is the simplest and the most widely used theory which describes nucleation process. Even though CNT was originally derived for the condensation of a vapor into a liquid [1-3], it has also been employed "by analogy" to explain precipitation of crystals from supersaturated solutions. For simplicity, the condensation of a vapor phase into a liquid phase is described in this section. The simplicity is due to the isotropic surface tension, γ, of the liquid which leads to spherical equilibrium shape of the small liquid [4]. Basically, the following description is qualitatively valid also for nucleation of crystals.

Considering a volume containing n_v molecules of a vapor with chemical potential μ_v which is a function of the temperature, T, and pressure, P, the thermodynamic potential of the initial state of this system at $T = const$ and $P = const$ is then given by [5]

$$G_1 = n_v \mu_v \tag{2.1}$$

A droplet of a liquid with bulk chemical potential, μ_l, is formed from n molecules of

the vapor phase and the thermodynamic potential of the system vapor-liquid droplet reads [5]

$$G_2 = (n_v - n)\mu_v + G(n) \tag{2.2}$$

where $G(n)$ is the thermodynamic potential of a cluster containing n molecules. The work of formation of a cluster which contains n atoms is then given by the difference $\Delta G(n) = G_2 - G_1$[5]

$$\Delta G(n) = G(n) - n\mu_v \tag{2.3}$$

This formula represents that the work of formation the cluster is the difference between the thermodynamic potential of cluster and the thermodynamic potential of the same amount of molecules in the mother (vapor) phase (nucleation work). In CNT, the thermodynamic potential of the liquid droplet is given by the sum of the chemical potential of the constituent atoms in the infinitely large liquid phase $n\mu_l$ and the surface energy $4\pi r^2 \gamma$ of the droplet [5]

$$G(n) = n\mu_l + 4\pi r^2 \gamma \tag{2.4}$$

where r is the radius of the droplet. CNT assumes that the surface free energy is independent of the droplet size (capillarity approximation) and temperature. The change of the Gibbs free energy on the formation of the droplet is then given by [5]

$$\Delta G = -n(\mu_v - \mu_l) + 4\pi r^2 \gamma \tag{2.5}$$

Since n can be described as $4\pi r^3/3v_l$ where v_l is the molecule volume of the liquid, Eq. (2.5) can be rearranged as [5]

$$\Delta G(r) = -\frac{4\pi r^3}{3} \frac{1}{v_l} \Delta\mu + 4\pi r^2 \gamma \tag{2.6}$$

where $\Delta\mu = \mu_v - \mu_l$ is the driving force for nucleation. In the case of crystal nucleation from an aqueous solution, the driving force can be expressed as [6]

$$\Delta\mu = kTln(1 + \sigma) \tag{2.7}$$

with

$$\sigma = \frac{C - C_e}{C_e} \tag{2.8}$$

where k is Boltzmann constant, σ is supersaturation, C is concentration of aqueous solution and C_e is equilibrium concentration at given temperature. Fig. 2.1 shows the difference of the Gibbs free energy-droplet size (particle size in case of crystal nucleation) profiles. As shown in Fig. 2.1, the change of the Gibbs free energy exhibits bell-shaped curve with local maximum point. The shape is the consequence of the interplay between the first term concerning the chemical potential which contributes to energy gain and the second term concerning the surface free energy which contributes to energy loss. The bell-shaped curve of the Gibbs free energy claims a cluster whose radius is less than a certain threshold to shrink, meanwhile, a cluster whose radius is more than the threshold to grow and becomes nucleus, meaning the existence of the critical size of nuclei. The threshold of the radius is termed as "*critical radius of nucleation*". The critical radius can be derived from Eq. (2.6) by finding the radius which leads the differential of Eq. (2.6) to zero. Therefore, the critical radius, r^*, is given by [5]

$$r^* = \frac{2\gamma v_l}{\Delta\mu}. \tag{2.9}$$

Substituting Eq. (2.9) to Eq. (2.6), the activation energy which should be overcome for nucleation to take place, ΔG^*, can be obtained as [4]

$$\Delta G^* = \frac{16\pi}{3} \frac{\gamma^3 v_l^2}{\Delta\mu^2}. \tag{2.10}$$

Eq. (2.10) indicates that the increment of supersaturation lowers the activation energy for nucleation. Becker has derived the kinetic expression for the steady state nucleation rate, J_0, as follows [5]

$$J_0 = \omega^* \Gamma Z_1 exp\left(-\frac{\Delta G^*}{kT}\right) \tag{2.11}$$

where ω^* is the frequency of the attachment of molecules to the critical nucleus and Z_1 is the steady state concentration of single molecule in the vapor phase. The parameter Γ is so-called Zeldovich factor expressed as follows: [5]

$$\Gamma = \left(\frac{\Delta G^*}{3\pi kT n^{*2}}\right)^{1/2} \tag{2.12}$$

Since the surface free energy and volume of the condensed phase are unambiguously determined in single-component system under the capillarity approximation nucleation rate is effectively governed by supersaturation in accordance with the statement of Eq. (2.11) and Eq. (2.10). Clusters of the condensed phase continually repeat the association and dissociation and the size of the cluster fluctuates. Thus, a statistical cluster size distribution reflecting the thermal fluctuation exists. Because the increment of supersaturation diminishes the critical radius, the existence probability of the clusters whose size exceeds the critical radius increases. This is the qualitative description of nucleation rate depending on high supersaturation. As shown below, the increment of the supersaturation as driving force for nucleation is obtained by condensing a saturated solution by evaporation of solvent in our crystallization experiment.
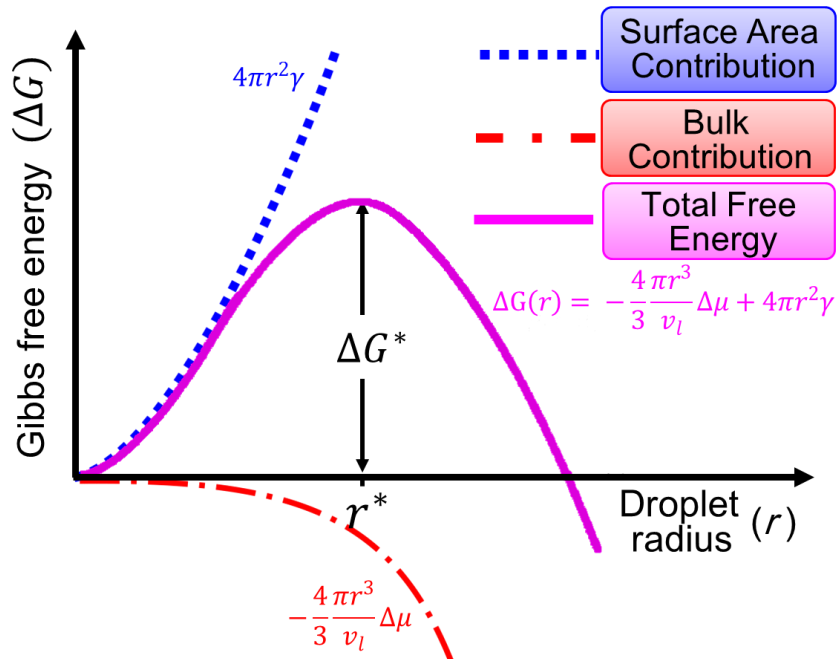
Fig. 2.1 Dependence of the Gibbs free energy on the droplet radius of the condensed phase.

2.3 Experimental –Principle of Polarized Light Microscopy and Principle of Identification of Crystal Handedness–

2.3.1 Principle and Feature of Polarized Light Microscopy

Polarized light microscopy (PLM) is capable of detecting information on optical property of a specimen. PLM uses linearly polarized light as illumination light and detects the change in polarization state of the linearly polarized light caused by interaction of the light with a specimen. Optical setting of PLM is constructed by illumination light source, two polarizers and objective lens (Fig. 2.2). Natural light emitted from the illumination light source passes through the first polarizer above the light source and the natural light is converted to linearly polarized light. The linearly polarized light propagates towards the second polarizer beneath the objective lens (called as "analyzer"). The vibration azimuth allowed by the analyzer is orthogonal to that of the polarizer. This orthogonal orientation of the polarizer and the analyzer is called as "crossed nicols", which is fundamental setting of PLM. Since the vibration azimuths of a pair of polarizers are orthogonal each other under crossed nicols setting, the linearly polarized light is optically blocked by the analyzer before reaching to the objective lens. Since illumination light is completely extinguished by analyzer, microscopic field is totally dark and extinction state under crossed nicols. The extinction state is maintained even if an optically isotropic medium such as glass is placed on microscope stage located between the two polarizers and lies cross the optical path because optically isotropic medium allows the linearly polarized light to pass though without any change in polarization state. Namely, an optically isotropic specimen exhibits total extinction under crossed nicols observation (Fig. 2.3 **A**). On the other hand, if an optically anisotropic, namely, birefringent specimen is placed on the microscope stage and lies cross the optical pass the specimen exhibits bright contrast because of birefringence. When linearly polarized light passes through a birefringent specimen the polarized light splits into two linearly polarized lights whose planes and velocities are mutually-perpendicular and distinct, respectively (Fig. 2.3 **B**). Namely, elliptically-polarized light generates after a linearly polarized light passes through the birefringent specimen. The elliptically-polarized light can pass through the analyzer since the light contains polarization components whose vibration azimuth is parallel to the azimuth allowed to transmit by analyzer. Therefore, when one observes a birefringent specimen under crossed nicols the specimen exhibits bright interference color. All crystalline materials are birefringent medium except for cubic crystal. Therefore, we can distinguish non-cubic crystal from cubic crystal using PLM since non-cubic crystal basically exhibits bright interference color and cubic crystal exhibits

complete extinction under crossed nicols. However, birefringent crystals exhibit complete extinction when a certain condition is fulfilled. There are two cases when birefringent crystals show complete extinction; (1) in the case that the optical path coincides with the optical axises of the birefringent crystal specimen. (2) in the case that the plane of linearly polarized light illuminated to the birefringent crystal coincides with either of the two vibration azimuth allowed by the crystal. The extinction state cause by the case (2) is useful to identify whether an objective specimen is birefringent crystal or not. The extinction state of a birefringent crystal takes place four times out of 360° rotation of crystal orientation. Therefore, if a bright object under crossed nicols shows four times extinction in 360° rotation of microscope stage it follows that the object is a crystal whose crystal system is non-cubic.

  PLM is also capable of identifying the handedness of chiral cubic crystals by detecting optical rotation caused by optical activity (Fig. 2.3 **C**, **D**). Since a cubic crystal is transparent to the illumination linearly polarized light, the linearly polarized light passes through the cubic crystal without any change. On the other hand, in the case when a cubic crystal has chirality, the plane of the linearly polarized light passing through the chiral cubic crystal is rotated by a few degrees by optical activity. The rotation generates polarization component whose vibration azimuth is parallel to that of the analyzer, making a cubic crystal slightly bright even under crossed nicols. Namely, chiral cubic crystal does not show complete extinction under crossed nicols observation. Only after rotating the analyzer by a few degrees from the crossed nicols orientation, the crystal shows complete extinction. Since the rotation direction of the plane of polarization depends on the handedness of chiral cubic crystals, the rotation direction of analyzer that leads to complete extinction is opposite between two enantiomorphs. Accordingly, we can identify handedness of chiral cubic crystal by checking the rotation direction that makes the crystal extinction. In summary, (1) PLM can distinguish non-cubic crystal from cubic crystal by detecting presence or absence of birefringence under crossed nicols observation and (2) PLM can also distinguish the handedness of chiral cubic crystal by checking which rotation direction of the analyzer leads to complete extinction of the crystal.
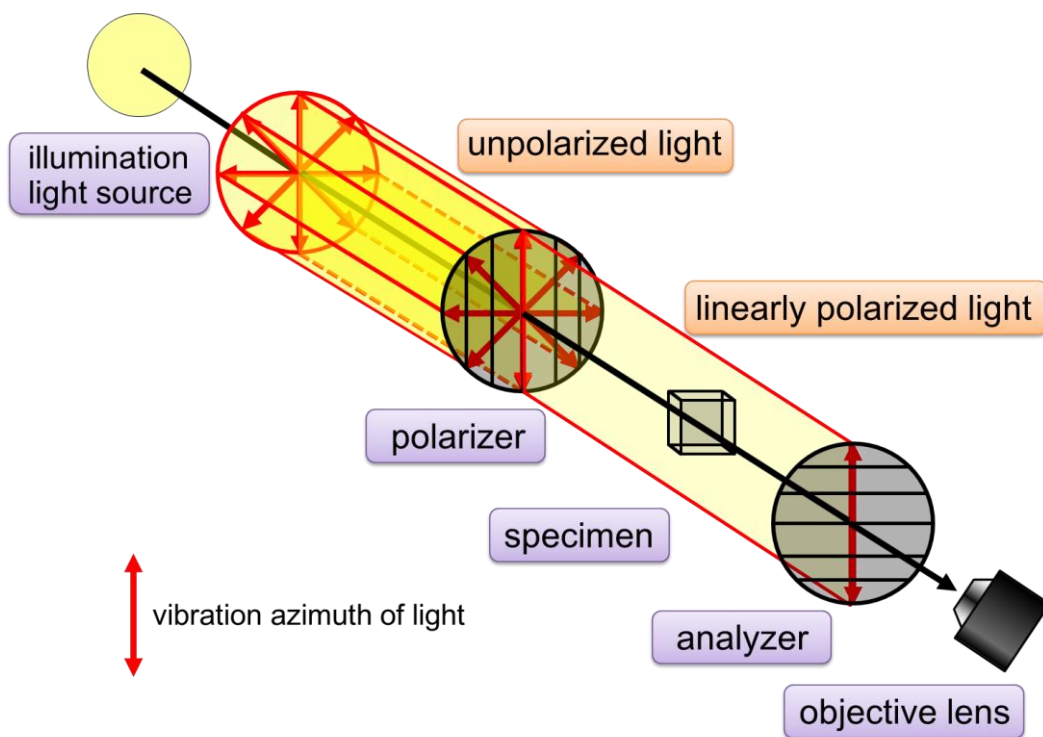
Fig. 2.2 Schematic illustration of geometry of polarized-light microscopy (crossed nicols orientation)

A

optically isotropic medium

e.g. cubic crystal
amorphous

shows extinction

B

vibration azimuth of ordinary light

vibration azimuth of extraordinary light

optically anisotropic medium

e.g. Non-cubic crystal

➤ shows bright color
➤ extincts four times every 360° rotation of medium orientation

C

optically isotropic chiral medium (*l*-form)

e.g. NaClO₃ cubic crystal

➤ shows slightly bright color
➤ extincts when analyzer is rotated to *counter-clockwise*

D

optically isotropic chiral medium (*d*-form)

e.g. NaClO₃ cubic crystal

➤ shows slightly bright color
➤ extincts when analyzer is rotated to *clockwise*

Fig. 2.3 Contrasts which various specimens exhibits under polarized-light microscopic observation. **A:** the case that the specimen is optically isotropic medium. Since an isotropic specimen transmits an incident linearly polarized light as it is the medium exhibits extinction under crossed-Nicols observation. **B:** the case that the specimen is optically anisotropic. Since the medium generates a light that can pass through the analyzer the specimen exhibits brilliant bright color under crossed nicols observation. **C** and **D:** the case that the specimen is chiral isotropic medium. Owing to the optical activity, the specimen exhibits slightly bright contrast under crossed nicols observation. When the analyzer is rotated to clockwise (counter-clockwise) dextrorotatory (levorotatory) medium becomes to exhibit extinction.

2.3.2 Observational Methods

2.3.2.1 Preparation of $NaClO_3$ an Aqueous Solution

Physical properties of sodium chlorate ($NaClO_3$) are shown below [6].

IUPAC name : Sodium Chlorate

Composition formula : $NaClO_3$

Formula weight : 106.44 g / mol

Shape : colorless crystalline solid, cubic crystal system

Density (solid) : 2.49 g / cm^2

Melting point : 248 °C

Boiling point : >300 °C

According to Chronological Scientific Tables, temperature dependence of solubility in water, C_I, is expressed as

$$C_I(T) = 1.1917T + 71.701 \text{ (g/100 ml } H_2O) \tag{2.13}$$

where T is Celsius temperature. Calculation of equilibrium concentration in this thesis is based on this formula.

An aqueous solution of $NaClO_3$ was prepared by dissolving 110 g of $NaClO_3$ powder (Analytical Grade, Wako Pure Chemical Industries, Ltd, Osaka, Japan) in ultrapure water (100 mL) in a 500 mL glass beaker at room temperature (22 °C). The resulting solution was heated to 30 °C under stirring with a magnetic hot plate stirrer. After assuring that the powder was completely dissolved in the water, the beaker was hermetically closed using laboratory film, and left for a week at the room temperature (22 ºC) to precipitate the solute dissolved in excess of the solubility. After the precipitation, the solution reached equilibrium at 22 ºC. The supernatant of the resulting solution was then used as a saturated solution for observations of crystallization process.

2.3.2.2 Observational Setup

Crystallization experiments were performed by pipetting a drop (6 μL) of the saturated solution on a glass slide. The glass slide was placed on a temperature-controlled stage governed by Peltier devices whose temperature set at 22 °C. The configuration of the Peltier stage is shown in Fig. 2.4. Baseplate of the stage is made by cupper with 10 mm thick and has a hole in the center so as to transmit illumination light from a microscope.

Two plate-type Peltier devices with dimensions of 30 mm × 30 mm × 3.9 mm is stacked in pairs and the stacked devices are tucked by the baseplate and jackets of cooling water made by cupper with dimensions of 50 mm × 33 mm × 15 mm. This configuration is set at two places and the all Peltier devices are connected in tandem arrangement. Cooling water is pumped into the jackets by a water circulation pump, which is made for PC cooling, with radiator. The Peltier devices are connected with a Peltier controller (FC-2410, Sensor Controls Co. Ltd., Kanagawa, Japan), which is driven based on feedback control using temperature value measured by a thermocouple (Pt 100). The thermocouple was set so as to measure the temperature of the baseplate. Herewith, the temperature of the baseplate was controlled with an accuracy of ±0.1 °C. The Peltier stage was placed on the microscope rotation stage of a PLM [BX51-P (custom-made); Olympus Corp., Tokyo, Japan]. The PLM is equipped with a high-definition (HD) recording system consisting of a high vision camera (SONY HDC-X300) in order to capture processes happen in microscope field *in-situ*. The droplet of solution on the glass slide was allowed to evaporate in air (temperature: 22 °C, humidity: 27 %, atmosphere: 1 atm). The evaporation increases concentration solution, which induces $NaClO_3$ crystallization. After approximately 10 minutes, crystals appeared in the droplet because of nucleation from a supersaturated solution. We observed *in-situ* the process of this crystallization with a polarized-light microscope mentioned above.
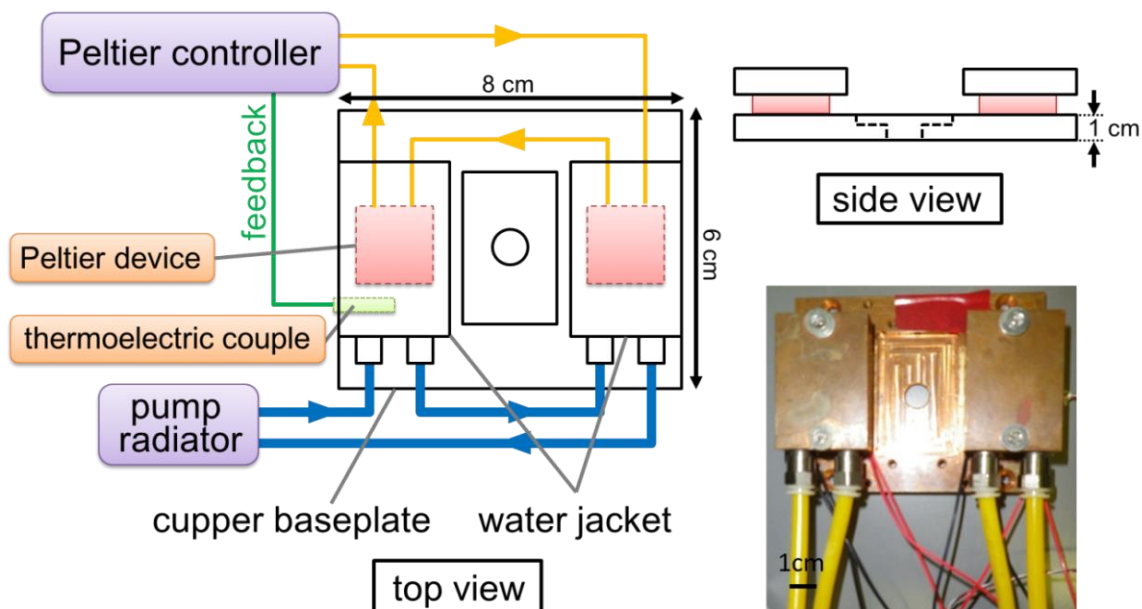
Fig. 2.4 Schematic illustration of Peltier stage for temperature control

2.4 Results

Fig. 2.5 shows time-lapse micrographs of the crystallization induced by the droplet-evaporation. The micrographs were captured under crossed nicols orientation.
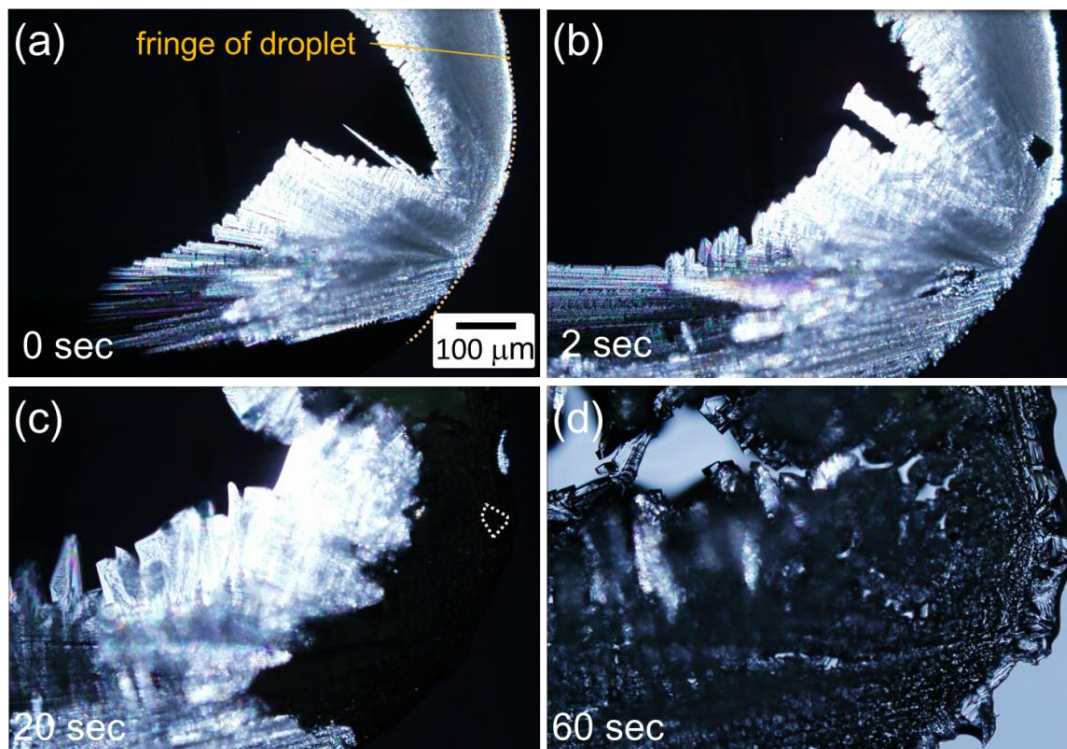
Fig. 2.5 (a)-(d) Time-lapse PLM micrographs of $NaClO_3$ crystallization process driven by evaporation of solvent. (a)-(c): crossed nicols observation. (d): non-crossed nicols observation.

Brilliant bright colored crystals initially appeared from the meniscus of the droplet-glass slide interface. The bright colored crystals started to grow preferentially along to the meniscus with dendritic shape. The bright dendrites continued to grow larger than 1 mm, and they simultaneously grew towards the center of the droplet [Fig. 2.5 (b)]. Additionally, when orientation of the bright dendrites was rotated by rotating the microscope circulation stage the bright color of the crystal was extinguished depending on the crystal orientation. The extinction occurred four times every 360° rotation of crystal orientation. Parallelogram shaped bright crystals with 105° of dihedral angle also formed at the vicinity of the dendrites (Fig. 2.6). The parallelogram crystals also exhibit extinction four times every 360° rotation of crystal orientation (Fig. 2.7). Several seconds after the formation of the bright dendrites, the bright contrast of the dendrites partially disappeared in the microscopic region where the dendrites initially formed. After the partial extinction, the dark region began to spread along the dendrites with a

velocity of about 20 μm/sec from the region where the partial extinction occurred [Fig. 2.5 (c)]. With time, the bright dendrites were completely converted into dark crystals. The resulting shape of the dark crystals nearly retained the shape of the bright dendrites, displaying a pseudomorph of the dendrites. The conversion into dark crystal is accomplished only in a few minutes [Fig. 2.5 (d)].
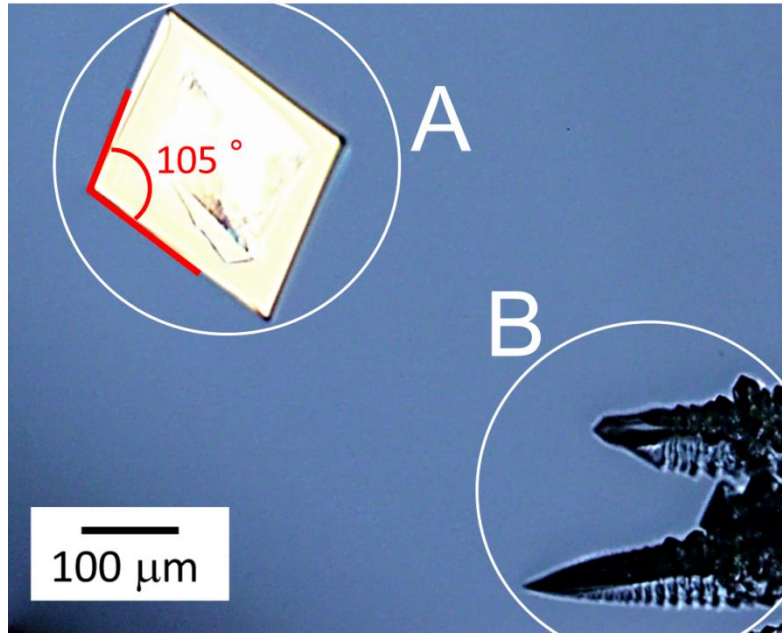
Fig. 2.6 A micrograph showing perfect-shaped non-cubic crystal and a cubic dendrite, captured by *in-situ* observation using polarized-light microscopy. (A): perfect-shaped non-cubic crystal (B): cubic dendrite.
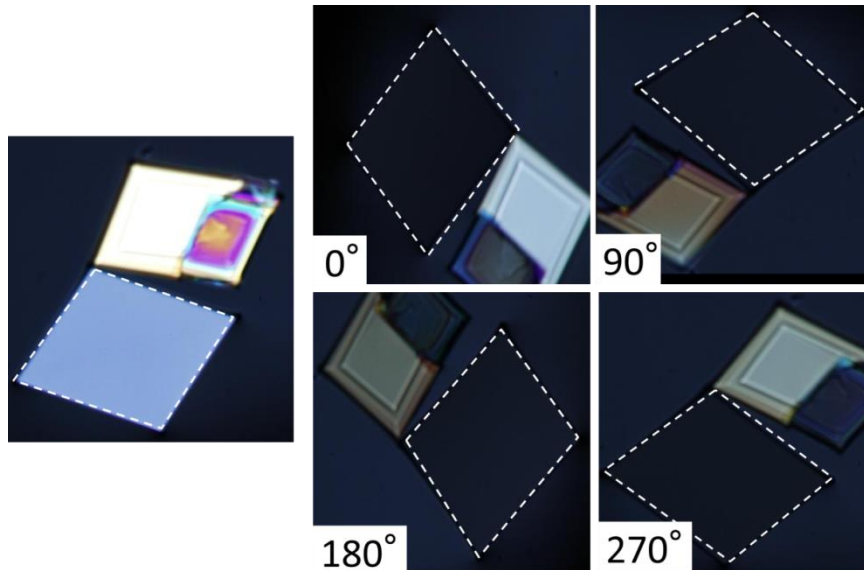
Fig. 2.7 Micrographs showing extinction of the non-cubic crystal under crossed nicol, which occurs four times every 360° rotation of crystal orientation. The dashed parallelogram shape indicates the non-cubic crystal.

2.5 Discussion

2.5.1 Non-Cubic Crystal Forming Prior to Chiral Cubic Crystal

Since the crystal system of $NaClO_3$ chiral crystals is cubic, crystals which exhibits complete extinction or slightly bright color is expected to initially appear. However, the initially formed crystals unexpectedly exhibited brilliant bright color. Additionally, the crystal showed four times extinction every 360° rotation of crystal orientation under crossed nicols. These optical properties indicate the feature of birefringence. Namely, the bright crystals are unknown non-cubic crystal. The parallelogram shape of the bright crystals can be the equilibrium shape of the non-cubic crystal. Indeed, the parallelogram shape is different from the equilibrium shape of well-known cubic squared crystal, supporting the consideration that bright crystal is not cubic crystal. Therefore, the author concluded that the crystals initially appeared in the crystallization is non-cubic crystals.

It was observed that the disappearance of the brilliant bright colored dendrites followed by simultaneous appearance of dark crystals. These observational results can be interpreted by a transformation from the non-cubic crystal to well-known chiral cubic crystal because the cubic crystal with no birefringence exhibits slightly bright color under crossed nicols.

The observation revealed that an unstable non-cubic crystal appears prior to the formation of chiral cubic crystal and the non-cubic crystal transforms into chiral crystal within a few minutes.

2.5.2 Ostwald's Rule of Stages and Nucleation of Polymorphs

Polymorphism is the phenomenon which shows several crystal structures even though the building material is the same. Polymorphs, distinct crystal structures composed by the same compound, have different chemical and physical properties. Accordingly, thermodynamic stabilities of each polymorph are different and polymorphs are classified as thermodynamically stable phase and metastable phases. The metastable form sometimes crystallizes as intermediates for the formation of the most stable form. The existence of metastable polymorphs as intermediates complicates practical nucleation process rather than the description of CNT assuming single-component system. In 1897, Wilhelm Ostwald has observed that in general the formation of metastable polymorph tends to precede the formation of the most stable one during crystallization process [8]. The observation led the celebrate Ostwald's rule of stages, which states that the polymorph having the Gibbs free energy closest to building component in the mother liquor will crystallize first, followed by polymorphic

transformations through increasingly more stable polymorphs before eventually arriving at the most stable polymorph. This rule has been experimentally observed in various systems such as macromolecular crystal, organic crystal, colloidal crystal, inorganic semiconductor crystals and forth [10-13].

As described as Eq. (2.10), the activation energy for nucleation is a function of not only supersaturation but also surface free energy. Whereas the chemical potential contributes with square, the surface energy does with third power. Therefore, the contribution of the surface free energy is predominant during the crystal formation process. Generally, a metastable polymorph has lesser surface free energy than that of the stable polymorph [9]. Therefore, the activation energy for the nucleation of the metastable polymorph is basically lower than that of the stable one, meaning that the metastable one is kinetically accessible than the thermodynamically stable one (Fig. 2.8). Owing to the accessibility, a metastable polymorph transiently appears as an initial phase followed by the transformation to the stable phase. This is the qualitative mechanism of the Ostwald's rule of stages (Fig. 2.9).
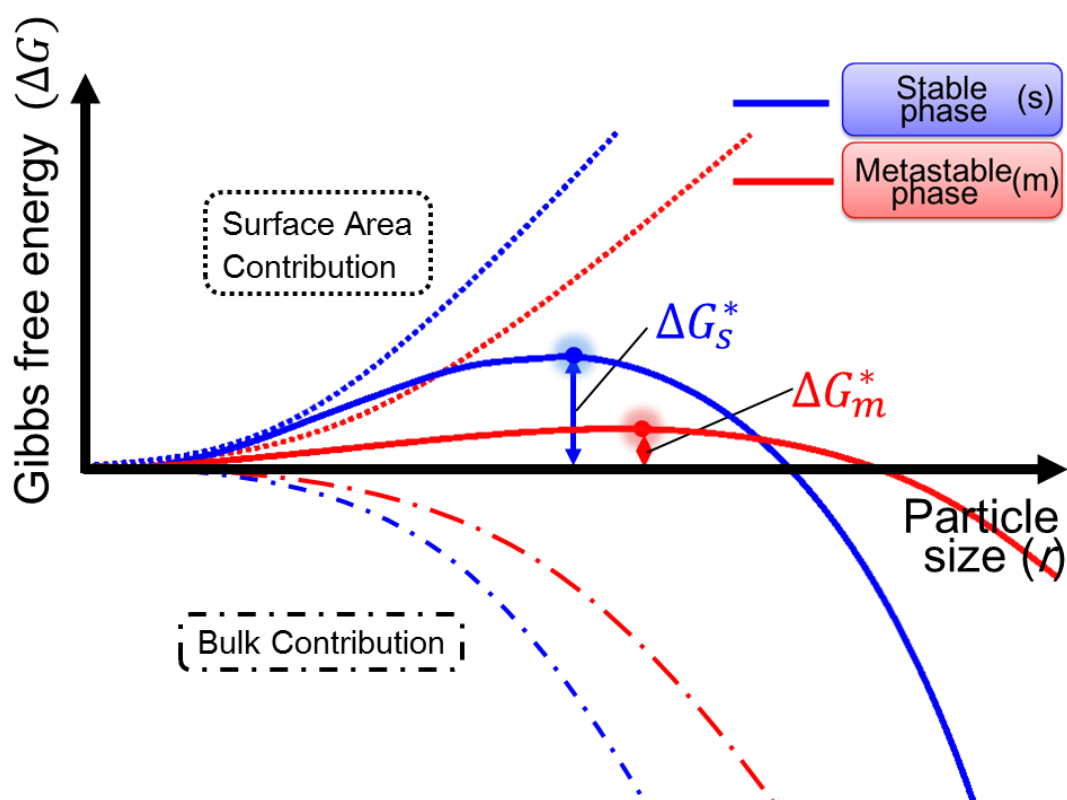
Fig. 2.8 Comparison of Gibbs free energy change depending on particle size during nucleation process between a stable phase and a metastable phase. This figure is adopted from Ref. [10]

Also in our observations, the non-cubic crystal initially and transiently appeared in the solution droplet. This process is consistent with the picture of the Ostwald's rule of stages, implying that the non-cubic crystal is a metastable phase in $NaClO_3$ crystallization from an aqueous solution. Therefore, a series of the formation process of chiral cubic crystal intermediated by the non-cubic crystal is estimated to be a consequence of the Ostwald's rule of stages. Therefore, the non-cubic crystal is presumably a metastable polymorph. Analysis on thermodynamic stability of the non-cubic crystal will be described in the next chapter.
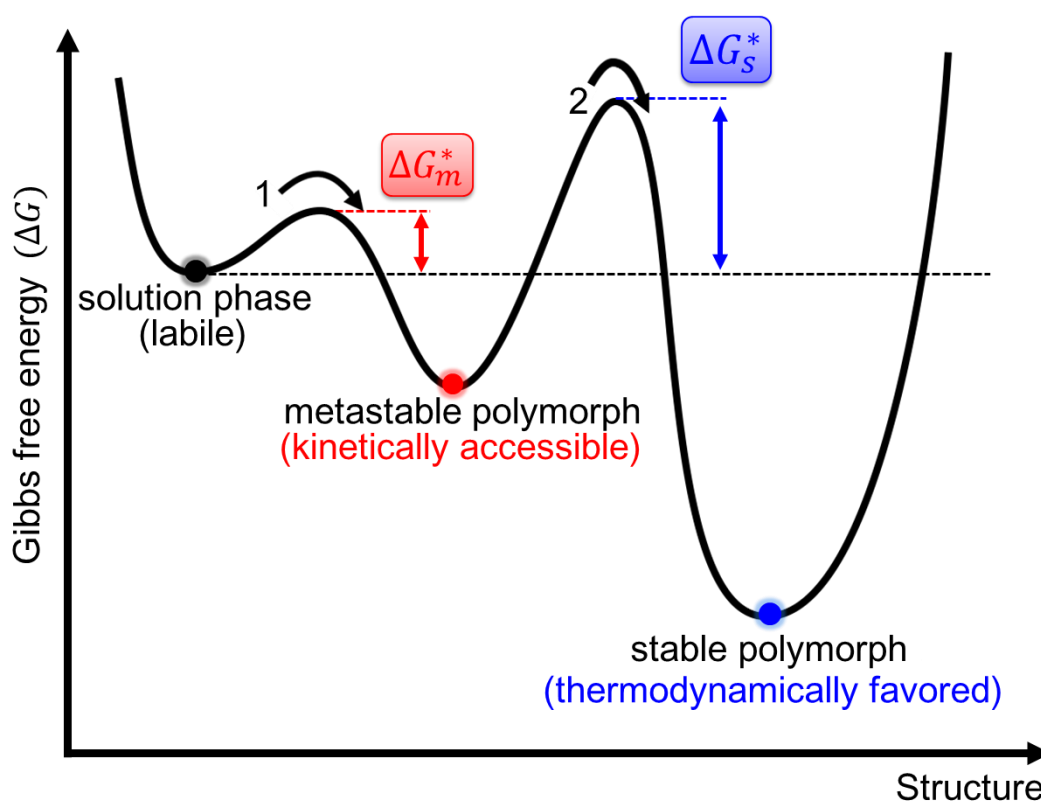
Fig. 2.9 Energetic pathway during the Ostwald's rule of stages. The numbers embed in this figure indicates the order of crystallization pathway. This figure is adopted from Ref. [11] (The figure is partially modified)

2.6 Summary of Chapter 2

In this chapter, *in-situ* microscopic observation of the early stage of $NaClO_3$ chiral crystallization from an aqueous solution was performed using a polarized light microscopy. The findings revealed by the observation were summarized below.

- Unstable non-cubic crystal forms prior to the formation of chiral cubic crystal in the early stage of $NaClO_3$ crystallization from an aqueous solution.
- The non-cubic crystal transforms into chiral cubic crystal within a few minutes.
- The series of the formation process of chiral cubic crystal intermediated by the non-cubic crystal is possibly a consequence of the Ostwald's rule of stages.

References

[1] M. Volmer and A. Weber, *Z. Phys. Chem.* **119,** (1926), 27.

[2] J. W. Gibbs, "*collected works* Vol. 1. *Thermodynamics"* (Longmans and Green, New York) (1928)

[3] R. Becker and W. Döring, *Ann. Phisik.* **24,** (1935), 719.

[4] D. Erdemir, A. Y. Lee and A. S. Myerson, *Acc. Chem. Res.* **42(5),** (2009), 621.

[5] I. V. Markov, "*CRYSTAL GROWTH FOR BEGINNERS*" (World Scientific, Singapore) 2nd Edition (2003)

[6] R. Boistelle and J. P. Astier, *J. Cryst. Growth* **90,** (1988), 14.

[7] M. Ohki, M. Tanaka, T. Ohsawa, H. Chihara. Kagakudaijiten, Tokyo Kagaku Doujin, 1989.

[8] W. Ostwald, *Z. Phys. Chem.* **22,** (1897), 289.

[9] M. Matsuoka, "*Advanced Technology, Application and Development of Polymorphic Crystals*" (CMC publications, Tokyo) (2005)

[10] V. J. Hall and G. J. Simpson, *J. Am. Chem. Soc.* **132,** (2010), 13598.

[11] S. Y. Chung, Y. M. Kim, J. G. Kim and Y. J. Kim, *Nat. Phys.* **5,** (2008), 68.

[12] A. L. Washington, II, M. E. Foley, S. Cheong, L. Quffa, C. J. Breshike, J. Watt, R. D. Tilly and G. F. Strouse, *J. Am. Chem. Soc.* **134,** (2012), 17046.

[13] T. H. Zhang and X. Y. Liu. *Angew. Chem. Int. Ed.* **48,** (2009), 1308.

CHAPTER 3
ANALYSIS ON UNKNOWN UNSTABLE NON-CUBIC PHASE

3.1Brief Introduction

In the previous chapter, non-cubic crystal, which transiently appears prior to the formation of chiral crystals, was found by *in-situ* polarized light microscopic (PLM) observation. However, crystallographic and thermodynamic stability of the non-cubic crystal still remain unclear. Accordingly, the role of the non-cubic crystal on the emergence of chirality is unclear. Namely, it is unclear which process, nucleation or polymorphic transformation, is responsible for the emergence of chirality. Therefore, it is necessary to clarify whether the non-cubic crystal has chirality or not. This chapter clarifies this point by single-crystal X-ray structural analysis on the non-cubic crystal. Since the non-cubic crystal is extremely unstable to conduct conventional XRD experiment cryogenic single-crystal X-ray diffraction (XRD) experiments were performed to circumvent the difficulty. The experiment reveals crystallographic properties of the non-cubic crystal, leading to more accurate understanding of the emergence process of chirality in the early stage of crystallization. Additionally, in order to clarify thermodynamic stability of the non-cubic crystal, solubility measurement of the non-cubic crystal was also performed. The obtained solubility data helps us to understand polymorphic phenomena between the non-cubic crystal and chiral cubic crystal.

3.2 Experimental -Structural Analysis on Unknown Unstable Crystal-
3.2.1 Cryogenic Single-Crystal X-ray Diffraction Experiment

The non-cubic crystal is extremely unstable. The lifetime of the crystal is about a few minutes at the longest in the case of crystallization driven by spontaneous evaporation. On the other hand, conventional single-crystal XRD experiment involves time-consuming process and whole process of the experiment takes from a half of a day to a day to resolve the structure of a crystalline specimen and structural analysis requires a specimen to be maintained as it is throughout the experiment. Therefore, it is difficult to determine the structure of the non-cubic phase by the conventional single-crystal XRD experiment because of instability of the non-cubic crystal. A method to maintain the unstable crystal throughout the experiment is necessary to be established to clarify whether the phase has chirality or not.

Here, the author applied cryogenic single-crystal XRD method [1] to overcome the instability of the target crystal. The cryogenic XRD method has been utilized to analyze a structure of unstable intermediates or precursors of chemical reactions or the structure of brittle protein crystals, which is easily broken by the evaporation of crystalline water [2]. Namely, the cryogenic XRD is known as a strong method to analyze the structure of a unstable crystal. Concretely, the progress of a chemical reaction or the change of transient state was suppressed by quenching the specimen in the course of a chemical reaction or a transformation in the cryogenic method. The frozen stage of a chemical reaction or a transformation can be analyzed by mounting the quenched specimen on a chilled stage. This is the way of the cryogenic single-crystal XRD experiment. In the case of $NaClO_3$ crystallization, a non-cubic phase crystallized in a solution droplet was quenched by liquid nitrogen. Experimental details are described below.

A single crystal of the non-cubic phase was produced upon a cover glass with about 170 μm thickness by means of the droplet-evaporation method described in the previous chapter. Temperature of the droplet was maintained at 22 °C using the Peltier stage described in the previous chapter. During the crystallization, non-cubic crystal was identified by checking the presence of birefringence using crossed nicol PLM. When the single crystal had grown to 100-300 μm, the solution surrounding the crystal was removed using a laboratory wipe, and the crystal was covered with glycerin, which acts as a cryoprotectant. Cryoprotectant prevents from producing crystalline ice, which generates undesired diffraction spots as background noise, during quenching process. The generation of diffraction spots which comes from crystals except for the target crystal is fatal for analyzing a diffraction pattern because it is difficult to identify only diffraction spots originating from the target crystal from the mixture of diffraction spots originating from two distinct crystals. Glycerin is widely used as cryoprotectant and the mixture of glycerin and water solidifies as an amorphous ice by quenching. Because diffraction pattern of amorphous specimen shows halo pattern in contrast with diffraction spots generated from a single crystal, the diffraction spots originating from the non-cubic single crystal can be easily separated from the background noise of the halo pattern. After replacing the surrounding fluid, the cover glass beneath the glycerin droplet containing the non-cubic single crystal was mounted on a hand-made sample holder of XRD system (Fig. 3.1 **A**). Then, whole sample holder and the specimen were quenched by being immersed in liquid nitrogen whose temperature is -198 °C before transformation to chiral cubic phase starts. After the quench, the solvent surrounding the crystal was confirmed to be amorphous ice by checking the absence of birefringence

using PLM. Checking the birefringence using the PLM also confirms that transformation of non-cubic crystal was successfully suppressed (Fig. 3.1 **A**). Fig. 3.1 **B** shows the schematic overview of the experimental setting for the cryogenic single-crystal XRD.   The system comprises three components: (1) a low-temperature instrument to keep the sample frozen (2) a XRD system (3) a PLM system to confirm that the non-cubic crystal was maintained while circumventing the transformation before and after of the experiment. Cryostream system (Oxford Cryosystems, Oxford, UK) was adopted for the low-temperature system to chill the atmosphere surrounding the sample and stage of XRD system. Cryostream can continuously blow low-temperature nitrogen gas to the sample. Using the Crypstream system, the temperature of the atmosphere surrounding the sample was maintained at -27($\pm$1) °C, which was measured by a K-type thermocouple, throughout the experiment. Consequently, the sample was successfully kept to be frozen throughout the experiment. R-AXIS IV++ (Rigaku Corp., Tokyo, Japan) with an imaging plate was used as the XRD system. Diffraction data were collected from the frozen sample with dimensions of 100 × 80 × 10 μm by the oscillation method. All the oscillation images were processed using the CrystalClear software (Rigaku) to determine the crystallographic parameters. The detailed experimental conditions for the XRD measurements are listed in Table 3.1.
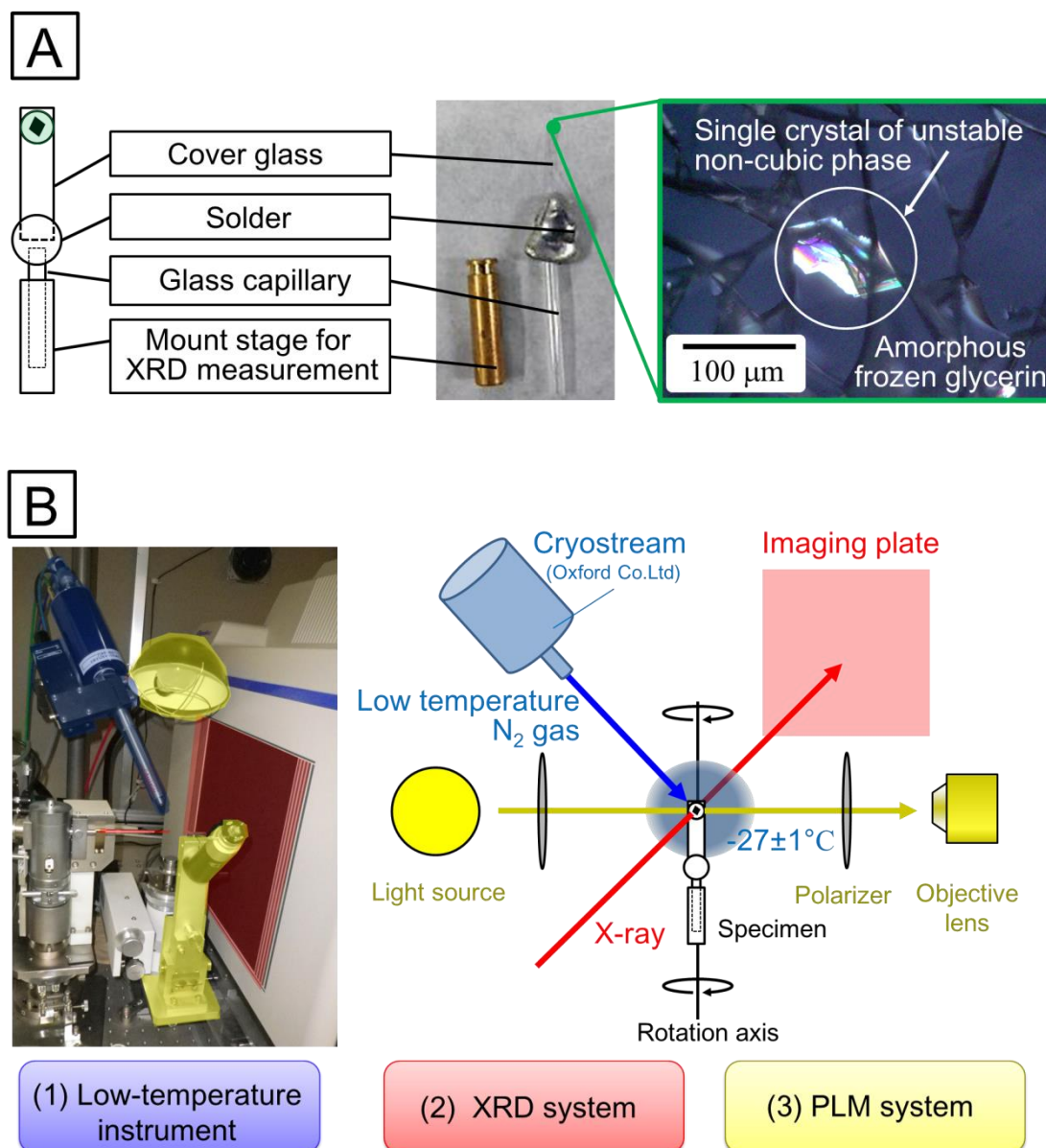
Fig. 3.1 Experimental setting for cryogenic single-crystal XRD experiment: **A** shows a schematic illustration (left) and an image of hand-made sample holder to mount the non-cubic crystal specimen (middle). Right micrograph shows polarized-light microscopic image of the frozen specimen (see experimental) mounted on the sample holder. **B** The left image shows experimental instruments for the experiment. Right schematic illustration shows the overview of the experimental system, corresponds to the left image. Blue, red, yellow colored parts are low-temperature instrument, XRD system, PLM system, respectively.

Table 3.1 Experimental conditions for cryogenic XRD experiment

Analytical method	Oscillation conditions
Radiation	Mo Kα
Wavelength (Å)	0.7107
X-ray output (kV, mA)	50, 20
Collimator size (μm)	300
Crystal to imaging plate distance (mm)	120
Oscillation range (degrees)	360
Oscillation step range per image (degrees)	2
Exposure time (s)	300

3.3 Results

Fig. 3.2 shows photographs of the X-ray oscillation image with 4° oscillation range in the case without the cryoprotectant (Fig. 3.2 **A**) and with the cryoprotectant (Fig. 3.2 **B**). The oscillation image without cryoprotectant shows that diffraction spots and Debye-Scherrer ring that originating from ice crystals of the solution droplet and diffraction spots originating from the non-cubic crystal were mixed. It is evidently difficult to distinguish the spots from the non-cubic crystal from the spots from the ice crystals in the image without cryoprotectant. On the other hand, the image with cryoprotectant exhibits clear diffraction spots from the non-cubic crystal and the halo pattern from the amorphous of the cryoprotectant. The halo pattern is only a background of the image since the diffraction spots can be easily extracted from the halo pattern by image processing without any confusion. The use of cryoprotectant allowed the author to analyze the structure of non-cubic crystal.

The cryogenic single-crystal XRD experiments successfully provided 4314 reflections in total. Through an analysis of the distributions of the diffraction spots, the lattice parameters of the non-cubic crystal were determined to be $a = 8.42(2)$, $b = 5.260(7)$, $c = 6.70(1)$ Å, $\beta = 109.71(1)°$, and $V = 279.8(8)$ Å^3, where V is the volume of unit cell. These results indicate monoclinic symmetry. In addition, three systematic absence rules were observed in the analytic dataset of the XRD intensities: $h = 2n + 1$ in the $h0l$ series, $k = 2n + 1$ in the $0k0$ series, and $h = 2n + 1$ in the $h00$ series. This systematic absence indicates that the space group of the monoclinic phase is $P2_1/a$ (the unique axis is b).

Fig. 3.3 shows a photograph of the X-ray oscillation image with 4° oscillation range which shows a systematic absence rule of $h = 2n + 1$ in $h0l$. One should note that crystals with space group $P2_1/a$ are achiral because the space group contains mirror symmetry as symmetrical element. Namely, the non-cubic crystal was found to be achiral.
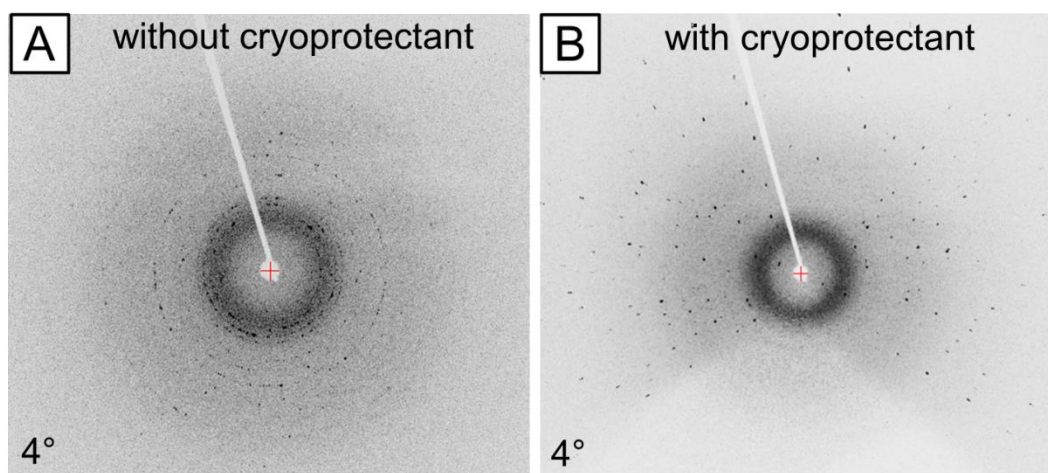
Fig. 3.2 A comparison of XRD images of the cryogenic experiment with/without use of cryoprotectant. **A** A diffraction image when the cryoprotectant was used. **B** A diffraction image when the cryoprotectant was not used.
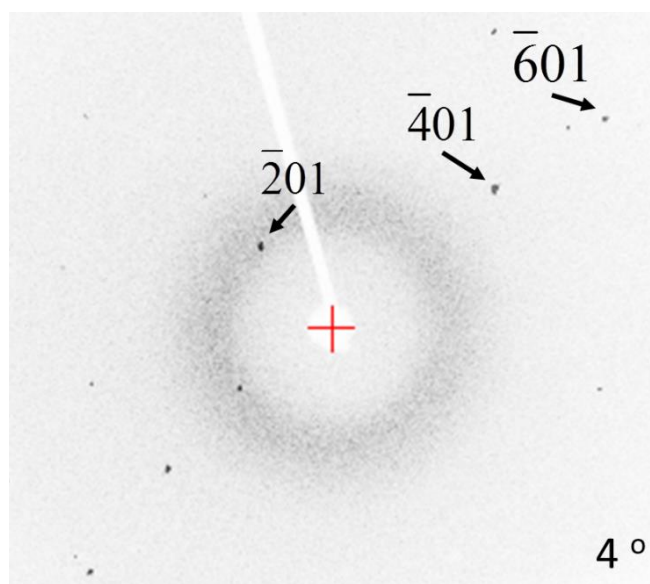
Fig. 3.3 XRD image showing the systematic absence rule of $h = 2n + 1$ in $h0l$. Halo is caused by frozen glycerin (amorphous) and diffraction spots which arise from the non-cubic crystal. Arrowed spots indicate $h0l$ series. Spots for $h = 2n + 1$ are absent from the series, indicating space group of $P2_1/a$.

3.4 Discussion

3.4.1 Similarity with Phase III

Polymorphism in $NaClO_3$ crystallization from its *melt* has been previously reported by Meyer *et al.* [3]. Fig. 3.4 shows a phase diagram of $NaClO_3$ indicating Gibbs free energy as a function of temperature. The phase diagram indicates that three polymorphs exist: Phase I, Phase II and Phase III. Phase I, which is the most stable phase widely from low-temperature region to melting temperature as shown in the Fig. 3.4, is the well-known chiral cubic phase and Phase II is undetermined phase. Phase III is the phase which appears as metastable phase when the $NaClO_3$ melt is cooled down and maintains until the temperature reaches to 237 °C during cooling process. The phase III transforms into chiral cubic phase when the temperature falls below 237 °C [4]. The Phase III is a monoclinic phase, which is the same crystal system as that of the unknown non-cubic phase the author discovered. The crystal system, space group and lattice constants of Phase III has been determined as follows: space group, $P2_1/a$; lattice parameters, $a = 8.78(5)$, $b = 5.17(5)$, $c = 6.83(5)$ Å, and $\beta = 110(1)°$ [5]. It should be emphasized that these lattice constants are very similar to those of the newly discovered achiral phase.
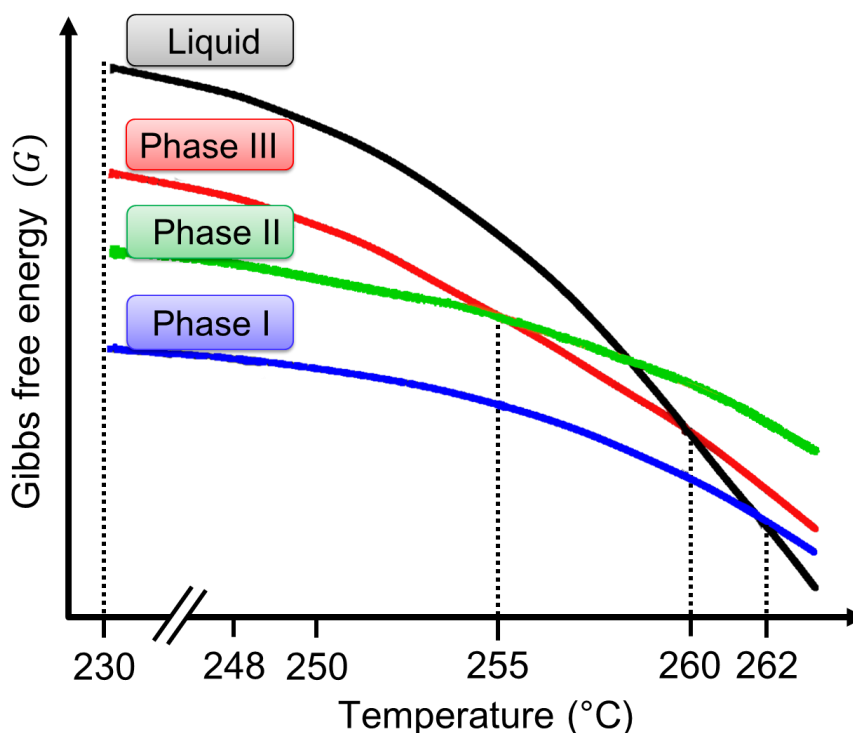
Fig. 3.4 A phase diagram showing Gibbs free energy of polymorphs in $NaClO_3$ melt growth as a function of temperature. This figure is adopted from Ref. [3] (partially modified)

Table 3.2 Comparison of lattice constants of non-cubic crystal crystallized from an aqueous solution with those of Phase III, a metastable phase crystallized from melt. Calculated values indicated in middle row are based on Eq. (3.1)

Phase	Non-cubic phase (this study)	Non-cubic phase (calculated values)	Phase III[5]
Crystal system	monoclinic	monoclinic	monoclinic
Space group	$P2_1/a$	$P2_1/a$	$P2_1/a$
a (Å)	8.42(2)	8.54(2)	8.78(5)
b (Å)	5.260(7)	5.34(1)	5.17(5)
c (Å)	6.70(1)	6.80(1)	6.83(5)
β (°)	109.71(1)		110(1)
Temp (°C)	-27	250	237–262
Unit cell volume (Å^3)	279.8(8)	292.2(8)	291(4)

However, the comparison of the lattice constants between the phase III and the newly discovered phase indicates the differences in the values, which cannot be explained exclusively in terms of statistical error (Table 3.2). The difference in the lattice parameters might be caused by the temperature at which diffraction data was collected. Whereas the diffraction data for the new phase was recorded at -27 °C, that for Phase III was obtained at 237–262 °C. By taking thermal expansion into account, it is possible to estimate the volume of the unit cell of the new phase at 237–262 °C and to compare its value to that of Phase III. Here, for simplicity, the unit-cell value of the new phase at 250 °C ,$V_{250°C}$, was estimated from the following equation:

$$V_{250°C} = V_{-27°C}\left(1 + \int_{-27}^{250} \beta(T)dT\right) = V_{-27°C}\left(1 + \int_{-27}^{250} 3\alpha(T)\,dT\right) \qquad (3.1)$$

since

$$\beta(T) = \frac{1}{V} \cdot \frac{dV}{dT} = \frac{1}{l^3} \cdot \frac{dV}{dl} \cdot \frac{dl}{dT} = \frac{1}{l^3} \cdot 3l^2 \cdot \frac{dl}{dT} = 3\alpha(T) \qquad (3.2)$$

where T is the temperature (°C), $\beta(T)$ is the volume thermal expansion coefficient, $\alpha(T)$ is the linear thermal expansion coefficient, $V_{-27°C}$ is the volume of the unit cell of the

newly discovered phase at -27 ºC and *l* is the length of the material. Assuming that (1) the thermal expansion coefficient of the new phase is equal to that of the cubic phase, and (2) the unit cell expands isotropically, $V_{250°C}$ was calculated to be 292.2(8) Å^3 by substituting the value of the linear thermal expansion coefficient of the cubic phase from the previous report [6]. This calculated value is equal, within the error, to the volume of the unit cell of Phase III [291(4) Å^3]. The author therefore concluded that the new phase of crystallization from an aqueous solution is identical to Phase III. The crystal structure of the phase III is shown in Fig. 3.5. In [010] projection (Fig. 3.5 **B**), it can be seen that chlorate anion and sodium cation are alternately packed to the direction of [100] and [001]. Because a two-fold screw axis exists in the direction parallel to the [010] direction, the orientations of each chlorate anions seen in the [010] projection shows the relationship of two fold symmetry. For example, a two-fold screw axis is present at the position of (1/4a, 1/2*c*) and an inversion center is present at the position of (1/2a, 1/2c) in the coordination shown in Fig. 3.5 **B**. In [100] projection shown in Fig. 3.5 **C** a *a*-glide planes perpendicular to the *b* axis are confirmed to be present at position of 1/4*b* and 3/4*b*. Since the new phase was found to be achiral phase III, it follows that the emergence process of chirality is the transformation of the Phase III into chiral cubic crystal during the formation process of chiral cubic crystal seen in the chapter 2.
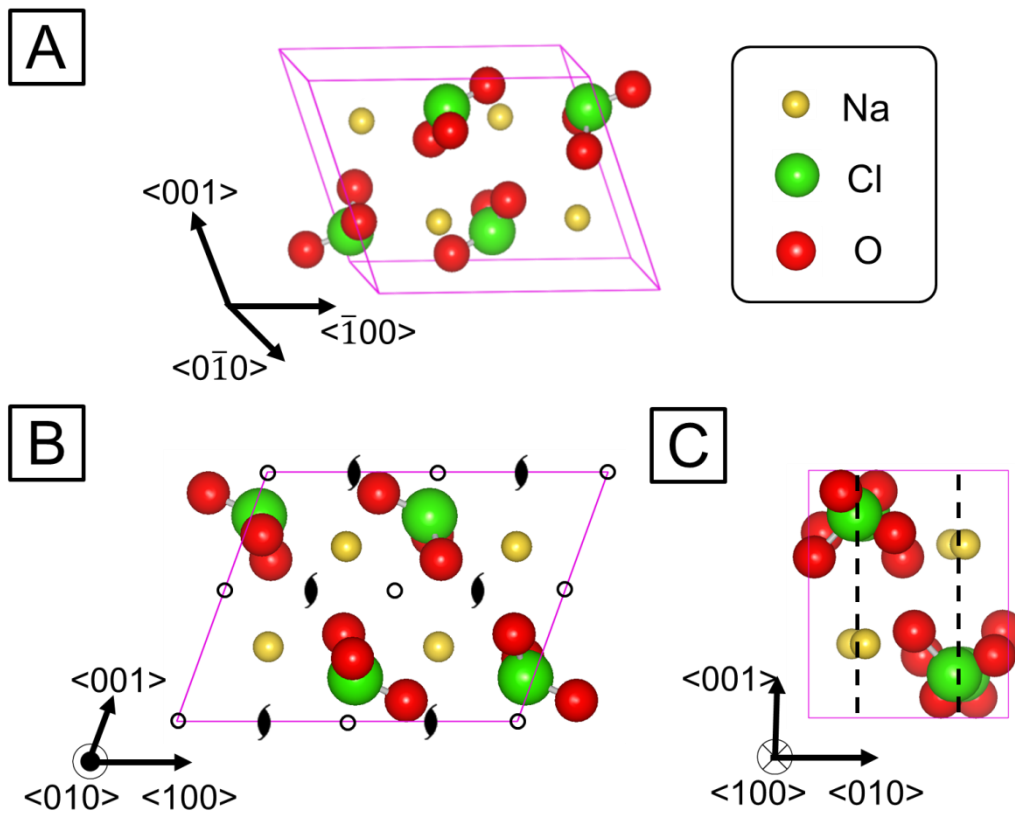
Fig. 3.5 Schematic illustrations showing the crystal structure of Phase III, which is a metastable phase in the crystallization from its melt. **A** Overview of the unit cell. Purple line indicates a unit cell. Yellow, green, red spheres represent sodium, chlorine, oxygen, respectively. **B** The [010] projection of the crystal structure. **C** The [100] projection of the crystal structure. The crystal structure was drawn with VESTA [7]

3.5 Experimental -Solubility Measurement-

Solubility is a fundamental property indicating the thermodynamic stability of a phase in solution. Especially, the relative solubility of polymorphs allows us to understand the kinetics of the polymorphic transformations seen in aqueous solution. To investigate solubility is the primitive stage of search for physical property of crystalline solid. The methodology of solubility measurement has been developed owing to demands from pharmaceutical industries because that solubility determines bioavailability and dosage formulation of drugs [8]. Therefore, Numerous methods to measure solubility of crystals, such as the methods using ATR-FTIR spectroscopy [9], Raman spectroscopy [10], have been developed. However, these methods require a substantial amount of the target crystal, being not suitable for the Phase III crystal because of its instability. Although the method using interferometer has been developed for crystals available only in small amount [11], even this method requires a stable sample crystal of the target material and to manipulate the sample crystal. However, owing to its instability, no method to control the phase III in solution growth has been established. Therefore, it is also necessary to establish the method controlling the crystal of phase III for solubility measurement.

The purpose of this section is to develop a method to produce a sample crystal usable for solubility measurement of the phase III in solution growth (The state of "usable for the measurement" in this context means that the phase III crystal is isolated from the mother liquor) and to measure the solubility. Here, it is shown that antisolvent crystallization [12-14] can be utilized to produce a usable sample crystal of phase III while overcoming the instability, and that the solubility of the phase III was roughly determined by observing growth or dissolution of the sample crystal immersed in aqueous solution with various condition using PLM.

3.5.1 Strategy for Control of Achiral Unstable Crystal

As mentioned above, the nucleation of the achiral phase prior to the formation of chiral crystal is probably a consequence of the Ostwald's rule of stages (In addition, the achiral phase can be deduced to be a metastable phase.). Quantitative analysis of the rule has been formalized by Stranski *et al.* [15]. The analysis shows milestones for selective crystallization of a metastable crystal because the analysis describes not only the requirement whereby the rule is valid but also the comparison between induction time for the nucleation of a metastable phase and a stable phase. This section briefly describes their consideration to explain the author's strategy for control the newly

discovered achiral crystal.

The first step to quantify the Oswald's rule of stages is to compare the nucleation rates of a metastable phase and a stable phase in a given system. The formula of steady state nucleation rate was introduced in the previous chapter as Eq. (2.11). The author assumes for simplicity that the pre-exponential factors are equal between a metastable phase and stable phase. Using Eq. (2.11), the ratio of the nucleation rate of a stable phase and a metastable phase can be expressed as [16]:

$$\ln\left(\frac{J_{0m}}{J_{0s}}\right) = \frac{b_s \gamma_s^3 v_s^2}{kT\Delta\mu_s^2} - \frac{b_m \gamma_m^3 v_m^2}{kT\Delta\mu_m^2} \tag{3.3}$$

where the subscription s and m refer to a stable phase and a metastable phase, respectively, and b_s and b_m are geometric factors. Eq. (3.3) indicates that Ostwald's rule of stages will be valid when the first term of the right-hand side is greater than the second one. Accordingly, the following condition is necessary to hold the rule of stages [16]:

$$\left(\frac{\Delta\mu_s}{\Delta\mu_m}\right)^2 < \frac{b_s}{b_m,}\left(\frac{\gamma_s}{\gamma_m}\right)^2\left(\frac{v_s}{v_m}\right)^2 \tag{3.4}$$

Physical meaning of the Eq. (3.4) can be seen in Fig. 3.6 where the activation energies for the nucleation of a metastable phase and a stable phase are plotted as a function of the concentration of solution (i.e. the indicator of the driving force caused by the difference of chemical potential). The figure states that the activation energy for metastable phase nucleation becomes lower than that for stable phase when solution concentration exceeds some critical point, C_{cr}, suggesting the nucleation of the metastable phase becomes kinetically favored in the concentration region beyond the C_{cr}. There could be two situations where Ostwald's rule of stages is valid taking kinetics into account. Fig. 3.7 shows the two situations: (a) the induction period of the stable phase is longer than that of the metastable phase. (b) the induction period of a stable phase is shorter than that of a metastable phase. The situation (a) is desired to achieve our purpose, namely, selective crystallization of the newly discovered achiral phase. The selective crystallization of the crystal requires higher nucleation rate of the achiral phase and longer induction period of the stable chiral phase. Therefore, the author shall show the conditional equation to achieve the situation (a).
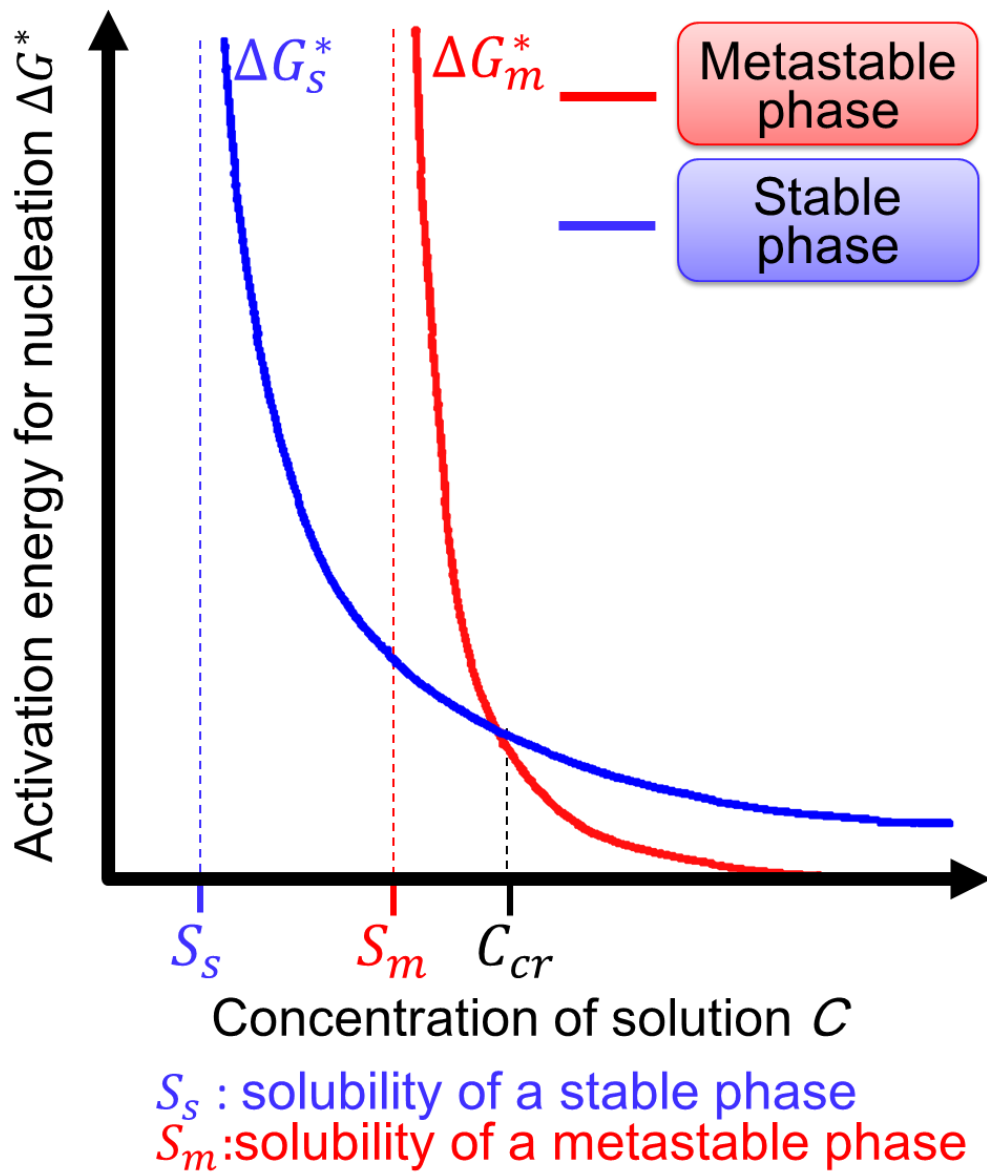
Fig. 3.6 A comparison of the activation energy for the nucleation of a metastable phase and a stable phase as a function of solution concentration. Blue line indicates the profile of a stable phase. Red line indicates the profile of a metastable phase. The figure is adopted from Ref. [16]

According to Kashchiev *et al.*, the induction period, τ, can be expressed as [17]:

$$\tau = \frac{16}{\pi} \frac{\gamma}{kT \left[ln\left(\frac{C}{C_e}\right) \right]^2 Cv\lambda} \exp\left(\frac{\Delta U}{kT}\right)$$

(3.5)

where k is Boltzman constant, T is temperature, ΔU is the activation energy required for dessolvation, C is solution concentration, C_e is equilibrium concentration, v is the vibrational frequency, λ is mean free path of solute molecule. Then, the situation (a), that is, the condition $\tau_s > \tau_m$ leads to [16]

$$1 < \left(\frac{\Delta\mu_s}{\Delta\mu_m}\right)^2 < \frac{b_s}{b_{m,}}\left(\frac{\gamma_s}{\gamma_m}\right).$$

(3.6)

Then the combination of Eq. (3.4) and Eq. (3.6) give rise to the conditional equation of the situation (a) as [16]:

$$1 < \left(\frac{\Delta\mu_s}{\Delta\mu_m}\right)^2 < \frac{b_s}{b_{m,}}\left(\frac{\gamma_s}{\gamma_m}\right) < \frac{b_s}{b_{m,}}\left(\frac{\gamma_s}{\gamma_m}\right)^2 \left(\frac{v_s}{v_m}\right)^2.$$

(3.7)

On the other hand, the conditional equation of the situation (2) can be expressed as [16]:

$$1 < \frac{b_s}{b_{m,}}\left(\frac{\gamma_s}{\gamma_m}\right) < \left(\frac{\Delta\mu_s}{\Delta\mu_m}\right)^2 < \frac{b_s}{b_{m,}}\left(\frac{\gamma_s}{\gamma_m}\right)^2 \left(\frac{v_s}{v_m}\right)^2.$$

(3.8)

Comparing these conditional equations, we can see that the square of the ratio in the chemical potential of the stable phase and that of the metastable phase is critically effects to determination of the situations. Fig. 3.7 shows schematic illustration showing the relationship between a degree of solution concentration and the square of the ratio in chemical potentials. It can be immediately seen from Fig. 3.8 that high concentration as much as possible is suitable to achieve selective crystallization of the metastable phase. The next section describes the method to achieve a high concentration.
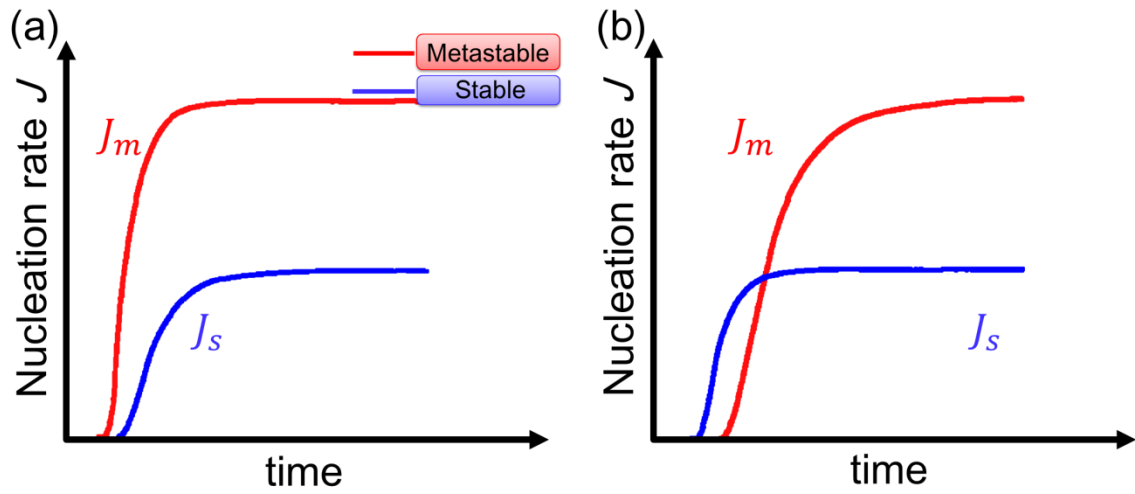
Fig. 3.7 Possible situations where Ostwald's rule of stages is valid. (a) The case that the induction period of a stable phase nucleation is longer than that of a metastable phase. (b) The case that the induction period of a stable phase is shorter than that of a metastable phase. The figure is adopted from Ref. [16]
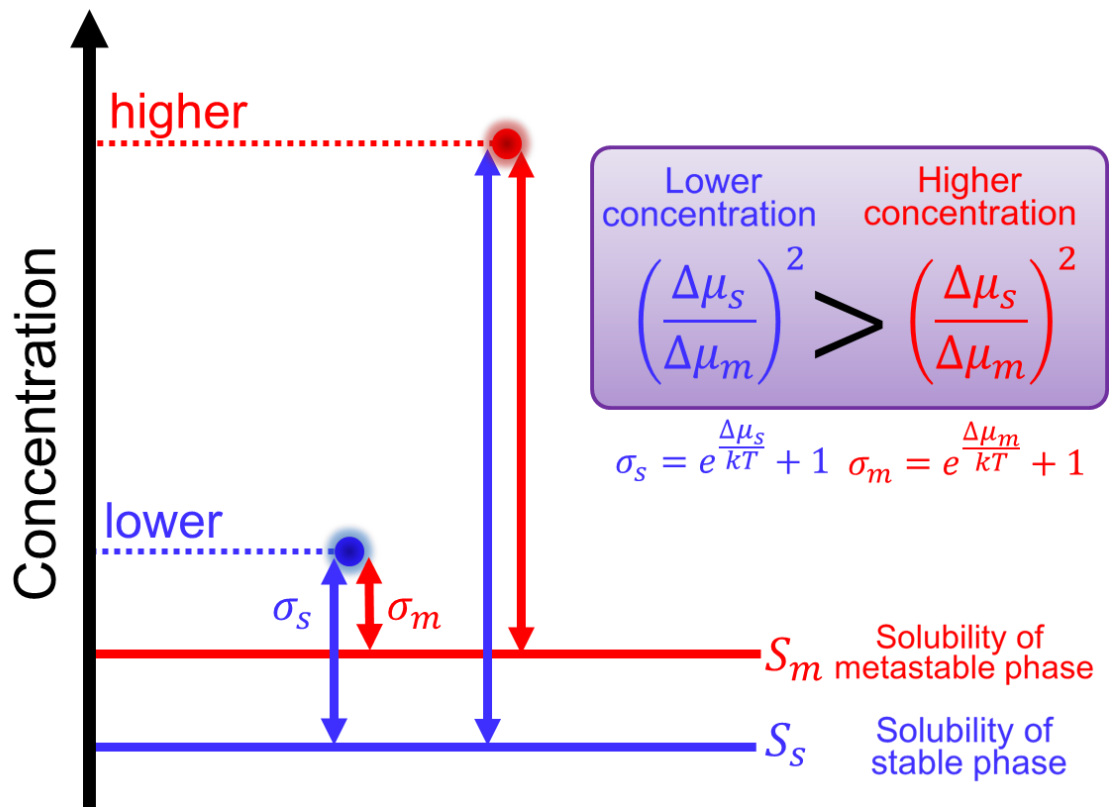
Fig. 3.8 The relationship between the degree of solution concentration and the ratio of the difference in chemical potentials with respect to a stable phase and a metastable phase.

74

3.5.2 Antisolvent Crystallization

Antisolvent crystallization is one of the method to achieve highly-concentrated condition (highly-supersaturated condition). Antisolvent crystallization is the method to crystallize by adding "antisolvent" to aqueous solution of the target material desired to be crystallized. Antisolvent is a solvent relatively poor to dissolve a target material than a certain solvent. For instance, 100 g of ethanol dissolves 0.055 g of sodium chloride (NaCl) at 25 °C, meanwhile, 100 g of water does 26.483 g of NaCl [18], meaning that ethanol is antislovent for NaCl compared to water. Upon mixing antisolvent to good solvent, solubility of the mixed liquid with respect to the target material decreases compared to the initial solubility of the good solvent. Therefore, if a saturated solution of a target material and the good solvent is taken as a starting solution, mixing of antisolvent causes supersaturation instantaneously. Consequently, the mixing of the ansisolvent leads to the crystallization of the target material. Solubility of a solvent for an ionic crystal is strongly influenced by relative permittivity, ε_r, of the solvent because electrostatic attraction force between the ions with opposite charges, which governs association of ions, becomes more effective with decreasing the relative permittivity. Bjerrum *et al.* has formulated the equilibrium constants regarding precipitation of ionic solid, composed by one caion and one anion, caused by the association of the ions [19,20]. Describing the association and dissociation of two ions with opposite charges, A^+ and B^- , as chemical formula,

$$A^+ + B^- \leftrightarrow AB \tag{3.9}$$

the equilibrium constant, K_{AB}, can be written as:

$$K_{AB} = \frac{[AB]}{[A^+][B^-]} = A + \frac{N_A e^2}{ln10RT} \cdot \frac{z_A z_B}{r_A + r_B} \cdot \frac{1}{\varepsilon_r} \tag{3.10}$$

where A is a constant, N_A is Avogadro's number, R is gas constant, r_A and r_B are the ion radius of A^+ and B^-, respectively, *e* is elementary charge, T is temperature (K), Z_A and Z_B is charge of A^+ and B^-, respectively. The formula indicates that a solvent with high relative permittivity leads small equilibrium constant, namely, high concentration of ions, meaning that the solvent with high relative permittivity is more soluble for a given ionic crystal. Indeed, the relative permittivity of ethanol is 24, meanwhile that of water is 80, being consistent with the formula of Bjerrum. Additionally, it follows that the

higher supersaturation can be obtained by antisolvent crystallization using a solvent with the lower relative permittivity. Therefore, appropriate selection of antisolvent provides controlled instant high supersaturation. In general, thermodynamically unfavorable polymorph is kinetically favored at the early stage of crystallization because of the predominant contribution of surface free energy (see the previous chapter). Thus, if the supersaturation of mother liquor is significantly high enough to enable to ignore the difference in chemical potentials of two polymorphs compared to that of surface free energy, the nucleation of the thermodynamically unfavorable polymorphs would dominate. In this regard, the antisolvent crystallization method is expected be suitable for selective nucleation of the kinetically favored polymorph since the method is capable of providing instant high supersaturation.

Using Acetone, which has 19.5 of relative permittivity, as antisolvent in this experiment, the author has performed two investigations: (1) evaluation of the sueprsaturation attained by the antisolvent crystallization method; (2) control of the phase III in solution growth. Experimental details are written below.

3.5.2.1 Evaluation of Supersaturation Attained by Antisolvent Crystallization Using Acetone

Supersaturation attained by antisolvent crystallization method was simply evaluated as a function of volume fraction of acetone. The supersatration with respect to phase I attained by the method was here defined as follows:

$$\sigma_{anti} = \frac{C_1 - C_2}{C_2} \times 100 = \frac{\dfrac{m_1}{m_{H_2O} + m_{ace}} - \dfrac{m_1 - m_2}{m_{H_2O} + m_{ace}}}{\dfrac{m_1 - m_2}{m_{H_2O} - m_{ace}}} \times 100$$

$$= \frac{m_2}{m_1 - m_2} \times 100$$

(3.11)

where C_1 is the mass concentration of the solute before the precipitation due to antisolvent crystallization occurs, C_2 is the mass concentration after the precipitation occurs, m_1 is the mass of solute dissolved in solvent before the precipitation, m_2 is the mass of the precipitate obtained by the antisolvent crystallization, m_{H_2O} is the mass of water in solvent and m_{ace} is the mass of acetone in solvent. The author used 5 mL of NaClO$_3$ aqueous solution the concentration of which is 95.7 (g/100gH$_2$O) as a starting solution and then, acetone (Analytical Grade, Wako Pure Chemical Industries

Ltd., Osaka, Japan) was add to the solution so that the amount of it corresponds to 10–80% of volume fraction at intervals of 10%, that is, eight separated crystallization were carried out. All crystallizations were processed in 50 mL centrifuge tubes at 22.1 °C. The centrifuge tube were set in a grinding agitator and grinded for twelve hours to precipitate the solute dissolving in the solution. After assuring complete precipitation, the resulting precipitate was isolated from the solvent by filtration. Since the precipitate is wet by the solution, the precipitate was washed with hexane so as to prevent additional precipitate caused by evaporation of the solution. Afterwards, masses of the precipitates were weighed with electronic balance. From the concentration of the starting solution and the value of the precipitate weighed, the supersaturation was calculated on the basis of Eq. (3.11) at each of eight crystallizations.

3.5.2.2 Selective Crystallization of Unstable Achiral Crystal in Solution Growth by Means of Antisolvent Crystallization Method

Sample crystals of $NaClO_3$ achiral phase were prepared by the antisolvent crystallization method using acetone. The saturated solution made by the method in previous chapter (6 μL) was dropped on a glass slide covered with a layer of polymer film using a micropipette and then, acetone was vigorously injected to the droplet using a micropipette (about 500 μL). After the injection, tiny crystals (about 50 μm or less) of the achiral phase immediately appeared in the droplets of the mixture of aqueous solution and acetone. The crystals were identified by detecting birefringence using PLM.

3.5.3 Experimental of Solubility Measurement

A primitive method for solubility measurement was adopted. The outline of the method is described below. An achiral crystal produced by the antisolvent crystallization method was immersed in solutions whose temperauture and concentration were predetermined. Afterwards, *in-situ* PLM observation of the crystal in the solution was carried out in order to check whether the crystal grows or dissolves. If the crystal grows it follows that the solution is supersaturated with respect to the achiral phase and *vice versa.* To repeat this observation at various solution conditions will show supersaturated region and undersaturated regions. The boundary between the two regions indicates the solubility curve.

3.5.3.1 Preparation of Solutions for Solubility Measurement

Six aqueous solutions of NaClO$_3$ with different conditions were prepared. The conditions are summarized in Table 3.3. All the conditions are supersaturated with respect to the chiral stable phase. The procedure to prepare the solution at the temperature and concentration of which are T_a (°C) and C_a (g/100gH$_2$O) is described below [In the case of the solution No. 1, for instance, T_a = 10 (°C) and C_a = 166 (g/100gH$_2$O)]. 0.2C_a g of the NaClO$_3$ powder of Phase I, 20 mL of ultrapure water and a magnetic stirrer were put in a glass container that can be hermetically closed with a screw cap. The container was heated in hot water at T_e + 10 (°C), where T_e is the saturation temperature with respect to the concentration C_a [In the case of the solution No. 1, the T_e = 80 (°C)], and the mixture in the container was stirred using a hot-plate stirrer. After complete dissolution of the powder, the stirrer bar was removed from the container. The glass container was set in an isothermal bath, and then it was gently cooled to T_a with care not to occur any nucleation of crystal (cooling rate c.a. 0.3 °C/min). The resulting solutions were used for the solubility measurement. Whole procedures described above were carried out in a clean room.

Table 3.3 Solution conditions used for solubility measurements

solution No.	Temperature (°C)	concentration (g/100g H$_2$O)	supersaturation with respect to phase I (%)
1	10	166	89
2	10	150	71
3	10	137	56
4	10	125	43
5	23	166	69
6	23	150	52

3.5.3.2 Setup for Solubility Measurement

The solubility measurement was performed on the basis of *in-situ* observations using PLM. The author evaluated whether each solution is undersaturated or supersaturated with respect to the achiral phase by observing the dissolution and growth of an achiral crystal immersed in the solutions. Observational procedure is described below. A flow cell was prepared as shown in Fig. 3.8. The flow cell contains an achiral crystal produced by the antisolvent crystallization, and is connected to solution in an isothermal bath and to a syringe using silicone tubes. Thus, it is possible to flow the solution into the cell by pulling the syringe (Fig. 3.8 **B**). The temperature of the cell was controlled at the same as that of the solution by using a Peltier stage described in previous chapter (Fig. 3.8 **A**). When the solution was flowed into the cell and soak the crystal, the author observed the crystal with attention to the change in the size and the interference color of the crystal. If the size becomes larger or the interference color changed to higher-order color, the crystal is regarded as growing. During the observation, the solution continued to be flowed in order to avoid the change in the concentration of the solution due to the generation of chiral crystals in the cell or silicone tube.
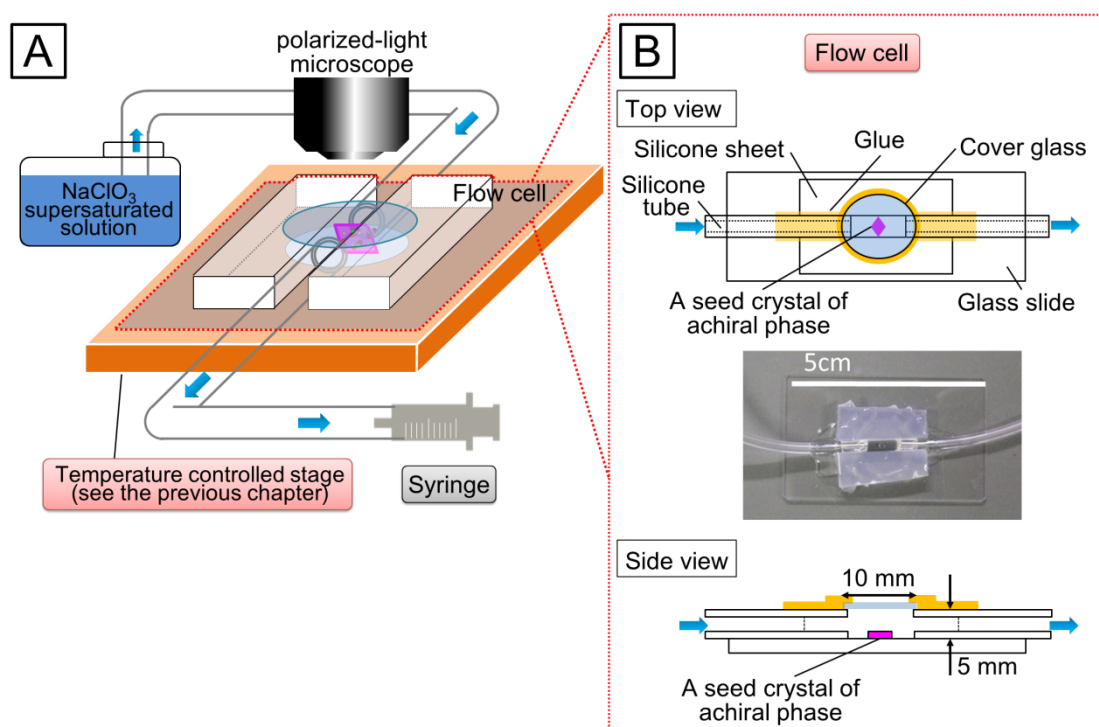

Fig. 3.8 Schematic illustrations of experimental setting of solubility measurement. **A** the overview of the observational setup for solubility measurement. **B** Schematic illustration of the flow cell set on temperature controlled stage.

79

3.6 Results

3.6.1 Selective Crystallization of Unstable Achiral Crystal by Antisolvent Crystallization

Difficulty in isolation of the achiral phase from mother solution is due to high solubility of the achiral crystal. Owing to the high solubility, in typical crystallization, even if the achiral phase crystallizes, it eventually dissolves or transforms to crystals of chiral cubic crystal because the concentration of the solution decreases with the growth of the crystal over time and nucleation rate of the chiral crystal is high. Therefore, the isolation requires following three conditions; (i) high supersaturation throughout the crystallization and (ii) suppression of nucleation rate of chiral cubic phase and (iii) complete evaporation of the mother liquor while keeping high supersaturation. This is because the achiral crystal is such unstable that just pecking with tweezers causes transformation (detailed description is in the next chapter), making a mechanical isolation difficult. The antisolvent crystallization method was able to fulfill these requirements. Fig. 3.9 is the supersaturation attained by antisolvent crystallization, which is defined as Eq. (3.11), versus the volume fraction of the acetone profile at 22 °C. Fig. 3.9 shows the supersaturation non-linearly increases depending on the volume fraction of the acetone, meaning high supersaturation can be instantly obtained by adding acetone to aqueous solution. In the current crystallization procedure, high supersaturation should be obtained because the injection of the acetone to the droplet of $NaClO_3$ solution results in high volume ratio of the acetone. Actually, the high supersaturation obtained by the procedure induced numerous nucleation of crystals of the achiral phase (Fig. 3.10). Moreover, the mixture of the acetone and solution quickly evaporates relative to pure aqueous solution because of the high volatility of acetone. The quick evaporation may enhance the supersaturation and realize sustainable growth of the crystals until the mother liquor completely dries (Fig. 3.11). Additionally, the change in interfacial energy depending on the composition of the mother liquor may suppress the nucleation rate of chiral crystals. Consequently, antisolvent crystallization method allowed the isolation of achiral crystals from the mother liquor successfully. The antisolvent crystallization using acetone was able to produce a sample crystal usable for solubility measurement. Subsequently, the polymer film under a crystal of the achiral phase was cut using a cutter in the size of 500 μm–100 μm while observing using the PLM and then, the crystal was transferred to the flow cell shown in the previous section by capturing the film using tweezers in order to avoid the phase transformation.
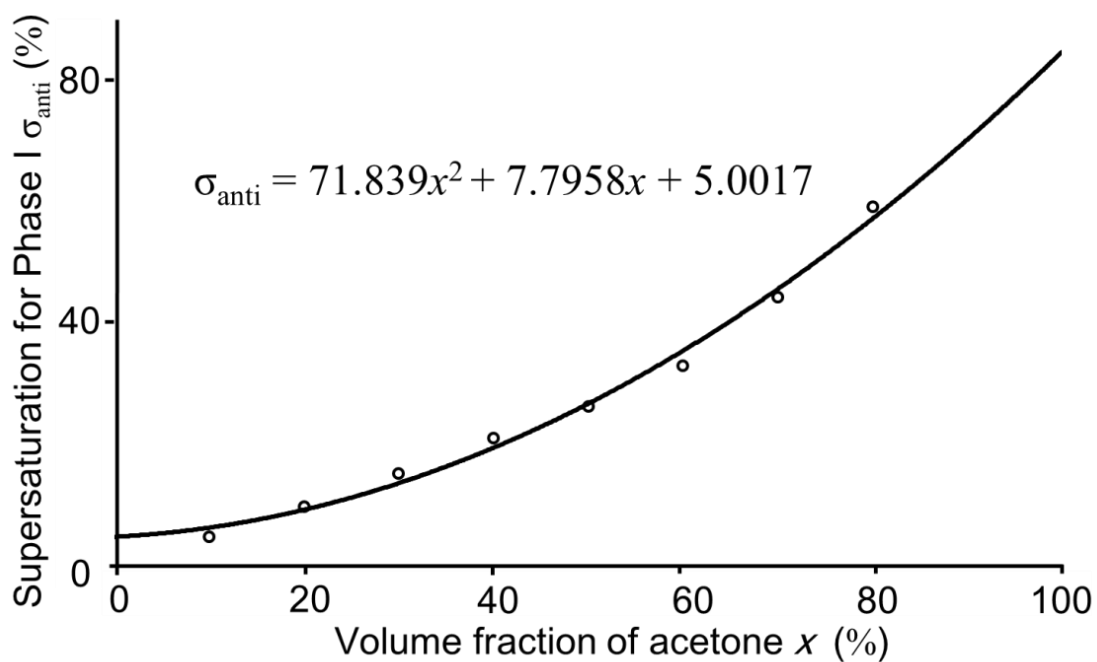
Fig. 3.9 Supersaturation attained by antisolvent crystallization using acetone as a function of volume fraction of acetone at 22°C. The supersaturation is for $NaClO_3$ chiral cubic phase I. The supersaturation in each volume fraction of acetone was plotted by circles. Black line denotes the fitted curve of the data. The formula on the graph expresses the fitted curve.
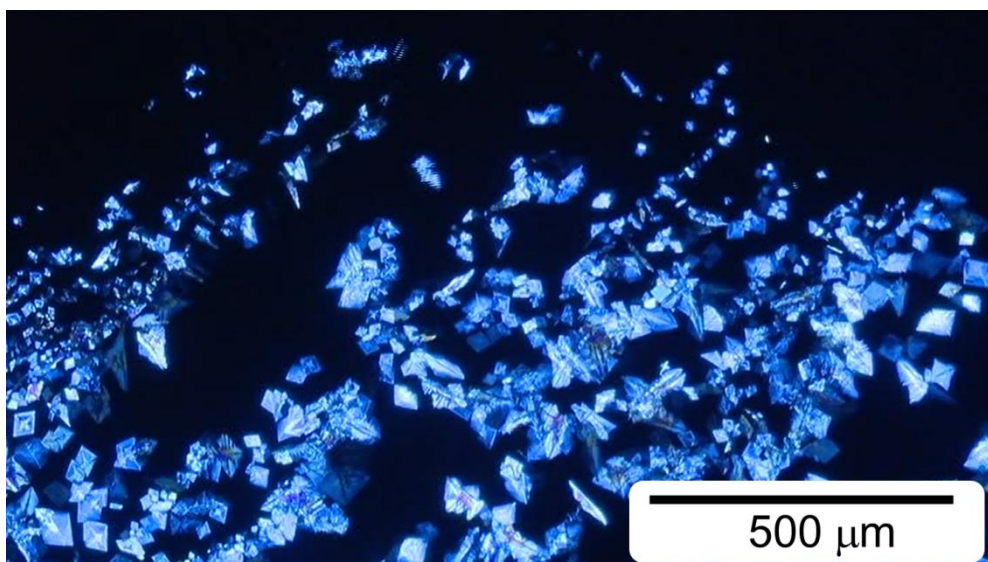
Fig. 3.10 A polarized-light microscopic image of achiral crystals crystallized by means of antisolvent crystallization using acetone. It can be seen that a huge numbers of the crystals are crystallized out immediate after the injection of acetone.
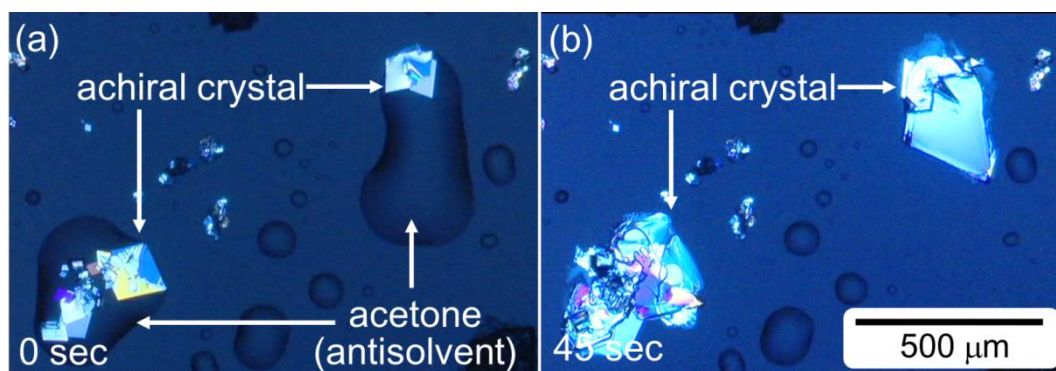
Fig. 3.11 Time-lapse polarized-light microscopic images of the selective crystallization of achiral phase by means of antisolvent crystallization using acetone. (a) A microscopic image just after antisolvent was flushed into a solution droplet. The time when this image captured was set to be 0 sec. (b) An image 45 sec after the flushing. It can be seen that the mother liquor completely dried out while leaving achiral crystals without phase transformation.

3.6.2 Solubility of Unstable Achiral Crystal

When a sample crystal of the achiral phase was immersed in the prepared solution, the crystal immediately grew or dissolved depending on solution conditions. Fig. 3.12 shows time-lapse micrographs of the *in-situ* observation of the sample crystal growing in the solution 1. After the sample crystal was immersed in the solution, the size of the crystal became larger, and interference color, which indicates the thickness of the crystal, changed to higher order color within 10 sec. This suggests growth of the crystal, indicating that the solution is supersaturated with respect to the achiral phase. Note that the change of color does not represent a solid–solid phase transformation because the optical rotatory power of a cubic crystal is not so large that the crystal exhibits bright color in this scale.
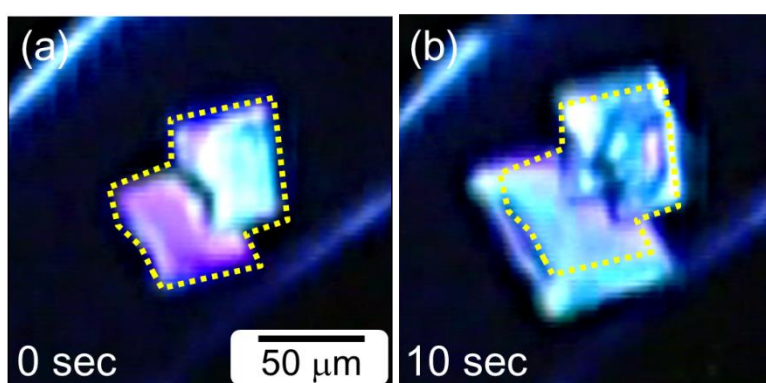
Fig. 3.12 Time-lapse polarized-light microscopic images showing growth of achiral crystal under supersaturated condition (solution No.1 in Table 3.3). (a) Immediately after the crystal was immersed in the solution. Yellow dot line indicates outline of the crystal at this moment. The time when this image captured is set to be 0 sec. (b) 10 sec after the crystal is immersed in the solution. It can be seen that the crystal became larger than the yellow dot line, indicating the crystal grew.

Fig. 3.13 shows all observational results of the experiment using six solutions with different concentration and temperature. It can be seen that three of the six solution conditions (condition 1, 2 and 5) and two conditions (condition 4 and 6) resulted in growth and dissolution, respectively. This indicates that the three and the two are supersaturated and undersaturated with respect to the achiral phase, respectively. Only the case of condition 3, it could not be determined whether the crystal grows or dissolves because the size of the crystal was slightly fluctuated. Therefore, the condition 3 is probably near to equilibrium. Assuming that the concentration of the condition 3 is the saturated point at 10 °C and that the intermediate concentration of the condition 5 and 6 is the saturated point at 23 °C and that solubility linearly depends on temperature, the solubility of the achiral phase for a temperature range from 10 °C to 23 °C, $C_{achiral}$ (T) (g/100gH$_2$O), can be expressed by following equation:

$$C_{achiral}(T) = 1.6154T + 120.85 \qquad (3.12)$$

On the other hand, the solubility curve of the chiral phase for the temperature range from 10 °C to 23 °C, C_{chiral} (T), is expressed by

$$C_{chiral}(T) = 1.1917T + 71.701 \qquad (3.13)$$

For simplicity, it was assumed that the solubility of the chiral phase linearly depends on temperature. Comparing the $C_{achiral}(T)$ with $C_{chiral}(T)$, it follows that the solubility of the achiral phase is about 1.6 times higher than that of the chiral phase. The fact that the solubility of the achiral phase is higher than that of the chiral phase indicates that the achiral phase is a metastable phase in NaClO$_3$ solution growth. In addition, the fact that the solubility of the achiral phase is 1.6 times higher than that of the chiral phase indicates that the appearance of the achiral phase requires the supersaturation with respect to the chiral phase to exceed 60%.
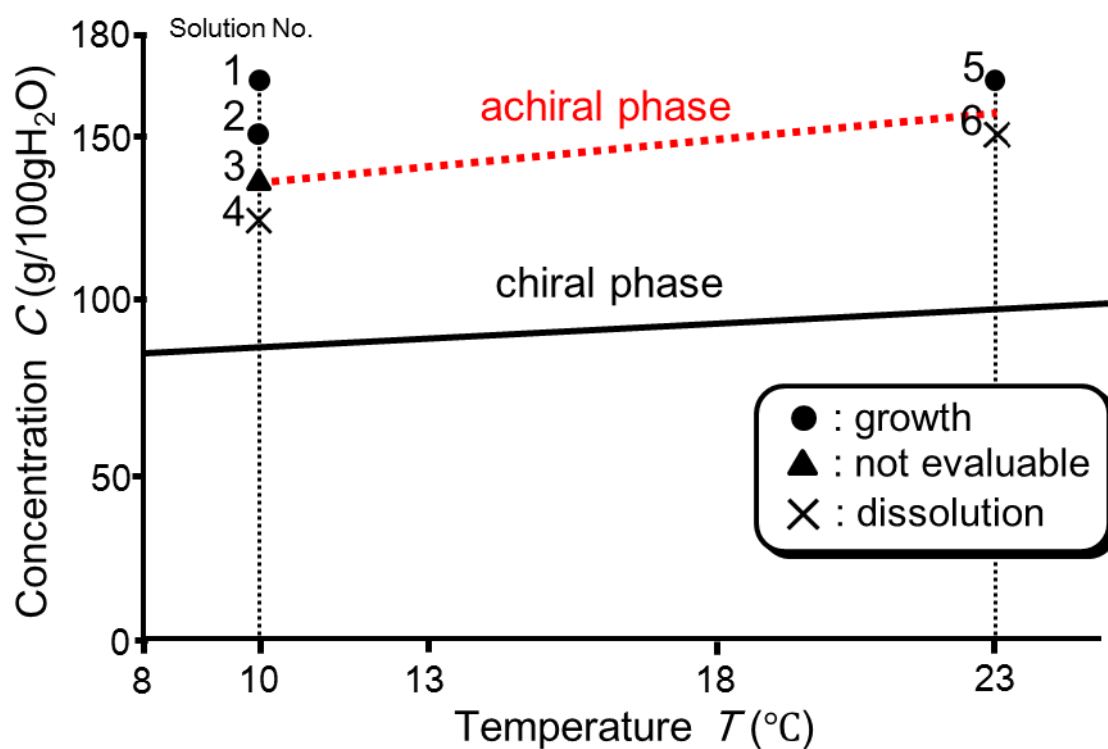
Fig. 3.13 Comparison of the solubility curve of achiral phase and that of cubic phase. The red dotted line denotes the solubility curve of achiral phase and the black line indicates that of cubic phase. Circles denotes the solution condition where achiral crystal grew. Cross denotes the solution condition where achiral crystal dissolved. Triangle denotes equilibrium condition for the achiral phase.

3.7 Discussion

3.7.1 Evaluation of Validity on the basis of Kinetics of Solvent-Mediated Polymorphic Transformation

The transformation of the achiral metastable crystal into chiral cubic crystal captured in the previous chapter was expected to be a consequence of Ostwald's rule of stages. According to the rule, after the nucleation of the kinetically favored metastable polymorph, the system is transiently occupied by the metastable phase because of their growth. The appearance of thermodynamically favored stable phase should follow the growth of the metastable phase. Eventually, the metastable phase will be replaced by the stable one by a phase transformation. In the case of crystallization from a solution, the phase transformation is often progressed by "solvent-mediated phase transformation (SMPT)".The SMPT is the phase transition progressed by the growth of crystals of a stable phase with consumption of crystals of a metastable phase. Because kinetics of crystal growth is closely related with the degree of supersaturation of ambient solution to understand the kinetics of SMPT provides a clue to evaluate the validity of the measured solubility in the previous section. Here, this section briefly describes the kinetics of crystal growth in solution at first. Especially, the dependence of the growth rate on the supersaturation, which is necessary to consider the validity of the measured solubility, will be presented. Subsequently, the general idea about the mechanism and kinetics of the SMPT will be shown. After that, the solubility data the author obtained in this chapter is evaluated on the basis of the kinetics of SMPT.

3.7.1.1Parabolic and Linear Law of Crystal Growth Rate in Solution Growth

This section presents kinetic law in growth rate of a crystal as a function of supersaturation. If we understand the kinetics of crystal growth, various information can be obtained by measuring of growth rate of a crystal. A typical information is supersaturation of ambient solution during the target crystal grows. Therefore, measurement of crystal growth rate during SMPT provides us the supersaturation in the course of the SMPT, allowing us to estimate the solubility of the metastable phase. Therefore, it is necessary to understand the kinetics of crystal growth for evaluation of validity of the measured solubility. Here the author decided to briefly introduce fundamental kinetics of the crystal growth quantitatively in this section.

Considering Kossel crystal, where the growth unit displays six unsaturated bonds located perpendicular to each face of a cube and a crystal as substrate is built by accumulation of the cubic growth unit [21], the surface structure of the crystal are

mainly classified to three as shown Fig. 3.14. There are differences in level originating from growth unit layers (atomic layers) on the crystal surface. The difference is called as "steps". Further, the atomically smooth surfaces between steps are called as "terrace" and the corner of the step ledge is called as "kink" site. Basically, growth of the crystal proceeds through the incorporation of growth unit at kink site followed by step advance. Solutes dissolving in solution, which are hydrated, diffuse to the terrace and undergo dehydration at vicinity of the terrace followed by attachment to the terrace. After attached to the terrace,
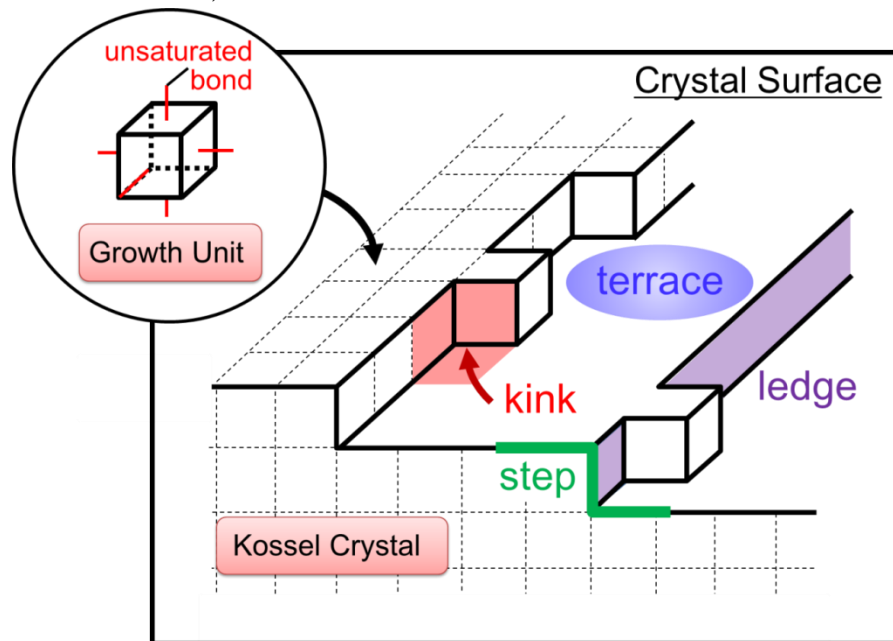
Fig. 3.14 A Schematic illustration showing crystal surface of Kossel crystal.

the solute molecules migrate to the step ledge by surface diffusion. Incorporation of the molecule to crystal from a kink site leads step advance. Eventually, successive step advances concerning all levels of steps results in crystal growth to a direction perpendicular to the crystal surface. The description above indicates that growth of the crystal requires steps as incorporation sites for growth units. The source of the step includes two possibilities: (1) Two dimensional nuclei on the crystal surface generates steps between the surface of the two dimensional nuclei and the surface of the substrate crystal; (2) Screw dislocation exposed on the crystal surface also generates a step owing to interatomic mismatch perpendicular to the crystal surface (Fig. 3.15). In order to deal with growth kinetics under from slightly supersaturated to highly supersaturated conditions, this section describes the kinetics of spiral growth originating from the existence of a screw dislocation.
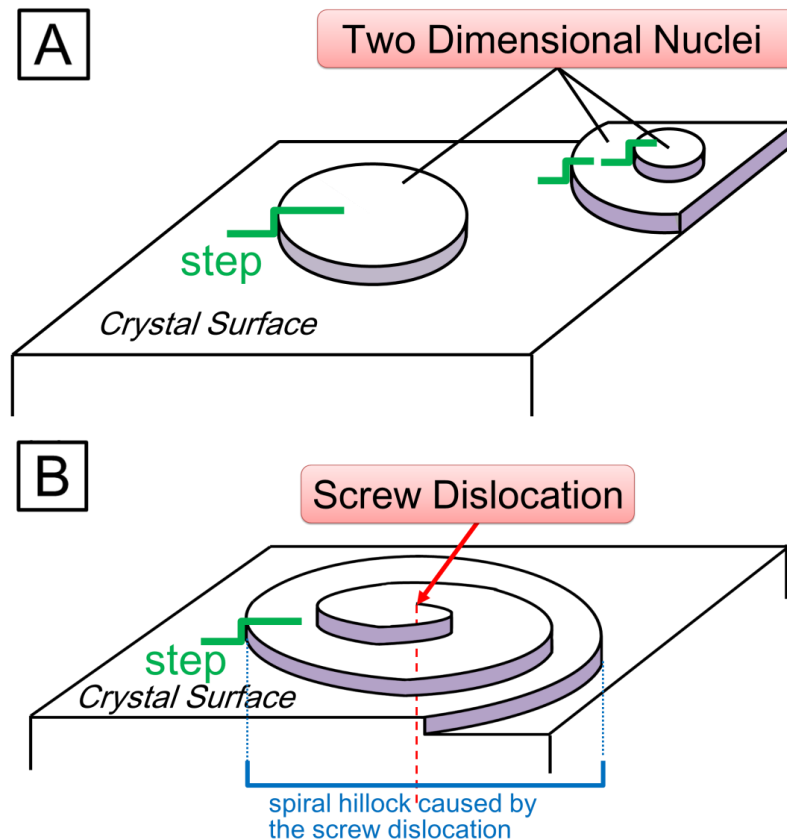
Fig. 3.15 Conceivable supply sources of step. **A** Steps caused by formation of two dimensional nuclei on atomically smooth surface. **B** Steps caused by interatomic mismatch due to a screw dislocation

First, general expression of the growth rate owing to advances of successive steps will be shown. Second, expression of the rate of successive advance in solution growth will be shown. Third, in order to apply these expressions to spiral growth, the distance between two successive turns of the single spiral will be shown. Finally, the transition of the growth law corresponding to supersaturation will be discussed in this section.

Fig. 3.16 shows a schematic illustration of sectional view of growing crystal which has successive steps on its surface. The relationship between growth rate, R, and rate of step advances, v, can be described as [16]

$$R = pv \qquad (3.14)$$

where p is density of steps.
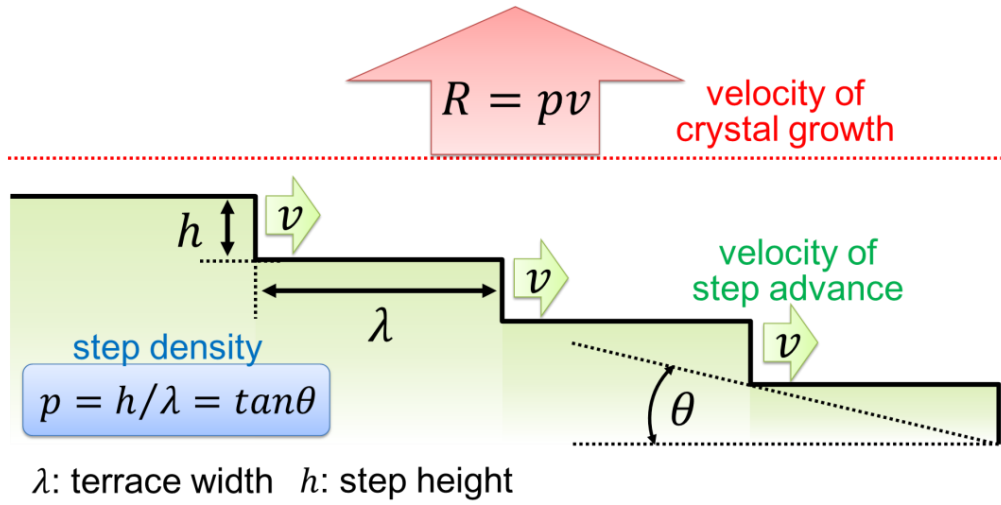
Fig. 3.16 A Schematic illustration of sectional view of growing crystal which has periodical successive steps.

In the growth from solutions the supply of growth units takes place predominantly through diffusion in the bulk of the solution. Although the solution as the transport medium of growth units moves by convection flows, a stagnant layer, where fluid movement of the solution is suppressed and becomes immobile owing to the existence of the crystal surface, mostly forms at the vicinity of the crystal surface. Therefore, it is usually assumed that the growth units are supplied to the surface by diffusion, generating concentration gradient between at the steps, C_{st}, and at far from the surface, C_{bulk} (Fig. 3.17). Assuming again that the advance rate of steps is sufficiently smaller than the rate of the diffusion in the stagnant layer, the concentration is described by the equation of the Laplace $\Delta C = 0$ because the concentration distribution reaches to the steady state. Solving the Laplace equation expressed in the cylindrical co-ordinate as shown in Fig. 3.17 (This co-ordinate is for convenience) with boundary conditions so as to satisfy the condition where the successive steps are present on the surface as follows [16],

$$\frac{d^2C}{dr^2} + \frac{1}{r}\frac{dC}{dr} = 0 \tag{3.15}$$

(The Laplace equation in cylindrical coordination)

$$y = 0 \text{ and } z = d, C = C_{bulk}, \tag{3.16 a}$$

$$y = 0 \text{ and } z = \frac{a}{\pi}, C = C_{st} \hspace{3cm} (3.16\text{ b})$$
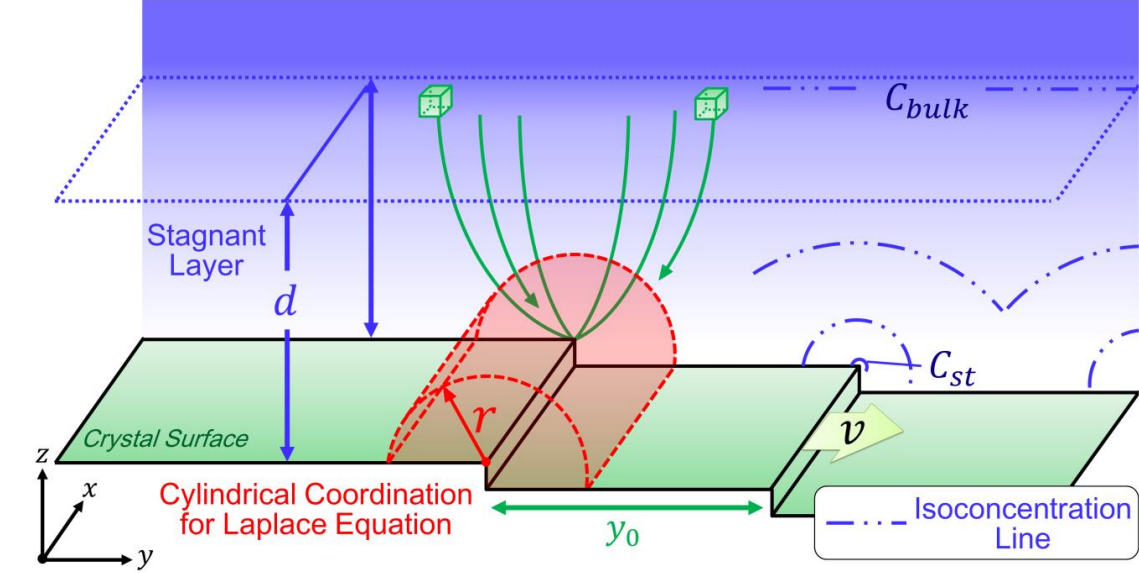
Fig. 3.17 Cylindrical symmetry of the volume diffusion field around a step and concentration field in the stagnant layer surrounding the crystal surface.

where a is a distance a growth unit occupies. Solving the equation, the expression for concentration distribution function, C, can be obtained as [16]

$$C = \frac{C_{bulk} - C_{st}}{ln\left[sinh\left(\frac{\pi d}{y_0}\right)\right] - ln\left[sinh\left(\frac{a}{y_0}\right)\right]} ln\left[sin^2\left(\frac{\pi}{y_0}y\right) + sinh^2\left(\frac{\pi}{y_0}z\right)\right]^{1/2} + C_{bulk} +$$

$$\frac{C_{bulk} - C_{st}}{ln\left[sinh\left(\frac{\pi d}{y_0}\right)\right] - ln\left[sinh\left(\frac{a}{y_0}\right)\right]} ln\left[sinh\left(\frac{\pi d}{y_0}\right)\right]. \hspace{2cm} (3.17)$$

Because the rate of step advance is described as [16]

$$v = v_c D \left(\frac{dC}{dr}\right)_{r=a/\pi}, \hspace{3cm} (3.18)$$

where v_c is the volume of the growth unit, D is diffusion coefficient, finally, with appropriate treatment, the rate of step advance can be obtained as [16]

$$v = \frac{\beta_{st} C_e v_c \sigma}{1 + \frac{a\beta_{st}}{\pi D} ln\left[\frac{y_0}{a} sinh\left(\frac{\pi d}{y_0}\right)\right]} \tag{3.19}$$

with

$$\beta_{st} = av\frac{a}{\delta_0} exp\left(-\frac{\Delta U}{kT}\right) \tag{3.20}$$

where v is the vibrational frequency, δ_0 is kink site spacing, ΔU is the activation energy required for dessolvation and C_e is equilibrium concentration.

According to Cabrera *et al.,* the distance Λ between the two successive turns of the single spiral or two successive steps is given by [22]

$$\Lambda = 19\rho_c = \frac{19\varkappa a^2}{kT\sigma} \tag{3.21}$$

where ρ_c is the critical radius of two dimensional nuclei, $\varkappa$ is the specific ledge energy. Since the distance is governed by the critical radius of nuclei which depends on the supersaturation as described in chapter 3, it follows that the distance is also governed by the supersaturation.

Substituting Eq. (3.19), Eq. (3.20) and Eq. (3.21) on Eq. (3.14) gives an expression for the rate of growth in a diffusion regime ($\pi D/a \ll \beta_{st}$) [17]

$$R = A\frac{\sigma^2}{\sigma_c} \frac{1}{ln\left[\frac{d}{\pi a}\frac{\sigma_c}{\sigma} sinh\left(\frac{\sigma}{\sigma_c}\right)\right]}, \tag{3.22}$$

where

$$\sigma_c = \frac{19\varkappa a^2}{\pi nkTd} \tag{3.23}$$

is the characteristic supersaturation and

$$A = \frac{DC_e v_c}{d} \qquad (3.24)$$

is the rate constant, d is thickness of the stagnant layer.

The equation indicates that behavior of growth rate on the supersaturation changes from parabolic dependence to linear dependence as supersaturation increases. The condition $\sigma \ll \sigma_c$ ($\sin\left(\frac{\sigma}{\sigma_c}\right) \cong \frac{\sigma}{\sigma_c}$) results in the parabolic dependence as follows [17]

$$R = A\frac{\sigma^2}{\sigma_c}\frac{1}{ln\left(\frac{d}{\pi a}\right)}. \qquad (3.25)$$

On the other hand, at $\sigma \gg \sigma_c$ the hyperbolic sine transforms into $\exp\left(\frac{\sigma}{\sigma_c}\right)/2$ and, neglecting $\ln(d\sigma_c/2\pi a\sigma)$ with respect to σ/σ_c one obtains the linear dependence [17]:

$$R = A\sigma \qquad (3.26)$$

Namely, the growth rate of a crystal quadratically increases as the degree of supersaturation increases until the degree reaches to a specific critical supersaturation and when supersaturation is beyond the critical supersaturation the growth rate becomes to show linear dependence on supesaturation.

3.7.1.2 Kinetics of Solvent-Mediated Polymorphic Transformation

The mechanism of SMPT is qualitatively considered to be the consequence of two kinetic processes: (1) the dissolution of a metastable phase (2) the growth of a stable phase. The coupled process of these two processes is conventionally called as "dissolution/precipitation" mechanism [23]. Fig. 3.18 shows the kinetic pathway of the solution concentration during the dissolution/precipitation process. Once kinetically accessible metastable crystals appeared in a closed system, the metastable crystals grow with consumption of solute dissolving in the solution. Eventually, the concentration of the solution reaches to the equilibrium with respect to the metastable crystal and the growth of the metastable phase is stopped. On the other hand, the equilibrium sate is still supersaturated with respect to the stable phase. Thus, the solution still has a

potential to cause nucleation of the stable phase. Once nucleation of the stable phase occurs, the concentration of the solution decreases from the equilibrium concentration with respect to the metastable phase, namely, the solution becomes undersaturated with respect to the metastable phase. In this state, the dissolution of the metastable phase and the growth of the stable phase simultaneously occur. This process is so-called "dissolution/precipitation" mechanism. The stable phase continues to grow until the metastable phase completely has disappeared. Davey *et al.* has quantified this process which progresses in a monotropic isothermal system based on the rate equation of the dissolution and the growth. Additionally, they have pointed out the existence of the supersaturation in which the outflow of the solute from the metastable phase is balanced with inflow of it to the stable phase, "plateau supersaturation". The plateau supersaturation is maintained for a certain period. The deviation of quantified plateau supersaturation is briefly described below.

Since the growth rate and the dissolution rates of the two phases must be balanced during a certain period of the transformation, the following equation must be hold:

$$-\frac{dM_1}{dt} = \frac{dM_2}{dt}$$

(3.27)

where the M_1 and M_2 are the mass of a metastable phase and a stable phase, respectively. The concentration of the solution, x_p, will remains constant during this period, namely, the pseudo steady state is achieved regarding the solution concentration.

If the equilibrium concentration with respect to the metastable phase and that with respect to the stable phase are given by x_1 and x_2, the supersaturation with respect to the stable phase when the solution concentration is equilibrium to the metastable phase, σ_{12}, and the plateau supersaturation, σ_p, can be defined as follows:

$$\sigma_{12} = \frac{(x_1 - x_2)}{x_2}$$

(3.28)

$$\sigma_p = \frac{(x_p - x_2)}{x_2}$$

(3.29)

where x_p is the solution concentration when the pseudo steady state is achieved. Assuming that both of the dissolution rate and the growth rate follow the linear law

described in the previous section, the Eq. (3.27) becomes:

$$\frac{\alpha_1}{\beta_1} \rho_1 A_1 k_D (\sigma_{12} - \sigma_p) = \frac{\alpha_2}{\beta_2} \rho_2 A_2 k_G \sigma_p \qquad (3.30)$$

where α and β are the volume and surface area shape factors for the phases, ρ is the density, A is the total surface area, k_D is the rate constant of dissolution and k_G is the rate constant of growth. Rearranging the Eq. (3.30) gives the plateau supersaturation as a function of σ_{12}:

$$\sigma_p = \frac{\sigma_{12}}{(1 + \lambda)} \qquad (3.31)$$

with

$$\lambda = \frac{k_G A_2 (\rho_2 \alpha_2 / \beta_2)}{k_D A_1 (\rho_1 \alpha_1 / \beta_1)} \qquad (3.32)$$

This leads qualitatively to an expected form of the experimental supersatuartion-time profile as shown in Fig. 3.18.
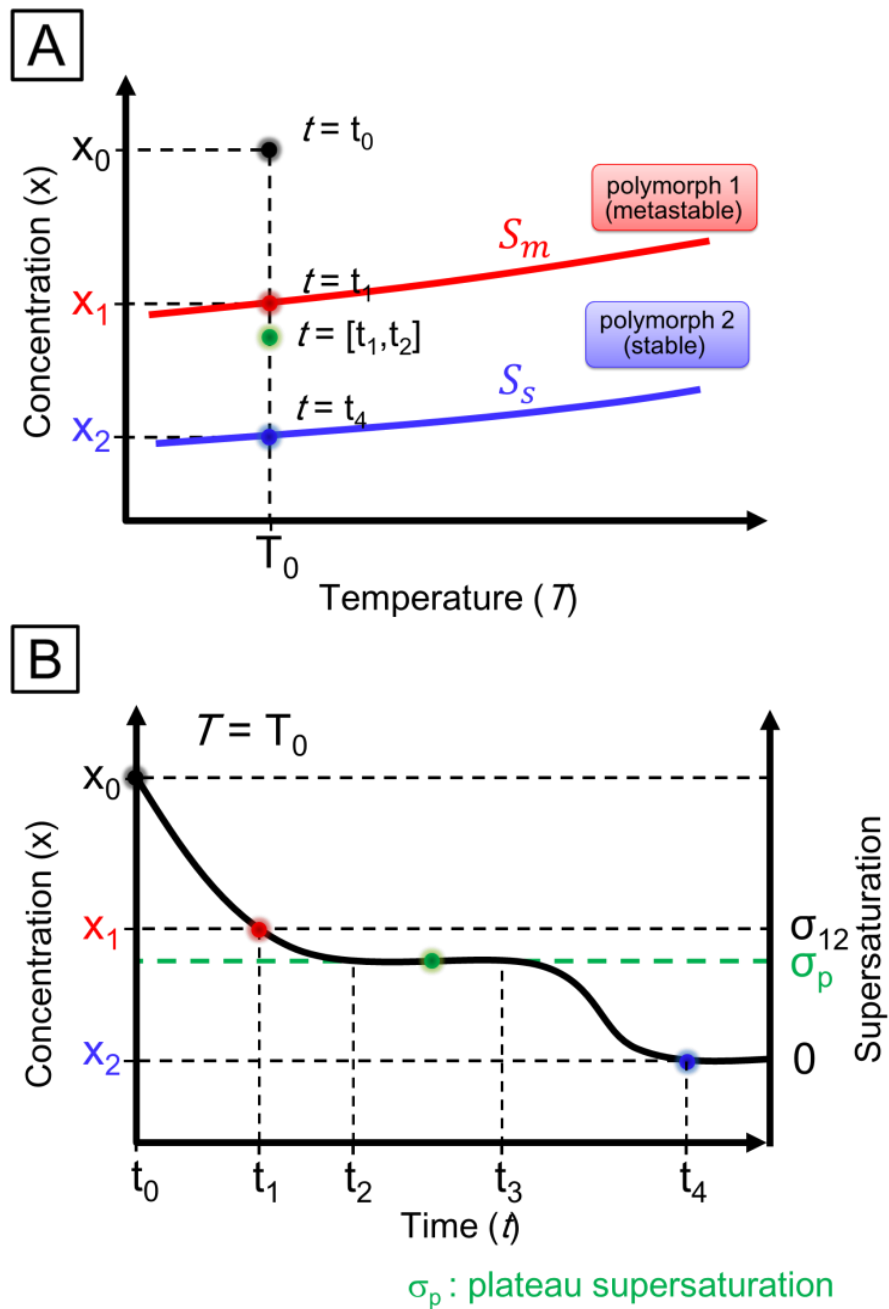
Fig. 3.18 Thermodynamic and kinetic features of a SMPT. **A** Solubility curves of monotropically related polymorph 1 (metastable form) and 2 (stable form). T_0 denotes the temperature at which crystallization initiated. The x_0, x_1 and x_2 is solution concentrations where crystallization initiates, the solubility of the polymorph 1 and the solubility of the polymorph 2 at temperature T_0, respectively. **B** The time dependence of concentration and supersaturation in a SMPT from polymorph 1 to polymorph 2. The σ_{12} and σ_p denote the supersaturation with respect to the polymorph 2 where the concentration is saturated to the polymorph 1 and "plateau supersaturation" during the SMPT.

3.7.1.3 Validity of Measured Solubility of Achiral Metastable Crystal

The plateau supersaturation of the achiral–chiral SMPT in $NaClO_3$ crystallization can be estimated by measuring the growth rate of a crystal of the chiral phase in the course of the SMPT. This is because the supersaturation can be determined by measuring the growth rate in reference to the investigation by Bennema *et al.* and Hosokawa *et al.* where the relationship between the growth rate and the supersaturation has been investigated precisely [24-25]. According to their investigations, linear law of the growth rate of the $NaClO_3$ cubic crystal is hold in the region more than 0.1 % of supersaturation. Hosoya *et al.* have indicated the growth rate of the (1 0 0) face of $NaClO_3$ crystal of chiral cubic phase versus supersaturation profile (Fig. 3.19). This profile shows that the growth rate, R_{chiral}, can be expressed as a linear function of supersaturation with respect to the chiral phase, σ_{chiral} (%), as follows:

$$R_{\text{chiral}} = 0.0339\sigma_{chiral} - 0.0635 \tag{3.33}$$

with

$$\sigma_{chiral} = \left[\frac{(x - x_2)}{x_2}\right] \times 100 \tag{3.34}$$

where x is concentration of solution (g/100gH$_2$O). Therefore, if the growth rate of the crystal of the chiral cubic phase during the SMPT is measured the supersaturation during the phase transition, which is the plateau supersaturation, can be calculated from Eq. (3.31).

In order to measure the growth rate during the SMPT, the author has performed additional observation of crystallization. The crystallization was induced by the droplet-evaporation method described in the previous chapter. Fig. 3.20 (a) and (b) show the time-lapse images of the phase transition taken by a PLM and Fig. 3.20 (c) shows an overlaid image of the two. The growth rate was measured in the twelve faces indicated by pink arrows denoted by g1–g12. To compensate inhomogeneity of actual supersaturation within the view field, the author adopted the average value of the twelve growth rates as the representative value. The value was calculated to be 1.71 μm/s. By substituting this value into Eq. (3.33), the plateau supersaturation was calculated to be 52.3 (%). Then, if the value of λ is obtained, the value of the σ_{12} can be estimated by Eq. (3.31) and (3.32). The accuracy of the value of measured solubility is able to be

evaluated by comparing the value of the σ_{12} estimated from Eq. (3.31) with the value of the σ_{12} that can be obtained from our solubility measurement. To estimate the value of the σ_{12} from Eq. (3.31), values of k_G and k_D are required since the λ includes the two values. The k_G can be obtained from the slope of Eq. (3.33). On the other hand, the k_D can be expressed by using a value of σ_{12} based on following consideration. First, dissolution rates of the achiral phase were measured from Fig. 3.20. The author measured change in the area of the achiral crystal occupying the micrograph in Fig. 3.20, and calculated the dissolution rate by dividing the change in the area with the length of the achiral crystal–solution boundary and time. This is to compensate large dispersion of the value of the dissolution rate, which depends on position.
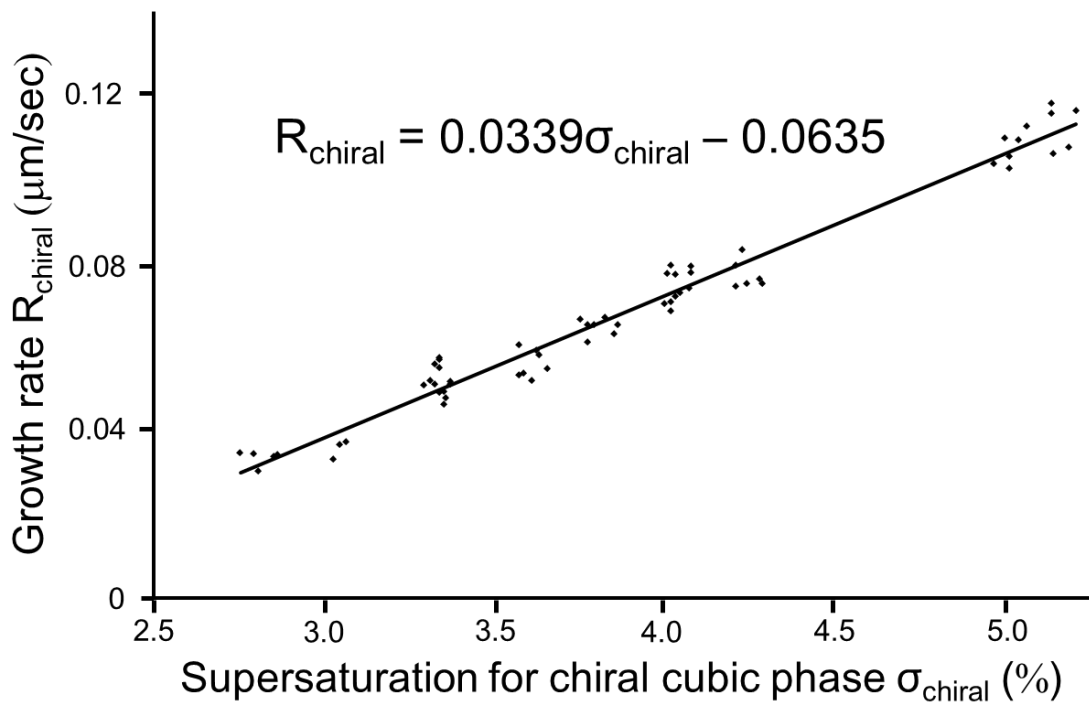
Fig. 3.19 A graph showing linear dependence of growth rate of (100) face of $NaClO_3$ cubic crystal on the degree of supersaturation in accordance with Hosoya *et al.*. The graph is adopted from Ref. [25] (partially modified).

96
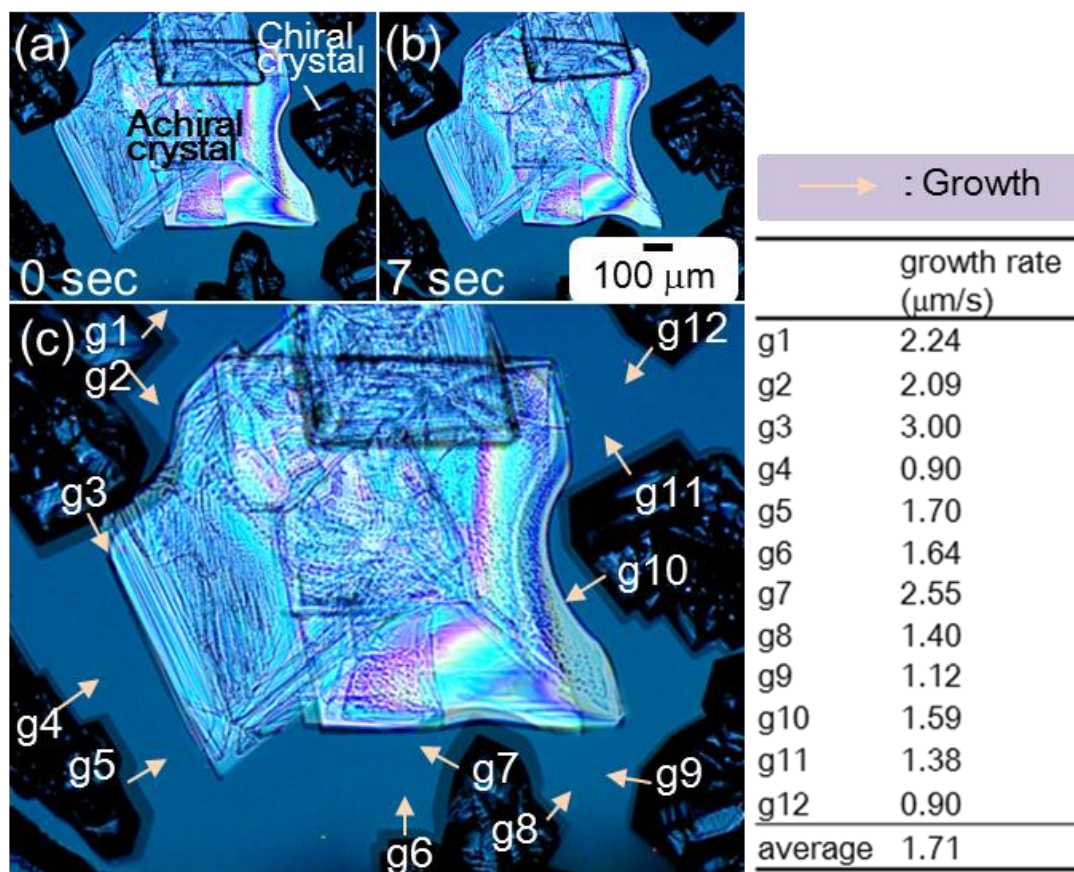
Fig. 3.20 The growth rates of (1 0 0) face of NaClO$_3$ chiral crystals during achiral–chiral solvent-mediated phase transformation. (a) Micrograph of PLM showing the coexistence of achiral monoclinic phase and chiral cubic phase. The crystals which exhibit brighter color are achiral monoclinic phase and the crystals which exhibit darker color are chiral cubic phase. (b) The micrograph showing the same view field as (a) 7 s after. (c) Overlaid image of micrograph (a) and (b). The pink arrows denote the faces and directions which were measured to investigate the growth rate of chiral cubic crystal. Table on the right of (c) indicates the growth rates of chiral cubic crystals at each measured point their average values.

Consequently, the dissolution rate was calculated to be 1.68 μm/s. Second, undersaturation with respect to the achiral phase during SMPT is expressed using the σ_{12}. The undersaturation, σ_U, is defined as minus value of the supersaturation with respect to the achiral phase, σ_{III}:

$$\sigma_U = -\sigma_{III} = -\left[\frac{(x - x_1)}{x_1}\right] \times 100 \tag{3.35}$$

Assuming that $x_2 = 100$ since the solubility of the chiral cubic crystal is about 100 (g/100gH$_2$O), from this assumption and Eq. (3.35), the undersaturation during the SMPT can be written as

$$\sigma_U = \left[\{(\sigma_p + 100) - (\sigma_{12} + 100)/(\sigma_{12} + 100)\}\right] \times 100 \tag{3.36}$$

Third, taking the assumption that dissolution rate is linear with respect to undersaturation and the fact 0 (%) of the undersaturation gives 0 (μm/s) of the dissolution rate into account, the k_D is simply given by the slope of dissolution rate and the undersupersaturation. Then, since $\sigma_p = 52.3$, the k_D is expressed as

$$k_D = \frac{1.68}{\sigma_U} = -\frac{[1.68(\sigma_{12} + 100)]}{[\{152.3 - (\sigma_{12} + 100)\} \times 100]} \tag{3.37}$$

Then, Eq. (3.31) reads quadratic equation with respect to the σ_{12} because the other factors which contribute to the λ can be obtained from micrographs in Fig. 3.20 and crystal structure data of the two phases [26,27] (The author used length of crystal-solution interfaces and the areas of crystals which occupy the micrographs as a substitute for the surface area factors and volume factors in λ , respectively, because Fig. 3.20 gives only two-dimensional information. Then, the $k_D\lambda$ was calculated to be 0.03646.). Solving the quadratic equation, the value of σ_{12} can be estimated as 52.3 (%). This value is from the calculation based on the kinetics of the SMPT. On the other hand, the value obtained by our measurement is 60 (%). The difference between the calculated value and the measured value is within 8 (%), indicating that the agreement of the two values is not bad. Therefore, accuracy of our measurement was deemed to be verified based on the kinetics of SMPT.

3.6 Summary of Chapter 3

 The crystallographic and thermodynamic properties of the unknown non-cubic crystal were revealed in this chapter. Structural analysis on the unknown crystal was achieved by means of cryogenic single-crystal XRD experiment. Additionally, the solubility of the unknown crystal was successfully measured at 10 and 23 °C by achieving selective growth of the unknown crystal and isolation of the crystal from mother liquor by means of antisolvent crystallization. The findings revealed in this chapter are summarized below.

- The crystal system, lattice parameters at -27 °C and space group of the unknown phase were determined as follows: monoclinic, $a = 8.42(2)$ Å, $b = 5.260(7)$ Å, $c = 6.70(1)$ Å, $\beta = 109.71(1)°$, and $V = 279.8(8)$ Å^3, $P2_1/a$, respectively.
- The unknown crystal was revealed to be achiral because of the existence of mirror symmetry in the space group $P2_1/a$.
- The unknown phase was concluded to be identical to Phase III, which is a metastable phase in $NaClO_3$ crystallization from a melt.
- Antisolvent crystallization using acetone can be utilized to selectively produce the unknown crystal as a seed crystal.
- The solubility of the unknown crystal was determined to be 1.6 times higher than that of the stable chiral cubic phase, assuring that the unknown phase is metastable phase in $NaClO_3$ crystallization from an aqueous solution.
- The accuracy of the solubility data the author measured was supported by the kinetics of SMPT.

References

[1] J. W. Pflugrath, *Methods* **34**, (2004), 415.

[2] D. Stalke, *Chem. Soc. Rev.* **27**, (1998), 171.

[3] P. Meyer, C. Seances, *R. Acad. Sci., Ser. C* **274**, (1972), 843.

[4] M. H. Brooker, J. G. Shapter and K. J. Drover, *Phys. Condens. Matter* **2**, (1990), 2259.

[5] P. Meyer, and M. Gasperin, *Bull. Soc. Fr. Mineral. Cristallogr.* **96**, (1973), 18.

[6] V. T. Deshpande and V. M. Mudholker, *Acta. Crystallogr.* **13**, (1960), 483.

[7] K. Momma and F. Izumi, *Commission on Crystallogr. Comput., IUCr Newslett.* **7**, (2006), 106.

[8] J. Alsenz, and M. Kansy, *Adv. Drug Delivery Rev.* **59(7)**, (2007), 546.

[9] D. D. Dunuwila and K. A. Berglund, *J. Cryst. Growth* **179**, (1997), 185.

[10] J. A. Falcon and K. A. Berglund, *Cryst. Growth Des.* **3(6)**, (2003), 947.

[11] G. Sazaki, K. Kurihara, T. Nakada, S. Miyashita and H. Komatsu, *J. Cryst. Growth* **169**, (1996), 355.

[12] J. W. Mullin, *"Crystallization"* (Butterworth-Heine-mann, London) (1993)

[13] A. G. Jones, J. Budz and J.W. Mullin, *Chem. Eng. Sci.* **42,** (1987), 619.

[14] T. G. Zijlema, R. M. Geertman, G. J. Witkamp, G. M. Rosmalen and J. Graauw, *Ind. Eng. Chem. Res.* **39**, (2000), 1330.

[15] I. N. Stranski and D. Z. Totomanow, *Phys. Chem.* **163**, (1933), 399.

[16] I. V. Markov, "*CRYSTAL GROWTH FOR BEGINNERS*" (WorldScientific, Singapore) 2nd Edition (2003)

[17] D. Kashchiev, *Surf. Sci.* **14**, (1969), 209.

[18] S. P. Pinho and E. A. Macedo, *J. Chem. Eng. Data* **50**, (2005), 29.

[19] C.M. Pina, L. Fernández-Díaz, M. Prieto and S. Veintemillas-Verdaquer, *J. Cryst. Growth* **222**, (2001), 317.

[20] N. Bjerrum, "*Danske vidensk, Selks"* 'Selected papers' (Einar Munsksgaard, Copenhagen) (1926)

[21] W. Kossel, *Annalen der Physik* **21,** (1934), 457.

[22] N, Cabrera and R. V. Coleman, *"The Art and Science of Growing Crytsals"* (Wiley, New York) (1963)

[23] A. G. Xyla and P. G. Koutsoukos, *J. Chem. Soc. Faraday Trans.1* **85(10)**, (1989), 3165.

[24] P. Bennema, *J. Cryst. Growth*, **1**, (1967), 287.

[25] S. Hosoya and M. Kitamura, *Miner. J.* **9(2)**, (1978), 73.

[26] W.H.Z. Zacharlasen, *Kristallograhie* **71**, (1929), 517.

[27] Refer to the data shown in Table 3.2 in this section.

CHAPTER 4
EMERGNECE AND AMPLIFICATION OF CHIRALITY VIA ACHIRAL-CHIRAL POLYMORPHIC TRANSFORMATION

4.1Brief Introduction

The unknown transient metastable crystal was revealed to be achiral in the previous chapter. This fact indicates that chirality emerges in the course of the polymorphic transformation from the achiral metastable phase to the chiral stable phase rather than primary nucleation process. This newly discovered process of emergence of chirality has a possibility to sheds a new light on understanding of chiral symmetry breaking in crystallization from a solution. However, the role of the polymorphic transformation on the resulting handedness still remains unclear because of the lack of detailed observations with intensive attentions to the transformation. To investigate the relationship between the kind of polymorphic transformation and the resulting handedness, this chapter presents detailed *in-situ* observations with intensive attentions to the polymorphic transformation using PLM with a high-resolution video recording system. The observations show that two different kinds of polymorphic transformations have a potential to play a roles on spontaneous emergence and amplification of chirality.

4.2 Experimantal -In-Situ Observation of Polymorphic Transformation-
4.2.1 In-Situ Observation of Polymorphic Transformation which spontaneously proceeds in Aqueous Solution

The experimental details are the same as described in the chapter 2.

4.2.2 In-Situ Observation of Polymorphic Transformation induced by stimulation in Air

In addition to the *in-situ* observation of crystallization from an aqueous solution, transformations of an achiral crystal which completely exposed to air were also examined. Namely, the transformation does not involve solvent were examined. An achiral crystal for the observation was prepared by the antisolvent crystallization method described in the previous chapter since the method is able to isolate achiral crystals from mother solution. The solution prepared by the aforementioned procedure (see Chapter 2) was used as a mother solution for the antisolvent crystallization. The

mother solution was placed on a glass slide using a micropipette (6 µL) and then about 500 µL of acetone was flushed into the mother solution. After flushing, the glass slide was dried by a dryer until the solvent cannot be observed around the crystal even by using PLM. The resulting achiral crystals were 50-100 µm in size. After assuring the complete evaporation of solvent under the PLM, the achiral crystal were stimulated by touching the crystal with the tip of a needle while observing the crystal using the PLM at 22 °C.

4.3 Results

4.3.1 Polymorphic Transformations in Aqueous Solution

Achiral dendrites appeared from the meniscus of a droplet of an aqueous solution, followed by the formation of parallelogram platy crystals in the vicinity of the dendrites. The dendrites started to transform to chiral dendrites and the parallelogram platy crystals were swept away to the center of the droplet. The chiral dendrites continued to grow towards the center of the droplet. Consequently, the chiral dendrites approached to the parallelogram platy crystals (Fig. 4.1).

The parallelogram achiral crystals showed two different types of behaviors depending on the distance from the chiral dendrites (Fig. 4.2 and Fig. 4.3). Firstly, when the chiral dendrites reached within 20 µm of a parallelogram achiral crystal, the achiral crystal started to dissolve [Fig. 4.2 **B** (a)]. The achiral crystal continued to dissolve in response to the growth of the chiral dendrite, resulting in a vermiculated shape [Fig. 4.2 **B** (d)]. The growth rate of the chiral dendrite towards the achiral crystal was approximately 6 µm/sec.
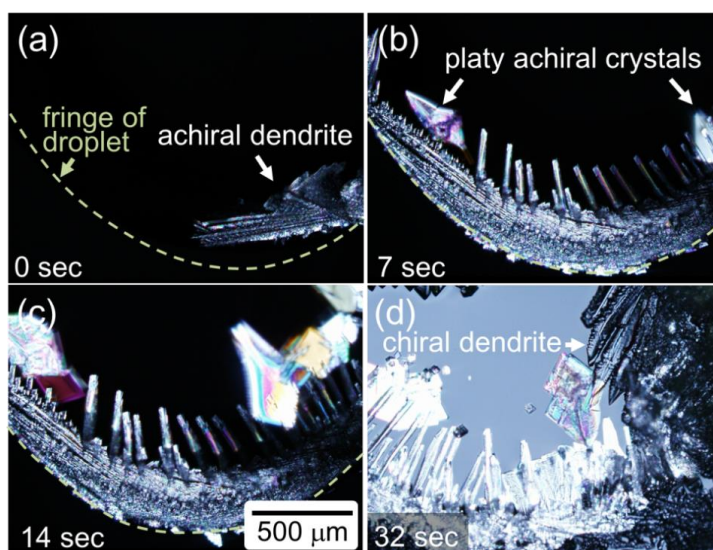
Fig. 4.1 Time-lapse PLM micrographs of NaClO$_3$ crystallization in a droplet of aqueous solution.
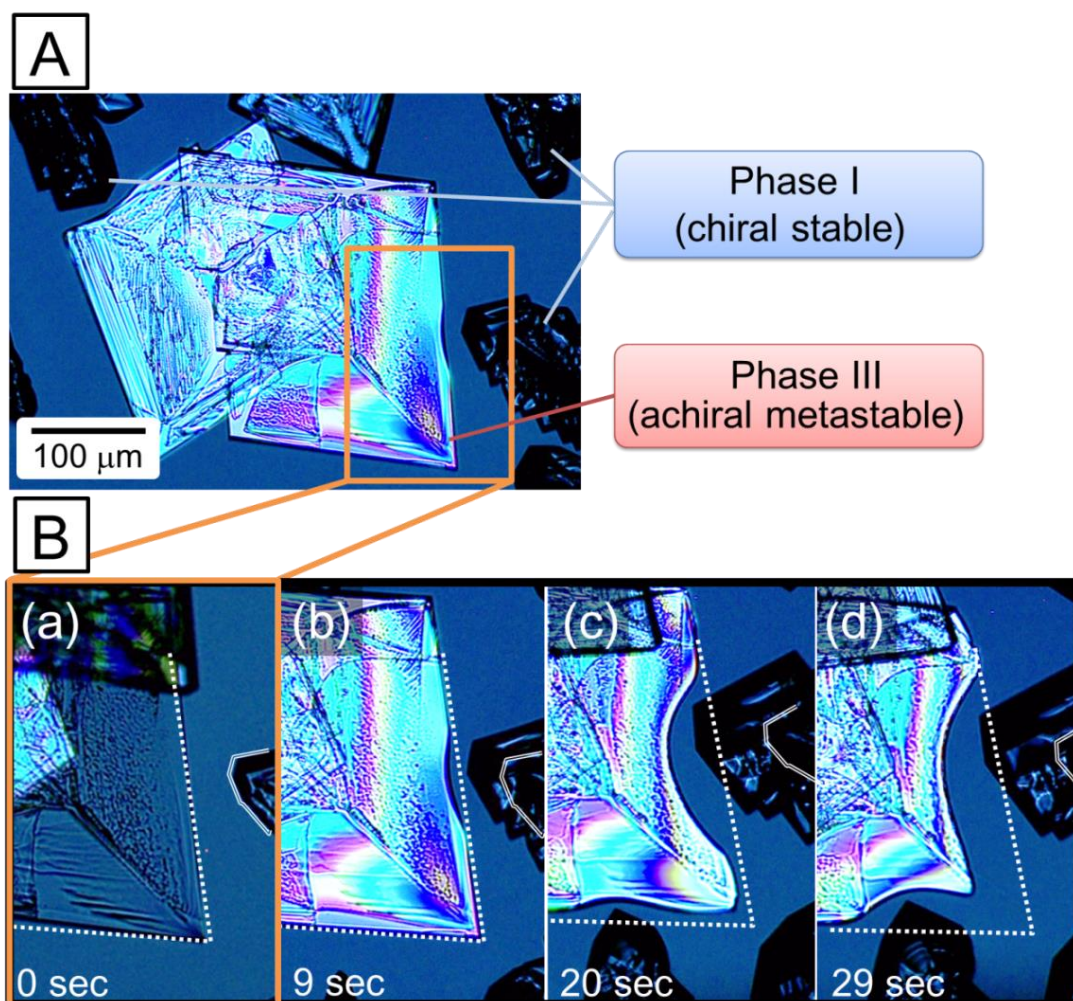
Fig. 4.2 Time-lapse PLM images showing the dissolution of an achiral phase III crystal in correspondence with the approach of chiral phase I. **A** A microscopic view showing phase III crystal which coexists with phase I crystals. **B** time-lapse magnified micrographs of the region designated by orange square embed in **A**, showing the dissolution of phase III crystal corresponding to the approach of dendrite of phase I.

Secondly, when the chiral dendrites approached to the vicinity of achiral crystal until the polarized-light microscopy cannot resolve the interfaces as a consequence of the competition between the growth of the chiral dendrite and the dissolution of the achiral crystal, the achiral crystal immediately began to transform from the point at which the chiral dendrite approached [Fig. 4.3 (a)-(f)]. The front line of the phase transition advanced radially from the point at which the chiral dendrite approached with a velocity of approximately 35 μm/s [Fig. 4.3 (d)-(e)]. Even after the front line reached the opposite side of the achiral crystal, the bright contrast originating from birefringence remained in some places and gradually darkened. After 29 sec, a 500 μm parallelogram platy achiral crystal was completely replaced by a chiral crystal [Fig. 4.3 (f)]. The optical rotation of the approaching chiral dendrites and the transformed one crystal that transformed one indicated that both crystals exhibited the same chiral sign. The author observed such approach-facilitated phase transformation four times except of that shown in Fig. 4.3 and confirmed the succession of chirality in all cases.

In addition, rapid transformations as compared to the transition mentioned above were also occasionally observed (Fig. 4.4). As shown in Fig. 4.4, the bright contrast due to the birefringence of a 250 μm sized achiral crystal rapidly disappeared within about 0.1 sec. The transition rate was approximately 2000 μm/s or more, which is two orders of magnitude higher than the transformation mentioned above. The rapid phase transition was rare event. Before the phase transformation, the bright crystal did not grow nor dissolve.
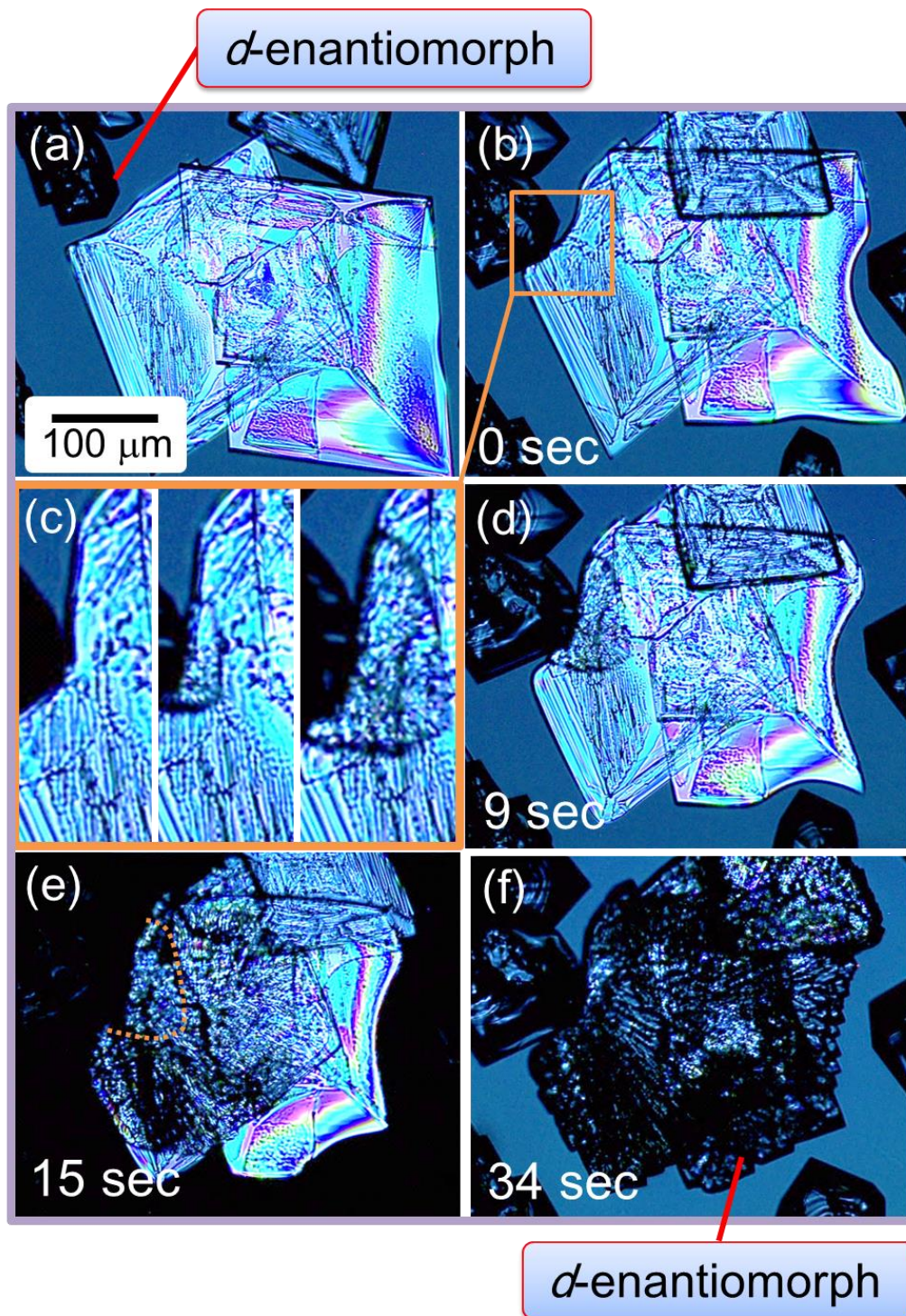
Fig. 4.3 Time-lapse PLM showing polymorphic transformation from achiral phase III to chiral phase I triggered by the approach of a phase I crystal with a phase III. (c) is time-lapse magnified micrographs of the region designated by orange square embed in (b).
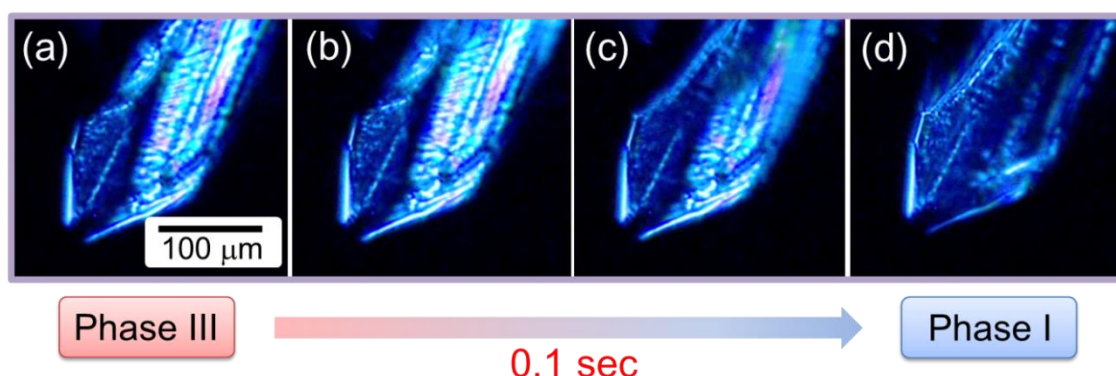
Fig. 4.4 Snapshots of rapid transformation from phase III crystal to phase I crystal. The transformation was accomplished within 0.1 seconds.

4.3.2 Polymorphic Transformation Induced by stimulation in Air

Touching the crystal with the tip of a needle successfully achieved to induce the transformation of a metastable achiral crystal into a chiral stable crystal (Fig. 4.5 **A**). Fig. 4.5 **A** shows a series of micrographs illustrating the transformation induced by the stimulation of touching. From the moment the achiral crystal was stimulated, the bright contrast of the achiral crystal started to change from the fringe of the crystal [Fig. 4.5 **A** (b)]. The optical change exhibited two-steps. Firstly, the initial interference color, which was homogeneously light blue, began to change into a non-homogeneous purple-based color. The purple-based color propagated from several points at the fringe of the crystal toward the center [Fig. 4.5 (c)-(f)]. The non-homogeneity of color appeared to be perpendicular to the propagation direction [Fig. 4.5 (e)]. Fig. 4.5 (**B**) shows the brightness distribution profiles in the cross lines denoted by a-a', b-b', and c-c'. Comparing the profiles of a-a' and b-b', a considerable difference in brightness can be seen between the crystals before and after stimulation was applied. Specifically, a brightness value before the stimulation was lower than 150, whereas the value after the stimulation was more than 150. When the front lines of the propagation of the purple-based color region collided and overlapped, the overlapped front lines became domain boundaries [Fig. 4.5 (f), pink dashed lines]. Secondly, the interference color started to disappear mainly from the domain boundaries and fringe of the crystal [Fig. 4.5 (f)-(i)]. The brightness profile in c-c' shows the region whose brightness was close to zero among the region whose brightness was 150-200 (Fig. 4.5 **B**). This observation indicates that the stimuli-induced transformation from an achiral crystal to a chiral crystal comprises two steps: (1) an optical change during which the brightness value increases and (2) an optical extinction.
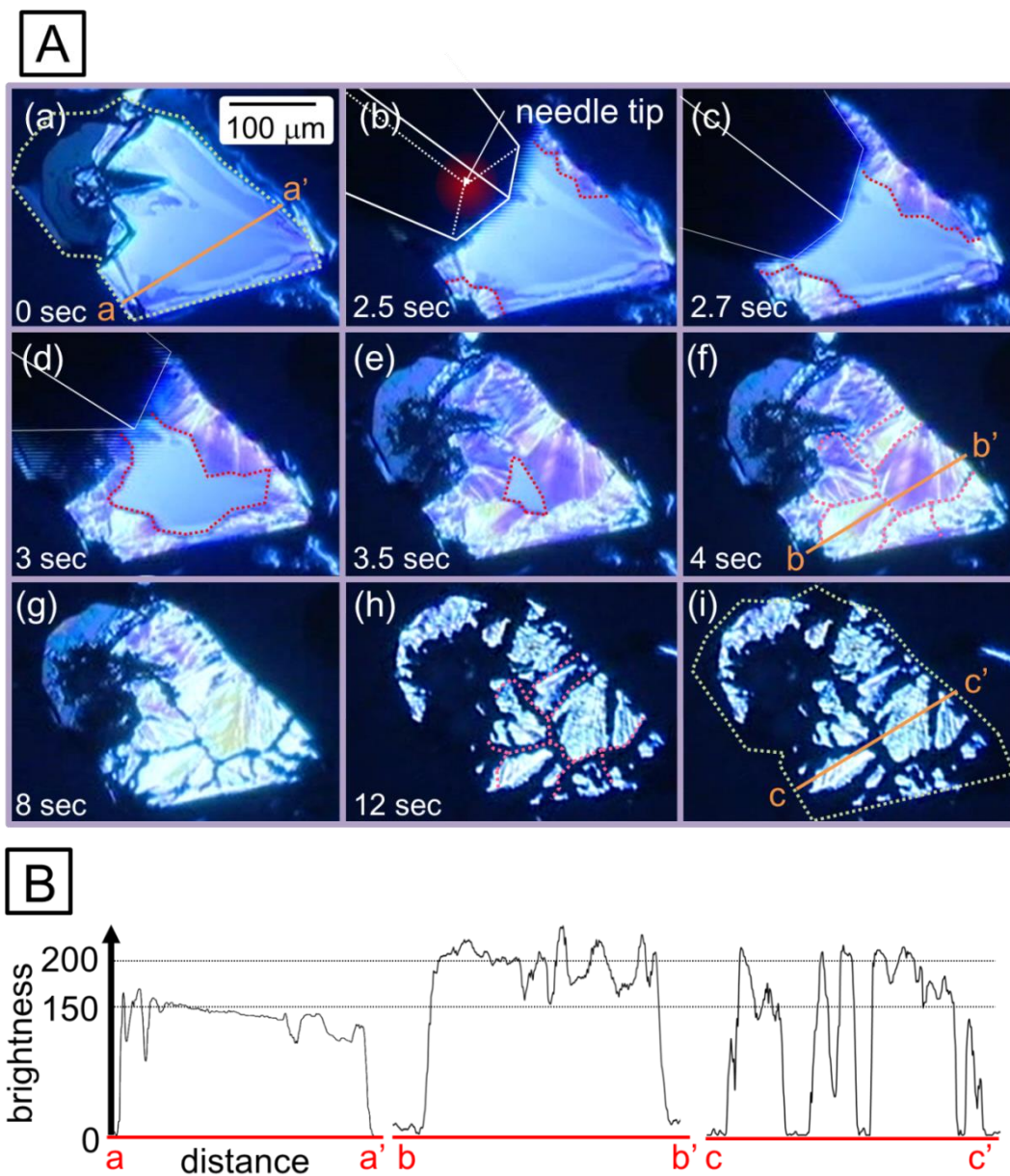
Fig. 4.5 A: *In situ* polarized light microscopic images showing the solid-solid phase transition induced by a stimulation using a needle: (a−b) Micrographs showing the change in the optical properties of the achiral crystal during the transformation triggered by stimulation using a needle. (a) An achiral crystal before the stimulation. The green dashed line indicates the outline of the achiral crystal [compared to the green dashed line in image (a)]. The moment when this image was captured is set at 0 s. (b) The achiral crystal just after stimulation. White lines indicate the outline of the needle used for stimulation, and the circle colored by gradational red indicates the contact point of the needle with the achiral crystal. The red dashed line indicates the front line of the change in optical properties. (f) The crystal after the first change in optical property. The pink dashed color indicates the boundary of the homogeneous interference color. **B:** Brightness distribution profiles for cross lines denoted a-a' in (a), b-b' in (f), c-c' in (i), respectively. Brightness of the red color in the RGB histogram was employed for the profile.

4.4 Discussion

4.4.1 Structural Phase Transformation from Achiral Phase III to Chiral Phase I

In general, polymorphic phase transformations which occur in aqueous solution may be classified into two types: (i) solid-solid structural phase transformation (SSPT) (ii) solvent-mediated phase transformation (SMPT). The SSPT is progressed by structural rearrangement of atoms and molecules in a metastable structure into stable structure. On the other hand, the SMPT is progressed by so-called dissolution/precipitation mechanism, where stable crystal grows simultaneously with the dissolution of the metastable crystal as introduced in the previous Chapter (Fig. 4.6). Therefore, the factor which governs the rate-controlling process of the SMPT is either slower one of the dissolution rate of metastable crystal or the growth rate of stable crystal. Here, let the author discuss which phase transitions, SSPT or SMPT, the phase transformation with the transition rate of ~2000 μm/sec should be classified into. Here the author once assumes that the phase transformation with the transition rate of ~2000 μm/sec can be classified into SMPT. Considering the rate-controlling process of the SMPT, the growth rate of chiral crystal is required to be more than 2000 μm/sec if the assumption is collect. Bearing in mind that the growth rate of chiral crystal is a linear function of supersaturation with respect to the chiral phase as described in the Chapter 3 [1], it follows that 58998 % of the supersaturation is required to obtain 2000 μm/sec of the growth rate. It's highly unlikely that such a value of the supersaturation (58998 %) was attained by the experimental procedure. Moreover, the observational fact that the metastable crystal did not grow nor dissolve indicates that the bulk concentration of the surrounding solution is near to the equilibrium with respect to the metastable phase. Therefore, supersaturation of the solution with respect to the chiral stable phase is possibly about 60%. The 58998% of the supersaturation is not feasible. Since it is found to be difficult to explain the fast transition rate by the mechanism of the SMPT, the phase transition is possibly classified into SSPT. Therefore, the author here concludes that the phase transition from the achiral crystal to chiral crystal with ~2000 μm/sec of transition rate is SSPT. Therefore, chirality of the crystal was determined by the collective rearrangement of the molecules in the achiral structure during the SSPT.
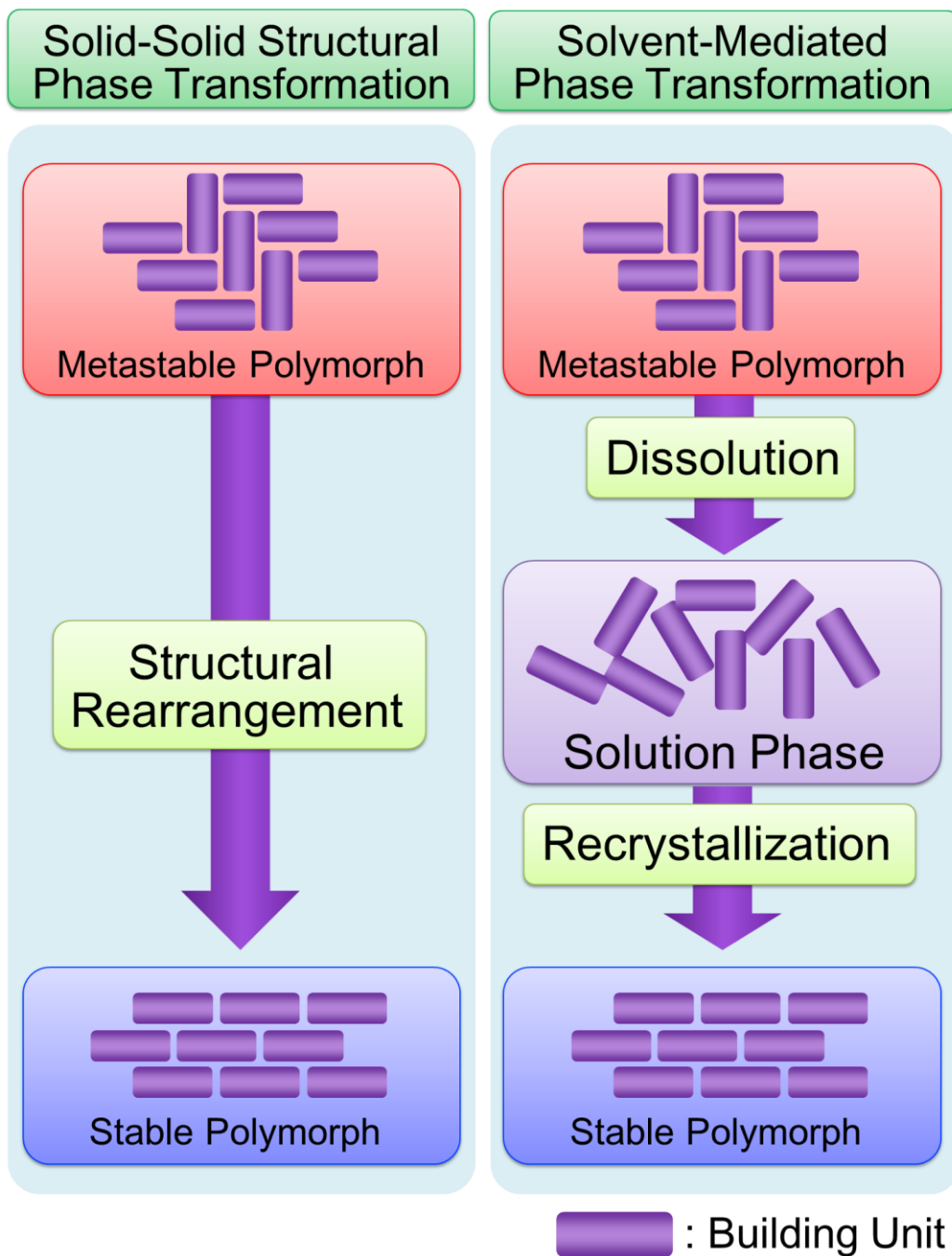
Fig. 4.6 Schematic comparison of two kinds of polymorphic transformation seen in crystallization from a solution. Left schematic indicates solid-solid structural transformation (SSPT). Right schematic indicates solution-mediated phase transformation (SMPT).

4.4.2 Solid-Solid Structural Phase Transformation Intermediated by a Transient Phase

It was found that achiral crystal separated from solution transforms into chiral crystal via two-step optical change by stimulation with a needle, indicating the existence of a transient crystalline phase during this stimuli-induced polymorphic transformation. In this case, SMPT can be ruled out for the candidate of the phase transition which explains the stimuli-induced transformation since solvent was not involved with this transformation. Therefore, here, the author discusses the two-step optical change on the basis of structural deformation.

4.4.2.1 Meyer's Deformation Model and Its Correspondence with Two-Step Optical Change in Stimuli-Induced Structural Transformation

Meyer *et al.* have figured out the structural displacements illustrating the structural deformation from Phase III to the chiral cubic phase I and they have pointed out that the phase transition is a martensitic transformation (MT) [2]. The deformation process of Meyer's model is comprised of two-step displacements. The first displacement is sliding of the layers that consist of unit cells along the (001) (unique axis b) to the direction parallel to the *a* axis by $1/4a$ relative to the adjacent layers. This displacement creates octahedral structures outlined by the sodium atoms. The second displacement is the straining of the octahedral structures (Fig. 4.7).

Illustrations boxed by blue color in Fig. 4.8 show the strained octahedral structures caused by the second displacement. The cubic structure of phase I is constructed by alternately stacking two kinds of layers, which are here denoted by A and B, to the $[\bar{1}10]$ direction. Although both of the layer A and B are constructed only by single-species strained octahedral structures, the arrangement sequence of the each octahedral is different between the layer A and B. Upper illustration in blue box in Fig. 4.8 shows the arrangement sequence of the layer A, whose configurational repeating unit is composed by four strained octahedral, and each the four octahedrals are denoted as a,b,c,d so that the alphabetical sequence draws a clockwise orbital. Whereas the alphabetical sequence of the layer A draws a clockwise orbital that of the layer B draws a counter-clockwise orbital. The stacking of these two layers constructs the cubic structure of phase I. The two deformations, which are sliding of layers and straining of octahedral structures outlined by sodium atoms, describe the structural deformation from Phase III to the cubic phase I.
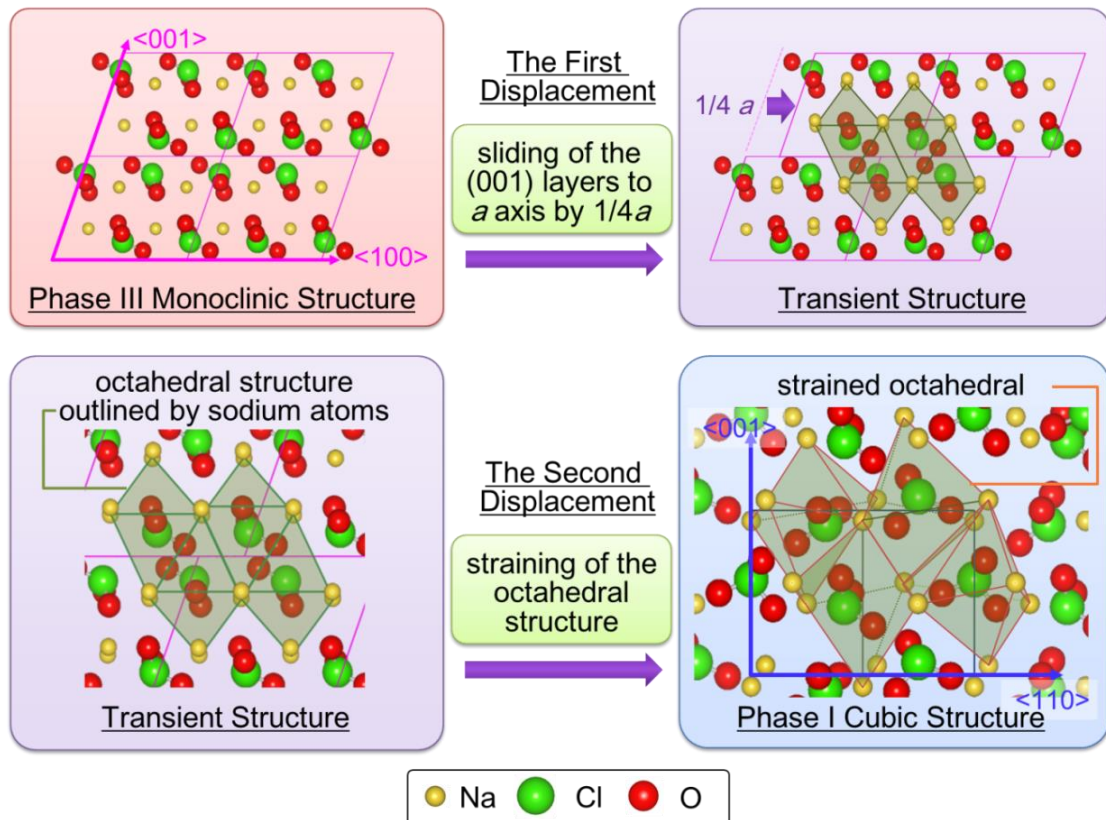
Fig. 4.7 Schematic illustrations describing Mayer's deformation model, which figures out structural rearrangement geometrically rationalizing SSPT from phase III to phase I [2]. The rearrangement process comprises two deformations: (1) sliding of (001) layers (2) straining of octahedral structure, which is denoted by green lines. Yellow, green, red spheres indicate sodium, chlorine, oxygen atoms, respectively.
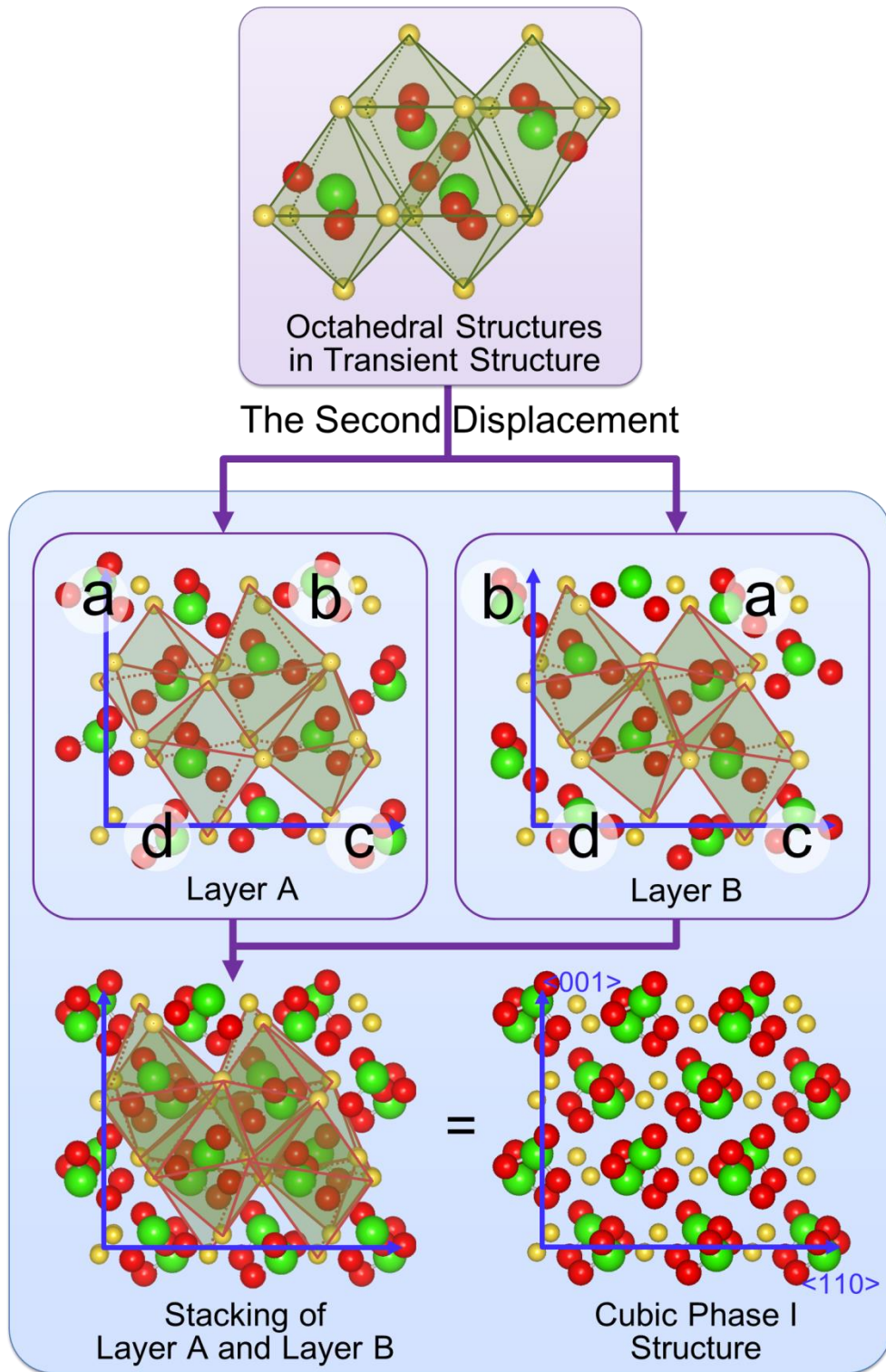
Fig. 4.8 Schematic illustrations describing a detail of change in the structural configuration accompanying with the second displacement of Meyer's model.

Since the Phase III is deemed to be identical to the achiral metastable phase, the deformation of SSPT observed in this study may be the same as the deformation from the Phase III to the cubic phase. Notably, our observation of stimuli-induced structural phase transformation showed that the transformation undergoes a two-step optical change. The first optical change was the increase in the brightness. The increased brightness should originate from the optical anisotropy of a non-cubic structure except for the achiral monoclinic phase, indicating the existence of a transient structure. Comparing the two-step optical change with the two-step deformation model of Meyer *et al.*, the transient structure may correspond to the structure after the first displacement in Meyer's model (Fig. 4.9 upper right). Here the author concluded that the deformation process during the stimuli-induced structural transformation may follows deformation model proposed by Meyer *et al.*.
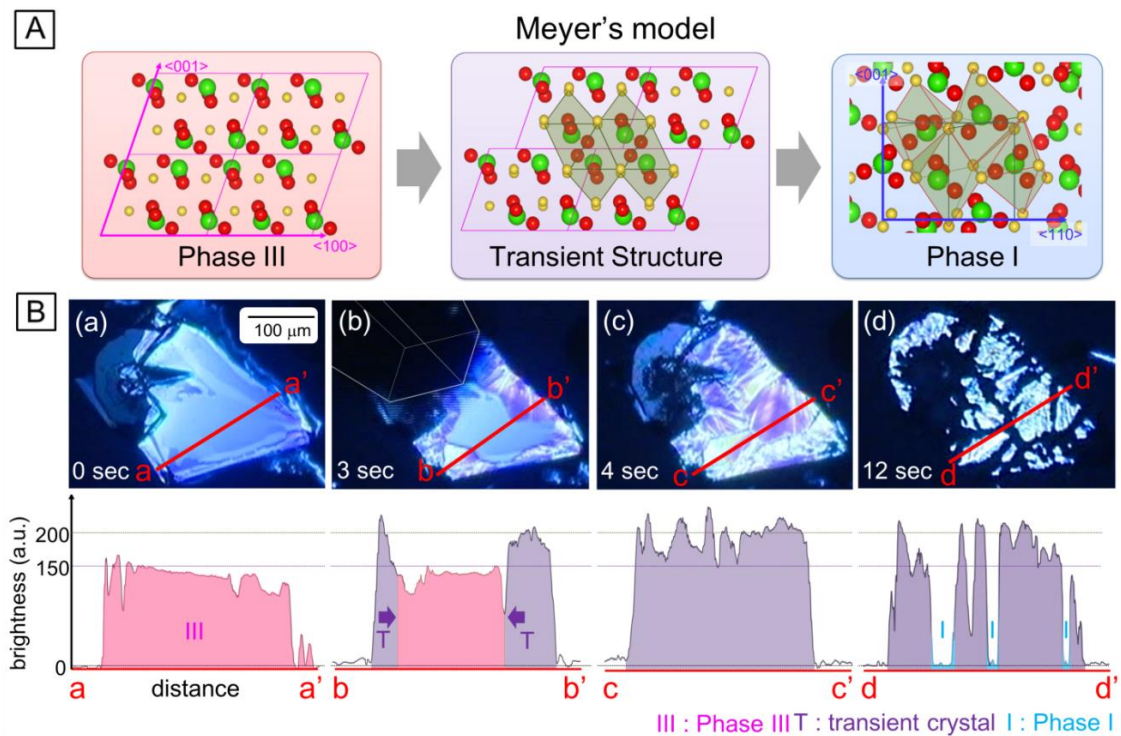
Fig. 4.9 Correspondence of optical changes during the stimuli-induced SSPT in air to Meyer's deformation model: (**A**) Meyer's model describing the structural deformation from phase III, (**B**) Change in the brightness profile of crystal with time and correspondence of the brightness to the structures outlined by Meyer's model. Time indicated in upper left corresponds to time indicated in Fig. 4.5 **A**.

These considerations above may give rise to a question that lifetime of the transient structure should be extremely short since displacements of atoms should be accomplished instantly. However, in practice, the transient structure remained more than 8 seconds and the lifetime was long. The long lifetime can be rationalized by consideration mentioned below. Bearing in mind the phase diagram of NaClO$_3$ crystallization from a melt, the polymorph other than phase I and phase III, which is designated as Phase II, exists as one of metastable crystalline phases (see Fig. 3.4 in the Chapter 3) [2,3]. The crystal structure of the Phase II still remains undetermined. According to the phase diagram, Phase II is the second most unstable phase after the Phase III up to 255 °C. Therefore, it is possible that Phase II appears as intermediate phase during the phase transformation by kinetic trapping. Based on this idea, we can speculate that the transient structure described in Meyer's model corresponds to crystal structure of Phase II, meaning the transient structure can be not just a structure required for geometric rationalization but a metastable structure. Therefore, the long lifetime of the transient structure is possibly rationalized by its own metastability.

4.4.2.2 Mechanism of Emergence of Chirality during Stimuli-Induced Structural Transformation

Considerations described in the precious section support the validity of the Meyer's deformation model for SSPT seen in crystallization from an aqueous solution. Assuming that the Meyer's deformation model valid for the stimuli-induced SSPT, here the author discusses which deformation process generates structural chirality (Fig. 4.10). Bearing in mind the structure after the first displacement in Meyer's model, the each octahedral structure caused by the first displacement has chirality (Fig. 4.10 upper). Although the framework of the octahedral drawn by sodium atoms is intrinsically achiral itself, the octahedral structure including a chlorate anion is chiral because the chlorate anion places so as not to overlap its mirror plane with the mirror plane of the octahedral structure. If we focus on the handedness of the octahedral structure, the structure after the first displacement can be regarded as a structure in which both of left-handed octahedral and right-handed octahedral are alternately packed. Namely, the structure after the first displacement is racemic and thus, the structure is achiral. Consequently, it follows that chirality emerges through the second displacement, which is straining of the octahedral structure, during the stimuli-induced SSPT. The strained octahedral structure also has chirality and there are left-handed strained octahedral structure and right-handed strained octahedral structure. The cubic structure is constructed by only

either of the chiral strained octahedral structure in contrast to the racemic transient structure (Fig. 4.10 lower). The strained crystal structure is generated by twisting of the tetragonal plane expanding to a (001) outlined by sodium atoms. The direction of the twisting may determine the resulting handedness of crystal.
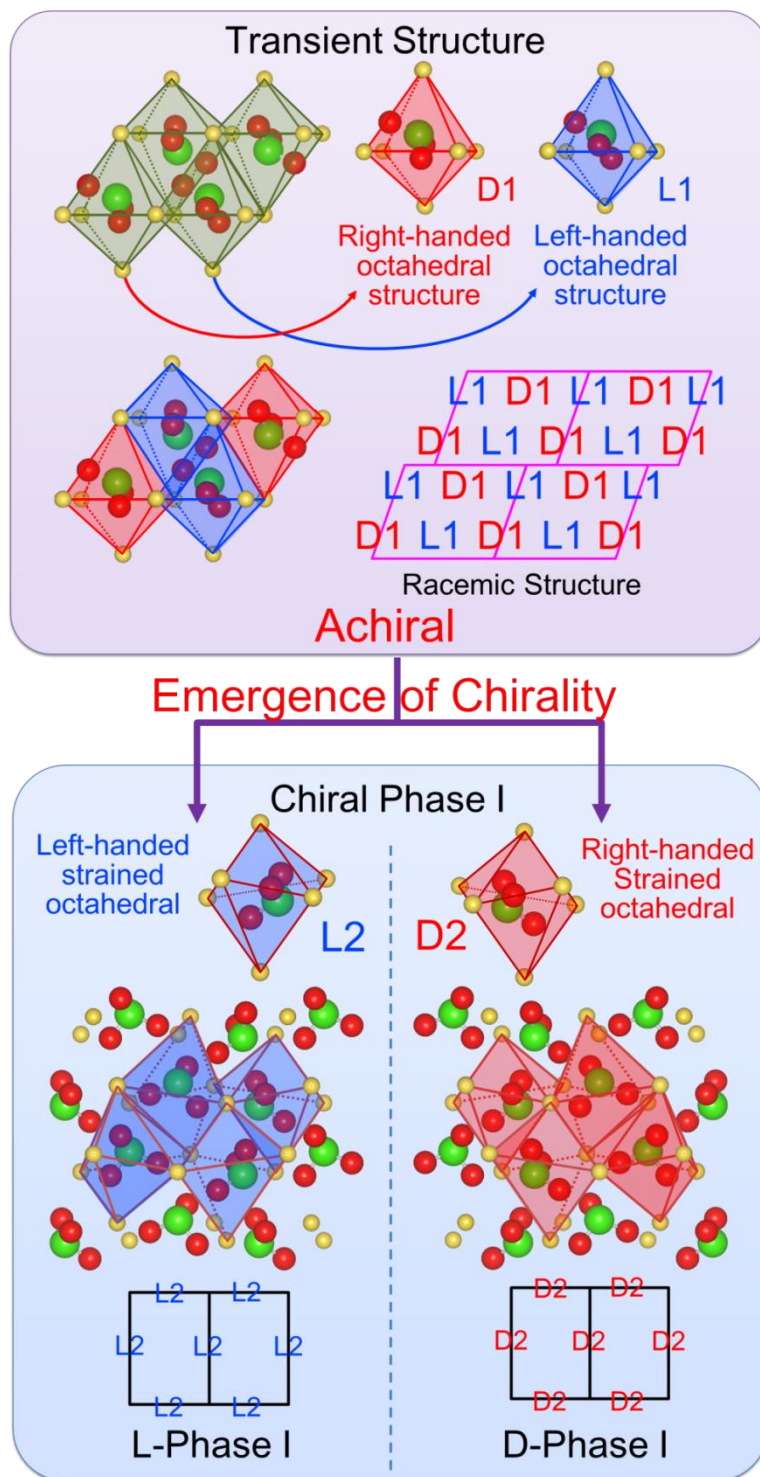
Fig. 4.10 The process of emergence of chirality during SSPT from phase III to phase I in Meyer's model. Upper schematic illustration indicates the structure of transient structure in the model. Lower illustration shows the structure of chiral phase I (left one shows left-handed structure and right one shows right-handed structure.)

4.4.3 Approach-Induced Transition of Rate-Controlling Process in Solvent-Mediated Phase Transformation: an Explanation for Approach-Facilitated Phase Transformation and Inheritance of Chirality

As shown in the section of results, it was observed that a chiral stable crystal grow simultaneously with the dissolution of an achiral crystal (Fig. 4.2 **B** and Fig. 4.3 (a-b)). When the chiral crystal is located at about 10 μm vicinity of the achiral crystal the achiral crystal dissolves as the chiral crystal grows. This process is typical in SMPT, that is, dissolution/precipitation mechanism. Therefore, here, the author discusses a series of the polymorphic phenomena from the SMPT to the approach-facilitated phase transformation on the basis of kinetics of the SMPT.

4.4.3.1 Growth-Controlled SMPT and Dissolution-Controlled SMPT

SMPT can be classified into two kinds depending on rate-controlling processes. This classification was theoretically done by Cardew *et al*. [2]. As mentioned above, the SMPT is the process coupled the dissolution of a metastable phase and the growth of the stable phase. Therefore, kinetic relations for the dissolution and the growth are, respectively,

$$\frac{dL_1}{dt} = -k_D(\sigma_{12} - \sigma), \tag{4.1}$$

$$\frac{dL_2}{dt} = k_G\sigma \tag{4.2}$$

where L_1 is size of the metastable phase and L_2 is size of the stable phase and others are same definition as the chapter 3. In fact the rate controlling processes are best appreciated by definition of three time scales:

(i) the dissolution time τ_D, defined as the time required for all phase 1 to dissolve at its maximum rate, i.e.

$$\tau_D = \frac{L_{1i}}{k_D\sigma_{12}}; \tag{4.3}$$

where L_{1i} is the initial size of a metastable phase.

(ii) the growth time, τ_G, defined as the time required for the phase 2 crystals to reach their final size at the maximum rate, i.e.

$$\tau_G = \frac{L_{2f}}{k_G \sigma_{12}};$$
(4.4)

where L_{2f}, is the final size of the stable phase.

(iii) the transformation time, τ, defined as the time as which all the metastable crystal disappear. It has been shown that

$$\tau = \tau_G + \tau_D,$$
(4.5)

which implies that if $\tau_D \gg \tau_G$ the transformation is dissolution controlled while if $\tau_G \gg \tau_D$ the transformation will be growth controlled (Fig. 4.11).
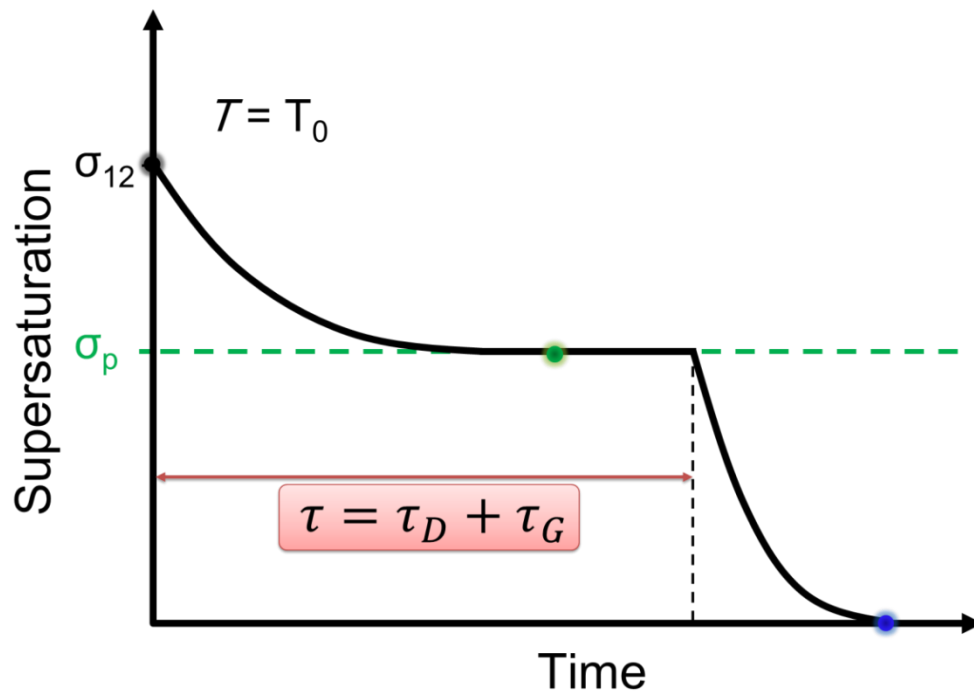
Fig. 4.11 Supersaturation profiles versus time during SPMT and its correspondence with the total time of the time required for complete disappearance of metastable phase and the time required for stable phase to reach their final size.

119

4.4.3.2 Mechanism of Approach-Facilitated SMPT and Mechanism of Inheritance of Chirality

Cardew *et al.* theoretically indicates rate-controlling process of the SMPT based on the comparison between the time required for complete dissolution of metastable phase and the time required for completion of growth of the stable phase. However, the theory does not take microscopic inhomogeneity of concentration field around crystals, which microscopically governs growth rate for stable phase and dissolution rate for metastable phase, into account. Since the rate of dissolution and growth can microscopically change owing to the inhomogeneity of the concentration field, in practice, the rate-controlling process possibly change in microscopic region. Therefore, here, the author qualitatively discusses the rate-controlling process on the basis of a conceivable microscopic concentration field surrounding a platy achiral crystal. Subsequently, the author demonstrates that the mechanism of the approach-facilitated SMPT can be rationalized by the microscopic change of the rate-controlling process of SMPT.

Generally, SMPT proceeds under unsaturated concentrations with respect to the metastable phase [4], namely, the achiral crystal dissolves during SMPT. Since the concentration around the vicinity of dissolving crystal is high compared to the concentration far from the crystal unless the rate of diffusion is anomalously high, the concentration field around the achiral crystal must be considered. According to the analysis of concentration distribution using interferometric techniques, the concentration around the dissolving crystal increases nonlinearly as it reaches surface of the crystal (Fig. 4.12) [5]. Moreover, the interfacial concentration around a dissolution crystal is conventionally considered to be saturated with respect to the dissolution crystal. For instance, Noyes-Whitney's diffusion model, which is widely accepted for explanation of dissolution phenomena, postulates that the concentration around the immediate vicinity is saturated with the dissolving substances [6]. Therefore, the author considers the concentration distribution around the dissolving achiral metastable crystal with the following assumptions: (1) the concentration far from the surface of the achiral crystal is slightly supersaturated with respect to the chiral phase; (2) the concentration increases nonlinearly as it reaches to the surface; (3) the concentration in the immediate vicinity of the surface is saturated with respect to the metastable achiral phase (Fig. 4.13). For simplicity, the concentration field is assumed to be not influenced by any changes of circumstance, e.g., fluid flow or concentration field originating from other crystals. Based on the above assumptions, the author discusses three situations: the growth front of a chiral crystal is located at (i) significantly far from the surface of the

achiral crystal, (ii) a specific position between (i) and (iii), or (iii) the immediate vicinity of the surface.

Dissolving NaClO₃ Crystal

exponential increment of concentration at the vicinity of surface
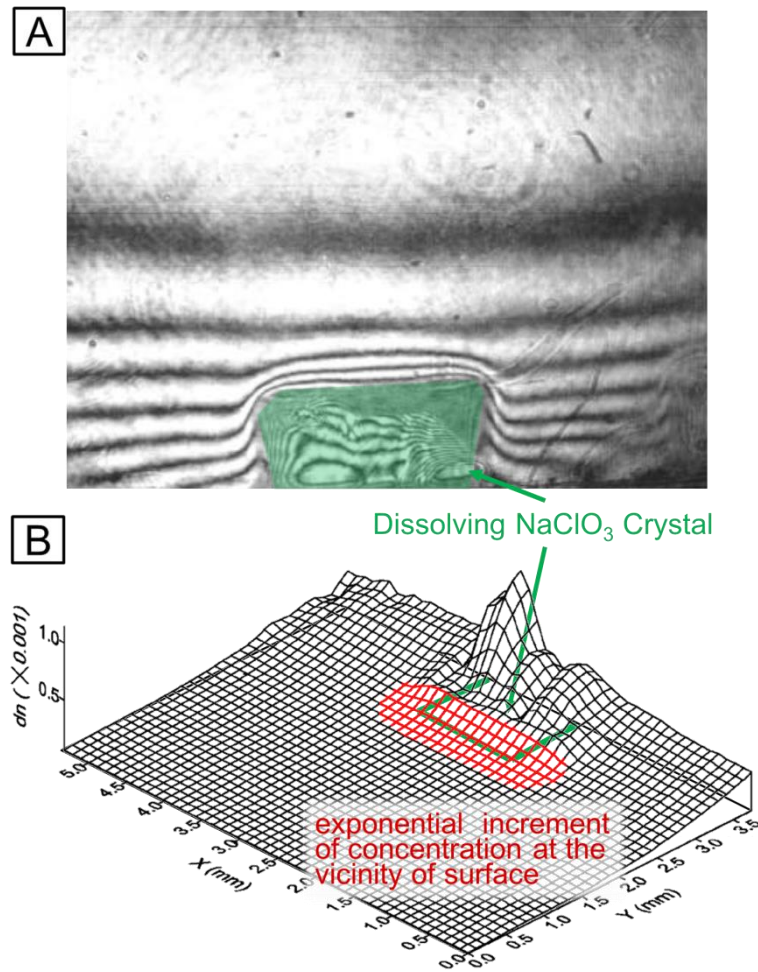
Fig. 4.12 Concentration distribution of solution surrounding a dissolving $NaClO_3$ phase I crystal investigated by means of interferometric technique: **A** Interference figure showing the solution around a $NaClO_3$ single crystal. The region highlighted by green color indicates the dissolving single crystal. **B** Concentration distribution mapping constructed based on the interference figure. The region colored by red indicates the position at the vicinity of the single crystal. This figure is adopted from Ref. [5].
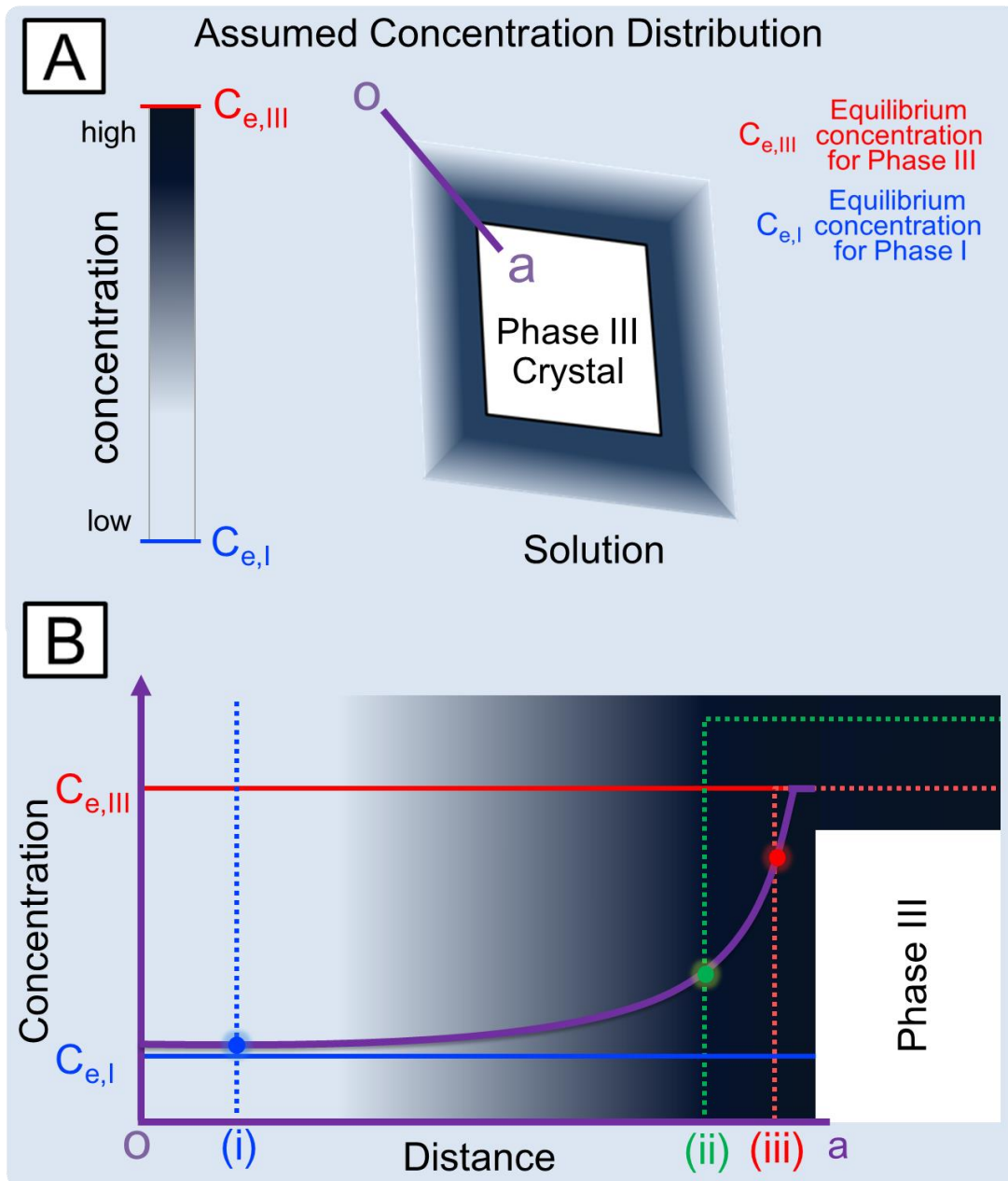
Fig. 4.13 The assumed concentration distribution of the solution surrounding an achiral phase III single platy crystal. **A** The distribution in plane with the platy crystal. Gradation of blue color indicates the degree of concentration. $C_{e,phaseI}$ and $C_{e,phaseIII}$ represents the equilibrium concentration with respect to phase I and phase III, respectively. **B** Concentration distribution in cross-section of the line o-a embed in (a). (i), (ii) and (iii) indicate the positions of three situations we will discuss.

Firstly, let the author consider situation (i), which corresponds to before the contact between the chiral crystal and achiral crystal [Fig. 4.13 (i) and Fig. 4.14]. In this situation, the growth front of the chiral crystal is located at the region where concentration is near equilibrium, causing a slow growth rate of the chiral crystal. Therefore, the growth rate, R_G, should be significantly slower than the dissolution rate of the achiral crystal, R_D. Assuming that both of the size of the achiral crystal, L_a, and the chiral crystal, L_c, are nearly equal, it can be said that this situation is transiently and locally growth-controlled SMPT because in this case τ_D and τ_G should be expressed as

$$\tau_D = \frac{L_a}{R_D};\qquad\qquad\qquad\qquad (4.6)$$

$$\tau_G = \frac{L_c}{R_G};.\qquad\qquad\qquad\qquad (4.7)$$

In practice, the growth of the chiral crystal would consume the solute dissolved in the surrounding solution and decrease the concentration. Consequentially, the relatively lower concentration would be compensated by dissolution of the achiral crystal, resulting in the vermiculated shape of the achiral crystal reflecting the concentration field surrounding the chiral crystal. For this reason, the dissolution of the achiral platy crystal, which can be seen in Fig. 4.2 **B** and Fig. 4.3 (b), is probably a consequence of growth-controlled SMPT.

Secondly, when the growth front moves closer to the surface of the achiral crystal, the growth rate should eventually become equal to the dissolution rate at a certain position. This position represents situation (ii) (Fig. 4.13 (ii) and Fig. 4.15). The transition from growth-controlled SMPT to dissolution-controlled SMPT occurs at this position. As will be discussed later, situation (ii) may represent the moment when the approach-facilitated phase transformation starts. Namely, trigger of the approach-facilitated phase transformation is the irruption of the growth front into the concentration region in which the growth rate of the chiral crystal overcomes the dissolution rate of the achiral crystal.

Thirdly, let the author consider what happens when the growth front reaches the immediate vicinity of the surface of the achiral crystal (situation (iii)). In this situation, the growth front of the chiral crystal irrupts into the concentration region in which the

growth rate becomes higher than the dissolution rate (Fig. 4.13 (iii) and Fig. 4.16). It should be emphasized that the interfacial supersaturation should be 60 % since the solubility of the achiral metastable phase, which were determined in the Chapter 3, is 1.6 times higher than that of chiral stable phase. Therefore, the immediate vicinity of the crystal surface is highly supersaturated with respect to the chiral crystal up to 60% of supersaturation, the supersaturation of the region allows the growth rate of the chiral crystal to be remarkably high. It should be also emphasized that this region should be very thin. Therefore, the high rate occurs exclusively within the thin region. The high growth rate proceeds preferentially along the thin region, causing lateral growth over the surface of the achiral crystal [Fig. 4.16 **B**, **C** (a)-(c)]. Thus, dissolution-controlled SMPT occurs in this situation. Above mentioned process for SMPT is supported by two observational evidences: (1) the bright contrast originating from the achiral crystal remained even after the front line of the transformation crossed the achiral crystal, and (2) the chiral sign of the resulting crystal was certainly the same as the sign of the chiral crystal that contacted the achiral crystal. Therefore, the observation in the approach-facilitated phase transition is concluded to be interpreted by the transition from growth-controlled SMPT to dissolution-controlled SMPT due to the irruption of growth front into the high concentration region. Even after the chiral crystal covers the entire surface of the achiral crystal, a very thin layer may exist between the chiral crystal and the achiral crystal and might mediate the interchange of building components as proposed by Boerrigter *et al.*. (Fig. 4.17 and Fig. 4.18) [7]. They have performed *in-situ* microscopic observation of polymorphic transformation which occurs in Steroid 7αMNa crystal in solution using polarized-light microscopy. Their observation has shown that a stable polymorph nucleated on a metastable polymorph spreads along with the mestastable crystal. Moreover, they have shown that the rate of transformation varied depending on the solvent surrounding a crystal of initial phase, implying that a thin solution layer exists between the interfaces of the metastable crystal and the stable crystal as shown in Fig. 4.18 **B**. Thin solution proposed by them possibly exists also in the current system.

  A significant aspect of the approach-facilitated SMPT in the chiral symmetry breaking is the inheritance of chirality. In contrast with MT, the resulting enantiomorph generated through approach-facilitated SMPT is strongly directed by the handedness of the crystal that "approached", meaning that chirality is amplified when a chiral crystal "approached". Once growth front of the chiral crystal irrupts into a high concentration region surrounding the vicinity of the achiral crystal, the chiral crystal grows over the

surface of the achiral along the high concentration region since the growth rate instantly significantly overcomes the dissolution rate.
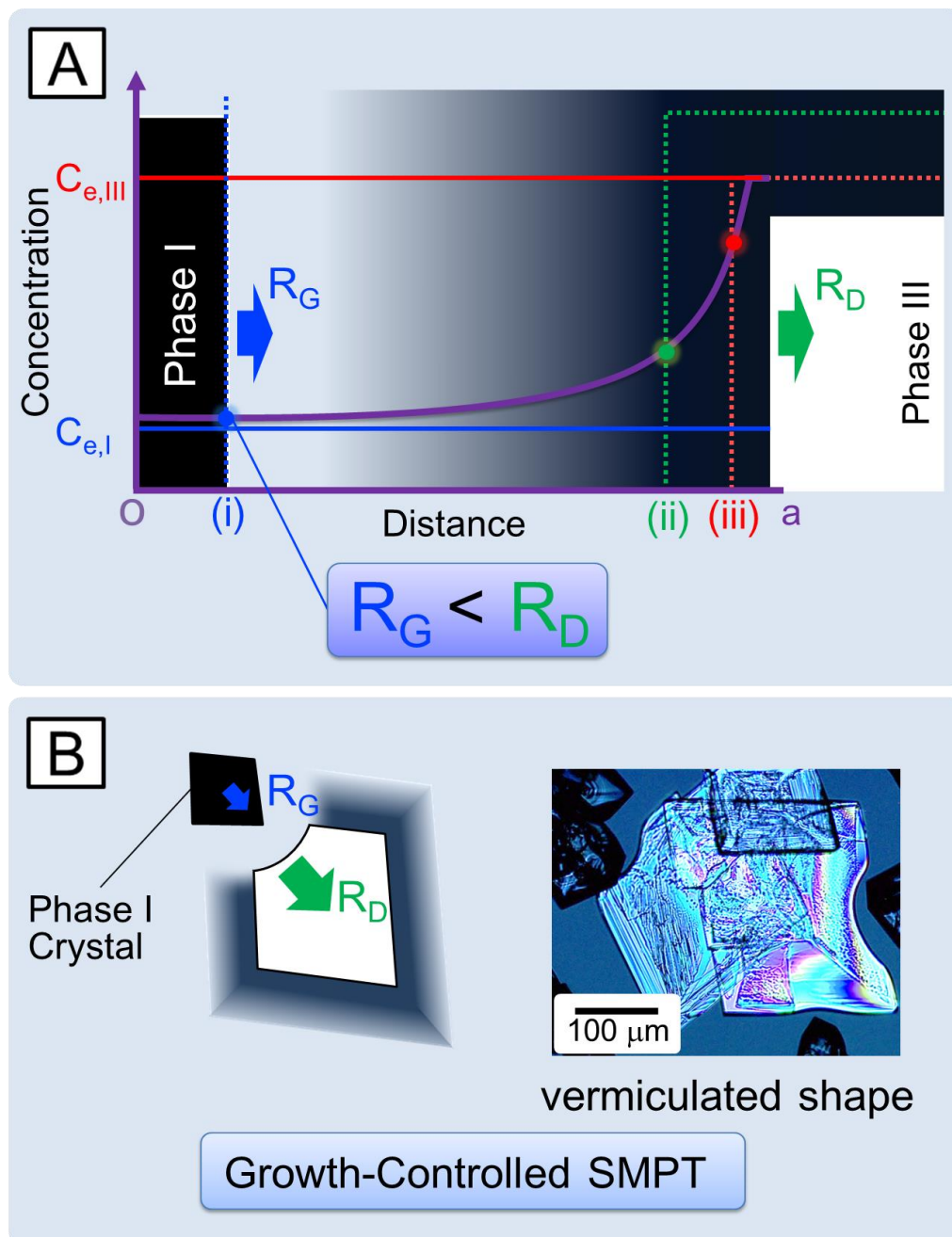
Fig. 4.14 The relationship between the growth rate of stable phase I and the dissolution rate of metastable phase III in the situation (i) where the growth front of a phase I crystal is positioned at far-from the interface of the phase III crystal. **A** Schematic illustration showing the positional relationship between the crystal surface of the phase I and the crystal surface of phase III and interfacial concentration of phase I crystal. **B** The crystal shape of phase III resulting from the relationship between the growth and dissolution rate.
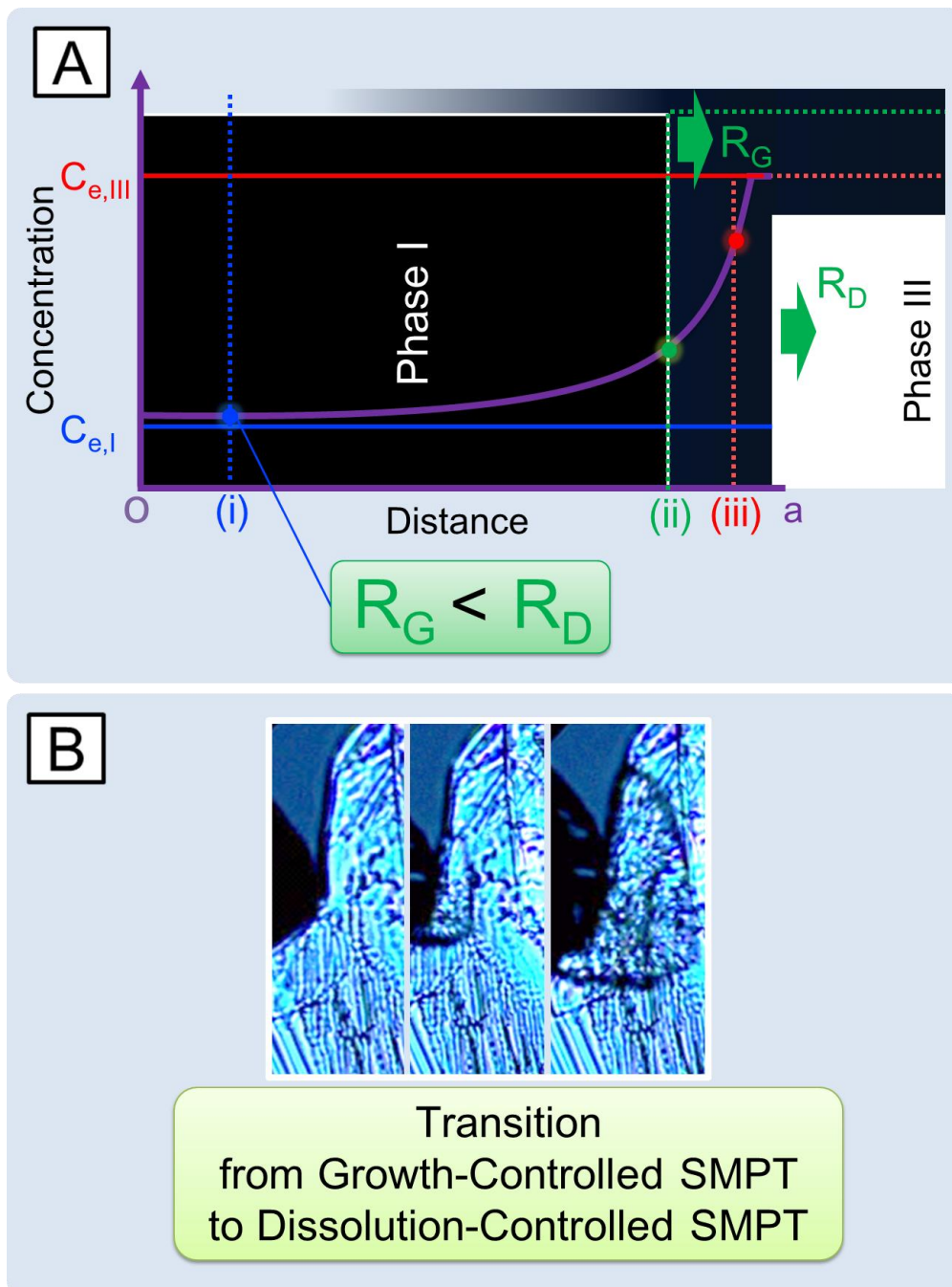
Fig. 4.15 A The relationship between the growth rate of the chiral phase I and the dissolution rate of achiral phase III in the situation (ii) where the growth front of the chiral phase I is at a specific position between the position of the situation of (i) and the situation (iii) **B** a polarized-light micrograph which corresponds to the situation (ii).
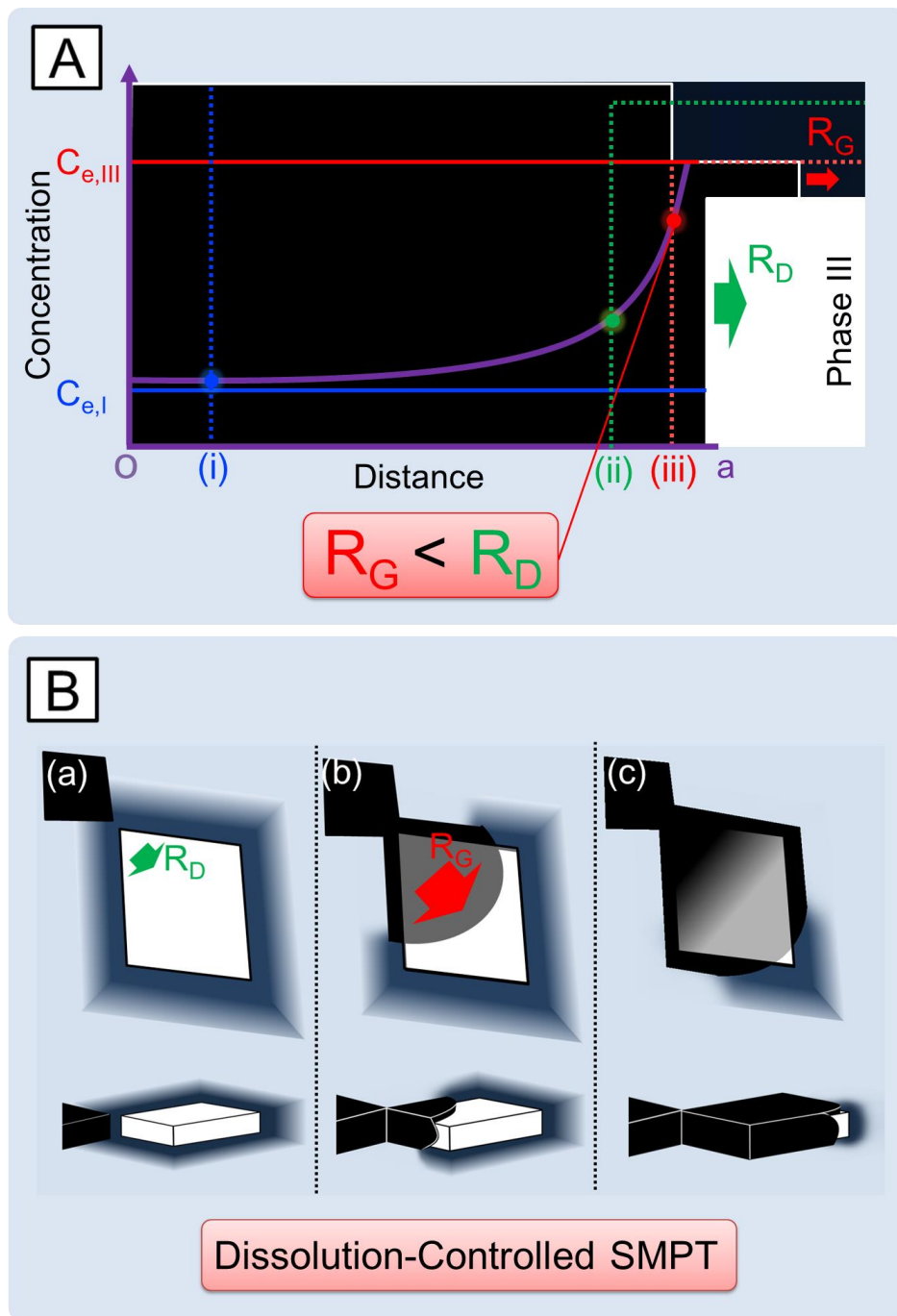
Fig. 4.16 A The relationship between the growth rate of phase I and the dissolution rate of phase III in the situation (iii) where the growth front of the phase I crystal is at the vicinity of the surface of the achiral phase III crystal (upper image). As a consequence of higher growth rate than the dissolution rate, the crystal of phase I is expected to growth over the surface of phase III crystal preferentially along with highly supersaturated thin layer surround the crystal surface of the phase III. **B** illustration showing time evolution of crystal shape estimated from the relationship between the growth rate of the phase I crystal and the dissolution rate of the phase III crystal.

Fig. 4.17 Schematic illustration of dissolution/precipitation mechanism after phase I crystal grew over the surface of phase III: Left illustrations boxed by the pink square shows the geometry of crystals when the phase I crystal grew over the surface of the phase III crystal after the growth front of the cubic crystal irrupts into the high concentration region surroun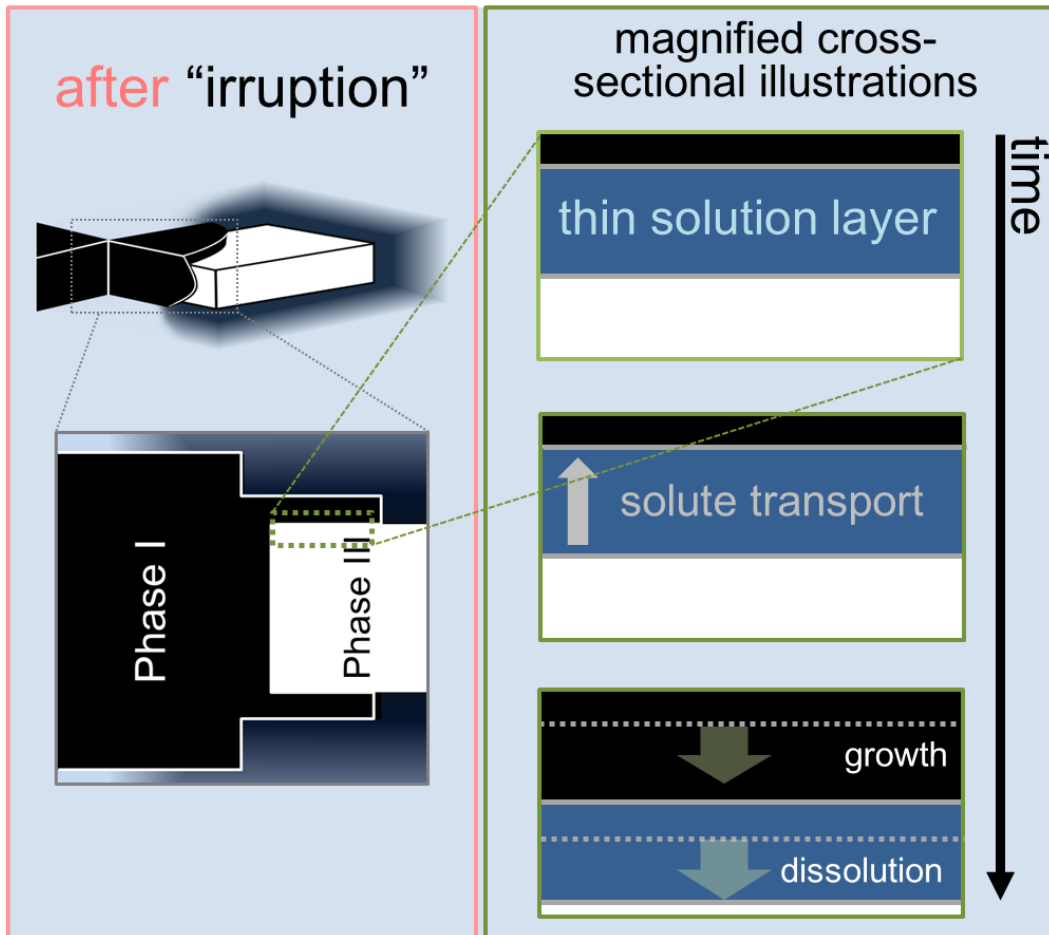ding the phase III crystal. Right illustrations boxed by the green square are magnified illustrations of interfaces between the phase I crystal and the phase III crystal at that time, and these illustrations shows change of the interfaces with time. A thin solution layer possibly exists between the two surfaces, and mediates an interchange of building units between the two crystals. The dissolution/precipitation possibly proceeds through the thin solution layer [7].
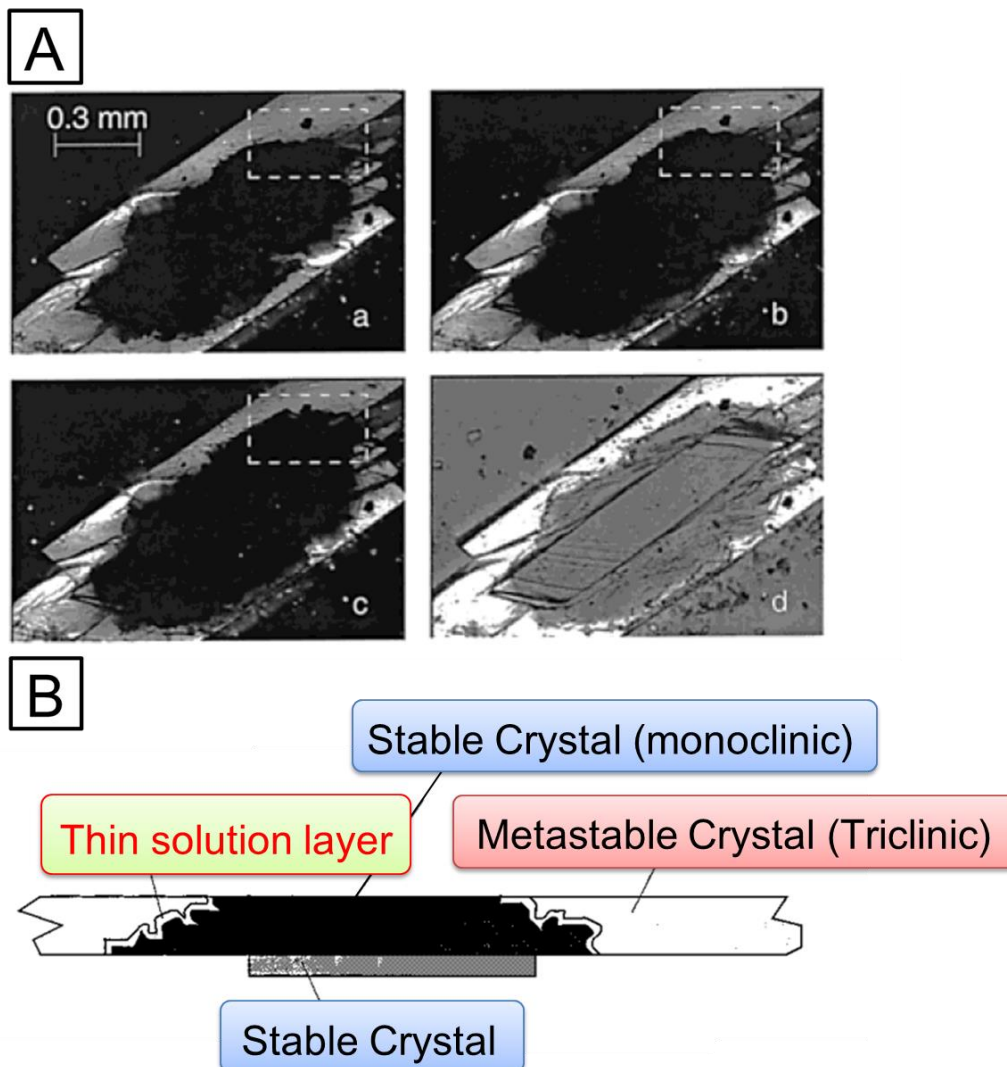
Fig. 4.18 A Polarization micrographs of the transition of the mestastable crystal (triclinic) into stable polymorphs modification (monoclinic) at t = 0 (a), 10 (b), and 20 min (c). In d, one of the polarization filters was turned a few degrees out of its extinction orientation. The bright colored crystal is the metastable crystal and the dark colored crystal is the stable crystal. It can be seen from the dotted square that the stable crystal spreads along with the metastable crystal with time. **B** Schematic representation of the hypothetical position of the original crystal and the epitaxially nucleated crystal on top of it. The proposed solution layer proceeds through the crystal transforming the triclinic into the monoclinic phase.

4.5 Summary of Chapter 4

Process of polymorphic transformation from the achiral phase III to chiral phase I in solution and in air were intensively examined using PLM. The findings revealed in this chapter are summarized below.

- The *in-situ* observation has revealed that achiral phase III crystal transforms into chiral phase I crystal via two kinds of polymorphic transformations, which are solid-solid structural transformation and solvent-mediated phase transformation.
- Two kinds of solid-solid structural transformation have been observed. One of them is the direct transformation from the achiral Phase III to chiral Phase I. On the other hand, the other, stimuli-induced structural transformation, is the transformation from the achiral phase III to chiral phase I intermediated by a transient metastable structure.
- The structural transformation intermediated by the transient metastable structure possibly follows the Meyer's deformation model. The transient structure which appears during the stimuli-induced structural transformation may correspond to the transient structure predicted by the Meyer's deformation model. In this case, chirality emerges during the deformation from the transient structure to chiral phase I.
- The transient crystal may correspond not only to the transient structure predicted by the Meyer's model but also to Phase II, which is second most unstable phase in $NaClO_3$ melt growth, which appears by kinetic trapping.
- In the two-step deformation intermediated the transient structure, chirality emerges through deformation from the transient structure to chiral phase I. The process deforms racemic structure composed by chiral octahedral structure outlined by sodium atoms to chiral cubic structure.
- In-situ observation showed that the solution-mediated phase transformation of an achiral crystal is remarkably facilitated by approaching to a chiral crystal. Moreover, the enantiomorph resulting from the contact-facilitated SMPT is found to be the same enantiomorphs of the chiral crystal approached certainly. Namely, chirality is found to be inherited by the approach-facilitated SMPT.
- The approach-facilitated SMPT was rationalized by a transition of rate-controlling process in SMPT, which is a transition from growth-controlled SMPT to dissolution-controlled SMPT. In growth-controlled SMPT, the growth rate of a chiral crystal is much smaller than the dissolution rate of the metastable, resulting that the vermiculate shape of the achiral platy crystal. On the other hand, In

dissolution-controlled SMPT, the growth rate of the stable phase largely exceeds the dissolution rate of the metastable phase, resulting the over-growth of the stable phase on the surface of the metastable crystal. These considerations successfully explained the observational facts: (1) the irruption of chiral crystal into high concentration layer, which covers over the surface of the achiral crystal, facilitates the phase transition. (2) Interference color temporarily remains even if the transition front reaches the opposite side of the metastable crystal. (3) The handedness of the chiral crystal that contacted with the metastable crystal is inherited to the resulting stable crystal.

References

[1] S. Hosoya and M. Kitamura, Miner. J. **9(2)**, (1978), 73.

[2] P. Meyer and A. Rimsky, *Acta Cryst. A*. **35,** (1979), 871.

[3] P. Meyer, S*eances Acad. Sci. Ser. C*, **274**, (1972), 843.

[4] P. T. Cardew and R. J. Davey, *Proc. R. Soc. Lond. A* **398**, (1985), 415.

[5] L. Duan and J. Z. Shu, *J. Cryst. Growth*. **223**, (2001), 181.

[6] A. A. Noyes and W. R. Whitney, *J. Am. Chem. Soc.* **19(12)**, (1897), 930.

[7] S. X. M. Boerrigter, C. J. M. van den Hoogenhof, H. Meekes, P. Bennema and E. Vlieg, *J. Phys. Chem. B* **106**, (2002), 4725.

CHAPTER 5
CRYSTALLIZATION PATHWAY TO FORM NaClO$_3$ CHIRAL CRYSTAL AND CONCEIVABLE SCENARIO OF CHIRAL SYMMETRY BREAKING

5.1 Brief Introduction

The previous chapters have shown the existence of achiral metastable crystal which acts as a precursor of chiral crystals and the polymorphic transformations by means of *in-situ* microscopic observation. This chapter summarizes these observational facts and proposes the novel formation pathway of NaClO$_3$ chiral crystal. In addition, this chapter also discusses a conceivable role of the achiral precursor on chiral symmetry breaking in NaClO$_3$ crystallization.

5.2 Nucleation Pathway of NaClO$_3$ Chiral Crystallization from an Aqueous Solution

Let the author overview the findings revealed in the previous chapters before the current formation pathway of NaClO$_3$ chiral crystal is introduced. In the chapter 2, the *in-situ* polarized-light microscopic observation has revealed that the crystals of non-cubic unknown phase appears prior to the formation of chiral cubic crystal during the early stage of crystallization from an aqueous solution. The chapter 3 has shown that the unknown phase is achiral monoclinic phase, which is identical to metastable phase III seen in NaClO$_3$ melt growth, and the solubility of the achiral crystal is 1.6 times higher than that of chiral cubic phase, thus indicating the achiral phase is metastable phase. The chapter 4 has shown that the achiral metastable crystal that appeared in an aqueous solution transforms into chiral stable crystal by two kinds of phase transformations, which are solid-solid structural phase transformation (SSPT) and approach-facilitated solution-mediated phase transformation (approach-facilitated SMPT). Whereas the SSPT yields both enantiomorphs in equal probability, the SMPT is instantly induced by the approach of a chiral cubic crystal with an achiral crystal and yields the same enantiomorph as the enantiomorph that contacted with the achiral crystal.

The results described in previous chapters imply that the formation process of NaClO$_3$ chiral crystal from an aqueous solution probably follow the pathway described in Fig.

5.1. The nucleation of the achiral metastable phase III precedes the formation of stable chiral cubic phase I at the earliest stage of the nucleation because of the energy gain originating from relatively lower surface free energy. The surface free energy of a metastable phase is generally lower than that of the stable phase because the interatomic binding force which constructs a metastable lattice is relatively weaker than that constructing a stable lattice as inferred by the fact that the enthalpy of a metastable phase is higher than that of a stable phase. Moreover, the fact that the solubility of the achiral phase is 1.6 times higher than that of the chiral phase indicates large difference in enthalpy between the two phases, thus allowing us to expect the large difference in the surface free energy between the two (the achiral phase has largely lower surface free energy.). Since the activation energy barrier for homogeneous nucleation becomes lower as the surface free energy becomes lower in accordance with thermodynamic description of classical nucleation theory, the achiral phase is much kinetically accessible than the chiral phase. Therefore, the formation of achiral crystal as precursor is reasonable in the case that the solution is supersaturated with respect to the achiral phase. If nucleation phenomena follow the CNT, the formation pathway should be valid only when the concentration of a solution excesses the solubility value of the achiral phase. However, as shown in Appendix 1, the achiral crystal may form simultaneously with chiral crystal and independently of their respective solubility values in nanoscale, which is the earliest stage of nucleation, against the CNT. Therefore, the formation pathway that the author proposed has a possibility to hold even for the crystallization from the solution slightly supersaturated with respect to the chiral phase but under-saturated with respect to the achiral phase. Moreover, as pointed out by Navrotsky, the metastable polymorph tends to become stable when the particle size is sufficiently small [1] (Fig. 5.2), thus allowing us to imagine that the achiral crystalline cluster forms at the earliest stage of crystallization and intermediates the formation of chiral crystal even in the solution slightly supersaturated with respect to the chiral crystal. The reason why the achiral crystal was not able to be detectable in slightly supersaturated solution under PLM observation might be short lifetime and the smallness of the achiral crystalline nuclei. Although time-resolved atomic scale investigation of the nucleation process is necessary to elucidate the actual nucleation pathway and the investigation is beyond this thesis, here let the author concludes that the achiral phase acts as the precursor of the chiral phase, which intermediates the formation of chiral crystal, by analogy of the non-classical pathway involving multiphase (see Appendix 1). In what follows, the achiral crystal is assumed to form as the precursor of the chiral crystal in
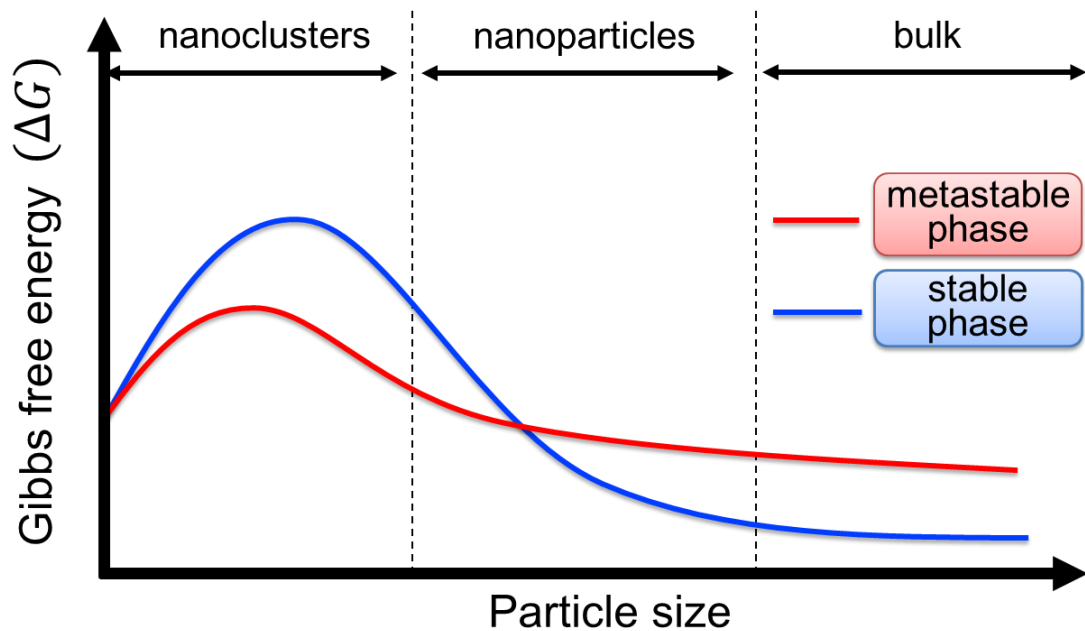
any conditions.

Fig. 5.3 is the comparison between the previous study and the current study in formation pathway of $NaClO_3$ chiral crystal from an aqueous solution. The difference is the stage in which chirality emerges and the handedness is determined. In previous thought, the handedness of crystal is already determined before primary nucleation stage, that is, the handedness is determined during clustering process. On the other hand, the current thought suggests that the crystal handedness is not determined at the primary nucleation stage (newborn crystals are ambidextrous!) but the stage of polymorphic transformation.

After the formation of achiral precursors, achiral precursor presumably transforms into chiral crystal by either of SSPT, which generates both enantiomorph in equal probability, or approach-facilitated SMPT, which is induced by the approach of achiral crystal and generates the same enantiomorph as the chiral crystal that approached. Bifurcation of the two transformations may be determined by whether an achiral crystal approached to a chiral crystal. If it does not approach, the transformation may proceeds by the SSPT, On the other hand, the approach-facilitated SMPT occurs if the achiral crystal approached enough to induce the approach-facilitated SMPT. Since determination of the resulting enantiomorph depends on these transformations, the pathway which achiral crystals pursue is possibly important for the chiral symmetry breaking in $NaClO_3$ crystallization. The next section discusses the role of the transformation on the chiral symmetry breaking on the basis of the pathway the author proposed.
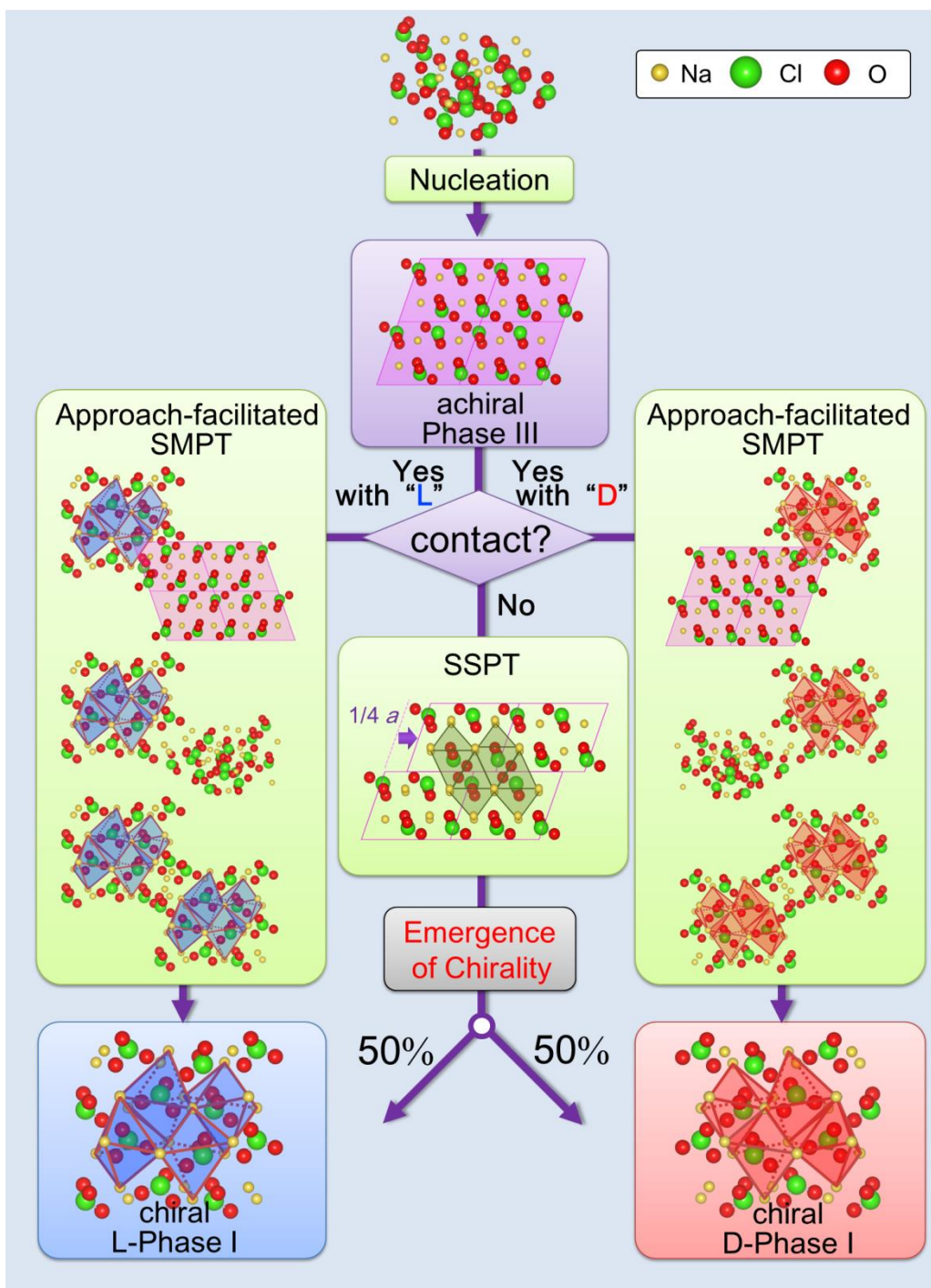
Fig. 5.1 The formation pathway of $NaClO_3$ chiral crystal via achiral crystalline precursor in crystallization from an aqueous solution.

Fig. 5.2 Schematic representation (free energy and particle size axes do not have numerical values) of energetics of two different polymorphs as a function of particle size. Difference in critical nucleus size and activation energy and crossover in phase stability of nanoparticles are shown. This schematic is adopted from Ref. 1 (partially modeified)
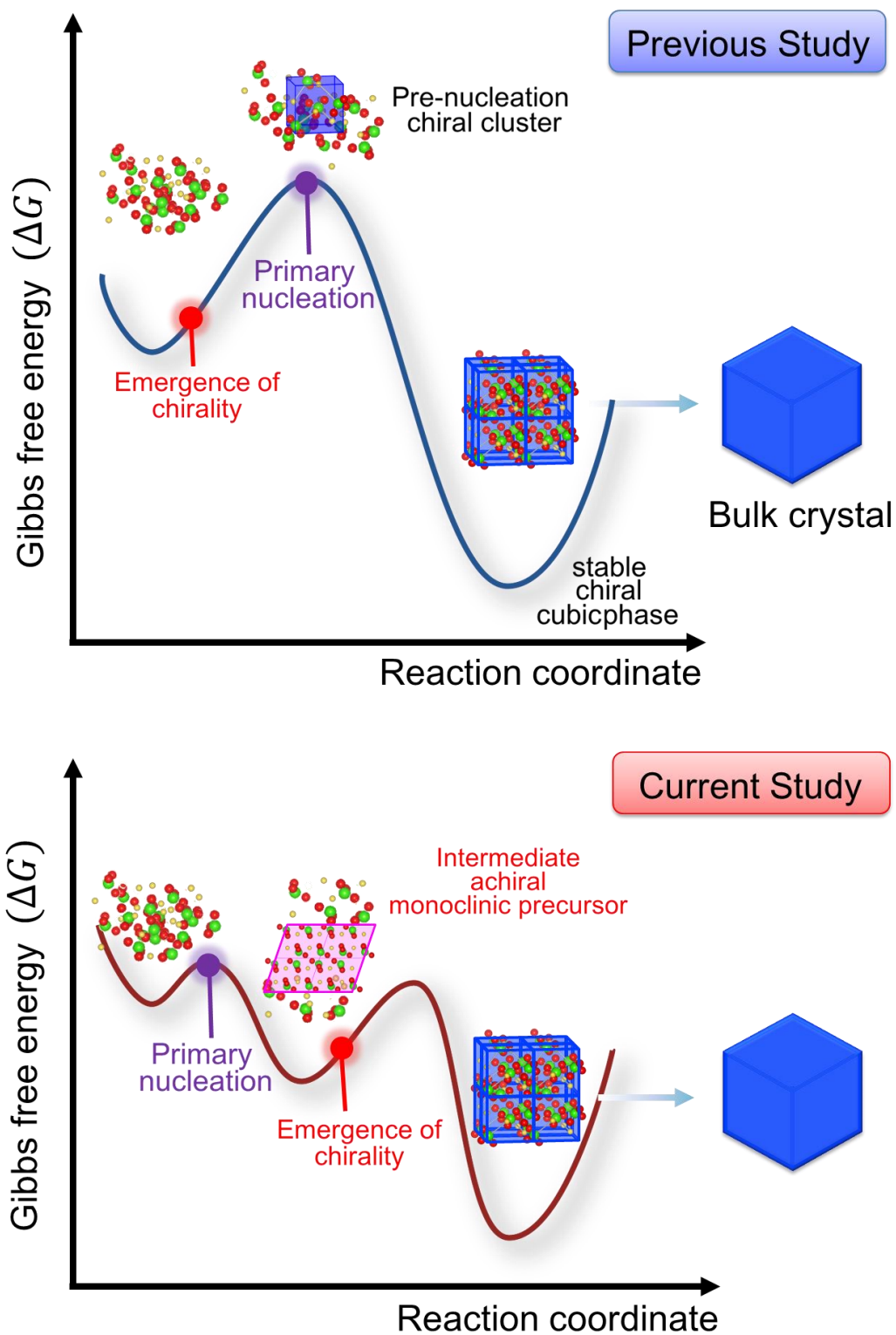
Fig. 5.3 Comparison of formation pathway of $NaClO_3$ chiral crystal from an aqueous solution between the previous study and the current study. Upper schematic shows the previous thought and lower schematic shows the pathway proposed in this study.
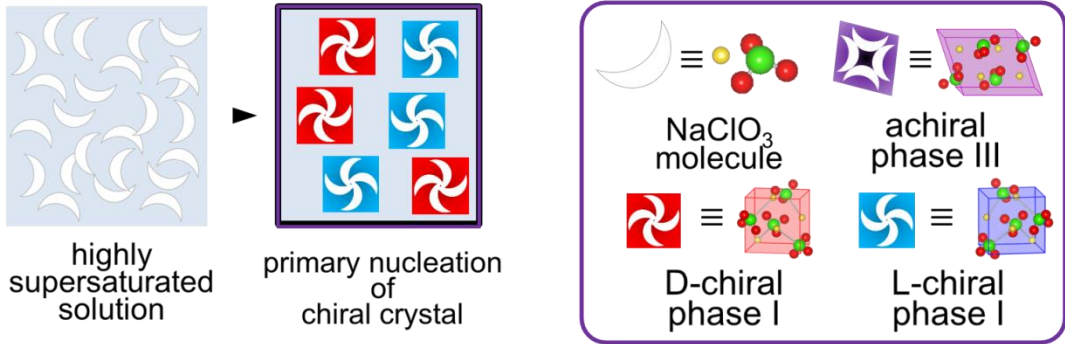
5.3 Conceivable Role of Achiral Metastable Crystals on Chiral Symmetry Breaking in NaClO₃ Crystallization and Scenario for Chiral Symmetry Breaking

5.3.1 The Scenario for the Chiral Symmetry Breaking in NaClO₃ Crystallization under Far-From-Equilibrium Condition
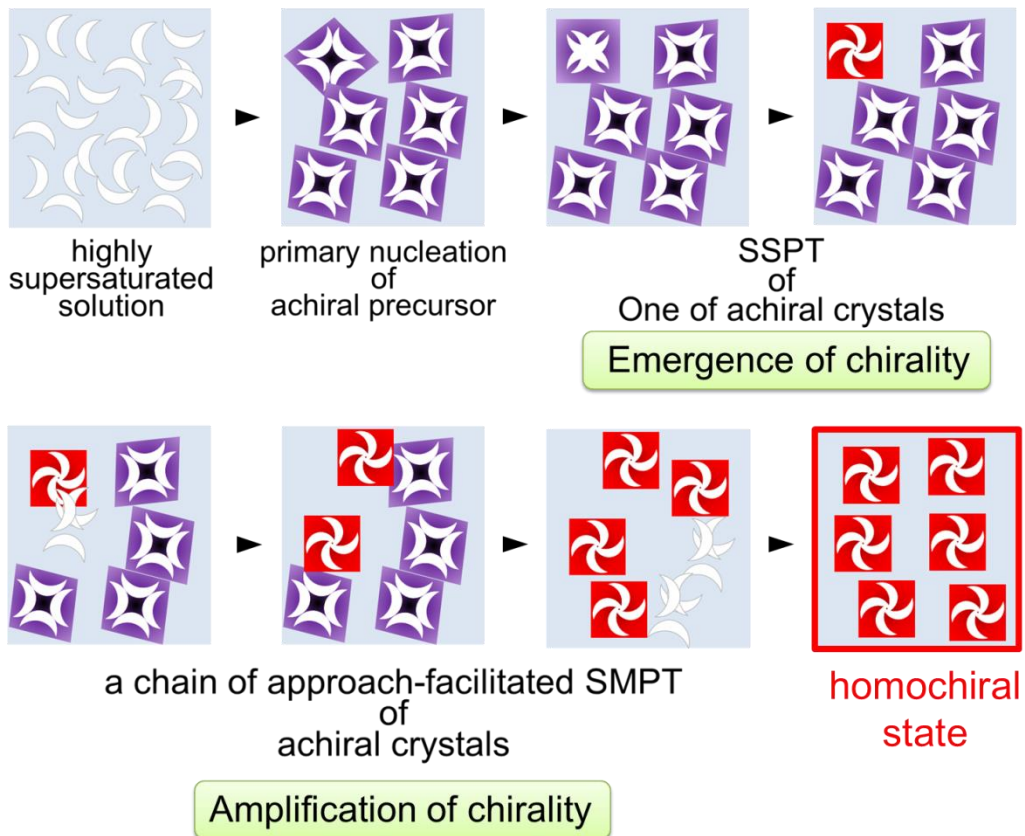
This section discusses what kind of scenario is conceivable to rationalize the experiments of chiral symmetry breaking that cannot be explained by the secondary nucleation scenario [2-12] by taking the formation pathway of chiral crystal described above into account. Firstly, the author considers the experiment of the chiral symmetry breaking under far-from equilibrium, especially, the Viedma's experiment [13]. In the Viedma's experiment, highly supersaturated metastable solution being ready to generate crystal (supersaturation is approximately 58%) was rapidly stirred, leading to catastrophic primary nucleation. According to the pathway that previously considered, the catastrophic primary nucleation should generate equal population of the both enantiomorphs, resulting in the absence of a specific one-single "Eve" crystal suggested in the secondary nucleation scenario. Namely, the reason why the secondary nucleation scenario failed to explain the Viedma's experiment is that initial high supersaturation state causes high rate of primary nucleation of chiral crystal. Owing to the high rate, the system should rapidly racemize. However, assuming that the formation of achiral crystal as precursor of chiral crystals is inevitable process, the initial high supersaturation state may be insufficient for catastrophic primary nucleation of chiral crystals. This is because that the high supersaturation state presumably generates kinetically-accessible achiral crystals and the generation of the achiral crystals reduces the degree of surpresaturation. As a consequence, catastrophic primary nucleation of chiral crystal was suppressed. Then, assuming that the rate of martensitic transformation is significantly higher than the rate of primary nucleation of chiral crystal under the supersaturation condition that is lowered by the generation of achiral crystals, SSPT in one of the achiral crystals presumably yields the one-single "Eve" crystal. Once the "Eve" crystal forms by the SSPT, the "Eve" crystal may contact with the other achiral crystals owing to the effect of rapid stirring. This leads to a chain of approach-facilitated SMPT. Since the SMPT yields the same enatiomorph as the "Eve" crystal, one-single handedness is expected to dominate the opposite handedness (Fig. 5.4). The scenario described above can explain the chiral symmetry breaking even for Viedma's experiment. Namely, the role of the formation of achiral crystal is to suppress the primary nucleation of chiral crystal by keeping the degree of supersaturation moderate.

Moreover, the SSPT and the approach-facilitated SMPT may be responsible for the emergence of chirality and amplification of one-single handedness, respectively. According to the Frank's statement, achievement of homochiral state requires following three processes; (1) the emergence of chiral imbalance, that is, the emergence of chirality (2) the amplification of the same handedness (3) mutual antagonism, that is, inhibition of the opposite handedness [14]. In the scenario described above, the SSPT and approach-facilitated SMPT are possibly responsible for (1) the emergence of chirality and (2) the amplification of the same handedness, respectively. If the inhibition process in the scenario is elucidated, the scenario will become comparable to the secondary nucleation scenario. The scenario based on the achiral-chiral polymorphic transformation gives an insight not only for the Viedma's experiment but also for other experiments under far-from equilibrium condition. Bearing in mind that El-Hachemi's experiment, where primary nucleation was induced by withdrawal of solvent from a reflux flow of a boiling aqueous solution [15,16], attains high degree of supersaturation, the scenario of the current study may be valid also for the experiment. Furthermore, the scenario could also be applied to the Kondepudi's seminal experiment that commonly starts a relatively high supersaturation values. Therefore, it follows that the formation of achiral phase cannot be neglected. The author advocates that it is necessary to reconsider the mechanism of chiral symmetry breaking from the view point of local supersaturation and the existence of the achiral metastable phase. Especially, further investigation focusing on the inhibition process is necessary.

The case of conventional formation pathway of chiral crystal

highly supersaturated solution → primary nucleation of chiral crystal

NaClO$_3$ molecule ≡

achiral phase III ≡

D-chiral phase I ≡

L-chiral phase I ≡

The case of current formation pathway of chiral crystal

highly supersaturated solution → primary nucleation of achiral precursor → SSPT of One of achiral crystals

Emergence of chirality

a chain of approach-facilitated SMPT of achiral crystals → homochiral state

Amplification of chirality

Fig. 5.4 Schematic illustrations comparing the conceivable scenario of the Viedma's crystallization experiment on the basis of the formation pathway of chiral crystal that previously considered and the pathway that proposed by the current study. Upper schematics indicate the scenario taking the pathway previously considered into account. In this case, equal population of the both enantiomorph generates during the catastrophic primary nucleation event, leading to racemic state, where the equal numbers of two enantiomorphs precipitate. Lower schematics indicate the scenario taking the pathway proposed in the current study into account. In this case, homochiral state can be achieved with the assumptions (1) The formation of achiral crystal as precursor of chiral crystal is inevitable process for the formation of chiral crystal. (2) The rate SSPT is significantly lower relatively to approach-facilitated SMPT. Firstly, achiral crystals appear in highly supersaturated solutions by primary nucleation. Secondly, one of the achiral crystals transforms into a chiral crystal by SSPT. Thirdly, the handedness of the chiral crystal is generated by SSPT and is amplified by approach-facilitated SMPT. Here, stirring promotes the contact of crystals and hence, approach-facilitated SMPT. Consequently, the handedness that emerged through SSPT dominates the system. This scenario is analogous to the so-called secondary nucleation scenario in the point that the handedness that first appeared in the system is amplified as consequence of kinetic competition between emergence of chirality and amplification of chirality. In the secondary nucleation scenario, the emergence and amplification of chirality corresponds to the primary nucleation of chiral crystals and its fragmentation, respectively. On the other hand, in the achiral–chiral polymorphic transformation, the two processes correspond to SSPT and contact-facilitated SMPT, respectively.

5.3.2 Conceivable Role of Achiral Metastable Crystal on Chiral Symmetry Breaking under Quasi-Equilibrium Condition

The achiral crystal probably forms during the process of chiral symmetry breaking under far-from equilibrium since the system presumably attains high degree of supersaturation. On the other hand, the achiral crystals presumably do not form during the process of chiral symmetry breaking under quasi-equilibrium condition because the presence of seed crystals and continuous stirring do not allow solution to attain high supersaturation. However, if we assume that pre-nucleation clusters of the achiral phase do form even in the solution slightly supersaturated with respect to the chiral phase as described in the appendix 1, where *in-situ* TEM observation of the earliest stage of nucleation from an ionic solution of $NaClO_3$ has shown, the achiral phase has a possibility to play a role on the effective deracemization during the experiments as following. Blanco *et al.* have pointed out that the Viedma deracemization can be interpreted as a consequence of the presence of distribution of cluster size below and above the critical size [17]. According to their study, the chiral crystals whose size are below the critical nucleation size contributes (here we call this crystal as prenucleation cluster) to inhibition process of the minor handedness, on the other hand, the chiral crystals whose size are above the critical nucleation size (here we call this crystal as postnnucleation cluster) contribute to chiral autocatalytic process. Both the inhibition process and chiral autocatalytic process are necessary to achieve chiral symmetry breaking, and thus, the both the prenucleation and postnucleation clusters must exist in adequate proportion to attain homochiral state. Namely, achievement of homochiral state requires adequate and moderate supersaturation because overmuch high supersaturation leads to depletion of the prenucleation clusters, on the other hand, overmuch low supersaturation leads to depletion of the postnucleation clusters. The formation of achiral cluster may keep the supersaturation value of solution near constant and might help to be effective deracemization.

5.4 Summary of Chapter 5

This chapter showed the formation pathway of $NaClO_3$ chiral crystals estimated from the observational facts described in the previous chapters and discuss the conceivable scenario explaining the chiral symmetry breaking experiments that cannot be rationalized by the secondary nucleation scenario. The discussion including speculations provided in this chapter is summarized below.

• At the earliest stage of $NaClO_3$ chiral crystallization from an aqueous solution, a nucleus of achiral metastable phase III would preferentially form because of kinetic trapping as precursor of stable chiral phase I crystal. Two kinds of transformations from the achiral precursor into chiral crystal, which are SSPT and approach-facilitated SMPT, would follow the formation of the achiral precursor. Bifurcation of the two transformations may be determined by whether an achiral crystal approaches to a chiral crystal. If it does not, the transformation possibly proceeds by the SSPT. On the other hand, if achiral crystal approaches to a chiral crystal, the approach-facilitated SMPT is preferentially induced.

• Chiral symmetry breaking under far-from equilibrium in the experiments that cannot be explained by secondary nucleation scenario because of initial high supersaturated state could be interpreted as a consequence of the reduction of supersaturation value caused by the formation of the achiral precursor. In contrast to the secondary nucleation scenario, in which the emergence of chirality and amplification of one-single handedness are ascribed to primary nucleation of achiral crystal and secondary nucleation from the "Eve" crystal, the "Eve" crystal was generated by SSPT of achiral precursor and the handedness of the "Eve" crystal is amplified by a chain of approach-facilitated SMPT in the scenario taking the achiral-chiral transformation into account. Namely, SSPT and approach-facilitated SMPT would be responsible for the emergence and amplification of chirality, respectively.

• In chiral symmetry in for-from equilibrium condition such as Viedma deracemization, the formation of achiral crystal might play a role to help effective deracemization by keeping supersaturation value of the solution at near to constant and moderate.

References

[1] A. Navrotsky, *Proc. Natl. Acad. Sci.* **101(33)**, (2004), 12096.

[2] D. K. Kondepudi, J. R. Kaufman and N.Singh, *Science* **250**, (1990), 975.

[3] Y. Song, W. Chen and X. Chen, *Cryst. Growth Des.* **8**, (2008), 1448.

[4] J. M. McBride and R. L. Carter, *Angew. Chem. Int. Ed.* **30**, (1991), 293.

[5] D. K. Kondepudi, K. L. Bullock, J. A. Digits, J. K. Hall and J. M. Miller, *J. Am. Chem. Soc.* **115**, (1993), 10211.

[6] R. Y. Qian and G. D. A. Botsaris, *Chem. Eng. Sci.* **52**, (1997), 3429.

[7] R. Y. Qian and G.D. A. Botsaris, *Chem. Eng. Sci.* **53**, (1998), 1745.

[8] T. Buhse, D. Durand, D. Kondepudi, J. Laudadio and S. Spilker, *Phys. Rev. Lett.* **84**, (2000), 4405.

[9] R.Y. Qian and G.D.A. Botsaris, *Chem. Eng. Sci.* **59**, (2004), 2841.

[10] D. K. Kondepudi and C. Sabanayagam, *Chem. Phys. Lett.* **217**, (1994), 364.

[11] B. Martin, A. Harrington and X. l. Wu, *Phys. Rev. Lett.* **77**, (1996), 2826.

[12] P. Cintas, *Cryst. Growth Des.* **8**, (2008), 2626.

[13] C. Viedma, *J. Cryst. Growth* **261**, (2004), 118.

[14] F. C. Frank, *Biochim. Biophys. Acta* **11**, (1953), 459.

[15] Z. El-Hachemi, J. Crusats, J.M. Ribó and S. Veintemillas-Verdaguer, *Cryst. Growth Des.* **9**, (2009), 4802.

[16] Z. El-Hachemi, J. Crusats, J.M. Ribó, J.M. McBride and S. Veintemilla-Verdaguer, *Angew. Chem. Int. Ed.* **50**, (2011), 2359.

[17] C. Blanco, J. Crusats, Z. El-Hachemi, A. Moyano, S. Veintemillas-Verdaguer, D. Hochberg and J. M. Ribó, *Chemphyschem.*, **14**, (2013), 3982.

CHAPTER 6
POSSIBLITY OF CHIRALITY CONTROL IN NaClO$_3$ CRYSTAL BY INDUCING ACHIRAL-CHIRAL POLYMORPHIC TRANSFORMATION BY CIRCULARLY POLARIZED LIGHT IRRADIATION

6.1 Brief Introduction

In the previous chapter, the author has shown the process of emergence of chirality in the course of NaClO$_3$ chiral crystallization from an aqueous solution. The series of the *in-situ* microscopic observations of the early stage of the crystallization implied that NaClO$_3$ chiral crystal forms through the solid-solid phase transformation (SSPT) of an achiral crystalline precursor. Therefore, the handedness of the chiral crystal is presumably determined during the SSPT, impling that the resulting handedness of the chiral crystal can be controlled by applying chiral perturbation during the SSPT. In this chapter, circularly polarized light (CPL), which possesses chirality and asymmetrically interacts with a chiral matter, was applied as chiral perturbation during the transformation to control the handedness by means of nonphotochemical laser induced crystallization. It will be shown that the nonphotochemical laser induced crystallization using CPL has a possibility to control the handedness of NaClO$_3$ chiral crystal.

6.2 Introduction

As shown in the chapter 1, control of crystal handedness has a great significance not only for the field of pharmaceutical industry but also for material science of spintronic devices. Furthermore, clarification of mechanism of chirality control may give implications for the origin of biohomochirality. Circularly polarized light (CPL), which is intrinsically chiral itself, has been widely applied to direct the handedness of chiral matter in the field ranging from liquid crystal [1] to asymmetric synthesis of chiral compounds [2] because CPL asymmetrically interacts with chiral compounds. The asymmetric interaction between the CPL and chiral compounds can be detected as "Circular Dichroism (CD)". Circular dichroism is the property that chiral compounds have distinct absorption coefficient for CPL depending on its handedness. CPL is the light whose electrical field vector periodically orbits a circular path in contrast to that of

linearly polarized light (LPL) (Fig. 6.1). The mathematical descriptions of difference in these polarized lights are introduced below. Here the author considers a light propagating along the x axis in a Cartesian coordination. Since electromagnetical field along the propagating direction is zero, x and y component of electrical field vector of the light can be expressed as a sine wave written below:

$$E_y(x,t) = E_{0y}sin(kx - \omega t + \theta_y) \tag{6.1}$$
$$E_z(x,t) = E_{0z}sin(kx - \omega t + \theta_z) \tag{6.2}$$

In the case of $\theta_x = \theta_y = \theta$, Eq. (6.1) and (6.2) can be written as:

$$\boldsymbol{E}(x,t) = \boldsymbol{E}_0 sin(kx - \omega t + \theta) \tag{6.3}$$

with

$$\boldsymbol{E}_0 = (0, \boldsymbol{E}_{0y}, \boldsymbol{E}_{0z}) \tag{6.4}$$

Since $\boldsymbol{E}_0$ is constant vector, this wave oscillates along the constant direction. Such a light is called as LPL. On the other hand, in the case of $E_{0y} = E_{0z} = E_0$ and $\theta_z = \theta_y + \frac{\pi}{2}$, the electrical field can be expressed as:

$$E_y(x,t) = E_0 cos(kx - \omega t + \theta) = E_0 cos(\omega t - kx - \theta) \tag{6.5}$$
$$E_z(x,t) = -E_0 cos(kx - \omega t + \theta) = E_0 sin(\omega t - kx - \theta) \tag{6.6}$$

Then, the time variation of the electrical field at the constant point, $x_0 = -\frac{\theta}{k}$, can be written as:

$$E_y(x_0,t) = E_0 cos\omega t \tag{6.7}$$
$$E_z(x_0,t) = E_0 sin\omega t \tag{6.8}$$

Namely, the oscillation plane of electrical field rotates counter-clock wise at a constant angular velocity, ω, with time when one observes the light from the propagation direction. Such the light is called as left-handed CPL (*l*-CPL). On the other hand, when the phase of x and y components of the LPL shits conversely against *l*-CPL, it follows that the oscillation plane rotates clockwise direction. Such the light is called as

right-handed CPL (*r*-CPL). It should be noticed that LPL can be expressed as the sum of *l*-CPL and *r*-CPL whose amplitudes and wavelengths are the same. In addition, when the phase shifts from the LPL is not quarter wavelength the electrical field vector orbits ellipsoidal path. Such the light is called as elliptically polarized light (EPL). The EPL can be expressed as the sum of *r*-CPL and *l*-CPL whose amplitudes are distinct.
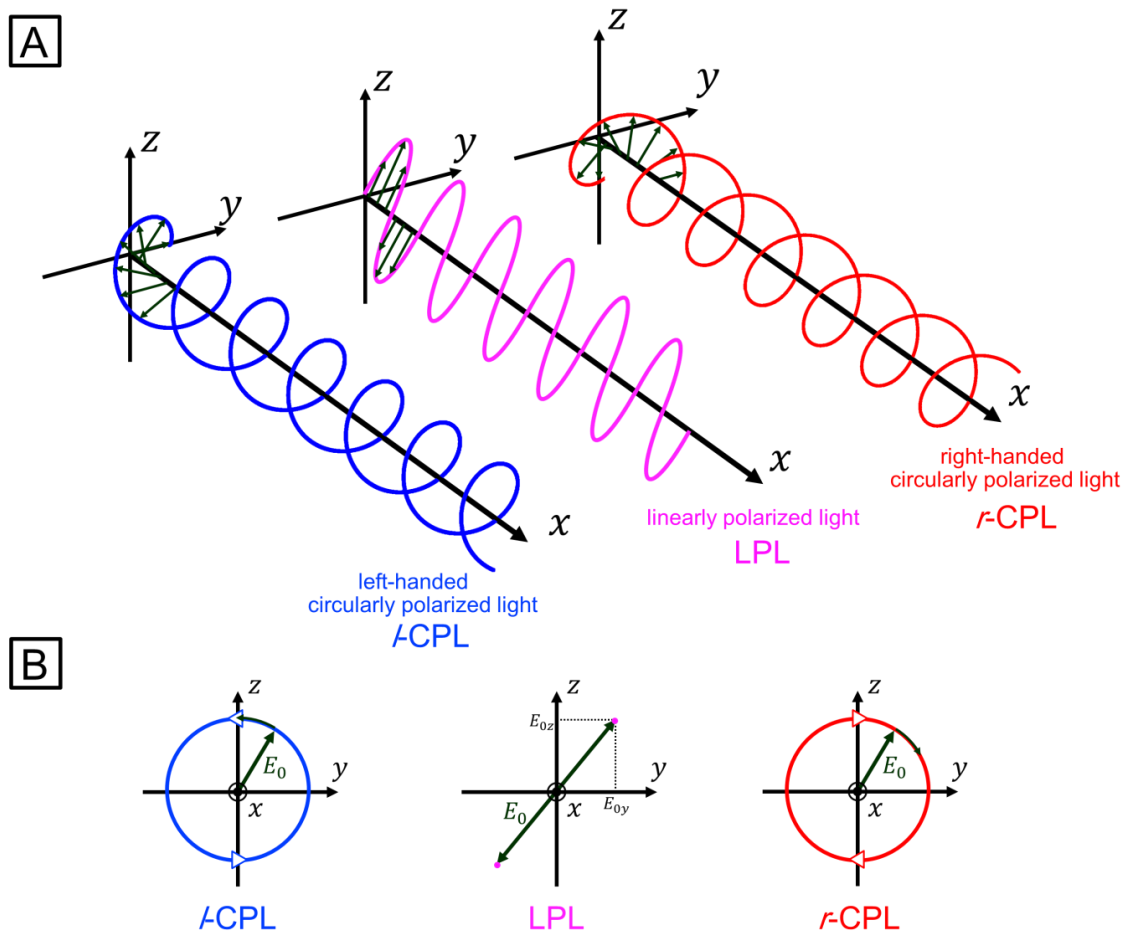
Fig. 6.1 Schematic illustrations of LPL and CPL. **A** shows trajectories of electrical field vector of *l*-CPL, LPL and *r*-CPL. In CPL, although amplitude of the electrical field vector does not change with location and time, the direction of the vector draws helical path along propagation direction. In LPL, The amplitude of the electrical field oscillates with location and time along constant direction. **B** shows projections of the trajectories of the electrical field vector onto x-y plane. The electrical field vector of *l*-CPL rotates counter-clockwise with the origin as the center and *vice versa*. On the other hand, In LPL, the direction of oscillation of the electrical field is fixed

As stated above, the circular dichroism is the difference in absorbance of CPLs and the magnitude of CD is expressed by circular dichroism absorbance, ΔA, which is the difference between the absorbance for r-CPL, ΔA_R, and that for l-CPL, ΔA_L:

$$\Delta A = A_L - A_R \tag{6.9}$$

CD is generally detected by measuring the ellipticity of the EPL resulting from transmission of LPL though a chiral medium. When LPL, which contains r-CPL and l-CPL whose amplitudes are equal, transmits a chiral medium the balance of the amplitude is lost because of CD. Consequently, the LPL is converted to EPL. The ellipticity reflects the difference in the loss of amplitude in r-CPL or l-CPL. Therefore, CD can be measured from the elliplicity. In practice, molar ellipticity is generally adopted to indicate CD as physical property. The molar ellipticity, $[\theta]$ is defined as:

$$[\theta] = 18000/4\pi log_{10} e \cdot \Delta\varepsilon \cong 3298\Delta\varepsilon \tag{6.10}$$

where $\Delta\varepsilon$ is molar circular dichroism. The molar circular dichroism is related to circular dichroism absorbance as like;

$$\Delta A = \Delta\varepsilon cl \tag{6.11}$$

where c is concentration of chiral compounds in a medium through which LPL transmits and l is length of the medium.

Direction of chirality using this asymmetric photoabsorption has been reported several systems. For instance, Kawasaki *et al.* have demonstrated that irradiation of CPL using ultrahigh pressure Hg lamp as a light source can direct the dominant handedness amplified by asymmetric autocatalytic reaction of racemic pyrimidyl alkanol [2]. They have mentioned that enantioselective photodecomposition of the racemic pyrimidyl alkanol triggered the initial chiral imbalance and subsequently the imbalance was amplified by the asymmetric autocatalysis. Additionally, Noorduin *et al.* have applied CPL irradiation to "Viedma deracemization" of racemic imine crystal.
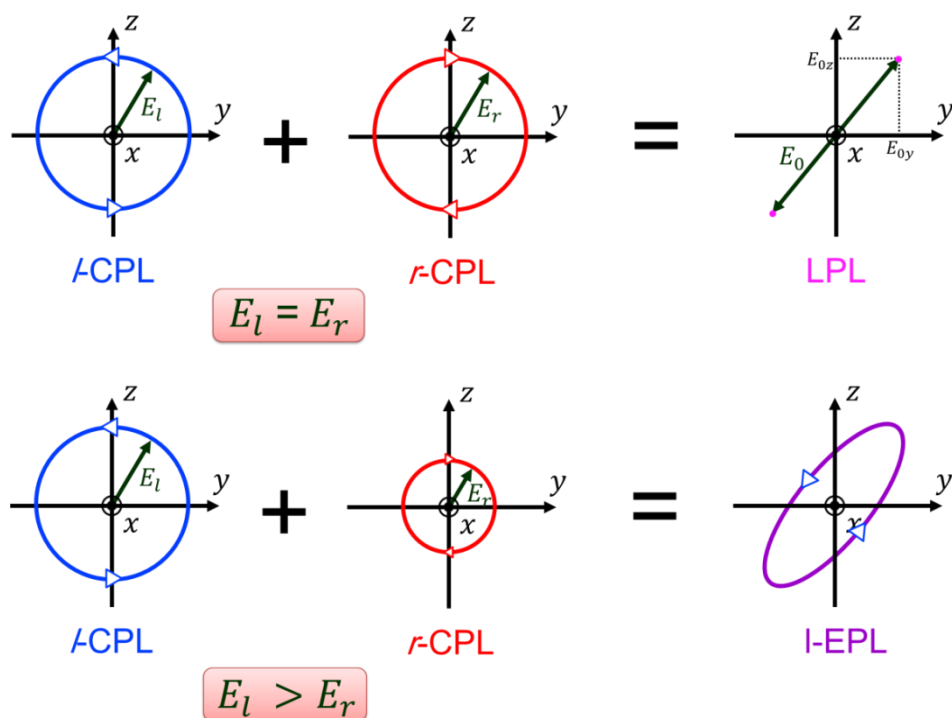
Fig. 6.2 Relationship of polarization states of light. Upper schematic shows that LPL is equal to the sum of *l*-CPL and *r*-CPL that possess the same amplitude of the electrical field. Lower schematic indicates that the sum of *l*-CPL and *r*-CPL that possess distinct amplitude produces EPL.

In this case, CPL irradiation caused asymmetric photoreaction of the imine, producing a growth inhibitor against the opposite enantiomorph. Combination of the amplification process by "Viedma deracemization" and the growth inhibitor led to CPL-directed-homochiral state [3]. Moreover, it has been reported that enantioselective amplification of chiral domain of bent-core liquid crystal was achieved by CPL irradiation during phase transition from achiral SmC$_A$ phase to chiral B$_A$ phase. As shown above, CD-based asymmetric chiroptical effect has been widely proven to have a possibility for controlling chirality.

  However, controlling the chirality in chiral crystallization by CPL irradiation still remains a challenge. Non-photohcemical laser induced crystallization (NPLIN) has been recently investigated because the method has a possibility to control polymorphs by changing the polarization of laser light. Garetz *et al.* have pioneered NPLIN in the system of urea crystallization from an aqueous solution. In their study, nucleation of

urea crystal was induced by irradiation of infrared pulsed laser to a supersaturated urea aqueous solution [4]. The induction of the nucleation was ascribed to the alignment of solute clusters, which has permanent dipole moment, along the polarization of the laser (optical Kerr effect). Subsequently, Sun *et al.* have reported that the resulting polymorph of glycine crystal can be completely controlled depending on the polarization state of laser light in a specific supersaturation range [5]. Several groups have extended the method to chiral crystallization to control crystal chirality. Although Murphy *et al.* have attempted to irradiate *r-* and *l*-CPL pulsed laser during a chiral crystallization of 4,4'-dimethylchalcone induced by evaporation of solvent of its ethyl acetate solution, they have concluded that significant chiral bias in the population of the resulting crystals was not observed [6]. Moreover, Ward *et al.* have investigated the effect of handedness of CPL on $NaClO_3$ chiral crystallization from its supercooled melt. They have shot a train of infrared CPL pulsed laser to the supercooled $NaClO_3$ melt and identified the handedness of the resulting crystals. This experiment also did not exhibit a significant chiral bias (This experiment may have a problem that the number of trials is few to evaluate the effect of the handedness of CPL). As can be seen above, NPLIN using CPL pulsed laser has not been achieved to control the handedness of crystal formed through chiral crystallization.

One conceivable reason of the failure to induce chiral bias by means of CPL-NPLIN is that the pulsed laser may act only as a trigger of nucleation from a supersaturated state, namely, the crystal formation process may not proceed under the influence of chiral CPL field owing to transient feature of pulsed laser. Indeed, NPLIN using continuous-wave (CW) focused CPL laser has been reported to exhibit chiral effect on crystallization of L-alanine from D_2O solution. Induction period for nucleation of L-alanine is reported to be different more than 3 times between *r*-CPL and *l*-CPL irradiation [7]. In the current study, the author attempts to control the handedness of $NaClO_3$ chiral crystals crystallized from an aqueous solution by inducing the SSPT of the achiral precursor under the influence of the chiral CPL field using CW laser.

6.3 Experimental

6.3.1 Sample Preparation

Supersaturated aqueous solution of $NaClO_3$ was prepared at 22°C by dissolving 30 g of $NaClO_3$ powder (>98 %, Wako) to 25 ml of ultrapure water fabricated with Direct-Q 3UV (Millipore) in a 100 ml glass beaker. The solution was then heated up to 50°C and was stirred using hotplate magnetic stirrer to dissolve the powder completely. After complete dissolution of the powder, the solution was hermetically closed and left for a week at 22°C in order to precipitate the solute that dissolving excessively. The resulting solute-solution mixture is in equilibrium at 22 °C. Namely, the supernatant of the mixture is a $NaClO_3$ aqueous solution saturated at 22°C. 6.25 μL of the saturated solution and 2.5 μL of dispersion liquid containing 10nm Ag nanoparticles whose concentration is 0.02 mg/mL were put in a hand-made crystal growth cell described below. The dispersion liquid contains citric acid, which is achiral molecule, as a stabilizer. The crystal growth cell is made by interleaving a silicone sheet with a pair of cover glasses (Fig. 6.3 **A**). The thickness of the silicone sheet is 1 mm and that of the cover glass is approximately 120 μm. The surface of the cover glass was preliminarily subjected to hydrophilic treatment using UV irradiator (Bioforce, Nanoscience). Owing to the hydrophilic surface, the liquid mixture becomes liquid thin film on the surface. The growth cell containing the liquid mixture was used for further experiments, that is, laser-induced crystallization experiments.

6.3.2 Optical Setup

Fig. 6.3 **B** shows a schematic illustration of an optical setup in the current experiment. A green laser from a CW Ti:Al_2O_3 laser (Spectra Physics, Millenia eV, λ = 532 nm) was used as light source. The laser emitted from the light source firstly passes through an optical device for control of laser intensity, which consists of a polarizing beam splitter and a half-wave plate. The laser intensity was adjusted by rotating the half-wave plate. Afterwards, Beam diameter of the light was expended from 2.3 mm to approximately 5.4 mm, which is identical to the pupil diameter of an objective lens described below, using Kepler-type beam expander constructed with two plano-convex lenses. After expansion of the beam diameter, polarization of the light was converted from linear polarization to circular polarization by a quarter wave plate. The handedness of the CPL can be switched by adjusting the angle between the plane of the LPL and the optical axis of the quarter wave plate. The CPL was introduced into an inverted optical microscope (Olympus, IX71) equipped with 60× objective lens (Olympus, UPLFN

60X, NA 0.9). Then, the CPL was introduced to the objective lens through the reflection by a Notch-Dichroic half mirror. It should be noted that the handedness of the CPL *is inverted* by the reflection. After the reflection, the objective lens concentrates the circularly polarized laser at the focal point. Ellipticity of the CPL that reflected by the half mirror, ϵ, was evaluated by rotating analyzer method in accordance with following definition:

$$\epsilon = \sqrt{\frac{I_{min}}{I_{max}}} \qquad (6.12)$$

where I_{min} is minimum intensity of the light, whose intensity depends on vibrational azimuth, and I_{max} is maximum intensity of the light. ϵ can have a value from 0 to 1. The value of 1 indicates that the evaluated light is complete CPL. On the other hand, the value of 0 indicates complete LPL. In this experiment, only the light whose ϵ is more than 0.93 was used as CPL.

6.3.3 Observational Setup

Fig. 6.3 **B** shows optical path for observation. The objective lens bears not only concentration of the circularly polarized laser but also observation lens. A halogen lamp was used as illumination light of observation. The function of polarized light microscopy was added to the inverted optical microscope by equipping a pair of polarizers, allowing us to identify polymorph of $NaClO_3$ crystal and handedness of stable chiral crystal. The illumination light emitted from the halogen lamp, which is unpolarized light, is converted to a linearly polarized light by passing through a polarizer. The LPL was focused at the focal spot of the objective lens by condenser lens and was introduced to the objective lens. Then, the light passes through the second polarizer. Afterwards, the light reaches to a CCD camera (ELMO, CN43H,) equipped with a notch filter which eliminates the 532 nm light. The image obtained by the CCD camera can be monitored and recorded by a video recording system *in-situ*.

6.3.4 Laser-Induced Crystallization Experiment

The growth cell containing the liquid mixture was placed on a hand-made temperature-control stage. The temperature of the stage was controlled by Peltier devices connected to a feedback type Peltier controller (Netsudenshi). The temperature

was kept at 17±1°C throughout laser-induced crystallization. Thereby, assuming that (i) the dispersion liquid of Ag nanoparticle can be regarded as pure water (ii) the temperature of the liquid mixture is successfully controlled at 17°C, supersaturation of the liquid mixture is -24 %. Namely, the liquid mixture (here call "solution" for convenience) is under-saturated solution. Then, the laser whose intensity is about 940 mW, was focused at the air-solution interface. As a consequence of laser irradiation, the crystallization was induced. The handedness of the crystal induced by the laser irradiation was identified by means of polarized light microscopy. This procedure was repeated 100 times using *l*-CPL, 100 times using *r*-CPL and 50 times using LPL.
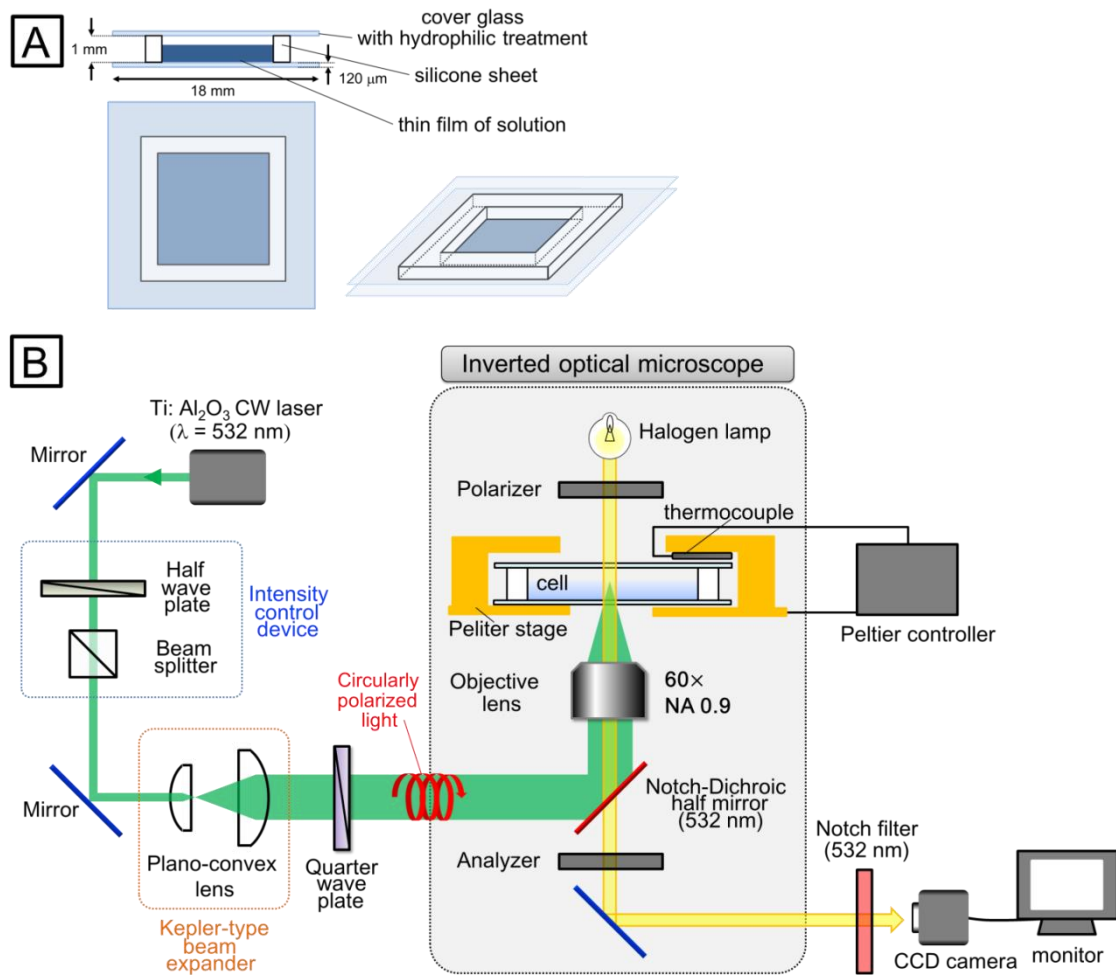

Fig. 6.3 Experimental setup of laser-induced crystallization using CPL. **A** : the crystal growth cell used in the laser-induced crystallization experiment. **B** : optical set up for the experiment.

154

6.4 Results

6.4.1 Laser-Induced Nucleation of Achiral Metastable Crystal from Focal Spot

Fig. 6.4 shows time-lapse micrographs of periphery of the focal spot of circularly polarized laser under non-crossed Nicols prism. Numerous black spots were observed on the solution-air interface. The black spots are possibly aggregates of Ag nanoparticles because charged colloidal nanoparticles easily aggregate in the presence of counter ion, which is sodium cation originating from the ionized sodium chlorate in this case. The reason why Ag nanoparticles in the dispersion liquid disperse is because that the negative surface charge of the Ag nanoparticles causes the Coulomb interparticle repulsive force. As long as the repulsive force is effective, the Ag nanoparticles will not aggregate and are not visible under the microscopic view because of their size below the limit of resolution. However, once a salt which easily ionizes in aqueous solution was dissolved into the dispersion liquid, Ag nanoparticles rapidly aggregate because the interparticle repulsive force is canceled out by positively charged ions originating from the salt. With time, the size of the aggregate exceeds the limit of resolution, and thus the aggregates of the nanoparticles are visible in the presence of the counter-ion. The aggregates of Ag nanoparticles (here we call the aggregates as nano-aggregate for convenience in what follows) flowed from outside of the microscopic field by advection of the solution. When the flowing Ag nano-aggregates approached to within about 20 μm of radius of the focal spot, the nano-aggregates are attracted to the focal spot independently of the direction of the advection flow. This is due to the gradient force of the electromagnetic field exerted on the Ag nano-aggregates because of the tightly focused laser (the effect of optical trapping) [8,9] (See Appendix 2). After the nano-aggregates were trapped at the focal spot, a parallelogram crystal appeared from the focal spot. The appeared crystal was trapped at the focal spot because of the gradient force of the electromagnetic field. The trapped crystal grew in the size of about 30 μm within 3 seconds. Continuous irradiation of the laser allows the crystal to grow. On the other hand, it should be noted that the crystal dissolves when laser irradiation was stopped or the crystal deviates from the focal spot (Fig.6.5), suggesting that the bulk solution was under-saturated with respect to the parallelogram crystal. The parallelogram crystal, which first appears at the focal spot, showed brilliant bright color under crossed-Nicols prism, indicating that the crystal is achiral metastable crystal revealed in the previous Chapters. Namely, the high supersaturation state, more than 60% supersaturation with respect to chiral stable phase at least, was generalized locally at the focal spot by optical trapping of Ag nano-aggregates.
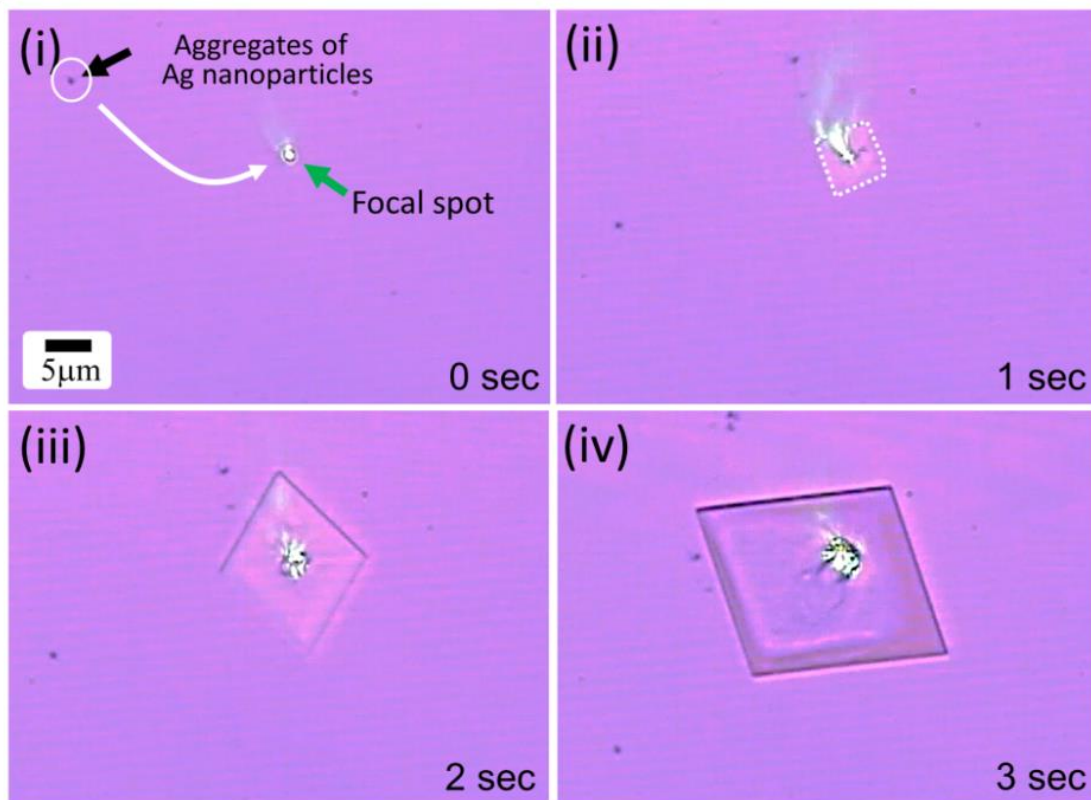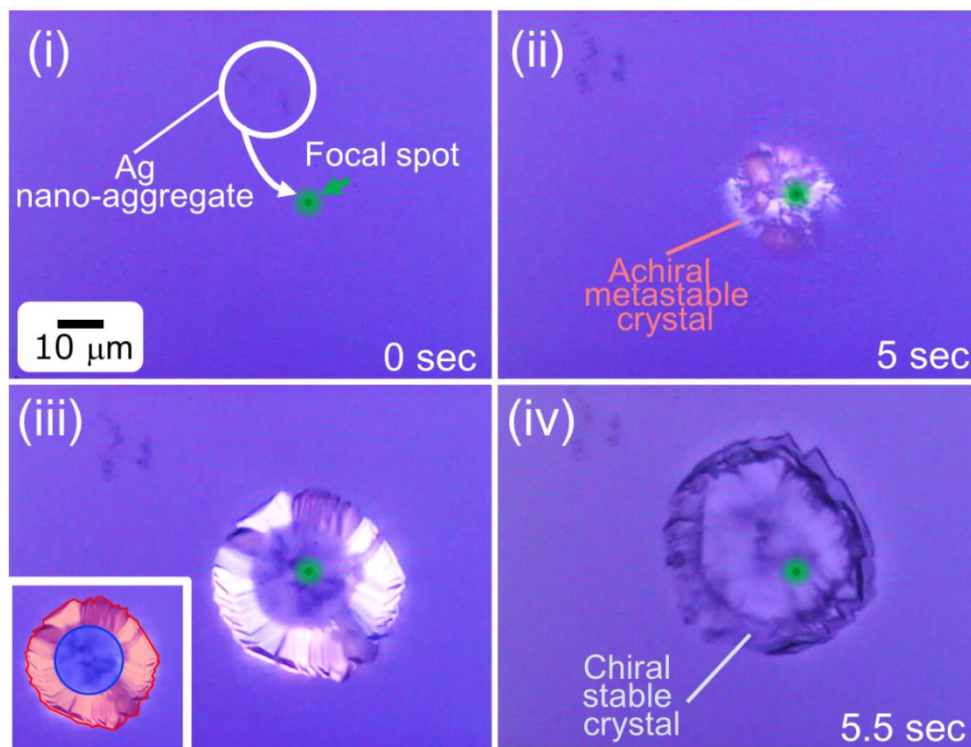
Fig. 6.4 Time-lapse micrographs showing the nucleation of achiral metastable crystal at the focal spot. (i) Before the nucleation. Ag nano-aggregates floated on the air-liquid interface was attracted to the focal spot. The moment when this image captured was set to be t = 0 (ii) Immediate after the nucleation. A visible crystal of the achiral phase appeared from the focal spot. (iii) The crystal became to exhibits crystal facet. (iv) The achiral crystal continued to grow while being trapped at the focal spot.
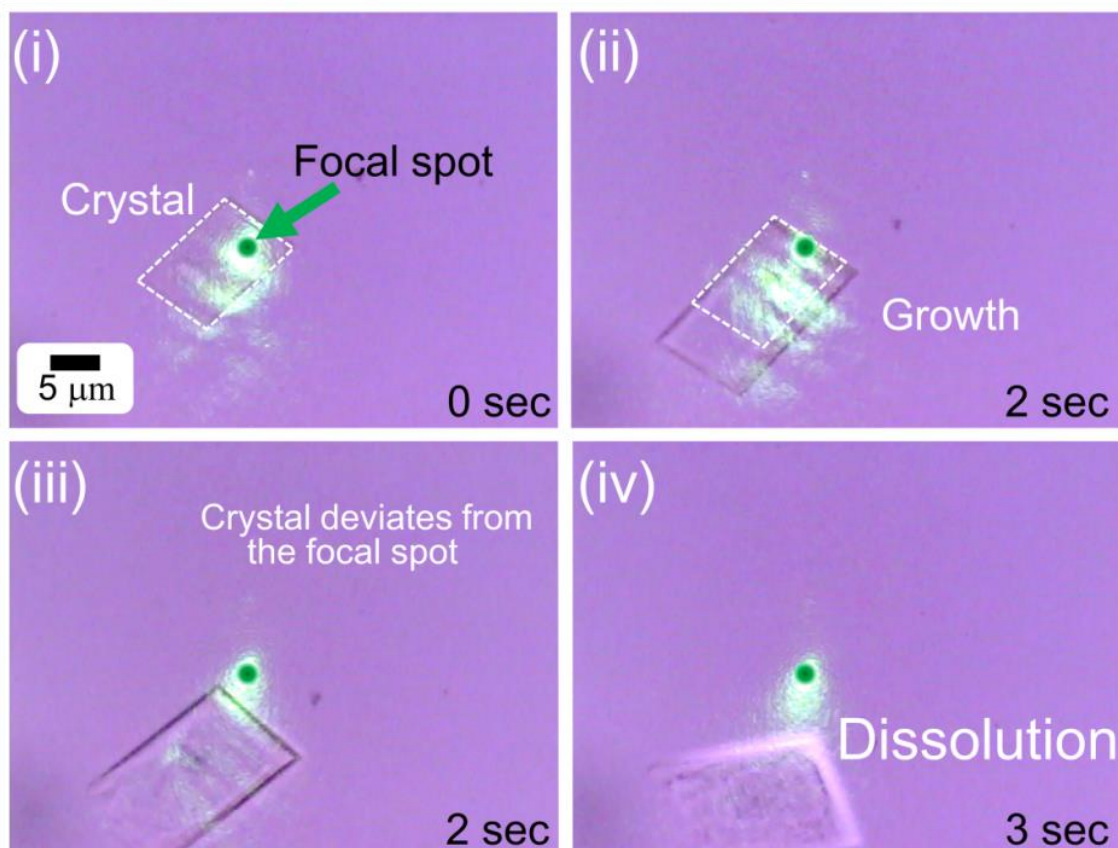
Fig. 6.5 Time-lapse micrographs showing the dissolution of achiral metastable crystal deviated from the focal spot. (i) After the nucleation of achiral crystal at the focal spot. Dotted line indicates the crystal-solution interface. The moment when this image captured was set to be t = 0. (ii) The growth of the achiral crystal trapped at the focal spot. The achiral crystal grew as long as the crystal was trapped at the focal spot. (iii) Deviation of the crystal from the focal spot owing to convection of solution. (iv) Immediate after the deviation, the achiral crystal immediately started to dissolve after the deviation.

6.4.2 Achiral-Chiral Polymorphic Transformation from Focal Spot

Continuous laser trapping of the achiral crystal allowed the crystal to grow. Over time, the bright color of the achiral crystal was rapidly changed to darker color at the focal spot, indicating that the polymorphic transformation to chiral stable phase occurred. After the transformation at the focal spot, the transformation radially proceeds from the focal spot. The front line of the transformation spread along the achiral crystal within 1 second. This chiral crystal formation via the achiral crystal was able to be observed in both case of LPL irradiation and CPL irradiation. Fig. 6.6 is time-lapse micrographs showing the transformation. As indicated by Fig. 6.6 (i)-(ii), a brilliant bright colored solid appeared at the focal spot, indicating the nucleation of achiral metastable crystal. Fig. 6.6 (iii) shows onset of the polymorphic transformation from achiral metastable crystal to chiral stable crystal from the focal spot. The red or blue colored region in Fig. 6.6 **B** indicates achiral metastable crystal and chiral stable crystal, respectively. After onset of the transformation, the achiral crystal was immediately converted by the chiral crystal. The process from the nucleation of achiral crystal to transformation was completed within 1 sec. On the other hand, Fig. 6.7 also shows the transformation. Continuous laser irradiation grows an achiral crystal larger than the microscopic view. After several seconds laser irradiation, the polymorphic transformation occurred from the focal spot and the front line of the transformation radially spread from the focal spot as similar to the former micrographs. As a consequence, chiral crystal was obtained from the focal spot.

Fig. 6.6 Time-lapse micrographs showing the laser-induced formation of chiral crystal intermediated by the achiral crystalline precursor from the focal spot. (i) Optical trapping of Ag nano-aggregates at the focal spot. The moment when this image was captured was set to be t = 0. (ii) Immediate after the optical trapping of the Ag nano-aggregates. Visible achiral crystal, which exhibits brilliant bright color, appeared from the focal spot. (iii) Achiral-chiral polymorphic transformation from the focal spot. The achiral crystal grew after the nucleation and the achiral crystal started to transform to chiral crystal, which exhibits dark color, from the focal spot. The inset shows the region of achiral crystal and that of chiral crystal of the image (iii) by coloring with red and blue, respectively. (iv) after the accomplishment of the polymorphic transformation. Bright achiral crystal completely converted to the dark chiral crystal. The transformation was instantly accomplished within 0.5 sec.
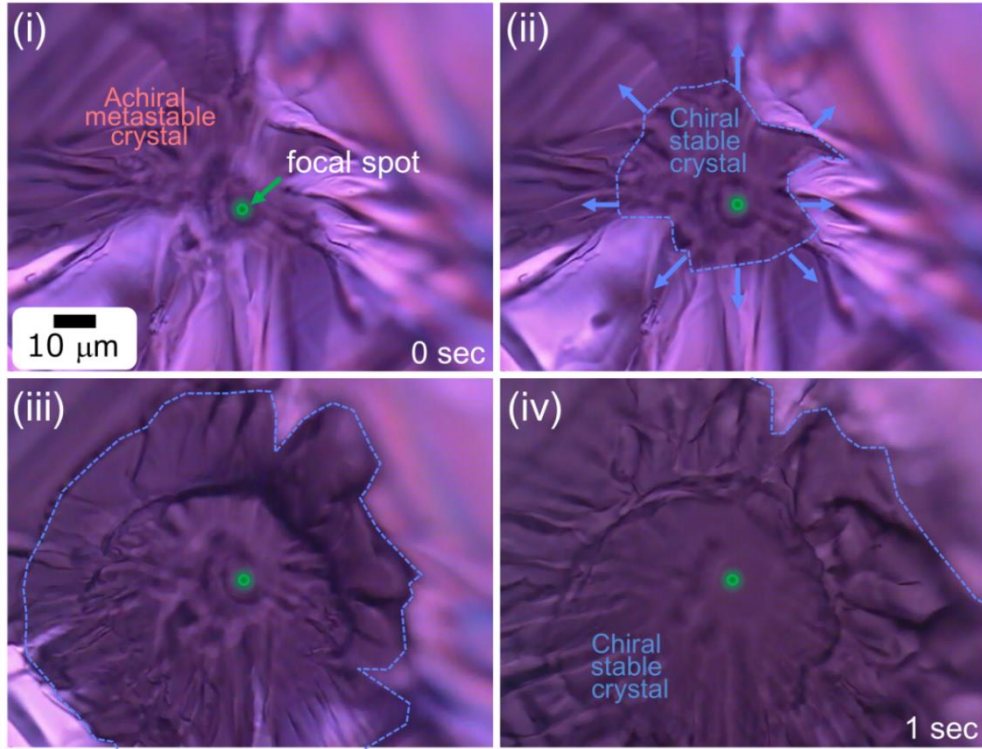
Fig. 6.7 Achiral-chiral polymorphic transformation progressed from the focal point. (i) 100 μm sized achiral crystal, which exhibits bright color, trapped at the focal spot. Green spot indicates the focal spot. The moment when this image was captured was set to be t = 0. (ii) Immediate after the onset of the polymorphic transformation. The bright color extinguished from the focal spot. The dark reason propagated with the focal spot as the center rapidly. (iii-iv) The progress of the transformation.

6.4.3 Chiral Bias under CPL Irradiation

Table. 6.1 shows the number of crystallization of the both enantiomorphs under *l*-CPL, *r*-CPL, LPL irradiation, respectively. The handedness of CPL was described taking the handedness-inversion by half-mirror reflection into account. *l*-enantiomorph dominated over the *d*-enantiomorph about twice under *r*-CPL irradiation, whereas, *d*-enantiomorph dominated over the *l*-enantiomorph under *l*-CPL irradiation. Under *r*-CPL irradiation, *l*-enantiomorph crystallized out 65 times out of 100 crystallizations. On the other hand, *d*-enantiomorph crystallizaed out 58 times out of 100 crystallizations under *l*-CPL irradiation. It follows that the number of crystallization of the predominant enantiomorph is 123 times out of 200 crystallizations. Assuming that the both enantiomorphs crystallizes in completely equal probability, the probability that the either of two enantiomorph crystallize out n times out of N crystallizations follows binomial distribution, B(N,0.5). Fig. 6.8 shows the binomial distribution, B(200,0.5). In B(200,0.5), median is 100 and the upper limit of 95 % confidence interval (2σ) in B(200,0.5) is 114.14. According to the equal thermodynamic stability of the both enantiomorphs, number of times of the occurrence of predominant enantiomorph should be within the range from 100 to 115. However, the CPL laser-induced crystallization provided 123 times crystallization of the predominant enantiomorph out of 200 crystallizations, showing deviation from the 95% confidence interval of the binomial distribution. Therefore, the probability of crystallization of one enantiomorph is possibly influenced by CPL irradiation.

Table 6.1 Relationship between the number of times of crystallization of *l*-enantiomorph and *d*-enantiomorph and polarization of light.

	left-handed CPL	right-handed CPL	LPL
l-enantiomorph	42	65	26
d-enantiomorph	58	35	24
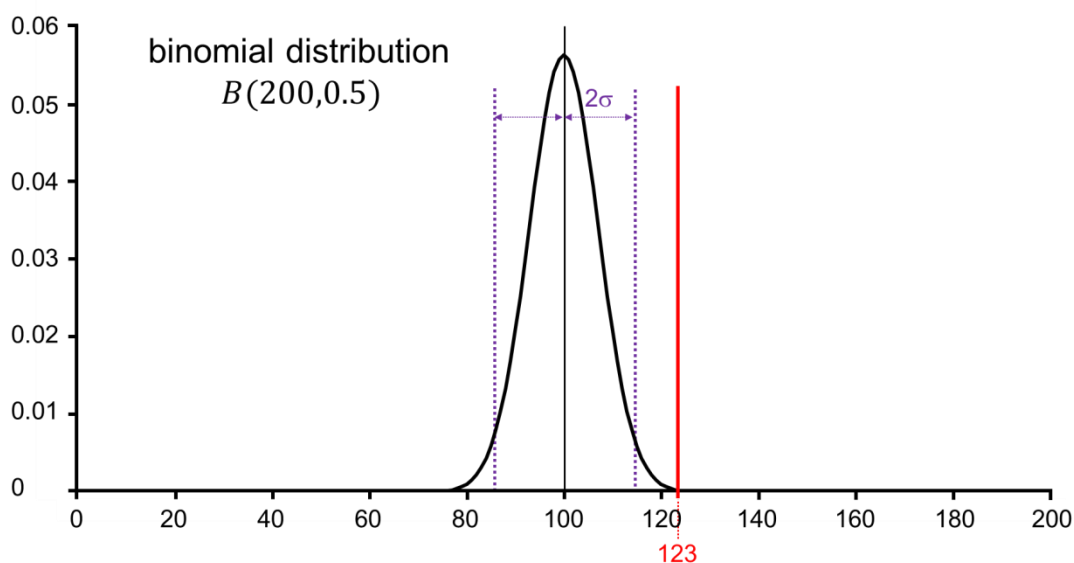
Fig. 6.8 Probability distribution of binomial distribution B(200,0.5), which is equivalent to the probability distribution of the number of times of crystallization of the specific enantiomorph out of 200 crystallization. The black, purple and red line indicates the median, 2 standard deviations and the current experimental result, respectively. It can be seen that the experimental result deviates from the 2 standard deviations.

6.5 Discussion

6.5.1 Conceivable Mechanism of Chiral Bias

Fig. 6.13 **A** shows the wavelength dispersion of circular dichroic (CD) spectrum of NaClO$_3$ chiral crystal from 220 nm to 300 nm [10]. The sign of CD band of *d*-crystal is negative from about 225 nm to about 255 nm and is positive from 255 nm to longer-wavelength side and *vice versa*. In addition, Figure. 6.13 **B** shows the wavelength dispersion of circular birefringence (CB) from 200 nm to 700 nm [11]. Because circular dichroic spectra and circular birefringence spectra correlates with each other by Kramers-Kronig relationship, the plus or minus sign of the CD band in longer-wavelength side than the 300 nm can be estimated from the CB band from the Kramers-Kronig relationship as follows

$$\text{CB}(\lambda) = \frac{2}{\pi} P \int_0^\infty \frac{\lambda' CD(\lambda')}{\lambda'^2 - \lambda^2} d\lambda' \tag{6.13}$$

$$\text{CD}(\lambda) = -\frac{2}{\pi} P \int_0^\infty \frac{\lambda CB(\lambda')}{\lambda'^2 - \lambda^2} d\lambda' \tag{6.14}$$

where P is Cauchy's principal value.
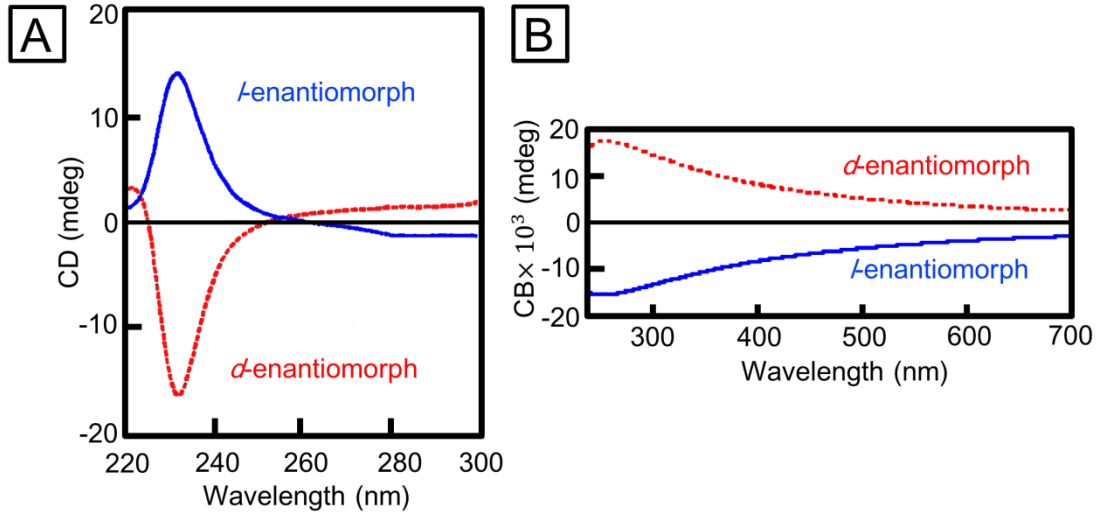
Fig. 6.13 Circular dichroism (CD) and circular birefringence (CB) of NaClO$_3$ chiral crystal. **A** Circular dichroism spectra of NaClO$_3$ chiral crystal in the range from 220 nm to 300 nm. Blue solid line indicates the CD band of *l*-enantiomorph and red dashed line indicates that of *d*-enantiomorph. **B** CB spectra of NaClO$_3$ chiral crystal in the range from 250 to 700 nm. Notation of the line is the same as **A**.

Since the shape of CD bands is estimated by differentiating the CB bands he CD sign at 532 nm of *d*-crystal is determined to be positive, indicating that absorbance of *d*-crystal for *l*-CPL is larger than that for *r*-CPL and *vice versa*. Because the light can be converted to heat by absorption, irradiation of *r*-CPL thermally excites *l*-crystal rather than *d*-crystal. Here, let the author consider the SSPT controlled by nucleation and growth taking the asymmetric photothermal effect into account. The SSPT from the achiral crystal to the chiral crystal may be initiated by the formation of critical nucleus that has chiral structure of the stable phase in the achiral structure. Thus, the author assumes that pre-critical "embryos" of two chiral species are present in the achiral crystalline precursor before onset of the transformation. According to CNT, activation energy for nucleation, ΔG^*, is given by

$$\Delta G^* = \frac{16\pi}{3} \frac{\gamma_{sm}^3 v_s^2}{\Delta \mu^2}. \qquad (6.15)$$

as shown in the chapter 2. The factor that depends on temperature among the factors determining the activation energy is the difference in the chemical potential, $\Delta \mu$.

According to the Van't Hoff equation, the solubility of a crystal, *i*, in aqueous solution is usually expressed as:

$$\ln a_i = \frac{\Delta H_{im}}{R}\left(\frac{1}{T_{im}} - \frac{1}{T}\right) \tag{6.16}$$

where a_i is activity of *i*, ΔH_{im} is enthalpy of fusion at T_{im}, which is melting point of *i*. The activity is shown as

$$a_i = \gamma_i \cdot x_i \tag{6.17}$$

where γ_i is activity coefficient and x_i is solubility in mole fraction. The solubility ratio of the polymorphs of the chiral stable phase and achiral metastable phase can be expressed as

$$\frac{\partial ln(a_m/a_s)}{\partial(1/T)} = \frac{1}{R}(\Delta H_{sm} - \Delta H_{mm}) = -\frac{\Delta H_{tr}}{R} \tag{6.18}$$

where the index of *s* and *m* denotes the stable phase and metastable phase, respectively and ΔH_{tr} is the enthalpy for the transformation between achiral metastable phase and chiral stable phase. It is assumed that activity coefficients of each polymorph in the same solution may be regarded as equal because the molecular structure of the polymorphs is the same. Accordingly, the activity ratio can be replaced by the solubility ratio:

$$\frac{\partial ln(a_m/a_s)}{\partial(1/T)} = \frac{\partial ln(x_m/x_s)}{\partial(1/T)} \tag{6.19}$$

Therefore, the difference in the chemical potential between the metastable and stable phase can be written as:

$$\Delta \mu = kT \ln \frac{x_m}{x_s} \tag{6.20}$$

[12]

Since the solubility ratio is constant, the chemical potential difference increases with the

increment of temperature. Eventually, it follows that activation energy for nucleation becomes lower as temperature increases. Owing to the difference of temperature increment between the two chiral "embryo" by CPL irradiation, the difference of the activation energy between the two chiral enantiomorphs occurs. Especially, *r*-CPL irradiation decreases the activation energy for nucleation of *l*-enantiomorph since the *l*-enantiomorph efficiently absorbs *r*-CPL relative to *d*-enantiomorph. Assuming that the enantiomorph that initially forms critical nucleus predominates and occupies the achiral crystal, *r*-CPL irradiation preferentially leads to the transformation to *l*-enantiomorph since the rate of transformation to *l*-enantiomorph is high. Moreover, it is expected incompleteness in chiral bias because of the competition between the rate rates of the transformation to *d*- and *l*-enantiomorphs (Fig. 6.14 and Fig. 6.15). These considerations are consistent with the tendency of the current experimental results. Therefore, asymmetric photothermal effect originating from the circular dichroism presumably caused the chiral bias in crystallization under CPL irradiation.
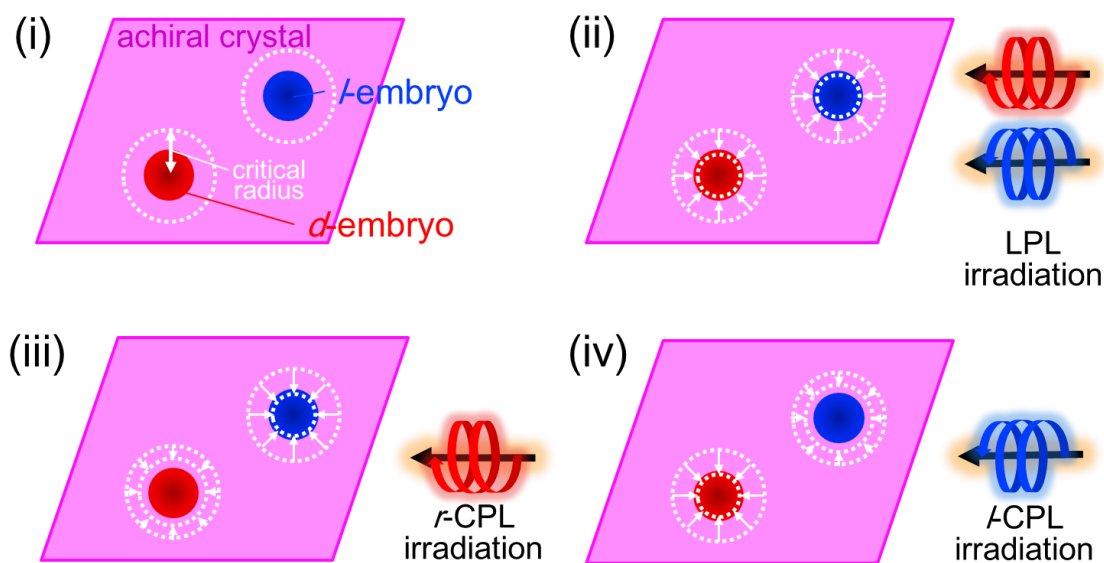

Fig. 6.14 Quantitative description of change in the critical radius for nucleation of chiral stable phase in SSPT depending on the polarization of incident light. (i) The case of no incident light. The purple rhombus denotes achiral metastable crystal. The blue and red circles indicates pre-critical embryo of *l*- and *d*-enantiomorphs. The white dashed circle indicates the critical diameter for nucleation of stable phase. (ii) The case in LPL irradiation. Owing to the temperature rising originating from the absorption of light, the critical radius can decrease. Especially, since the LPL is the sum of *r*-CPL and *l*-CPL, the decrement of the critical radius is the same between both enantiomorphs. (iii) The case in *r*-CPL irradiation. Since *l*-chiral structure can absorb *r*-CPL more efficiently relative to r-chiral structure, the decrement of the critical radius for *l*-embryo is possibly larger than that for *d*-embryo. (iv) The case in *l*-CPL irradiation. The decrement of the critical radius is *vice versa* of the case in *r*-CPL irradiation.
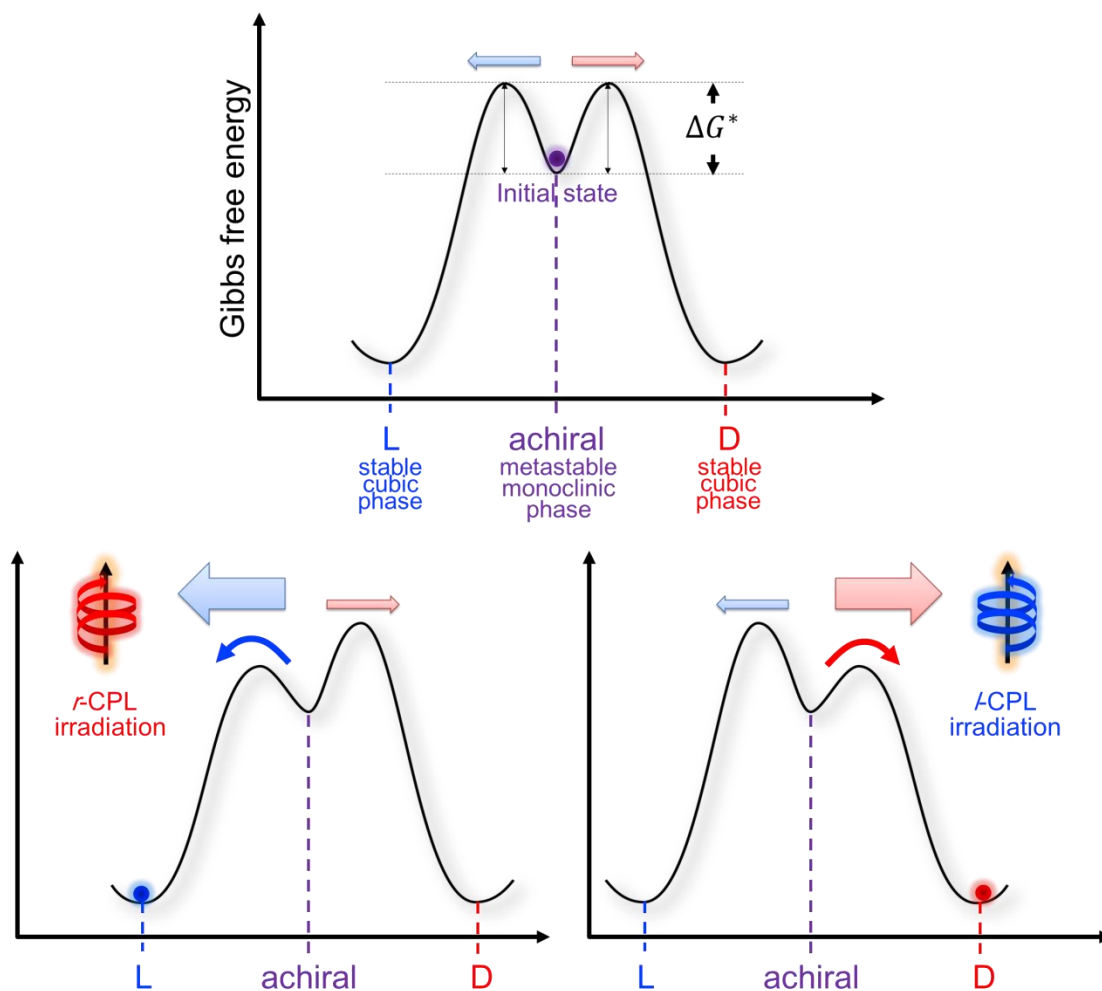
Fig. 6.15 Energetic description of the influence of CPL irradiation. Upper figure shows the case without light irradiation. The activation energy for nucleation of chiral stable phase, ΔG*, is equal between *l*- and *d*-enantiomorph. Lower left figure shows the case in r-CPL irradiation. The activation energy for *l*-enantiomorph is lowered relative to that for *d*-enantiomorph. Lower right figure shows the case in *l*-CPL irradiation. The activation energy for *d*-enantiomorph is lowered relative to that for *l*-enantiomorph.

6.6 Conclusion

In conclusion, spatially controlled induction of $NaClO_3$ crystal nucleation was achieved by laser trapping of Ag nano-aggregates dispersed in a $NaClO_3$ unsaturated aqueous solution at the solution-air interface (The mechanism of the crystallization was discussed in the Appendix 3). The crystallization process induced by laser irradiation was consistent with the formation pathway of chiral crystal via achiral crystalline precursor, which proposed in the chapter 6. Moreover, it was found that probability of crystallization of one enentiomorph can be enhanced by CPL irradiation. Based on the consideration of nucleation in SSPT, the enhancement may be ascribed to asymmetric photoabsorption originating from circular dichroism of $NaClO_3$ chiral crystal, implying that formation of achiral precursor may be required to induce the chiral bias (Fig. 6.16).
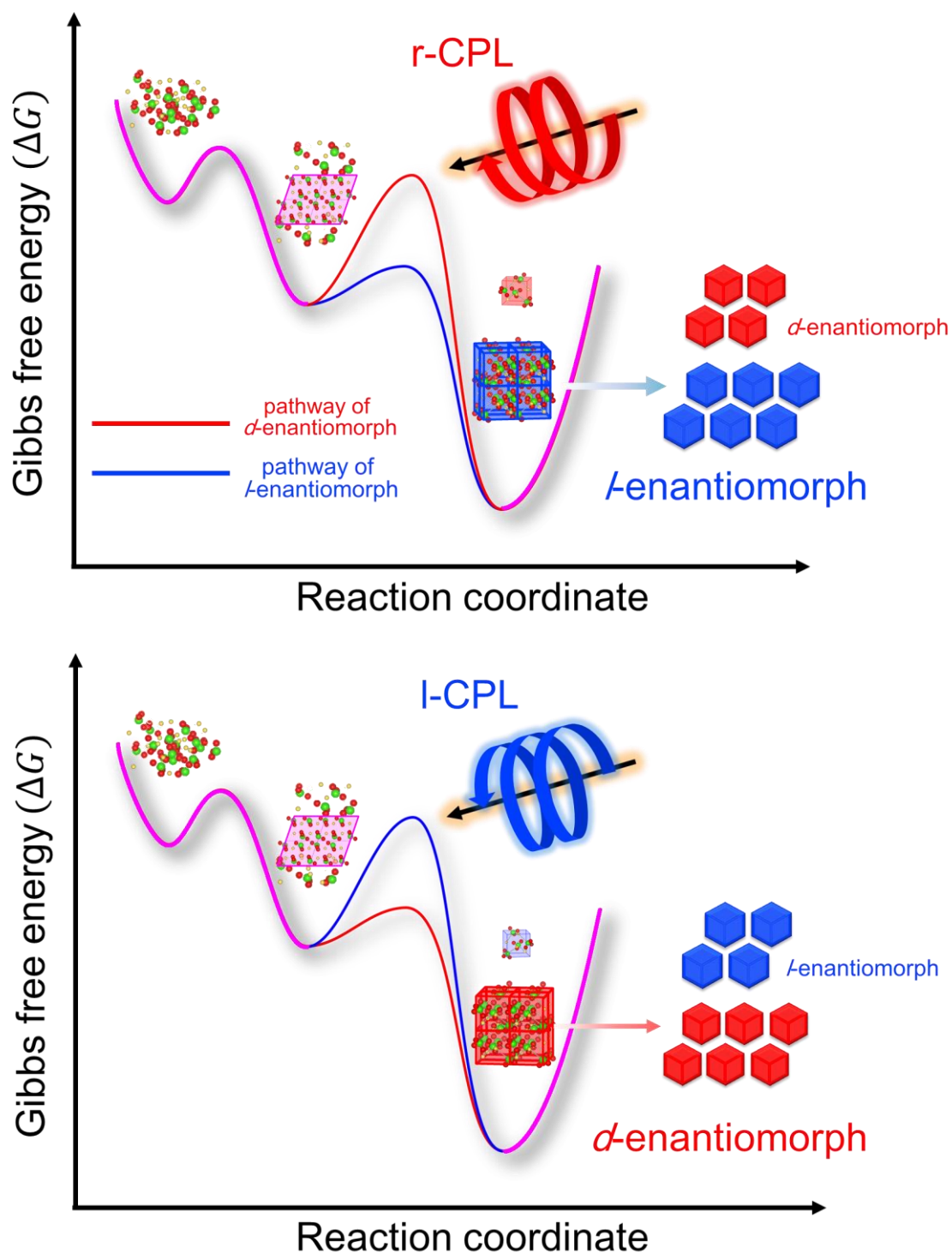
Fig. 6.16 Energetic pathway for NaClO$_3$ chiral crystal formation depending on the handedness of CPL. Upper schematic indicates the case in *r*-CPL irradiation and lower schematic indicates the case in *l*-CPL irradiation.

6.7 Summary of Chapter 6

In this chapter, non-photochemical laser induced crystallization using CPL from NaClO$_3$ aqueous solution was carried out to exploit the possibility to control crystal chirality in NaClO$_3$ chiral crystallization from an aqueous solution. The conclusions in this chapter were summarized below.

• It was found that the optical trapping of Ag nano-aggregates dispersed in NaClO$_3$ unsaturated aqueous solution induces the nucleation at the focal spot of laser.

• It was found that the laser-induced crystallization using CPL, which asymmetrically interacts with chiral crystals, enhances the probability of crystallization of one enantiomorph. In the case of NaClO$_3$ chiral crystallization, *r*-CPL tends to yield *l*-enantiomorph and *vice versa*.

• Correspondence between crystal handedness and the handedness of CPL was attributed to asymmetric photothermal effect originating from circular dichroism of NaClO$_3$ chiral crystal and the feature that nucleation rate of stable phase during SSPT can be promoted by temperature rising. The nucleation of achiral precursor might contribute to the chiral bias of the current experimental result.

References

[1] S. W. Choi, T. Izumi, Y. Hoshino, Y. Takahashi, K. Ishikawa, J. Watanabe and H. Takezoe, *Angew. Chem. Int. Ed. 45, (2006), 1382.*

[2] T. Kawasaki, M. Sato, S. Ishiguro, T. Saito, Y. Morishita, I. Sato, H. Nishino, Y. Inoue and K. Soai, *J. Am. Chem, Soc.* **127**, (2005), 3274.

[3] W. L. Noorduin, A. A. C. Bode, M. van der Meijden, H. Meekes, A. F. van Etteger, W. J. P. van Enckevort, P. C. M. Christianen, B. Kaptein, R. M. Kellogg, T. Rasing and E. Vlieg,, *Nat. Chem.* **1**, (2009), 729.

[4] B.A. Garetz, J. E. Aber, N. L. Goddard, R. G. Young and A. S. Myerson, *Phys. Rev. Lett.* **77(16)**, (1996), 3475.

[5] X. Sun, B. A. Garetz and A. S. Myerson, *Cryst. Growth Des*. **6(3)**, (2006), 684.

[6] N. C. Murphy, R. N. Compton and R. M. Pagni, *Cryst. Growth Des.* **7(2)**, (2007), 449.

[7] K. Yuyama, K. Ishiguro, T. Sugiyama and H. Masuhara, *Proc. SPIE* **8458**, (2012), 84582D.

[8] A. Ashikin, *Proc. Natl. Acad. Sci. USA* **94**, (1997), 4853.

[9] S. Sato, Y. Harada and Y. Waseda, *Opt. Lett.* **22(19)**, (1994), 1807.

[10] J. Bartus, D. Wang and O. Vogl, *Monatshefte für Chemie* **125**, (1994), 671.

[11] T. Harada, T. Sato and R. Kuroda, *Chem. Phys. Lett*. **413**, (2005), 445.

[12] M. Kitamura, *Pure. Appl. Chem.* **77(3)**, (2005), 581.

CHAPTER 7

CONCLUSION

This study has discovered unknown unstable non-cubic $NaClO_3$ crystal that appears prior to the formation of chiral crystal by *in-situ* PLM observation focusing on the early stage of crystallization from an aqueous solution. It was achieved to determine the crystal structure of the unknown phase by means of cryogenic single-crystal XRD experiment. The XRD measurement has revealed that the unknown crystalline phase is achiral. In addition, it was achieved to control the crystallization of the unstable achiral crystal by means of antisolvent crystallization method, enabling us to measure the solubility of the achiral crystal. The measured solubility indicates that the achiral unstable phase is metastable phase. Moreover, the *in-situ* PLM observation focusing on polymorphic transformation from achiral precursor to chiral crystal have revealed that the achiral precursor transforms into chiral crystal though either of solid-solid martensitic transformation (SSPT) or approach-facilitated solvent-mediated phase transformation (SMPT). The observational results, which are summarized below, imply that the SSPT and the approach-facilitated SMPT has a possibility to be responsible for the emergence process of chirality and the amplification process of one-handedness, respectively. For these observational results, this study proposed a novel formation pathway of $NaClO_3$ chiral crystal intermediated by an achiral crystalline precursor. Namely, the handedness of $NaClO_3$ crystal is not determined at the early stage of crystallization and a crystal which has just been born is ambidextrous. The direction of SSPT determines the handedness in crystal structure. This study has also attempted to direct the handedness by irradiating focused CPL as chiral perturbation during the transformation. As a consequence, chiral bias was observed in the occurrence ratio of enantiomorphs.

Here, the knowledge obtained in each chapter is summarized below. The Chapter 1 provided the background of this study.

- To understand the mechanism of emergence of crystal chirality has a great significance for elucidation of biohomochirality and chirality control of pharmaceutical compounds and magnet materials for spintronic devices.
- Chiral symmetry breaking in $NaClO_3$ chiral crystallization has been widely investigated because of the possibility to provide insights into biohomochirality and practical methodologies for chiral separation. The crystallization experiments of the

chiral symmetry breaking are mainly classified into two types: (i) chiral symmetry breaking under far-from-equilibrium, which involves with primary nucleation process (ii) chiral symmetry breaking under quasi-equilibrium known as so-called "Viedma deracemization", which is seemingly irrelevant to the primary nucleation.

• The mechanism of chiral symmetry breaking still remains controversial. To explain the experiments under far-from-equilibrium, although the secondary nucleation scenario has been proposed and been widely accepted, several experiments cannot be explained by the scenario because of the high rate of primary nucleation. On the other hand, for the experiments under quasi-equilibrium, the conflict between the theory based on Ostwald ripening and that based on chiral cluster reaction can be seen.

• The approach in the current study is to investigate determination process of handedness in $NaClO_3$ chiral crystals one-by-one by means of direct in-situ microscopic observation with intensive attention to the early stage of crystallization.

In the chapter 2, *in-situ* microscopic observation of the early stage of $NaClO_3$ chiral crystallization using PLM were performed. The knowledge revealed by the observation is summarized below.

• Unknown unstable crystal, which is birefringent, forms prior to the formation of chiral crystal in the early stage of the crystallization.
• The unknown crystal transforms into chiral crystal within a few minutes.

In the chapter 3, the analyses of the unknown phase, which are single crystal structural analysis and solubility measurement, were carried out. The knowledge revealed by the analysis is summarized below.

• Cryogenic single-crystal XRD experiment successfully provided crystallographic information of the unknown phase, which are crystal system, lattice parameters, space group, as follows: monoclinic, $a = 8.42(2)$ Å, $b = 5.260(7)$ Å, $c = 6.70(1)$ Å, $\beta = 109.71(1)°$, and V = 279.8(8) Å^3, $P2_1/a$, respectively. These values are similar to those of Phase III, which appears in $NaClO_3$ melt growth as metastable phase. The space group of $P2_1/a$ indicates that the unknown phase is achiral.
• Anisolvent crystallization method allows us to control the crystallization of the achiral phase and to manipulate it. Using an achiral crystal produced by the antisolvent method, it was achieved to measure the solubility of the achiral phase in the range

from 10°C to 23°C. The measurements showed that the solubility of the achiral phase is 1.6 times higher than that of the chiral stable phase, indicating that the achiral phase is metastable phase.

In the chapter 4, *in-situ* PLM observation with intensive attention to the polymorphic transformation from the achiral phase to chiral phase was performed. The knowledge revealed by the observation is summarized below.

- The achiral metastable crystal transforms into chiral crystal through either of two kinds of polymorphic transformations: (i) SSPT (ii) approach-facilitated SMPT. Determination of the handedness depends on the two transformations.
- Two kinds of SSPT were observed. The one directly transforms to phase I. The other is a transformation intermediated by transient phase, which is possibly transient structure predicted by Meyer's deformation model and phase II seen in $NaClO_3$ melt growth. In the former case, chirality possibly emerges during the transformation. On the other hand, in the latter case, chirality presumably emerges during the transformation from the transient structure to chiral phase I. Since the activation energy to overcome for the transformation should be equal between the both enantiomorphs, the SSPT yields both enantiomorphs in equal probability.
- The approach of a chiral crystal to an achiral crystal triggers rapid SMPT from the approached point. The author denominated this transformation as "approach-facilitated SMPT". In this transformation, the achiral crystal certainly transforms into the same enantiomorph as the enantiomoph that approaches to achiral crystal.

Chapter 5 summarized observational results obtained in the Chapter 1-4 and proposed a novel formation pathway of $NaClO_3$ chiral crystal via achiral precursor and a conceivable scenario that explains the chiral symmetry breaking under far-from-equilibrium. The proposals are summarized below.

- Achiral metastable crystal intermediates the formation of chiral crystal in the early stage of $NaClO_3$ chiral crystallization from an aqueous solution in such a way as to follow Ostwald's rule of stages. Namely, the handedness of the crystal is not determined at the primary nucleation process in contrast to the previous thought, in which the handedness is already determined at primary nucleation. The achiral

precursor transforms into chiral crystal by either of SSPT, which yields both enantiomorphs in equal probability, or approach-facilitated SMPT, which yields the same enantiomorph as the enantiomorph that approached to achiral crystal.

• The chiral symmetry braking under far-from-equilibrium that cannot be explained by the secondary nucleation scenario may be rationalized by taking the formation pathway the author proposed into account. The high rate of primary nucleation originating from the extremely high-supersaturation state before primary nucleation event, which is the cause of difficulty in explanation by the secondary nucleation scenario, can be lowered by the formation of the achiral precursor. Moreover, the emergence and amplification of chirality, which are two of three requirements for homochiral state proposed by Frank, may be rationalized by the solid-solid martensitic transformation and the approach-facilitated SMPT, respectively.

Chapter 6 showed the possibility to direct the handedness of the chiral crystal by means of nonphotochemical laser-induced induced polymorphic transformation using CPL. The knowledge obtained in the chapter is summarized below.

• Optical trapping of Ag nano-aggregates dispersed in $NaClO_3$ unsaturated aqueous solution was found to induce the nucleation at the focal spot of laser by two kinds of plasmonic phenomena. *In-situ* observation of the nucleation process showed that the chiral crystal formation consistently follows the pathway the author proposed.

• Non-negligible chiral bias was observed in the occurrence ratio of each enantiomorph. *l*-CPL irradiation tends to yield *d*-enantiomorph and *r*-CPL irradiation tends to yield *l*-enantiomorph. This chiral bias was attributed to asymmetric decrement of critical nucleation radius of each enantiomorph originating from circular dichroism.

ACKNOWLEDGEMENT

PRESENTED PAPERS

The publications constructing this thesis are listed below

[1] H. Niinomi, T. Yamazaki, S. Harada, T. Ujihara, H. Miura, Y. Kimura, T. Kuribayashi, M. Uwaha and K. Tsukamoto, "Achiral Metastable Crystals of Sodium Chlorate Forming Prior to Chiral Crystals in Solution Growth", *Crystal Growth and Design,* **13(12)**, (2013), 5188-5192.

[2] H. Niinomi, A. Horio, S. Harada, T. Ujihara, H. Miura, Y. Kimura and K. Tsukamoto, "Solubility Measurement of a Metastable Achiral Crystal of Sodium Chlorate in Solution Growth", *Journal of Crystal Growth*, **394(15)**, (2014), 106-111.

[3] H. Niinomi, H. Miura, Y. Kimura, M. Uwaha, H. Katsuno, S. Harada, T. Ujihara and K. Tsukamoto, "Emergence and Amplification of Chirality via Achiral-Chiral Polymorphic Transformation in Sodium Chlorate Solution Growth", *Crystal Growth and Design*, **14(7)**, (2014), 3596-3602.

[4] Y. Kimura, H. Niinomi, K. Tsukamoto and Juan M. García-Ruiz, "In Situ Live Observation of Nucleation and Dissolution of Sodium Chlorate Nanoparticles by Transmission Electron Microscopy", *Journal of American Chemical Society,* **136(5)**, (2014), 1762–1765.

Oral Presentations in International Conferences

[1] H. Niinomi, H. Miura, Y. Kimura, T. Kuribayashi, M. Uwaha, S. Harada, T. Ujihara and K. Tsukamoto, "Two Pathways Determining Chirality in $NaClO_3$ Crystals Grown from Solution via Achiral Precursors", The 17th International Conference on Crystal Growth and Epitaxy, 28911, Warsaw, Poland, August, 2013.

Poster Presentations in International Conferences

[1] H. Niinomi, K. Tsukamoto, T. Kuribayashi, H. Miura, "When dose the chirality of $NaClO_3$ crystals arise in solution growth?", International Union of Crystallography 2011, 1450, Madrid, Spain, August, 2011.

[2] H. Niinomi, K. Tsukamoto, M. Uwaha, H. Miura, "A Precursor of $NaClO_3$ Chiral crystals" 8th Japan-China-Korea Workshop on Microgravity Sciences for Asian Microgravity Pre-Symposium, Sendai, Japan, September, 2010

[3] H. Niinomi, K. Tsukamoto, M. Uwaha, H. Miura, "A Precursor of $NaClO_3$ Chiral Crystals", The 16th International Conference on Crystal Growth, PA266, Beijing, China, August, 2010

[4] <u>H. Niinomi</u>, S. Harada, T. Ujihara, H. Miura, Y. Kimura, T. Kuribayashi, M. Uwaha and K. Tsukamoto, "Emergence and Amplification of Chirality in Sodium Chlorate Chiral Crystallization from an Aqueous Solution", Future Vision of Green Mobility and Advanced Technologies for Realizing the Vision, Hanoi ,Vietnam, November, 2013.

[5] <u>H. Niinomi</u>, A. Horio, Z. Can, K. Seki, S. Harada, M. Tagawa and T. Ujihara, "Influence of Third-Element Addition on Surface Morphology of SiC in Solution Growth", International Crystal Growth School School in Sendai, Sendai, Japan, July, 2012.

[6] <u>H. Niinomi</u>, K. Tsukamoto, M. Uwaha, H. Miura, Y. Araki, "A Precursor of NaClO$_3$ Chiral crystals", The 14th International Summer School on Crystal Growth, 30, Dalian, China, August, 2010.

Oral Presentation in National Conferences

[1] <u>新家寛正</u>, 原田俊太, 宇治原徹, 三浦均, 木村勇気, 上羽牧夫, 塚本勝男, "NaClO$_3$溶液成長におけるアキラル・キラル多形転移を介したキラリティ発生と増幅", 日本地球惑星科学連合大会 2014 年大会, MIS36-05, 横浜, 2014 年 5 月

[2] 木村勇気, 山崎智也, 古川えりか, <u>新家寛正</u>, 塚本勝男, Juan M. Garcia-Ruiz, "TEM による溶液中結晶化過程の直接観察", 日本地球惑星科学連合大会 2014 年大会, MIS36-04, 横浜, 2014 年 5 月

[3] <u>新家寛正</u>, 原田俊太, 宇治原徹, 三浦均, 木村勇気, 栗林貴弘, 上羽牧夫, 塚本勝男, "NaClO$_3$溶液成長におけるアキラルな準安定相を介したキラル結晶形成過程", 第 43 回結晶成長国内会議, 長野, 2013 年 11 月

[4] <u>新家寛正</u>, 三浦均, 木村勇気, 栗林貴弘, 塚本勝男, "溶液から成長する NaClO$_3$結晶のキラリティ発生の解明", 第 41 回結晶成長国内会議, 茨城, 2011 年 11 月

[5] 木村勇気, <u>新家寛正</u>, 三浦均, 塚本勝男, "TEM を用いた液中"その場"観察：塩素酸ナトリウムの核生成", 第 41 回結晶成長国内会議, 茨城, 2011 年 11 月

[6] <u>新家寛正</u>, 塚本勝男, 栗林貴弘, 三浦均 "溶液から成長する NaClO$_3$結晶のキラリティ発生の解明, 日本地球惑星科学連合 2011 年大会, MIS020-06, 千葉, 2011 年 5 月

[7] <u>新家寛正</u>, 塚本勝男, "溶液から成長する NaClO$_3$結晶のキラリティ発生の解明", 計算機センター特別研究プロジェクト結晶成長の数理第五回研究会-鏡像対称性と結晶成長-, ,東京, 2010 年 12 月

[8] <u>新家寛正</u>, 塚本勝男, 上羽牧夫, 三浦均, "NaClO$_3$結晶成長その場観察～キ

ラル結晶の前駆体の発見〜”, 日本地球惑星科学連合 2010 年大会, MIS012-06, 千葉, 2010 年 5 月

Poster Presentation in National Conferences

[1] <u>新家寛正</u>, 村山健太, 原田俊太, 田川美穂, 宇治原徹, “円偏光レーザー誘起結晶化によるキラリティ制御の可能性”, 第 44 回結晶成長国内会議,06PS28, 東京, 2014 年 11 月

[2] <u>新家寛正</u>, 原田俊太, 宇治原徹, 三浦均,木村勇気,栗林貴弘,上羽牧夫, 塚本勝男, “$NaClO_3$ 溶液成長におけるアキラルな準安定相の溶解度測定”, 第 43 回結晶成長国内会議, 長野, 2013 年 11 月

[3] 木村勇気, <u>新家寛正</u>, 塚本勝男, “溶液成長における核形成と溶解過程の TEM 中“その場”観察”, 日本地球惑星科学連合 2012 年大会, MIS24-P03, 千葉, 2012 年 5 月.

[4] <u>新家寛正</u>, 塚本勝男, “溶液から成長する $NaClO_3$ 結晶のキラリティ発生の解明”, 計算機センター特別研究プロジェクト結晶成長の数理第五回研究会 -鏡像対称性と結晶成長-, 東京, 2010 年 12 月

Awards

[1] <u>H.Niinomi</u> “International Mohri Poster Award Outstanding Poster Award”, 8th Japan-China-Korea Workshop on Microgravity Sciences for Asian Microgravity Pre-Symposium, September, 2010.

[2] <u>新家寛正</u>, “ハイライト論文選出”, 日本地球科学連合 2011 年大会, 2011 年 5 月

[3] <u>新家寛正,</u> “第 11 回日本結晶成長学会講演奨励賞” 第 43 回日本結晶成長学会国内会議, 2013 年 11 月

[4] <u>新家寛正</u>, “学生優秀発表賞” 日本地球科学連合大会 2014 年大会, 2014 年 6 月

SIMULTANEOUS FORMATION AND DISSOLUTION OF ACHIRAL AND CHIRAL NANOPARTICLES IN SATURATED CONDITION WITH RESPECT TO CHIRAL PHASE –*IN-SITU* OBSERVATION USING TRANSMISSION ELECTRON MICROSCOPY-

A1.1 Brief Introduction

The author has found the precursory formation of an achiral metastable crystalline phase followed by two different types of polymorphic transformation into chiral crystal in $NaClO_3$ chiral crystallization from aqueous solution. The detailed observation indicates that determination of enantiomorphs depends on the type of the transformation, providing a new sight for emergence and amplification processes of chirality in chiral symmetry breaking in $NaClO_3$ crystallization. However, based on our solubility measurements by observation using optical microscopy, the novel formation pathway of chiral crystal via achiral precursor holds only under limited condition. According to the measurement, the formation of achiral precursor requires 1.6 times higher concentration than the solubility value of chiral phase at least because the condition where achiral crystal can grow ranges above 1.6 times of the solubility value. Namely, the novel formation pathway of chiral crystal via achiral precursor takes place only when the degree of supersaturation with respect to chiral phase exceeds 60%. Therefore, it seemingly follows that the pathway via achiral precursor does not hold under relatively lower supersaturation below 60% at least under the scale of resolution of optical microscope. However, the phase stability of polymorphs at nanoscale, which is the earliest stage of nucleation, often becomes matter of debate. It has been pointed out that the relationship of phase stability between metastable phase and stable phase can be reversed at the nanoscale or below nanoscale because of predominant contribution of the surface on free energy originating from the high surface-to-volume ratio in the system of TiO_2, ZnS and forth [1], indicating that a metastable phase may form at nanoscale, which is invisible under optical microscopic observation, even in slightly supersaturated condition with respect to stable phase. To clarify polymorphic behavior under the supersaturation condition below 60% in $NaClO_3$ crystal nucleation from a solution from a nanoscopic view, an *in-situ* observation using transmission electron

179

microscopy (TEM) is necessary.

However, a live observation of the dynamics of phase behavior during the earliest stage of nucleation from a solution, those estimated to take place before the formation of a stable crystal, has never been achieved. The reason is that *in-situ* observation of nucleation from a solution at the nanoscale using TEM faces serious difficulties, particularly those related to solvent evaporation, charge dissipation and image acquisition speed. As the TEM observation requires specimen chamber to be high level of vacuum, it is forbidden to introduce volatile substances such as water to the specimen chamber. Therefore, it is difficult to observe the crystallization from a solution by means of conventional method. Although graphene cell, whereby a liquid droplet can be encapsulated between a pair of graphene sheet, or ingenious fluid cell, in which the Si_3N_4 membrane is employed for the observation window, have been developed in order to circumvent the problem of evaporation and charge dissipation [2,3], it is also true that these methods are costly, technologically difficult. In contrast to these approaches, in this study, to circumvent the problem of evaporation and charging, the author's group has used an ionic liquid, which have negligible vapor pressure and relatively high electrical conductivity, as solvent [4]. To overcome the problem of visualization, we have used saturated ionic solution, where crystalline clusters are expected either not to form or to do it at a slow rate and will never reach a critical size, thus making the observation of the dynamics easier. In addition, the use of saturated ionic solution provides the dynamics of nanoparticle formation under unsaturated condition with respect to the chiral metastable phase. In this chapter, the author describes simultaneous formation and dissolution of both achiral and chiral nanoparticles in saturated condition with respect to chiral phase on the basis of *in-situ* TEM observation.

## A1.2 Experimental -Challenge in In-Situ TEM Observation and Solution-

Ionic liquids have previously been used for direct observation of organic materials, such as seaweed by scanning electron microscopy (SEM) [5] and dispersed metallic nanoparticles by TEM [6]. There are several hundreds of ionic liquids that have been categorized into several systems, such as aliphatic, imidazolium, or pyridium. We selected the following five ionic liquids (Kanto Chemical Co., Inc., Tokyo, Japan) as candidate solvents, taking into account their melting point, dissociation temperature, price, and availability. The ionic liquid must be liquid at room temperature for nucleation and must be stable, showing no dissociation during the heating experiments

described below; 1,3-diallylimidazolium bromide, 1-allyl-3-butylimidazolium bromide, 1-ethyl-3-methylimidazolium tetrafluoroborate, 1-butyl-3-methylimidazolium tetrafluoroborate, and 1-allyl-3-ethylimidazolium bromide. The first of these ionic liquids was found the best solvent to study $NaClO_3$ nucleation. Its chemical formula weight is 229.12 and its decomposition temperature is 271 ° C. Its chemical formula is $C_9H_{13}BrN_2$ (Fig. A1.1).
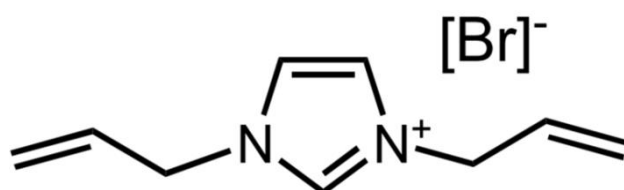
Fig. A1.1   Molecular structure of the 1,3-diallylimidazolium bromide

Saturated solutions of $NaClO_3$ (analytical grade, Wako Pure Chemical) in ionic solution at 80 ° C were prepared as follows. $NaClO_3$ powder was poured into the ionic liquid (500 μL) and stirred using ultrasound. The solution was stored for 2 days at 85 ° C, then cooled down to 80 ° C and stored for 1 day. A residue of undissolved $NaClO_3$ was observed at the bottom of the ionic solution confirming that the supernatant ionic liquid solution was saturated with $NaClO_3$ at 80 ° C. Saturated ionic solution of 5 − 10 μL was removed from the middle of the solution using a pipet previously warmed to 80 ° C. The solution was then dropped onto two different types of substrates. The first one was a temperature-controlled glass substrate for observation by polarized-light microscopy, which allows the identification of the polymorphs of $NaClO_3$ (Fig. A1.2). The second substrate was an amorphous carbon holey film supported on a standard copper TEM grid (Fig. A1.3). The contrast of the solution in TEM image depends on the thickness of the solution. We controlled the amount of the bulk solution dropped onto the microgrid and selected a hole, which has a weaker contrast at the center compared with the periphery. Therefore, thickness of the solution is thinner than the thickness of the microgrid (100 − 200 nm) and can be estimated to be in the range from 50 to 100 nm.
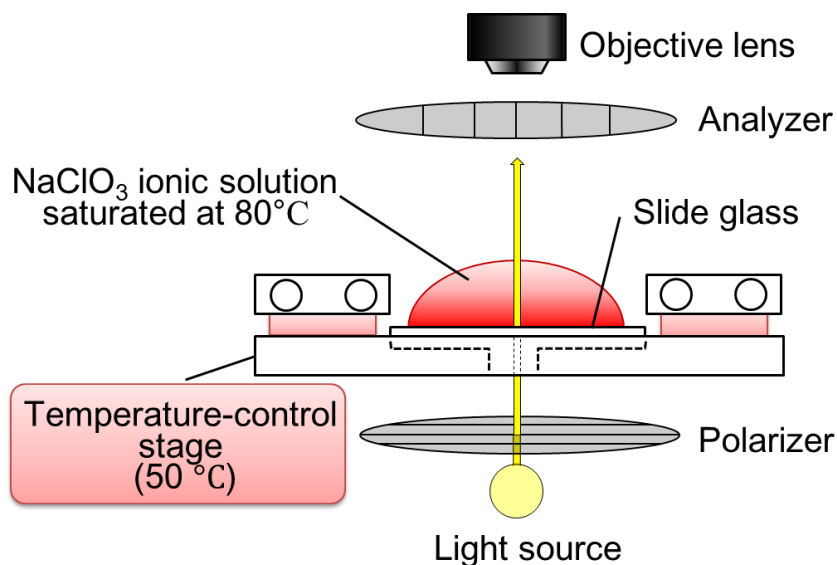
Fig. A1.2 Schematic illustration indicating the geometry for polarized-light microscopic observation. The same temperature control stage as described in chapter 2 was used to control temperature during observation.
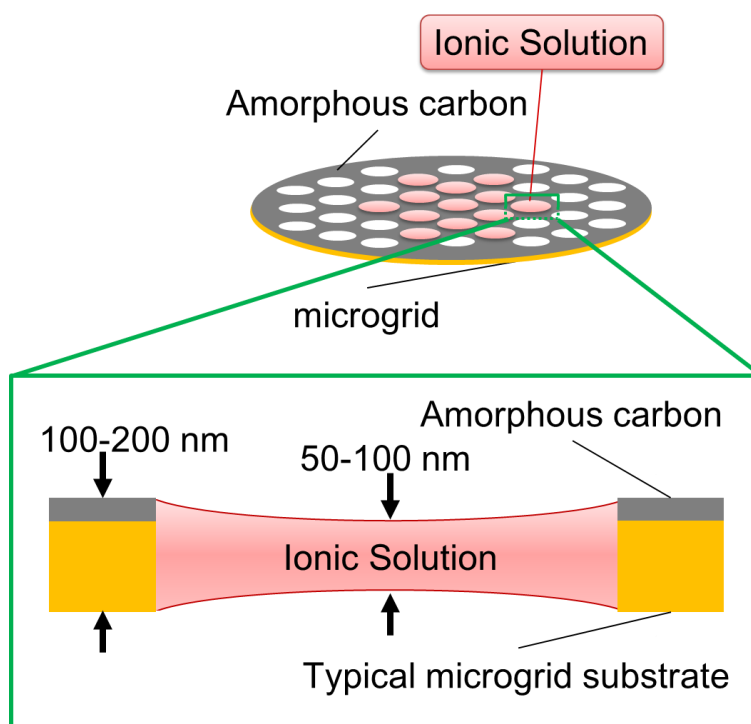
Fig. A1.3 Schematic illustration showing the TEM grid supporting the ionic $NaClO_3$ solution. The diameter of each hole of the grid is of the order of several micrometers. The ionic solution is hold in the hole and the ionic solution is self-supporting as a result of surface tension. The volume of the ionic solution held in a hole in the holey film was approximately from 10^{-19} to 10^{-18} m^3. The schematic in the green box indicates side view of the holey film on the TEM grid.

We used two TEMs: (1) a Hitachi H-8100 and (2) an H-9500 (located at Hitachi High-Technologies Corporation, Ibaraki, Japan) equipped with a double-tilt heating holder. The H-8100 TEM was operated at an accelerating voltage of 200 kV and had a tungsten filament. In this TEM experiment (1), where the H-8100 was used, the 80°C ionic solution was cooled to room temperature (~25°C) and the supercooling of the solution, ΔT, reached to 55 °C inside the sample chamber of the TEM (Fig. A1.4 left). The aim of this observation is to capture the moment of nucleation from the ionic solution. On the other hand, the H-9500 was operated at an accelerating voltage of 300 kV. In this TEM experiments(2), where the H-9500 with heating holder was used, the microgrid that used in thel TEM experiment (1) was then placed on the heating holder equipped with the H-9500 and then the microgrid was heated from room temperature to 60°C (Fig. A1.4 right) while observing. Namely, the solution becomes undersaturated condition during observation.
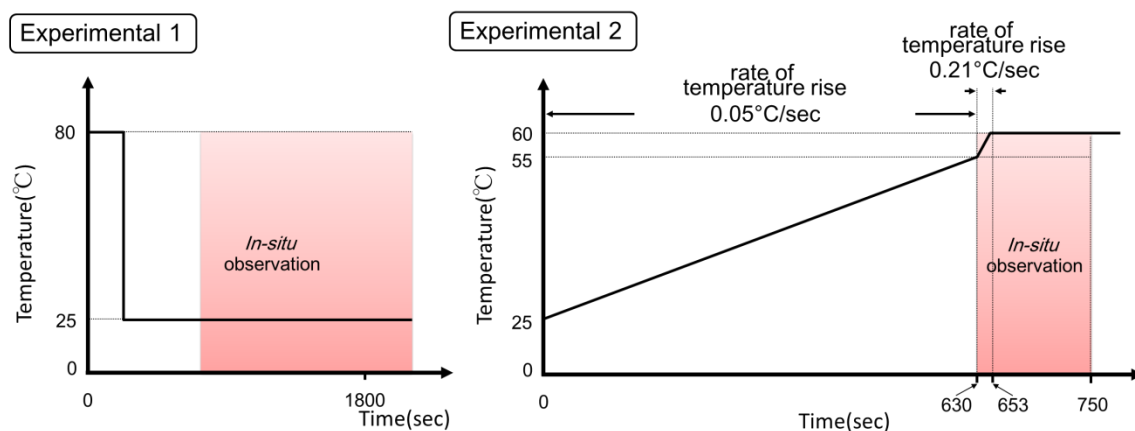

Fig. A1.4 Temperature sequence in two TEM observations. Upper schematic shows the temperature sequence in experiment 1. In the experiment 1, the ionic solution saturated at 80°C was cooled down to 25°C, leading to supersaturated state. Lower schematic shows temperature sequence in experiment 2. An ionic solution saturated at 25°C which contains precipitate crystals in the solution was heated up to 55°C taking 630 sec and further heated up to 60°C taking 23 sec.

A1.3 Results and Discussion

A1.3.1 Observation using Polarized-Light Microscopic Observation

The waiting time before the nucleation ranged from 180 to 10 min. Fig. A1.5 shows polarized-light microscopic images of $NaClO_3$ crystals which appeared in the droplet of ionic liquid solution 180 minutes after putting the droplet on the glass substrate the temperature of which was set at 60 °C ($\Delta T = 20$ °C). As shown in Fig. A1.5 (a), numerous crystals, whose sizes are uniformly about 10 μm, formed in the ionic solution. The crystals exhibited extinction under crossed-Nicols observation, indicating the phase which nucleated is Phase I.
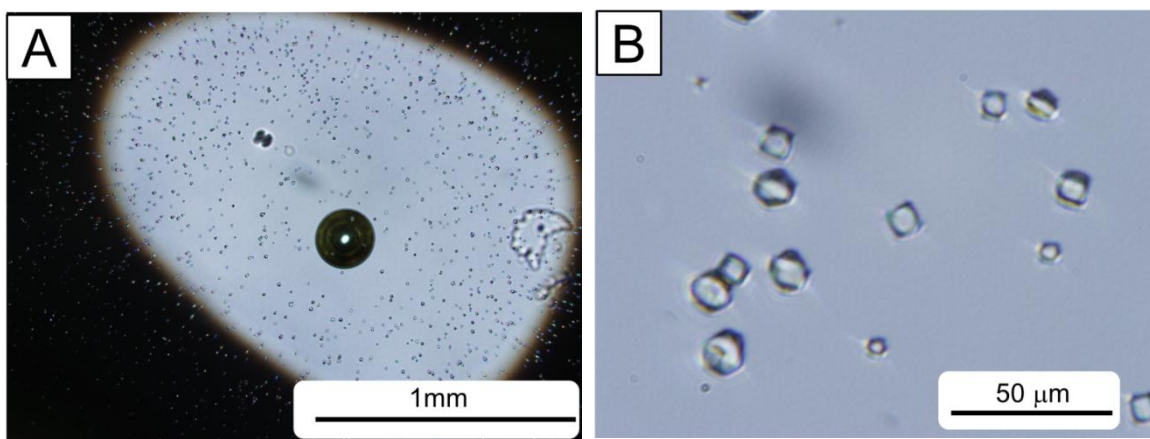

Fig. A1.5 Optical micrographs showing $NaClO_3$ stable cubic crystals which appeared inside the supersaturated ionic $NaClO_3$ solution. (a) is a micrograph captured using objective lens of 4 magnifications. It can be seen that numerous crystals appears inside the ionic solution. (b) is a micrograph captured using objective lens of 50 magnifications. 5–10 μm sized cubic crystals which forms inside the solution are shown.

A1.3.2 In-Situ TEM Observation of NaClO₃ Crystal Nucleation from Supersaturated Ionic Solvent

Fig. A1.6 shows snapshots of the *in-situ* observation using Hitachi H-8100 TEM [the experiment(1)]. Fig. A1.6 (a) shows a micrograph captured immediately after the specimen was installed into the sample chamber. The ellipse which exhibits dark contrast is ionic solution captured by holes of microgrid. In this moment, the ellipse shows uniform contrast, indicating that no object is inside the supercooled ionic solution. Fig. A1.6 (b) shows a micrograph captured 30 minutes after the micrograph (a) was captured. In contrast to the micrograph (a), several tens of numbers of spots which exhibit strong dark contrast can be seen inside the ionic solution. These spots showed up with Brownian motion about 30 minutes after the observation was started. Moreover,

the strong contrast of the spots should be due to diffraction of electron, indicating the spots are crystal. Actually, selected-area electron diffraction (SAED) pattern of the dark objects, which is shown in the inset of Fig. A1.7, exhibits Debye ring. Namely, the dark objects are proven to be crystals. Therefore, it can be said that we achieved to observe nucleation of $NaClO_3$ crystal from the supersaturated ionic solution *in-situ*. In addition, the diffraction pattern indicates that the resulting $NaClO_3$ crystal was cubic phase I.
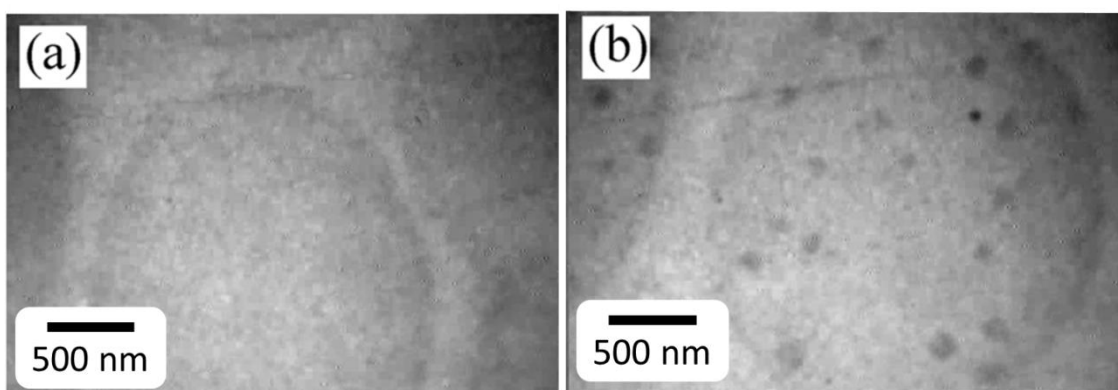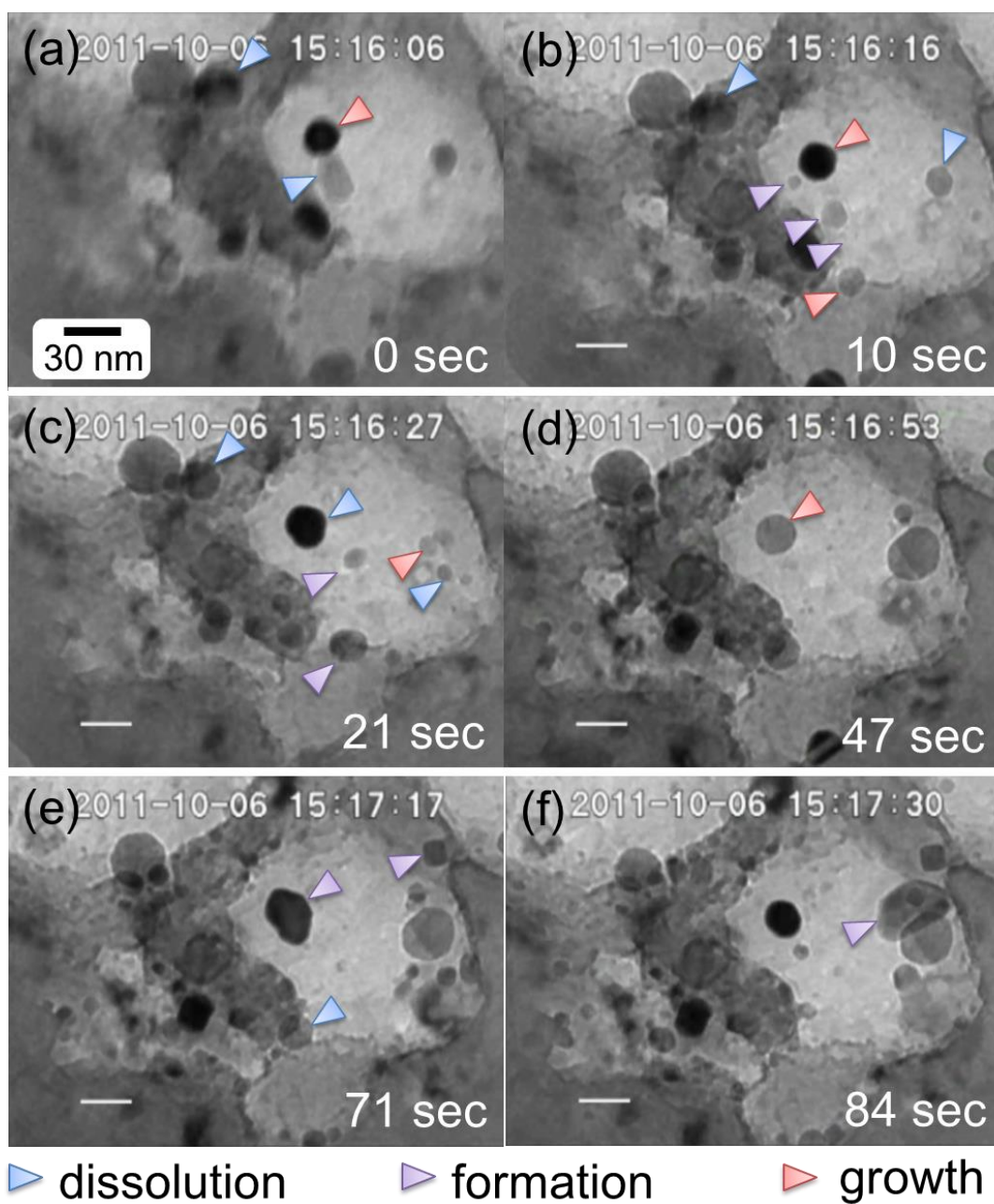

Fig. A1.6 Snapshots of *in-situ* TEM observation in experimental 1. (a) Starting ionic solution of $NaClO_3$. The ionic solution is supersaturated state because the solution was initially saturated at 80°C and it was cooled down to ~25°C (room temperature). (b) The same solution observed after 30 min at a temperature of ~25°C (supercooling $\Delta T = 55$°C). Strong contrasts in (b) show crystals of $NaClO_3$ with a diameter of 50–150 nm. The growth rate was ~10 nm s^{-1}.
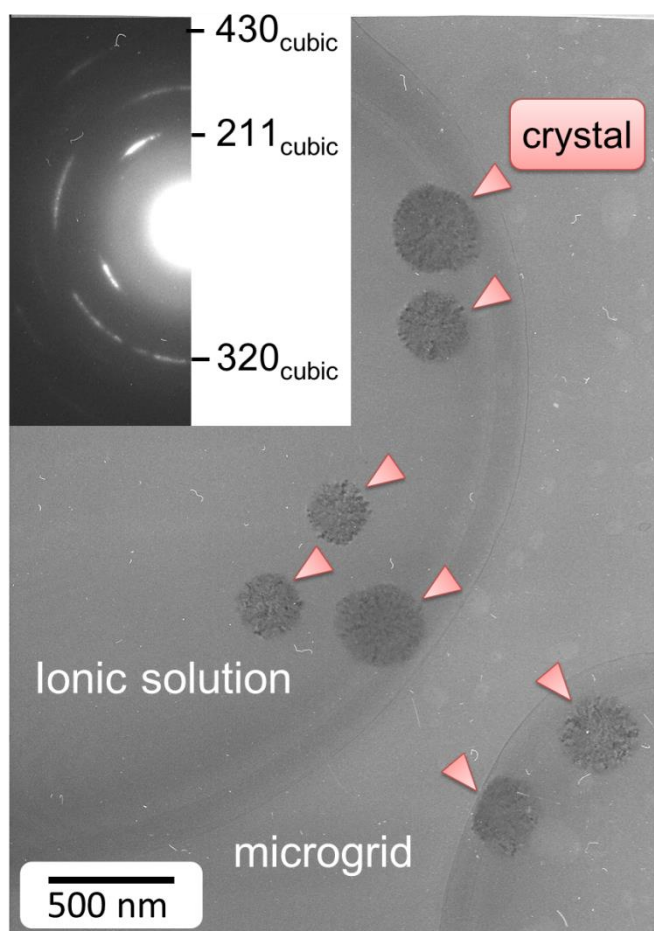
Fig. A1.7 Transmission electron micrograph of $NaClO_3$ nanocrystals formed in the ionic solution in the experimental 1 and the diffraction pattern of the crysatls (inset). The spherical strong contrast shows the nanocrystals. The diffraction pattern of the nanocrystals was rationalized by cubic crystal system of phase I.

A1.3.3 In-Situ TEM Observation of Nucleation and Dissolution of NaClO₃ Nanoparticles in Saturated Ionic Solution and Metastable Phase Formation under Unsaturated Condition.

Fig. A1.8 is still snapshots of *in-situ* bright-field TEM observation at 60 °C [the experiment(2)]. As expected, the crystals that formed in the experiment (1) started to dissolve as indicated by blue triangle in Fig. A1.8 (a) because the temperature increment of solution leads to under-saturated condition originating from the increment of solubility. Upon dissolution, the concentration of the solute in the vicinity of the crystal increases until saturation. Although no crystals are expected to form in the resulting equilibrium solution in accordance with classical nucleation theory, they actually do form as shown in Fig. A1.8 (b). As clearly shown in Fig. A1.8, particles appear and disappear rapidly in the equilibrium solution surrounding the dissolving crystal. Namely, precritical nuclei might form spontaneously under conditions at equilibrium. We propose that existence of these clustering processes must be triggered by density fluctuation. In fact, these fluctuations provoking local nanovolumes of higher concentration where precritical nuclei might form have been already observed in noncrysatllizing solutions [7]. Moreover, it has been suggested that formation of nanovolumes by density fluctuation might occur during the earliest stage of "two-step nucleation" mechanism. In the two-step nucleation mechanism, the formation of crystals in solution is viewed as a transition along two order parameters: concentration and structure. Whereas the two order parameters synchronously increases during nucleation process in the classical view, the increment of concentration is followed by the increment of structure parameter independently in the two-step nucleation mechanism [8,9] (Fig. A1.9). In the course of the two-step nucleation, density fluctuation induces localized increment of concentration parameter, leading to the formation of dense liquid phase as a precursor of stable crystalline phase. This non-classical view of nucleation has been applied to many other proteins, small organic molecules and inorganic compounds, including biominerals and colloids.

Fig. A1.8 Still snapshots of *in-situ* bright-field TEM observation at 60°C (experimental 2). The NaClO$_3$ nanocrystals repeated growth and dissolution and fluctuated their size during the observation. Blue, purple and red triangles indicate the dissolving nanocrystals, formation of nanocrystals and growing nanocrystals.
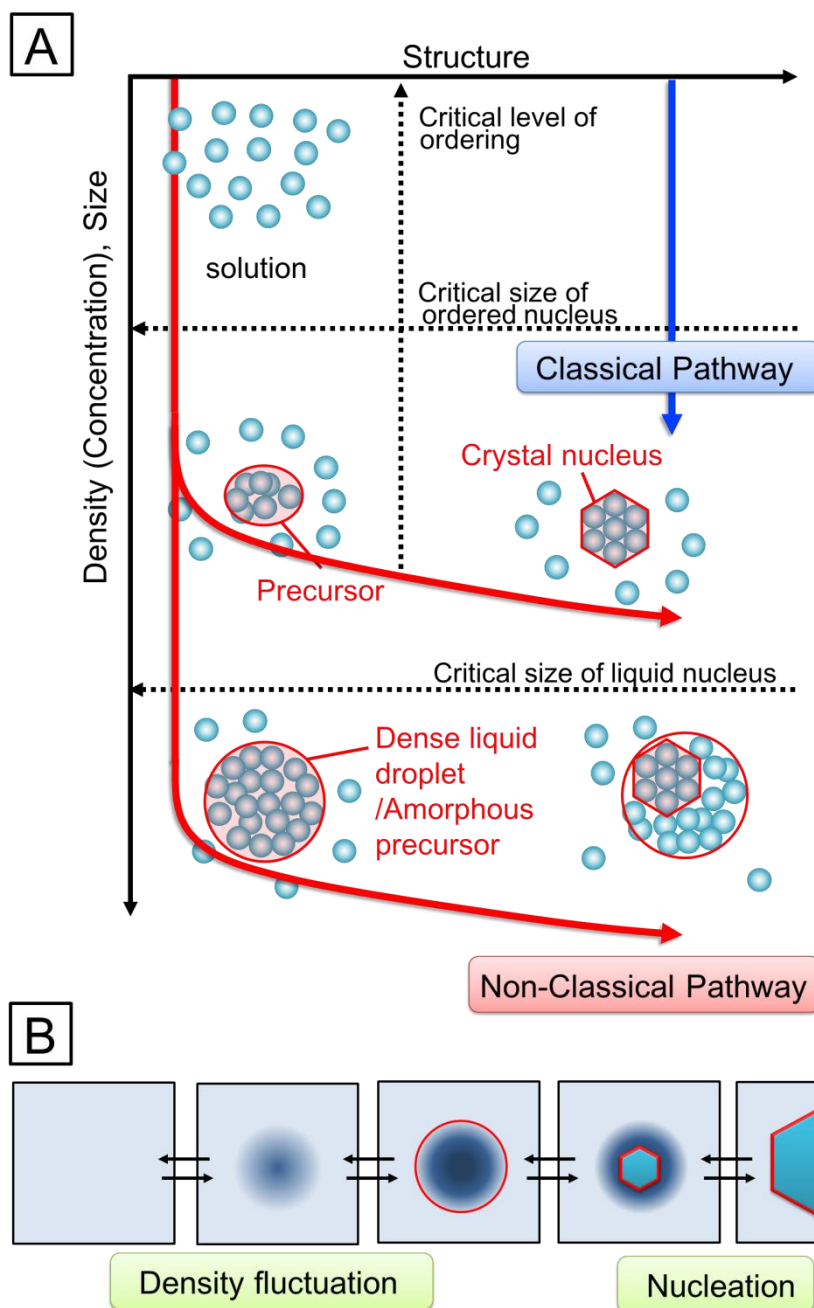
Fig. A1.9 Schematic illustration comparing classical pathway of nucleation and non-classical "two-step" nucleation pathway. (**A**) is a schematic comparing the increment of two order parameters, which are density and structure, in the classical pathway and in the non-classical pathway. Blue arrow indicates the case of classical pathway, which assumes that the molecules in the nucleus is already ordered so as to be the same as the nucleation phase from the onset of increment in density. Red arrow indicates the case of non-classical pathway in which the two order parameters are independent each other and increment of structure parameter is superimposed with the increment of density. (**B**) is a schematic showing time-evolution of two-step nucleation process. The gradation of the blue color indicates concentration of solution. The crystallization follows the formation of dense liquid droplet and occurs in the high density domain. The schematics is referred to Ref. [9]

Fig. A1.10 shows snapshots of *in-situ* bright-field TEM observations at 60°C and Fig. A1.11 shows time evolution of particle size seen in the snapshots of the Fig. A1.10. From the Fig.A1.11, we have found that the formation rate of crystalline clusters is unexpectedly high (~3×10^{20} m^{-3} s^{-1}), and the radial growth rates of the crystalline clusters are fast (4.2 ± 2.7 nm s^{-1} (Fig. A1.12). Therefore, repetitive dissolution and formation of the nanoparticles is possibly due to the formation of pre-critical nuclei originating from density fluctuation, not due to the typical nucleation caused by bulk supersaturation .

  In addition to the stable cubic nanoparticles, we also observed the metastable phase III crystals identified by *in-situ* electron patterns (Fig. A1.10). As shown in Fig. A1.11, the lifetime of the metastable phase III nuclei, whose particle size versus time profile is indicated by green triangle, is shorter than that of the stable phase I crystal indicated by black triangle for instance. It is also clear that, whereas the growth rates of the stable phase I crystal are similar (4.2 ± 2.8 nm s^{-1}) to the metastable crystals (3.6 ± 1.1 nm s^{-1}), the dissolution rate of the metastable crystals (12.6 ± 5.4 nm s^{-1}) is faster than that of the stable crystal (7.6 ± 6.1 nm s^{-1}). Thus, the solubility of the metastable monoclinic phase can be inferred to be higher than the solubility of the cubic phase for the whole range of temperature of the experiment. Ostwald's rule of stages states that the precipitation sequence of polymorphs starts with the less stable phase and ends with the more stable one [10]. Our results demonstrate that pre-nucleation clusters of different polymorphs form simultaneously and independently of their respective solubility values. The arrangement of the molecules or ions arising from a maximal local concentration seems to be merely the result of a compromise between the disorder of the accumulation, i.e., the rate at which molecules or ions cluster in a single location and the degree of structural order of the different polymorphic configurations. The lifetime of the nuclei with different structural arrangements depend on their individual surface energy and its variation with size [1], thus explaining the exclusive detection of the cubic phase at micrometer or larger scale. The formation of polymorphs simultaneously at the earliest stages of nucleation is a plausible explanation for the formation of metastable phases as precursors well below the equilibrium solubility, reported by Van Driessche *et al.*[11]. Van Driessche *et al.* have figured out based on the cryo-HRTEM observation that nanocrystalline metastable phase can precipitate even in "forbidden" condition below its predicted solubility as a precursor of stable phase in calcium sulfate system [11] (Fig. A1.13). Our observational results might indicate the possibility that the formation pathway of chiral crystal via achiral metastable precursor holds in the wide range of

concentration condition even in slightly supersaturated with respect to the chiral stable phase.
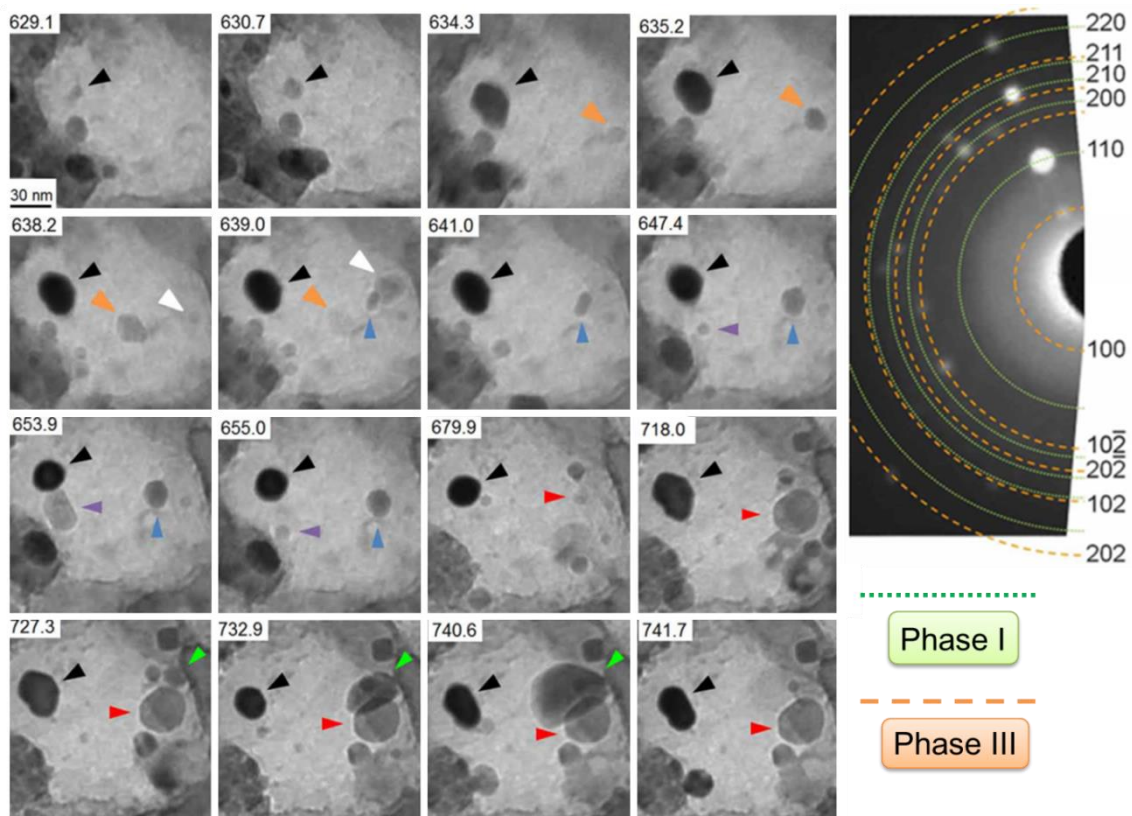

Fig. A1.10 Still snapshots of the *in-situ* bright-field TEM observation at 60°C (experimental 2) and the still snapshot of in-situ diffraction pattern of the in-situ birght-field observation. Left micrographs shows the snapshots. Black, orange, white, blue, purple, red and green triangle are corresponds to the colors in the following Figures. Right image shows the diffraction pattern of the in-situ bright field observation. The diffraction pattern exhibits a pattern that cannot be rationalized by cubic symmetry (the symmetry of phase I). The pattern can be rationalized by monoclinic symmetry (the symmetry of phase III).
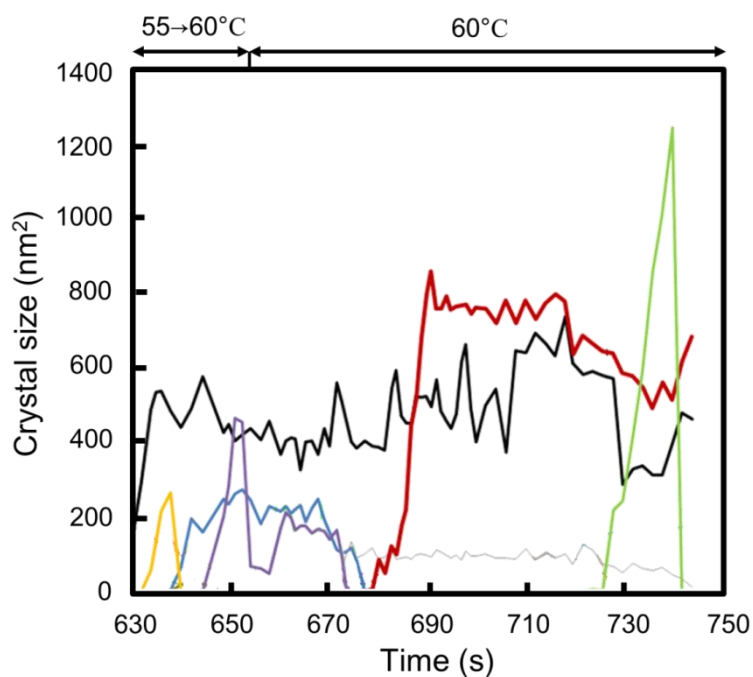
Fig. A1.11 Time evolution of particle size. The size was measured from the surface of their projected areas on the focal plane of the TEM. Each line is marked with the same colors and symbols used in Fig.6.13. Note that some of the crystals fluctuate in size. A most noticeable phenomenon is that crystal dissolution did not occur smoothly by continuous loss of mass. The amplitude of these size fluctuations is sometimes as large as 20 nm.
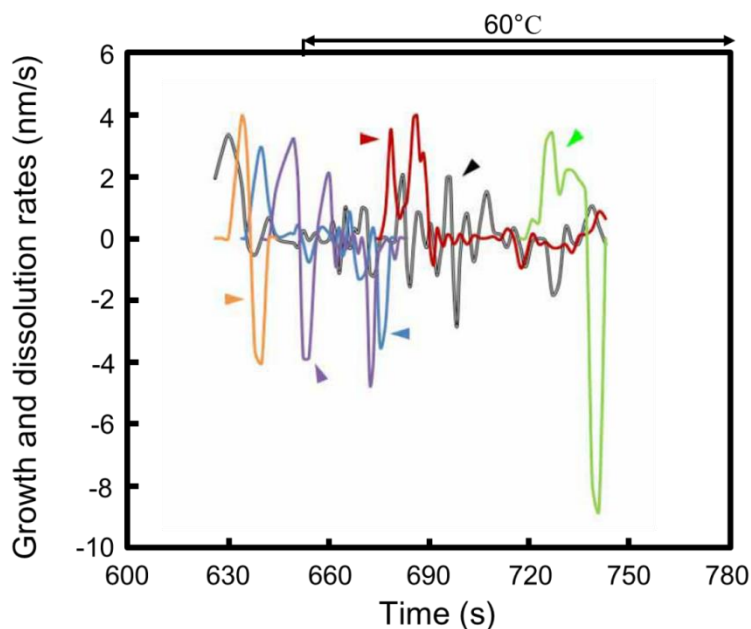
Fig. A1.12 Growth and dissolution rates calculated from the date shown in Fig. 6.14. Each line is marked with the same colors and symbols used in Fig. 6.13. Note that some of the crystals fluctuate in rate both of positive and negative. Crystals marked red triangle merge into a single crystal thereby the rates go out of the graph due to instantaneous increase of their size. A most noticeable phenomenon is that growth and dissolution rate did not change gradually by time.

192
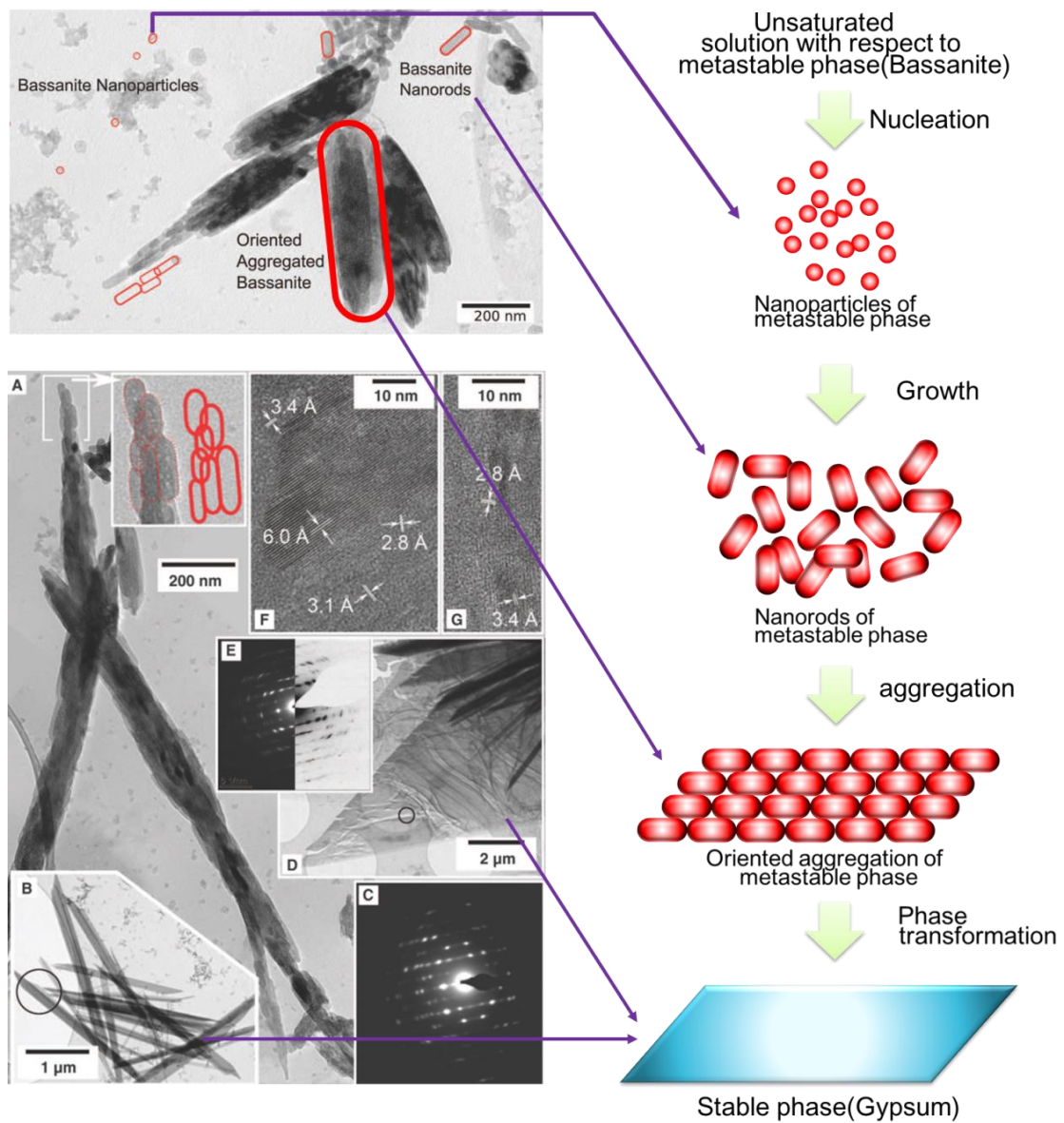
Fig. A1.13 The formation process of gypsum crystal intermediated by aggregation of bassanite, which is a metastable phase, nanocrystals [11]. Bassanite nanoparticle forms in under-saturated solution at the initial stage of crystallization and the nanoparticles elongates towards c-axis as they grow. Then, the resulting nanorods aggregate while orienting along the c-axis. Ultimately, the oriented aggregation of the nanorods transforms to stable gypsum crystal. This formation process, which is suggested by Van Driessche et al., is a typical example of non-classical pathway.

A1.4 Summary of Appendix 1

The earliest stage of NaClO$_3$ chiral crystallization from solution was directly and nanoscopically observed *in-situ* by means of TEM using ionic liquid as solvent. The findings revealed in this chapter are summarized below.

- Polarized-light microscopic observation has shown that ionic liquid can be used as a solvent for crystallization experiment of NaClO$_3$. Nucleation of NaClO$_3$ phase I takes place in supercooled ionic solution of NaClO$_3$.
- The author's group have achieved to nanoscopically observe nucleation of NaClO$_3$ chiral crystals that takes place in supercooled ionic solution by means of TEM *in-situ*.
- The author's group have achieved to directly capture the dynamics of nucleation and dissolution of NaClO$_3$ nanocrystals, which are presumably pre-nucleation cluster, in saturated ionic solution at the resolution of 0.75 nm by means of TEM *in-situ*.
- The NaClO$_3$ nanoclusters repeatedly forms and dissolve even in a saturated condition, where no crystals are expected to form or dissolve. The formed nanovolumes are possibly provoked by density fluctuation in the solution, thus suggesting that they are pre-nucleation cluster.
- Combination of *in-situ* diffraction pattern and bright-field TEM observation have shown that nanocluster of metastable achiral phase III of NaClO$_3$ and stable chiral phase I do from simultaneously and independently of their respective solubility values even in saturated condition with respect to the phase I. This phenomenon is presumably due to the order and disorder of accumulation of ions dissolving in the solution and also due to the competition between bulk energy contribution and surface free energy contribution, which have been considered to be enhanced as the particle size decreases.
- The formation of polymorph simultaneously and independently of their solubility as the earliest stage of nucleation might be plausible explanation for the formation of metastable phases as precursors well below the equilibrium solubility [11].

References

[1] A. Navrotsky, *Proc. Natl. Acad. Sci.* **101(33)**, (2004), 12096.

[2] D. Li, M. H. Nielsen, J. R. I. Lee, C. Frandsen, J. F. Banfield and J. J. DeYoreo, *Science* **336**, (2012), 1015.

[3] J. M. Yuk, J. Park, P. Ercius, K. Kim, D. J. Hellebusch, M. F. Crommie, J. Y. Lee, A. Zettl and A. P, Alivisatos, *Science* **336,** (2012), 61.

[4] R.D. Rogers and K. R. Seddon, *Science* **302**, (2003), 792.

[5] S. Arimoto, M. Sugimura, H. Kageyama, T. Torimoto and S. Kuwabata, *Electrochim. Acta* **53**, (2008), 6228.

[6] H. Itho, K. Naka and Y. J. Chujo, *J. Am. Chem. Soc.* **126,** (2004), 3026.

[7] A. Vailati, R. Cerbino, S. Mazzoni, C. J. Takacs, D. S. Cannell and M. Giglio, *Nat. Commun.* **290**, (2011), 290.

[8] P. G. Vekilov, *J. Cryst. Growth* **275**, (2005), 65.

[9] P. G. Vekilov Nanoscale. **2**, (2010), 2346.

[10] W. Z. Ostwald, *Phys. Chem.* **22**, (1897), 289.

[11] A. E. S. Van Driessche, L. G. Benning, J. D. Rodriguez-Blanco, M. Ossorio, P. Bots and J. M. Gacía-Ruiz, *Science* **336**, (2012), 69.

APPENDIX 2
PRINCIPLE OF OPTICAL TRAPPING

Optical trapping is the technique to spatially trap a small dielectric particle by tightly focusing light at the focal spot. This technique has been widely applied as "optical tweezers" to manipulate various micron or submicron objects, for instance, biological cell, virus, colloidal particle and fourth. This appendix briefly describes the principle of the optical trapping, which plays important role in the laser-induced crystallization experiments shown in the chapter 6. The principle of the optical trapping can be explained by two interpretations; (1) the geometric optical interpretation on the basis of the ray optics approximation and (2) the electromagnetic interpretation on the basis of the Rayleigh approximation, depending on the size of the particles to be trapped. If the radius of the particles, r, is much larger than the wavelength of the light, λ, (usually r > 10λ, called as Mie regime), the geometric optical interpretation can be applied. On the other hand, if the radius is much smaller than the wavelength (usually r < λ/10), the electromagnetic interpretation can be applied.

For Mie regime, the principle of optical trapping can be explained by the conservation of momentum of light. Light has the momentum and the momentum obeys the law of conservation. Therefore, when the direction of the momentum of the light is changed by reflection or refraction the difference of the incident momentum and reflected or refracted momentum must be compensated by some way. The difference is compensated by exerting the force called as "radiation pressure" on the medium which caused the reflection or refraction of the light. Fig. A2.1 **A** shows geometric schematics explaining radiation pressure. In the case of reflection, the difference between the incident momentum and the reflected momentum, ΔP, is outward and perpendicular to the refractive surface. Thus, radiation pressure inward to the refractive medium generates to compensate ΔP. We can understand the radiation pressure which generated by the refraction of the light in the same manner. Fig. A2.1 **B** shows the schematics explaining the principle of optical trapping of dielectric Mie particle, the particle larger than the wavelength of the focused light. The deviation of the focal spot from the center of the particle results in the generation of the radiation pressure so as to coincide the center of the particle with the focal spot. As a consequence, the particle is trapped at the focal spot. Fig. A2.2 shows optical trapping of polystyrene colloidal particle (2 μm) dispersed in water using the optical setup for the laser-induced crystallization experiment. As shown in Fig. A2.2, stable trapping of a particle at the focal spot and its manipulation is

possible by focusing laser light.
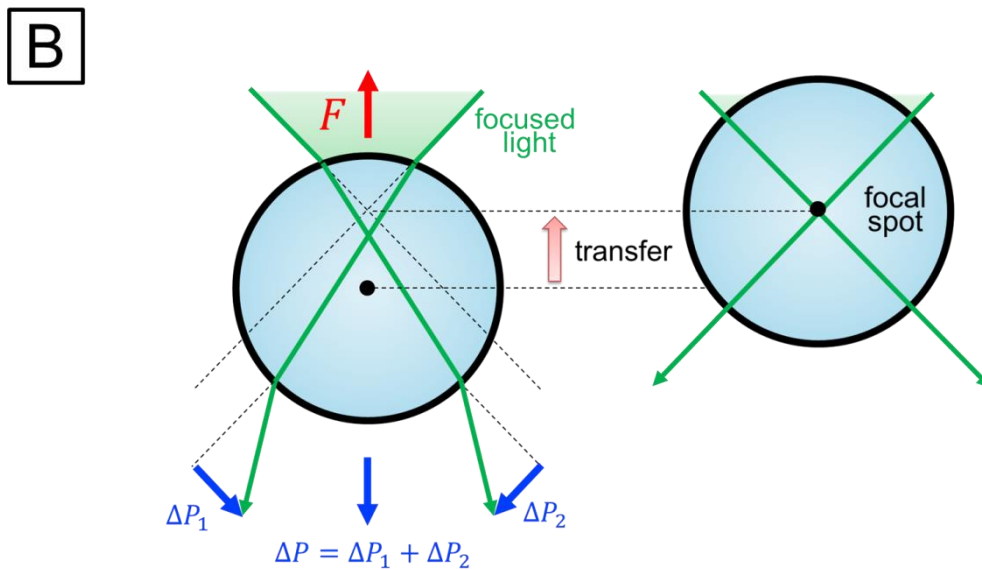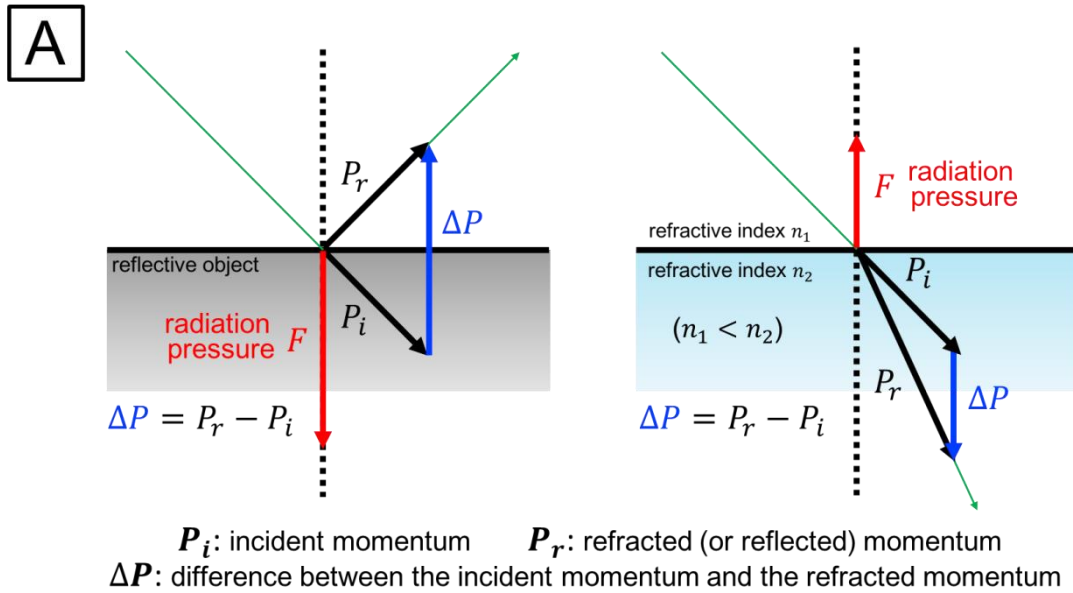
Fig. A2.1 The principle of the optical trapping based on the geometric optics in the Mie regime. **A**: the generation of the radiation pressure because of the conservation of momentum of the light. Left schematic shows the case of reflection. Right schematic shows the case of refraction. When the light path changes the radiation pressure generates. **B**: the optical trapping of the Mie particle by irradiating a focused light to the particle. The particle is subjected to the radiation pressure so as to coincide the focal spot with the center of the particle.
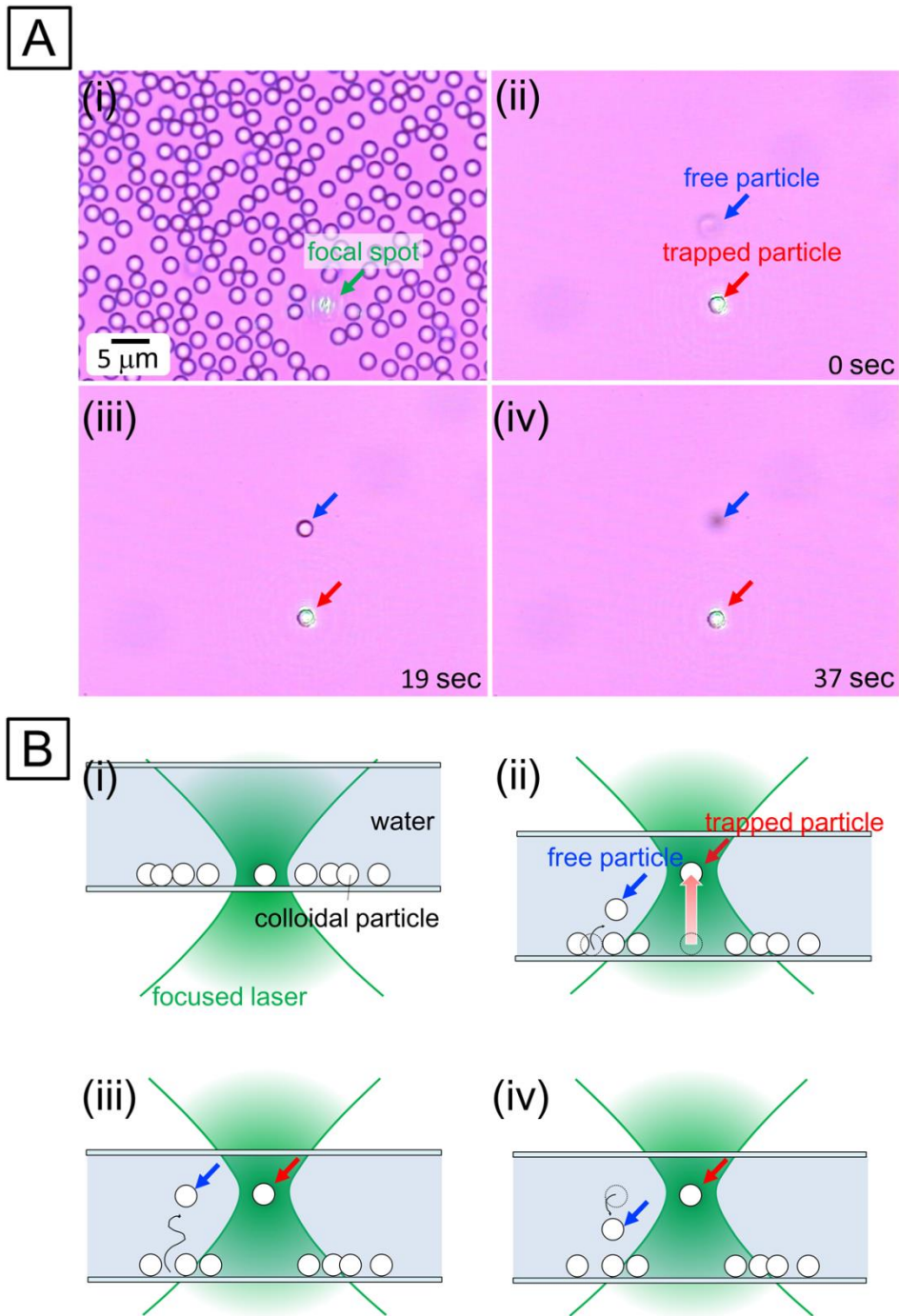
Fig. A2.2 Optical trapping of a polystyrene colloidal particle dispersed in water. **A:** shows optical micrographs of the optical trapping, and **B:** the geometry of the colloidal particles and focal point. Each schematic corresponds to the situations where micrographs shown in **A** are captured. The colloidal particles can be stably trapped and manipulated.

On the other hand, for Rayleigh regime, the principle of the optical trapping is explained by Lorentz force exerted on the particle. The particle in the field of light is approximated to be a point dipole in the Rayleigh regime (Rayleigh approximation). The point dipole is subjected to the Lorentz force from the surrounding electromagnetic field. The Lorentz force, F, can be expressed as:

$$F = q\left(E + \frac{dx}{dt} \times B\right) \tag{A2.1}$$

where q is the electrical charge, E is electrical field, B is the magnetic flux density. Because the Lorentz force exerted on a point dipole can be calculated by substituting the two terms for the electric field in the Eq. (A2.1). The polarization of a dipole is given by

$$p = qd \tag{A2.2}$$

where d is the distance between the two charges. The distance, $x_1 - x_2$, is infinitesimal because of the point dipole approximation. Taking into account that two charges have opposite signs, the Lorentz force can be expressed as

$$F = q\left(E_1(x_1, y, z) - E_2(x_2, y, z) + \frac{d(x_1 - x_2)}{dt} \times B\right) \tag{A2.3 a}$$

$$F = q\left(E_1(x, y, z) + ((x_1 - x_2) \cdot \nabla)E - E_1(x, y, z) + \frac{d(x_1 - x_2)}{dt} \times B\right) \tag{A2.3 b}$$

Since E_1 is canceled out. Eq. (A2.3 b) can be simplified as

$$F = (p \cdot \nabla)E + \frac{dp}{dt} \times B = \alpha\left[(E \cdot \nabla)E + \frac{dE}{dt} \times B\right] \tag{A2.4}$$

where α is the polarizability (p = αE). Using two equations (1) vector analysis equality (2) one of the Maxwell's equations,

$$(1) \quad (E \cdot \nabla)E = \nabla\left(\frac{1}{2}E^2\right) - E \times (\nabla \times E) \tag{A2.5}$$

$$\text{(2)} \quad \nabla \times \mathrm{E} = -\frac{\partial \mathrm{B}}{\partial t} \tag{A2.6}$$

Eq. (A2.4) can be rewritten as:

$$\mathrm{F} = \alpha \left[\frac{1}{2} \nabla E^2 + \frac{d}{dt}(E \times B) \right] \tag{A2.7}$$

The second term in Eq. (A2.7) is the time derivative of Poynting vector of incident electromagnetic field, which describes the power per unit area and per unit time passing through a surface. Since the time average of the Poynting vector of a laser light, which is used as incident light for optical trapping, is constant with respect to time the second term becomes zero. Thus, the Lorentz force can eventually be reduced to:

$$F_{grad} = \frac{1}{2} \alpha \nabla E^2 \tag{A2.8}$$

Since this force is proportional to the gradient of the square of the electrical field, this force is called as "gradient force of electrical field". In the Rayleigh regime, this gradient force acts as trapping force. However, in practice, scattering force also works to the particle against to the gradient force to the direction of optical axis. The scattering force, F_{scat}, can be written as

$$F_{scat} = \frac{n\langle S \rangle \sigma}{c} \tag{A2.9 a}$$

$$\sigma = \frac{8}{3} \pi k^4 r^6 \left(\frac{m^2 - 1}{m^2 + 2} \right)^2 \tag{A2.9 b}$$

where n is the refraction index of the medium of the particle, $\langle S \rangle$ is the time average of the Poynting vector of the incident light, c is the speed of light, k is the wavenumber, r is the radius of the particle to be trapped, m is relative refractive index of the particle. Since the scattering force works to the direction of optical axis, stable optical trapping requires the gradient force to overcome the scattering force.
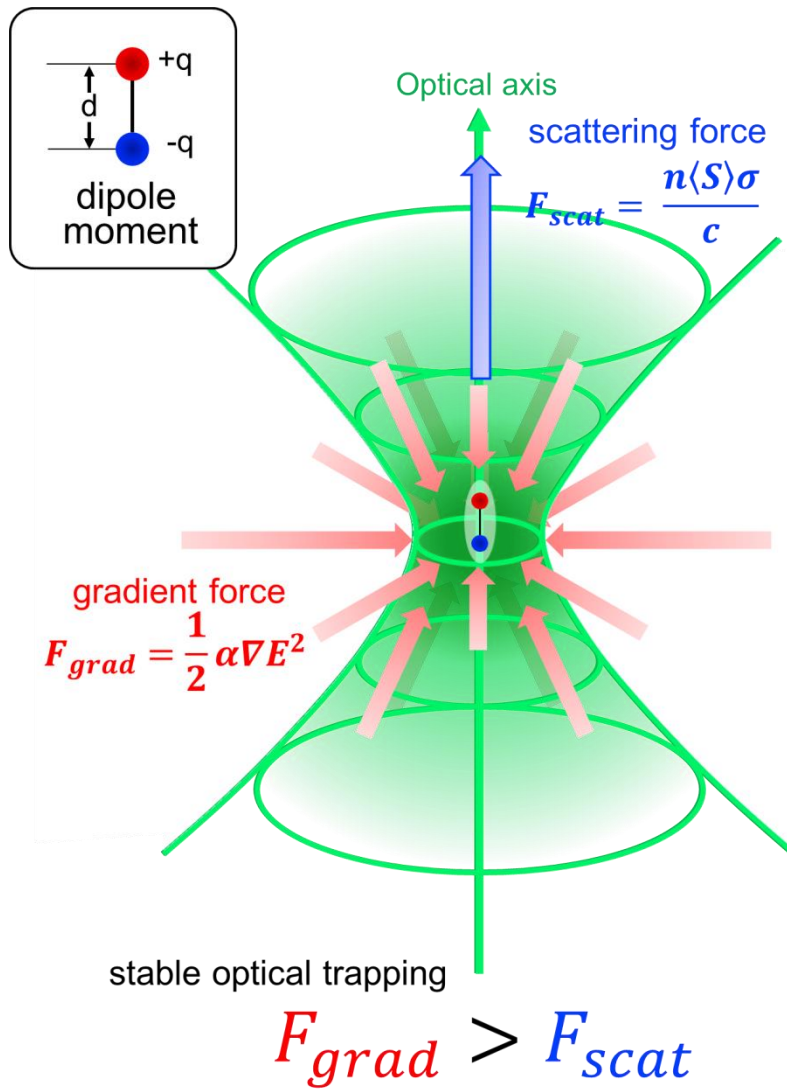
Fig. A2.3 Schematic overview of the optical trapping of Rayleigh particle in the Rayleigh approximation. A Rayleigh particle is approximated to be a point dipole. The point dipole is subjected to two kinds of optical forces: (1) gradient force of the electrical field, which acts as trapping force (2) scattering force, which makes the particle to deviate from the focal spot. The optical trapping of the Rayleigh particle requires the gradient force to overcome the scattering force.

Fig. A2.4 shows spatially-controlled aggregation of DNA-functionalized Au nanoparticles (NP) (10 nm) dispersed in solution by means of optical trapping. DNA-NPs are considered to behave colloidal particles which possess attractive force. Therefore, increment of its concentration leads to the formation of the aggregate. 36 minutes after the laser irradiation, the aggregation of the DNA-AuNPs are formed from the focal spot, implying the concentration of DNA-AuNPs locally increases at the vicinity of the focal spot because of the optical trapping of the Rayleigh NPs.
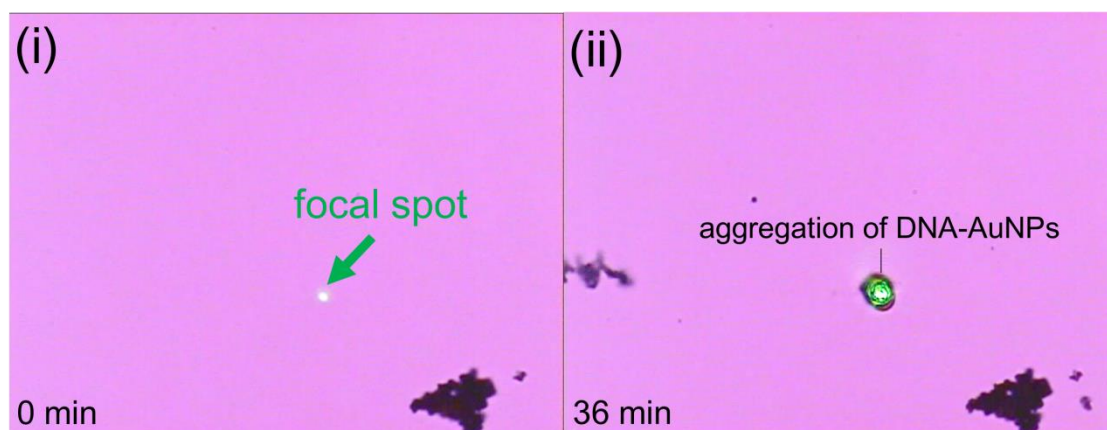
Fig. A2.4 Optical micrographs showing spatially-controlled aggregation of DNA-functionalized Au nanoparticles induced by the optical trapping of Rayleigh Au nanoparticles at the focal spot.

APPENDIX 3
CONCEIVABLE MECHANISM OF NUCLEATION FROM FOCAL SPOT IN LASER-INDUCED CRYSTARLLIZATION

It is evident that the optical trapping of Ag nano-aggregates triggered the nucleation of an achiral metastable crystal as shown in Fig. 6.4 and 6.6. Here, the author discusses how the optical trapping of Ag nano-aggregates effects the crystal nucleation. It is known that laser irradiation to a metal nanoparticle excites collective oscillations of delocalized electron on the surface of the metal nanoparticle, localized surface plasmon, because of the resonance between the electromagnetic oscillation and the collective oscillation of electrons on the surface of the nanoparticle, which originates from the electron polarization [1]. The collective oscillation of electrons gives rise to additional electromagnetic field which expands to near the surface of the nanoparticle, evanescent field. This field resulting from the coupling of light and delocalized electrons is called as "surface plasmon polariton". The surface plasmon polariton strongly enhances the electromagnetic field locally near the surface of the metal nanoparticle. Especially, when nano-scaled junctions exist between metal nanoparticles, the enhancement of the electromagnetic field becomes much stronger than without the junction. The magnitude of the enhancement has been estimated to be more than 10^6 [1]. Thus, the junction is called as "plasmonic hotspot". Such plasmonic hotspots presumably consist in Ag nano-aggregates seen in the author's experiment. Therefore, the electromagnetic field of incident light is possibly enhanced strongly at the trapping point of Ag nano-aggregates.

The wavelength in which the plasmonic resonance occurs depends on the material that constructs the nanoparticle and corresponds to the specific absorption peak. In the case of single Ag nanoparticle (10 nm), the absorption peaks is about 400 nm. Therefore, surface plasmon resonance is seemingly weak. However, it has been pointed out that the absorption peak shifts to long-wavelength side as the nanoparticles forms longer chain by aggregation (Fig. A2.1) [2]. Therefore, The 532 nm laser, which is used in the current experiment, possibly induces surface plasmon of Ag nano-aggregates. Because the Ag nano-aggregates presumably have several plasmonic hotspots the electromagnetic field can be locally enhanced at the hotspots in the current experiment.
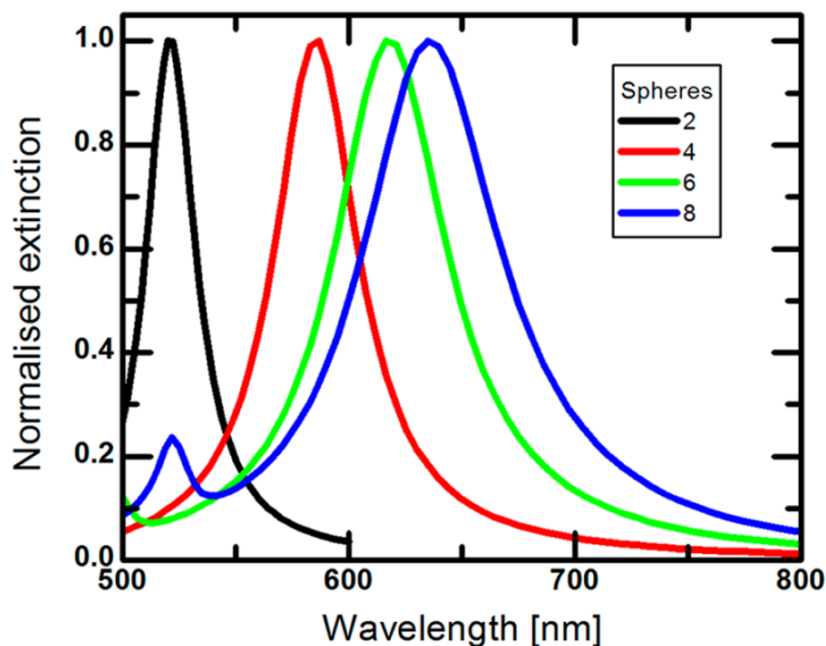
Fig. A2.1 Theoretically predicted extinction (absorption + scattering) spectra in plasmonic resonance of a chain of Ag nanoparticles (34 nm). These results were obtained from full electrodynamics calculations carried out using finite element modeling [3]. The calculation was carried out by assuming 1.5 nm particle spacing of the chain. The black, red, green and blue line indicates the case that the number of particles is 2, 4, 6, 8, respectively. It can be seen that absorption peak exhibits red-shift as the number of particles increases.

The plasmonic phenomena that possibly promotes the nucleation may include (i) enhanced optical trapping at the hotspots, (ii) plasmonic heating. Sugiyama *et al.* have demonstrated that optical trapping of crystal cluster existing in D_2O solution of glycine increases the concentration of the solution locally at the focal spot of IR laser irradiation and induces the nucleation of glycine crystal from the focal spot [4]. Namely, optical force exerted on cluster gathers the clusters to the focal spot, inducing the nucleation. Moreover, Xu *et al.* has calculated the attainable optical force at a plasmonic hotspot between two Ag nanoparticles dimer on the basis of extended Mie theory (Fig. A2.2) [5]. According to their study, the net optical force at the hotspot was calculated to be 62 pN in the direction towards the other particle of the dimer in the case that a dimer of 50 nm sized Ag nanoparticles with 1 nm gap was excited by light whose intensity is 1 mW/μm^2 (λ = 760 nm). This can be compared to a usual optical force, which is only 0.3 pN. Therefore, sodium chlorate ions dissolving in aqueous solution, which is relatively insensitive to the optical force compared to organic molecules, might be gathered by the

surface-plasmon-enhanced optical trapping. This effect may contribute to the promotion of the nucleation of the achiral metastable crystal. Additionally, it has been reported that the surface-plasmon-enhanced electromagnetic field causes significant local heating, called as plasmonic heating [6,7]. Bendix *et al.* have directly and quantitatively measured temperature rising caused by the plasmonic heating using the feature of phase transition of lipid bilayer. In their study, a gold nanoparticle adhered to a supported lipid bilayer whose phase transition temperature is 33°C was optically trapped by focused IR laser (λ = 1064 nm) at 28°C (therefore, the bilayer undergoes phase transition from gel phase to liquid disordered phase when the temperature in the region around the trapped nanoparticle was elevated by more than 5°C .).The temperature rising at the focal spot was estimated by measuring the diameter of the region where the lipid bilayer was melted and by fitting using a function that expresses temperature increment by steady-state diffusion of heat from a point heat source. The temperature rising by the plasmonic heating was found to be significant as shown in Fig. A2.3. Fig. A2.3 shows a profile of the temperature rising at the focal spot versus incident intensity.
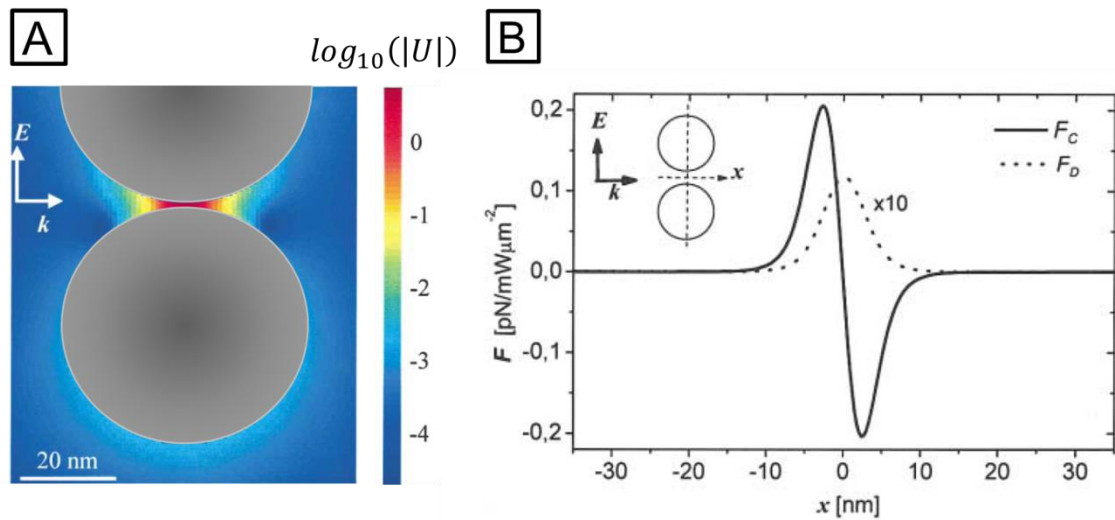

Fig. A2.2 A Spatial variation of optical potential U in units of $k_B T$ (T = 300 K) around a chain composed by three Ag nanoparticles in water excited at a collective surface plasmon resonance. The radius of Ag nanoparticles is 25 nm, the particle spacing is 1 nm and the intensity of incident light is 10 mW/μm^2. The excitation wavelength is 760 nm. k is the wave vector and E is electrical field vector of incident LPL. **B** The gradient force and the dissipative force along the *x* axis through a gap of the Ag nanoparticle dimer. The particle radius is 45 nm, the particle spacing is 1 nm and the excitation wavelength is 550 nm. The solid line indicates the gradient force, F_c, and the dashed line indicates the scattering force, F_D. The scattering force is indicated with intensity of 10 times. According to Xu *et al.*, it was shown that $|\langle F_c \rangle| > 10|\langle F_d \rangle|$, indicating that trapping force is enough to overcome the scattering force.

In the case that the diameter of Au nanoparticle is 200 nm and incident intensity is 100 mW, for instance, temperature rising was estimated to be more than 150 K [8]. In our experiment, incident intensity is about 1W, thus, allowing us to estimate that the temperature rising at the focal spots was enough to evaporate the solvent rapidly. Although one may expect that moderate temperature rising can suppress the nucleation since temperature rising increases the solubility of the solvent, this effect may be insignificant because the temperature rising by the plasmonic heating is possibly large enough to boil the solution. The solvent evaporation by the plasmonic heating possibly promotes the nucleation of achiral metastable crystal. Therefore, optical trapping of Ag nano-aggregates at the solution-air interface possibly induces the nucleation of achiral metastable crystal by two kinds of plasmonic phenomena: (1) surface-plasmon-enhanced optical trapping of solute molecule (2) rapid localized evaporation of solvent caused by the plasmonic heating. (Fig. A2.4)
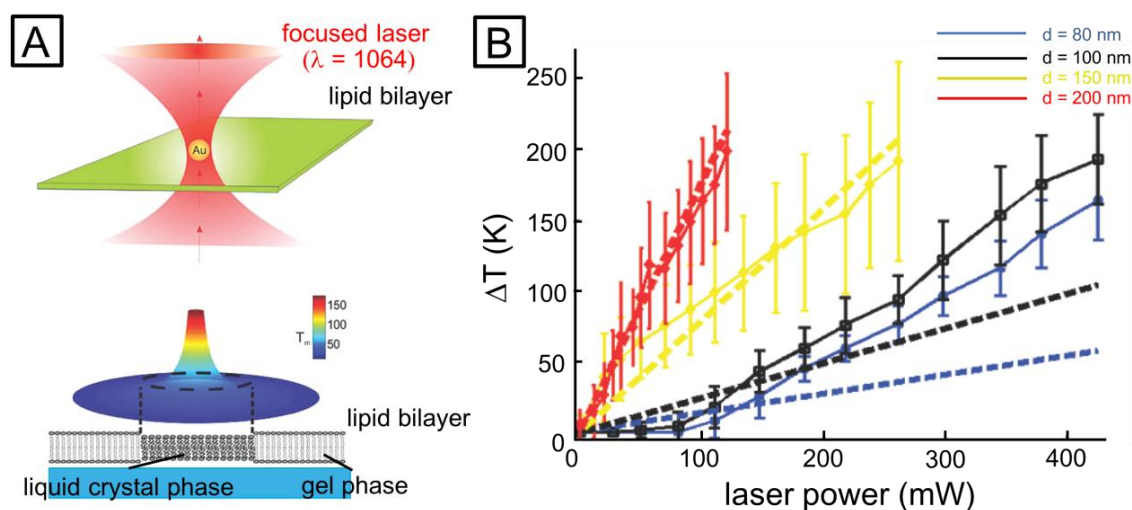
Fig. A2.3 Direct measurement of temperature rising caused by plasmonic heating investigated by Bendix *et al.* **A** schematic overview of the measurement. Au nanoparticles adhered to a lipid bilayer, whose phase transition temperature from gel phase to disordered liquid crystal phase is 33°C, was optically trapped using Infrared focused laser at 28°C. Since the plasmonic heating by the optical trapping leads to phase transition of the lipid bilayer, the radius of the domain of liquid crystal phase allows us to estimate the temperature of the trapping point. **B** Profile of temperature rising versus laser power. Blue, black, yellow, red solid line indicates the case when the particle diameter is 80, 100, 150 and 200 nm. The dashed lines are the temperature rising predicted by calculations based on Mie theory.
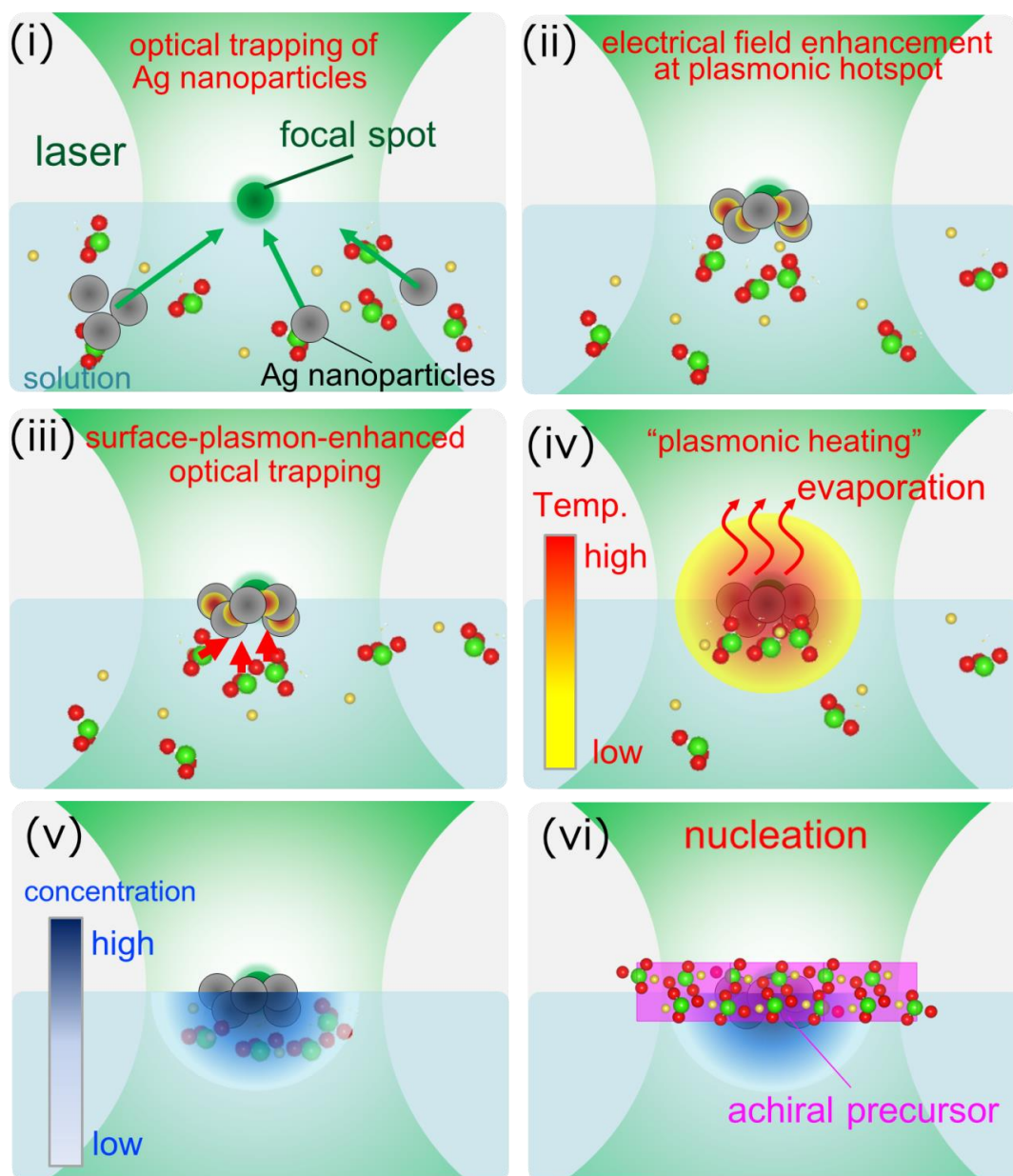
Fig. A2.4 The mechanism of crystallization from the focal spot. (i) optical trapping of Ag nano-aggregates dispersed in solution. The Ag nano-aggregates are attracted to the focal spot by gradient force of electromagnetic force. (ii) electrical field enhancement at plasmonic hot spot. The field enhancement causes strong gradient of electrical field, leading to strong trapping force as shown in Fig. 7.10 (iii) Surface-plasmon-enhanced optical trapping of solute molecule. (iv) plasmonic heating. Optical trapping of Ag nano-aggregates leads to temperature rising caused by plasmonic heating. The temperature rising causes the localized evaporation of solvent. (v) The concentration increment at the focal spot. The concentration at the focal spot was increased by these plasmonic phenomena, surface-plasmon-enhanced optical trapping and plasmionic heating. (vi) Nucleation of achiral precursor at the focal spot.

References

[1] T. Okamoto and K. Kajiwara, *"plasmonics -fundamental and application-"* (Koudansha, Tokyo) (2013)

[2] R. Gill, L. Tian, W. R. C. Somerville, E. C. L. Ru, H. van Amerongen and V. Subramaniam, *J. Phys. Chem. C* **116**, (2012), 16687.

[3] C. G. Khoury, S. J. Norton, T. Vo-Dinh, *ACS Nano* **3**, (2009), 2776.

[4] T. Sugiyama, T. Adachi and H. Mashuhara, *Chem. Lett.* **36(12)**, (2007), 1480.

[5] H. Xu and M. Käll, *Phys. Rev. Lett.* **89(24)**, (2002), 246802.

[6] G. Baffu, R. Quidant and F. J. G. de Abajo, *ACS Nano* **4(2)**, (2010), 709.

[7] M. Perner, S. Gresillon, J. März, G. von Plessen and J. Feldmann, *Phys. Rev. Lett.* **85(4)**, (2000), 792.

[8] P. M. Bendix, S. Nader, S. Reihani and L. B. Oddershede, ACS Nano **4(4)**, (2010), 2256.

APPENDIX 4
LIST OF ABBREVIATIONS

CNT: Classical Nucleation Theory

PLM: Polarized-Light Microscopy

XRD: X-Ray Diffraction

SMPT: Solution-Mediated Phase Transformation

SSPT: Solid-Solid Structural Phase Transformation

MT: Martensitic Transformation

CPL: Circularly Polarized Light

CD: Circular Dichroism

LPL: Linearly Polarized Light

EPL: Elliptically Polarized Light

NPLIN: Non-Photochemical Laser-Induced Nucleation

CW: Continuous Wave

CB: Circular Birefringence

DNA: DeoxyriboNucleic Acid

NP: NanoParticle